Author:
Rivero, Andres E

Title:
Structural and aerodynamic performance of a three-dimensional compliance-based composite camber morphing wing

Structural and aerodynamic performance of a three-dimensional compliance-based composite camber morphing wing

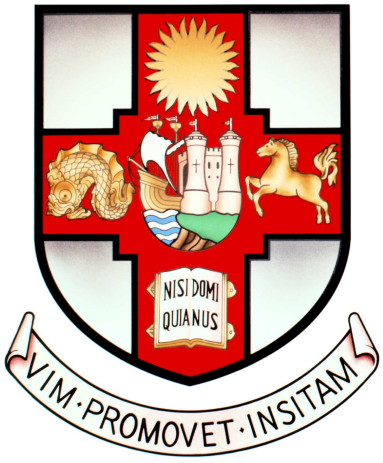

Andrés Eduardo Rivero Bracho

Bristol Composites Institute
Department of Aerospace Engineering
UNIVERSITY OF BRISTOL

A dissertation submitted to the University of Bristol in accordance with the requirements of the degree of Doctor of Philosophy in the Faculty of Engineering.

DECEMBER 2019

Word count: fifty one thousand, six hundred

For citations: Rivero, AE. (2019), Structural and aerodynamic performance of a three-dimensional compliance-based composite camber morphing wing. University of Bristol, PhD Thesis

Abstract

Fixed-wing aircraft are traditionally controlled using deflectable trailing edge rigid flaps, commonly known as control surfaces. When deflected, these flaps modify the camber distribution of the aerofoil, which changes the aerodynamic pressure distribution over the wing. These changes in aerodynamic pressure result in net aerodynamic forces and moments that can be used to control the lift generation and orientation of the aircraft. However, flaps change aerofoil shape in a sharp and discontinuous way, resulting in surface discontinuities and gaps. These discontinuities induce flow separation, which leads to a significant increase in drag. Alternatively, if these control surfaces could vary camber distribution in a smooth and continuous way, similar control authority can be achieved with a significantly reduced drag penalty. This alternative approach is known as camber morphing, and its implementation on fixed-wing aircraft could lead to a reduction in fuel consumption and noise.

One of these promising camber morphing concepts is the Fish Bone Active Camber (FishBAC) device, a compliance-based design capable of achieving large, smooth and continuous changes in camber. A preliminary 3D printed prototype of this concept was wind tunnel tested, and results showed a 25% drag reduction at the 2D aerofoil level when compared to a flap. However, this first-generation of FishBAC devices were designed using low-fidelity structural and aerodynamic models and manufactured using 3D printed plastic. To implement this technology in real aerospace structures, it is necessary to manufacture this morphing device using aerospace-graded materials. Also, it is crucial to develop modelling tools that can fully capture the complex coupled three-dimensional structural and aerodynamic behaviour of a 3D morphing FishBAC wing. These modelling techniques must be physically rich enough to accurately capture the detailed response of the morphing device while also being computationally efficient to allow for rapid design iterations and optimisation that results in better performing devices.

To address the modelling requirements, two discontinuous structural models based on composite plate model theories (i.e. Kirchhoff-Love and Mindlin-Reissner) and an aerodynamic model based Weissinger's Lifting Line Theory with viscous 2D panel method corrections were developed. Additionally, the large changes in shape that the FishBAC produces are associated with large changes in aerodynamic pressure (and vice-versa), resulting in a strong coupling between aerodynamics and structural loads. Consequently, to accurately capture both structural and aerodynamic behaviour of these morphing wings, a Fluid-Structure Interaction (FSI) analysis that couples the two different physics was developed. These structural, aerodynamic and FSI modelling techniques capture the highly orthotropic structure of the composite FishBAC, the 3D aerodynamics of the morphing wing and the interaction between structural and aerodynamic loads. Moreover, these models have a useful and appropriate level of fidelity for design and optimisation tasks: they converge using one to two orders of magnitude fewer degrees of freedom than fully coupled Computational Fluid Dynamics (CFD)/Finite Element Method (FEM)-based routines and all structural and material properties are parametrically defined and can be easily modified, allowing for wide-ranging explorations of the design space.

The development of these novel modelling techniques is complemented and validated by the design, manufacture and test of a composite FishBAC wind tunnel wing model. This prototype was manufactured using a combination of manufacturing techniques, including autoclave curing of carbon fibre prepreg, additive manufacturing (3D printing), and traditional metal machining. The composite FishBAC wing was then tested under static actuation loads, and these results were used to validate structural models. Additionally a 2D wind tunnel test was performed, where force balance, wake rake and Particle Image Velocimetry data were collected and analysed to further explore the aerodynamic behaviour of the FishBAC, and to benchmark it against both rigid (non-morphing) and flapped aerofoils.

Results presented in this thesis show that the discontinuous Mindlin-Reissner plate-based model predicts the structural behaviour of the FishBAC using 99% fewer degrees of freedom than FEM, whereas the aerodynamic viscous corrected Lifting-Line model is suitable to analyse the 3D aerodynamics of the FishBAC morphing wing at low Mach numbers and at attached flow regimes. Additionally, the FSI results showed that the 3D FishBAC wing can achieve a lift control authority (i.e. change in lift coefficient) between 0.5 and 0.63 for a wide range of angles of attack. In terms of aerodynamic efficiency, the FishBAC wing showed a 44% increase in lift-to-drag ratios at low lift coefficients, when compared to a flap. Lastly, the 2D wind tunnel test results showed efficiency gains over flaps of between 16% and 50% at the 2D aerofoil level. In summary, these results highlight the potential aerodynamic benefits that a FishBAC morphing wing can bring to a full-size aeroplane and also suggest that the developed modelling tools are suitable for future design iteration and optimisation studies of composite morphing aerostructures.

Para Valeria Chacín Mijova

Por tu apoyo incondicional a pesar tantos años de distancia e incertidumbre,
Por subir mi ánimo en ciertos momentos de tanta frustración,
Por ayudarme a ser mejor persona,
Por acompañarme a conocer el Mundo,
Por los sueños que faltan por cumplir,
Y las metas que faltan por lograr.

"No sólo no hubiéramos sido nada sin ustedes, sino con toda la gente que estuvo a nuestro alrededor desde el comienzo; algunos siguen hasta hoy. ¡Gracias totales!"
Gustavo Cerati

"Only the disciplined ones in life are free. If you are undisciplined, you are a slave to your moods and your passions."
Eliud Kipchoge

Acknowledgements

First and foremost, I would like to thank my parents Francisco Rivero and Doly Bracho for their support throughout my entire education. You created an ideal environment for us to thrive by always giving us the right level of support. You always encouraged me to pursue my dreams of studying aerospace engineering and then a PhD, even though that meant moving far away from our home in Caracas, Venezuela; first to Blacksburg, Virginia and then to Bristol, UK. You taught us the values of excellence, persistence, discipline and integrity, which have been crucial values throughout my studies. I would also like to thank my twin sister Andrea for always reminding me that no goal is unachievable. Your work ethic and discipline are admirable and they inspire me to always step outside of my comfort zone.

During my undergraduate studies, I became interested in morphing wings. Coming to Bristol to do a PhD in morphing (as part of the ACCIS CDT) was a dream come true, which would not have been possible without the fully-funded scholarship offered by Prof. Paul Weaver as CDT director. As an overseas student, I am aware of how fortunate I am for being offered a fully-funded scholarship, and I will always grateful for the trust that Prof. Weaver placed in me.

I was also fortunate to have an excellent primary supervisor, Dr Benjamin King Sutton Woods, who gave outstanding supervision in the past three years. You gave me enough freedom to become intellectually independent while still offering enough support when I needed it. You also made sure that I learned a broad set of skills that I am sure will be useful throughout my career. You care about your students' well-being, and you have created a healthy work environment for us. I am glad to consider you a friend, and it is an honour to be your first PhD student to graduate.

I would also like to thank Prof. Paul Weaver as one of my secondary supervisors. You have also been very supportive of my PhD work and I have learned many things from you, especially on structural mechanics and composite laminates. You always give priority to students and their work and I have enjoyed the discussions we have had in the past four years. Additionally, I thank Prof. Jonathan Cooper as my other secondary supervisor for all the useful feedback he gave me during my project, especially on the aerodynamics and FSI parts of it. You always brought fresh ideas to my research and offered good suggestions on where to go next.

Furthermore, I would like to acknowledge my colleagues and friends in ACCIS, especially my CDT cohort (CDT15); I am grateful for your support and friendship. Special thanks to Vincent Maes, Aewis Hii, Rob Worboys, Behjat Ansari, Olivia Leao, Yannick Mayer, Beth Russell, Tamas Rev, Beth Hickton, David Brigido, Mark Schenk, Matt O'Donnell, Sergio Minera and Michael Dicker. Additionally, special thanks to Stephane Fournier for helping me build and wind tunnel test the composite FishBAC wing. I have enjoyed working with you and I'm sure next year will be a fun one working together in SABRE. I would also like to acknowledge my Swansea University colleagues, Dr Chen Wang and Dr Marinos Manolesos, for their support during the wind tunnel experiments. I also appreciate the support from our technicians, especially Ian Chorley and Matt Fitzgerald, and from our support staff in ACCIS office, especially from Sarah Hallworth, Nikki Horrobin and Sarah Hassall, Kat Watts and Sophie Spence. Thank you all for your help!

I am also very fortunate to have a strong group of friends and extended family that support me. Even though we are all over the world, as most of us left our country Venezuela due to the unbearable socio-economic and political crisis, I am glad that I am still in constant communication with many of them. I have to thank my uncles, aunts, cousins and grandparents. My grandfather Heli, who unfortunately passed away earlier this year, always encouraged me to stay focused on my goals. I have to thank my friends from home—especially Carlota Ágreda, Carlos García, Alfredo Vetencourt (also my godfather), Mariella Cárdenas and Paola León—as well as my friends Matt Young, Ryan Ligon, Giancarlo Di Biase and Eduardo Latouche from Virginia Tech, for the many

conversations we had during the past four years. My godparents Zoleida and Raul González have always been very supportive of this journey, and I have to thank them for always checking on me.

Last, but not least, I have to thank my then-girlfriend, now wife Valeria for her unconditional support throughout these years, especially during the last six months. I am thankful for your patience and love, for your understanding when I had to work late hours and weekends and for your encouragement during stressful times. After so many years living in different continents, it has been fantastic to have you in Bristol during the past two years. You made my PhD studies happier and more manageable and I am excited that I will get to share with you the next stages in my professional career. I am also thankful for the support from Valeria's parents—Martín and Natalia—–and brother and sister-in-law—Andrés and Mele.

The past four years have been full of wonderful experiences that I am thankful for. I attended many concerts of my favourite artists, went gliding, got married, completed three marathons and six half marathons. I discovered long-distance running as a hobby, and I am thankful for that discovery. Running kept me physically and mentally healthy during the past four years, and I thank everyone that encouraged me to keep running. I also got to present my work at five international conferences in four countries (Poland, South Korea, Australia and US), and had the chance to visit a few other countries as a tourist. I am thankful for all these wonderful experiences that came along with my studies.

Por siempre agradecido,

Andrés Eduardo Rivero Bracho
Bristol, United Kingdom
December 2019

Author's Declaration

I declare that the work in this dissertation was carried out in accordance with the requirements of the University's Regulations and Code of Practice for Research Degree Programmes and that it has not been submitted for any other academic award. Except where indicated by specific reference in the text, the work is the candidate's own work. Work done in collaboration with, or with the assistance of, others, is indicated as such. Any views expressed in the dissertation are those of the author.

SIGNED: ..... DATE: .....

List of Publications

Some of the work presented in this PhD thesis has either been published/submitted as journal articles or presented at academic conferences.

Journal Articles

[1] Rivero, A. E., Weaver, P. M., Cooper, J. E., and Woods, B. K. S. (2018), "Parametric structural modelling of fish bone active camber morphing aerofoils," Journal of Intelligent Material Systems and Structures, 29(9), 2008–2026

[2] Rivero, A. E., Weaver, P. M., Cooper, J. E., and Woods, B. K. S. (2020), "Structural Modeling of Compliance-Based Camber Morphing Structures under Transverse Shear Loading," Accepted. AIAA Journal

[3] Rivero, A. E., Fournier, S., Cooper, J. E., Manolesos, M. and Woods, B. K. S. (2020), "Wind Tunnel Comparison of Flapped and FishBAC Camber Variation for Lift Control," Accepted. AIAA Journal

Conference Papers

[4] Rivero, A. E., Weaver, P. M., Cooper, J. E., and Woods, B. K. S., "Progress on the Design, Analysis and Experimental Testing of a Composite Fish Bone Active Camber Morphing Wing," ICAST 2017: 28th International Conference on Adaptive Structures and Technologies, Cracow, Poland, October 2017, pp. 1–11.

[5] Rivero, A. E., Fournier, S., Weaver, P. M., Cooper, J. E., and Woods, B. K. S., "Manufacturing and characterisation of a composite FishBAC morphing wind tunnel model," ICAST 2018: 29th International Conference on Adaptive Structures and Technologies, Seoul, Republic of Korea, October 2018, pp. 1–14 [1]

[6] Rivero, A. E., Weaver, P. M., and Woods, B. K. S., "Structural Modelling of Compliance-Based Morphing Structures under Transverse Shear Loading,"AIAA SciTech 2019 Forum, AIAA 2019-0229, American Institute of Aeronautics and Astronautics, San Diego, CA, USA, January 2019. pp. 1–17 [2]

[7] Rivero, A. E., Fournier, S., Weaver, P. M., Cooper, J. E., and Woods, B. K. S., "Progress on the Design of a Composite FishBAC Morphing Device for Spanwise Lift Control," 22nd International Conference on Composite Materials, Melbourne, Australia, August 2019, pp. 1–8

[1] Awarded an ICAST 2018 Best Oral Presentation Award

[2] Awarded the AIAA Harry H. and Lois C. Hilton Best Student Paper in Structures 2019

[8] Rivero, A. E., Cooper, J. E., and Woods, B. K. S., "Numerically Efficient Three-Dimensional Fluid-Structure Interaction Routine for Composite Camber Morphing Aerostructures," AIAA SciTech 2020 Forum, American Institute of Aeronautics and Astronautics, Orlando, FL, USA, January 2020[3,4]

[9] Rivero, A. E., Fournier, S., Cooper, J. E., Manolesos, M. and Woods, B. K. S., "Wind Tunnel Comparison of Flapped and FishBAC Camber Variation for Lift Control," AIAA SciTech 2020 Forum, American Institute of Aeronautics and Astronautics, Orlando, FL, USA, January 2020

Magazine Articles

[10] Rivero, A. E., Fournier, S., Weaver, P. M., Cooper, J. E., and Woods, B. K. S., "Structural Characterization of a Composite FishBAC Morphing Trailing-Edge Device," JEC Composites Magazine, N° 128, May-June 2019, pp. 29–31

Use of Published Work in Thesis

1. Chapters 1 and 2: introduction and literature review chapters may contain information that was already published in publications [1-10].
2. Chapter 3: this chapter is based on publication [1] and on the author's 2016 AENGM0006 Extended Research Project (XP) Report, submitted as part of the CDT in Advanced Composites coursework.
3. Chapters 4: this chapter is based on publications [2] and [6].
4. Chapter 5: this chapter is based on publications [4] and [5].
5. Chapter 6: this chapter is based on publications [3] and [9].
6. Chapter 7: this chapter is based on publication [8].

[3] Awarded the Royal Aeronautical Society Aerospace Speakers Travel Grant (AeSTG)
[4] Awarded the MDPI Aerospace 2020 Travel Award

Nomenclature

Roman Symbols

$\dot{m}$	Mass flow rate
$\overrightarrow{dl}$	Vortex filament infinitesimal length
V_B	Airflow velocity at the wake
$V_{A\infty}, V_{B\infty}$	Induced velocity by trailing edge semi-infinite vortices
V_{AB}	Induced velocity by bound vortices
$\hat{c}$	Unit vector parallel to aerofoil chord
$\hat{n}$	Unit vector normal to aerofoil chord
$\overline{Q}$	Ply reduced stiffness matrix
$\overrightarrow{n}$	Normal vectors at horseshoe elements' control points
$\overrightarrow{r}, \overrightarrow{r_0}, \overrightarrow{r_1}, \overrightarrow{r_2}$	Horseshoe vortex control point location vectors
$\overrightarrow{V_{\text{eff}}}$	Effective flow velocity
a	FishBAC's length along the chord
A_{ac}	Cross-sectional area of material testing specimen
A_{fg}	Laminate's membrane stiffness matrix terms
b	Wingspan
B_{fg}	Laminate's extension-bending coupling stiffness matrix
C	Wind tunnel test section cross-sectional area
c	Wing chord length
C_D	3D drag coefficient
C_L	3D lift coefficient
C_m	3D pitching moment coefficient
c_m	2D pitching moment coefficient
C_{D_0}	Total profile drag coefficient
c_{d_0}	2D profile drag distribution
C_{D_i}	Total induced drag coefficient

C_{d_u}	Uncorrected 2D drag coefficient
C_d	2D drag coefficient
$C_{L_{\text{err}}}$	FSI convergence criteria
C_{l_u}	Uncorrected 2D lift coefficient
C_l	2D lift coefficient
D	Drag force
D_{fg}	Laminate's bending stiffness matrix
DF	Nonlinear lifting-line damping factor
E	Young's modulus
E_x^b	Effective Young's modulus in bending mode
f_{mn}	Aerodynamic influence coefficients
F_{wd}	Function wake drag
F_{x_1}, F_{x_2}	Bottom and top balance forces in the x-direction, respectively
F_{y_1}, F_{y_2}	Bottom and top balance forces in the y-direction, respectively
G	Shear modulus
H	Laminate's transverse shear matrix
h	Wind tunnel test section's height
H_p	Total aerodynamic pressure
I	Current
K_1	Wind tunnel solid blockage constant
k_k	Penalty spring stiffness
K_T	Strain energy matrix individual row
L	Lift force
L'	Lift force per unit-span
$L_{mn}, O_{mn}, P_{mn}, R_{mn}, S_{mn}$	Shape functions' unknown amplitudes
M_x	Actuation torque inputs
p	Static pressure
P_{down}	Lower surface aerodynamic pressure
P_{up}	Upper surface aerodynamic pressure

P_{load}	Axial load applied by tensile test machine
q	Transverse aerodynamic net pressure distribution
Re	Reynolds number
Re_u	Uncorrected Reynolds number
S	Wing planform area
T	Kinetic energy
t	Laminate thickness
T_n	Chebyshev polynomials of the first kind
U	Strain energy
u^0, v^0, w	Displacements in x-,y- and z-directions, respectively
U_p	Artificial penalty energy
V, W	Potential energy due to transverse and in-plane external loads, respectively
V_∞	Freestream velocity
V_{model}	Wing tunnel wing model volume
X_m, Y_n	Polynomial expansion along the x- and y-directions, respectively

Greek symbols

α	Angle of attack
α_i	Induced angle of attack
α_u	Uncorrected angle of attack
α_{eff}	Effective angle of attack
δ	Actuation input angle
ϵ	Actuation mechanism efficiency
$\epsilon_x, \epsilon_y, \epsilon_z$	Normal Strains
ϵ_{sb}	Solid blockage correction factor
ϵ_{wb}	Wake blockage correction factor
$\epsilon_{xy}, \epsilon_{xz}, \epsilon_{yz}$	Tensorial shear strains
γ(TE)	Kutta condition
Γ_x	Boundary condition circulation function

$\gamma_{xy}, \gamma_{xz}, \gamma_{yz}$	Engineering shear strains
κ	Timoshenko shear correction factor
κ_t	Actuator's torque constant
λ_w, λ_p	FSI relaxation factors on displacement and pressure, respectively
ν	Poisson's ratio
ϕ	Potential flow
Π	Total energy
ψ_x, ψ_y	Plate rotations about the x- and y-axis, respectively
ρ	Air density
σ	Streamline correction factor
$\sigma_x, \sigma_y, \sigma_z$	Normal stresses
τ_{xy}, τ_{xz}, τ_{yz}	Shear stresses
$\mathbf{\Gamma}$	Aerodynamic vortex strength matrix
θ	Wing twist angle
ζ, η	Non-dimensional coordinates along the x- and y-directions, respectively
K	Condition number

Superscripts

$(+), (-)$	Positive and negative position, respectively, at structural discontinuity
M,N	Polynomial order in the x- and y-direction, respectively
i, j	nth structural element along x-, y-directions, respectively
n	Chebyshev polynomial order
n_{bc}	Boundary condition exponent (circulation function)
r	Quantity after relaxation

Subscripts

$1, 2, 3$	Fibre, matrix and transverse material directions, respectively
$\hat{i}, \hat{j}, \hat{k}$	Unit vector directions
∞	Freestream flow property

max	Maximum value
new	New value after an iteration
old	Previous value before iteration
^{0}	Plate's midplane
fg	ABD matrix terms
i,j	nth structural element along x-, y-direction, respectively
kl	Adjacent structural elements
x,y,z	Cartesian x- , y-, and z-directions, respectively
m,n	Polynomial expansion term along the x- and y-direction, respectively

Acronyms

ABS	Acrylonitrile Butadiene Styrene
AOA	Angle of Attack
CFD	Computational Fluid Dynamics
CFRP	Carbon Fibre-Reinforced Polymer
CLT	Classical Laminate Theory
DC	Direct Current
DOF	Degree of Freedom
FEM	Finite Element Method
FishBAC	Fish Bone Active Camber
FSDT	First Order Shear Deformation Theory
FSI	Fluid-Structure Interaction
HECS	Hyper Elliptical Camber Span
HV	High Voltage
LLT	Lifting-Line Theory
NACA	National Advisory Committee for Aeronautics
PAM	Pneumatic Artificial Muscles
PIV	Particle Image Velocimetry
RMS	Root Mean Square

RPK	Revenue Passenger per Kilometre
SLS	Sea-Level Standard Conditions
SMA	Shape Memory Alloy
SMP	Shape Memory Polymer
UD	Unidirectional
UoB	University of Bristol
VG	Videogauge
VLM	Vortex Lattice Method
VSS	Variable Stiffness Spar

Definitions

Chordwise	Along the wing chord. Aligned with the global Cartesian x-axis
Spanwise	Along the wingspan. Aligned with the global Cartesian y-axis
Through-Thickness	Along the transverse direction. Aligned with the global Cartesian z-axis

Table of Contents

List of Tables

List of Figures

Chapter 1

Introduction

Ever since its beginning in 1914, commercial aviation has been steadily growing, especially after World War II. Specifically, in the past 25 years, passenger air traffic—commonly measured in Revenue Passenger per Kilometre (RPK)—has steadily grown at an average annual rate of 5% (Figure 1.1). There are several reasons behind this significant steady growth, such as market liberalisation, improvements in household incomes, the introduction of more efficient aircraft and the growth of low-cost airlines [1, 2]. Currently, there are no signs of this growth rate slowing down in the next two decades and, consequently, current passenger numbers could double up to an estimate of 8.2 billion (per year) by the year 2040 [2]. This expected growth represents a huge environmental challenge for the aviation sector since, even though technologies have significantly increased fuel efficiency of aeroplanes in the past decades, there is evidence that fuel burning is increasing at a faster rate than the fuel efficiency gains [3]. To guarantee the sustainability of the aviation sector, there needs to be a more significant effort on tackling the increasing environmental impact of aviation.

Most of the improvements in aircraft efficiency have come from two main sources: reduction in weight due to the use of lightweight materials—such as composites—and the development of more efficient engines. However, the rate at which fuel efficiency is increasing due to weight reduction and engine improvements has been slowing down in the past two decades [4]. Therefore, without improvements in other areas, the additional environmental impact due to aviation growth will not be offset. For example, further development is needed in using alternative fuels and electric propulsion, optimising flight plans and airport operations and introducing novel technologies to improve aerodynamic efficiency [5]. Traditional aircraft structures are rigid and, therefore, their geometries are designed to achieve maximum aerodynamic efficiency and one specific flight scenario (usually at cruise). Consequently, operations at other flight scenarios are far from optimal, leading to higher fuel consumption. One way to improve aerodynamic efficiency is to continuously modify the shape of the vehicle during flight, so it can better adapt to the different flight scenarios and environmental conditions. This adaptability is already observed in nature, as birds are able to vary their body configuration depending on the flight conditions, which allows for achieving high levels of efficiency and manoeuvrability at different flight conditions and scenarios [6].

Although fixed-wing aircraft do effectively change shape during flight, specifically the camber distribution of their aerofoils, they do so by using a series of rigid devices (trailing edge flaps) that are hinged to the trailing edges of their wings (Figure 1.2a). When these hinged flaps deflect, they vary the aerofoil camber distribution, inducing a change in the distribution of aerodynamic pressure over the wings and therefore changing the net forces and moments. These changing forces and moments can be used to manoeuvre and control the aircraft's direction of flight. However, the use of trailing edge flaps comes with a significant disadvantage: a drag penalty that reduces the overall efficiency of the aircraft. When these flaps deflect, the change in camber occurs in a sharp and discontinuous way. Also, since they are hinged, a structural gap must exist to allow flap rotation without structural interference. This structural gap and the discontinuous change in camber induce earlier flow separation, which results in a significant increase in drag, and higher drag translates into higher fuel consumption and noise. Consequently, their use is restricted to certain flight scenarios and for control purposes and not for actively optimising wing geometry during flight.

Aeroplanes progressively lose weight during flight due to fuel burn; hence, the amount of lift force required to sustain equilibrium flight is continuously decreasing. Therefore, to maintain wings level equilibrium flight, the amount of lift force that is generated must be reduced in accordance with this reduction in weight. One way of reducing lift during flight is to reduce air density by gradually increasing cruise altitude; however, these changes in altitude may be limited by the aircraft service ceiling and other operational constraints.

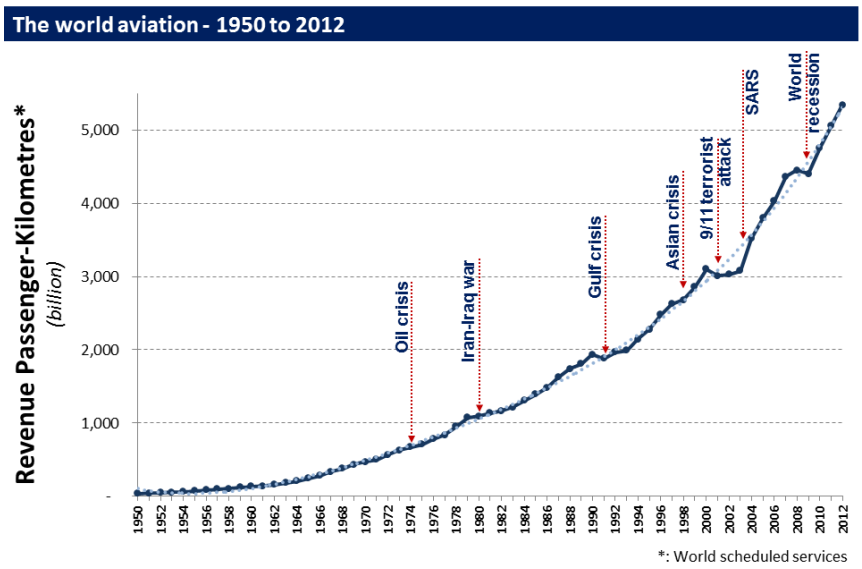

Figure 1.1: Aviation growth since 1950. Reproduced in agreement with ICAO's Copyright and Terms and Conditions [1].

Another option is to reduce the angle of attack (pitch angle) to reduce lift force. Although effective in reducing lift, varying pitch angle would result in an increase in total drag force as higher fuselage and wing profile drag, respectively, are expected. A third option is to continuously reduce aerofoil camber so that lift can be reduced without having to change either altitude or angle of attack. As already mentioned, if the continuous camber reduction is performed using hinged flaps, the drag penalty may offset any efficiency gains. Therefore, camber morphing devices offer a more efficient approach for this specific application.

If aeroplane wings could instead vary their shape in a smooth way that is free from surface discontinuities and gaps (Figure 1.2b), similar aerodynamic control authority could be achieved, but with a much lower drag penalty [7]. Also, since the drag penalty is lower, these continuous changes in camber could be throughout the duration of the flight to continuously adapt the shape of the wing, and thus achieving higher aerodynamic efficiencies at all flight stages. By doing so, higher aerodynamic efficiencies may be achieved, leading to additional fuel efficiency gains. Moreover, flaps are unable to gradually change camber distribution along the wing span, which can be exploited to optimise spanwise lift distribution and minimise induced drag. These smooth and continuous changes in camber are known as camber morphing, and there have been significant research efforts to push this concept forward in the past two decades [7, 8].

In terms of fuel efficiency gains, there are studies in the literature that have quantified the potential benefits of varying aerofoil camber during flight. Recksiek (2009) estimated that fuel consumption could be reduced between 1-2% in a full-size Airbus A350 XWB if traditional hinged ailerons are actively used to account for weight-loss due to fuel burn [9], and Greff (1990) estimated that these fuel efficiency gains could triple if hinged ailerons are replaced by camber morphing devices [10].

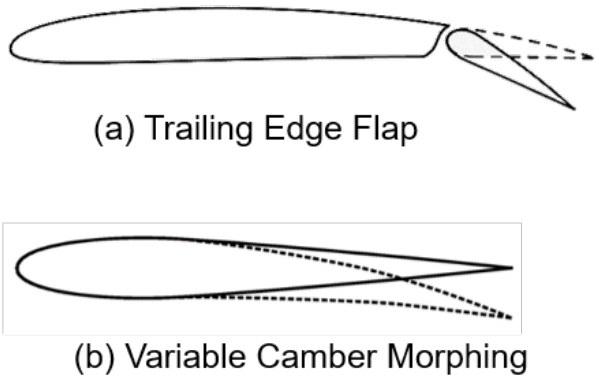

Figure 1.2: Traditional hinged flap (a) vs variable camber morphing (b)

1.1 Camber Morphing: Main Challenges

Even though the aeronautical community has been aware of the benefits of camber morphing for almost a century (there are camber morphing concepts dating from as early as 1920 [11–13]), it has been in the past two decades that camber morphing has started to be considered as a feasible alternative to rigid control surfaces. This has been partly due to new developments in smart materials and lightweight structures, but also due to advances in structural modelling and manufacturing techniques—such as additive manufacturing—that have allowed the development of new manufacturing processes and actuation methods for novel camber morphing concepts [7]. Most research efforts to date have focused on two separate areas: developing the 2D aerofoil morphing concept [14–20] and studying the benefits and challenges of camber morphing from a systems-level point-of-view [21–23]. However, more work is needed on developing lightweight and airworthy camber morphing structures, and on their integration into three-dimensional wings.

The research presented in this thesis is motivated by the need to develop an integrated, comprehensive approach for designing camber morphing wings. Such an approach would need to tackle the complexity of the subject from different angles simultaneously, to be able to make progress in the highly coupled domains of design and analysis, manufacture, and experimental testing. Furthermore, the compliance-based approach to camber morphing considered here requires coupling between the structural and aerodynamic analysis, and also the consideration of the hierarchical nature of this problem—to capture the aeroelastic performance at both the component level and the wing level. Specifically, this thesis undertakes a comprehensive design, analysis, and experimental validation research campaign for the Fish Bone Active Camber (FishBAC) morphing technology, which has been previously introduced by Woods and Friswell (2012) [24].

The FishBAC is a compliance-based camber morphing device that has been carefully engineered to have high stiffness in critical directions—i.e. along the span to resist bending moments—while being compliant in thicknesswise bending so that continuous changes in camber can occur. To achieve this high orthotropic level, several types of structural members and materials are combined, such as a carbon-fibre/epoxy central bending spine (main load-bearing member), a series of ABS 3D-printed spanwise stringers, silicone skin sheets and antagonistic Kevlar tendons for inducing actuation moments to drive the camber morphing (Figure 1.3).
The first generation of FishBAC devices were developed as proof-of-concept, and they showed promising results such as aerodynamic efficiency improvements of at least 25% (compared to a hinged flap) [25]. Besides these significant improvements in aerodynamic efficiency, there are other factors that make the FishBAC a more attractive camber morphing concept than similar devices in the literature, such as: *(i)* the tailorability of its elastic properties (e.g. by varying the thickness of the spine, the number and size of the stringers, and the skin material and thickness), *(ii)* its ability to gradually vary the amount of camber along the span by having multiple spanwise actuation points, *(iii)* its actuation-agnostic design (i.e. the tendon-pulley

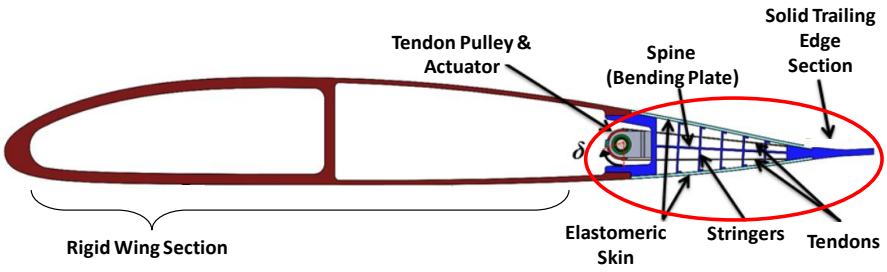

Figure 1.3: Schematic of the Fish Bone Active Camber (FishBAC) morphing concept

actuation mechanisms can be driven by any type of actuator), *(iv)* its large lift control authority of $\Delta C_L \approx 0.7$, which is similar to that of hinged flaps and *(v)* its orthotropic nature that allows for targeted tailoring of stiffness—e.g. chordwise bending vs spanwise bending or torsion vs bending stiffness. However, this first generation of FishBAC devices were designed using low fidelity structural and aerodynamic modelling tools [26, 27] and manufactured using 3D-printed plastic.

To successfully implement the FishBAC in real large scale aerospace structures, it is necessary to develop modelling tools that can capture the three-dimensional nature of a fixed-wing fitted with a FishBAC device, from both structural and aerodynamic points-of-view. Additionally, the use of high-performance aerospace-grade materials is of extreme importance so that the FishBAC can move towards industrial application. Therefore, the aims of this thesis are: *(i)* to develop modelling tools that can capture both chordwise and spanwise structural behaviour of composite FishBAC devices, as well as the 3D aerodynamics of FishBAC morphing wings; and *(ii)* to design and manufacture a carbon-fibre FishBAC device that can be used to experimentally validate both structural and aerodynamic simulations and *(iii)* to obtain additional wind tunnel data to further understand the potential benefits of using the FishBAC instead of hinged flaps.

The novelty of the work presented in this thesis is twofold: first, it introduces novel structural, aerodynamics and three-dimensional fluid-structure interaction modelling tools that can be used to simulate not just the FishBAC, but other bending driven compliance-based composite morphing devices; and second, the introduction of the first composite-spine FishBAC device, which was used to perform an extensive testing campaign to experimentally study the structural and aerodynamic behaviour of this morphing device. These experimental results, along with preliminary design space explorations using the 3D FSI, constitute the first research efforts on developing the FishBAC for three-dimensional fixed-wing applications.

1.2 Objectives

Considering the aims presented in the previous section, this section outlines the objectives of this thesis. A schematic of how these objectives are realised is shown in Figure 1.4.

1. To develop a computationally efficient, parametrically driven, structural model capable of capturing both chordwise and spanwise behaviour of the FishBAC under both structural and aerodynamic loads. The model must be capable of:

    a) Stiffness tailoring due to the use of composite laminates

    b) Capturing the FishBAC static structural behaviour due to different aerodynamic pressure distributions and actuation loads

    c) Obtaining in-plane and out-of-plane displacements along both chordwise and spanwise directions

    d) Modelling the discontinuous nature of the FishBAC due to the presence of stringers and chordwise taper from aerofoil geometry

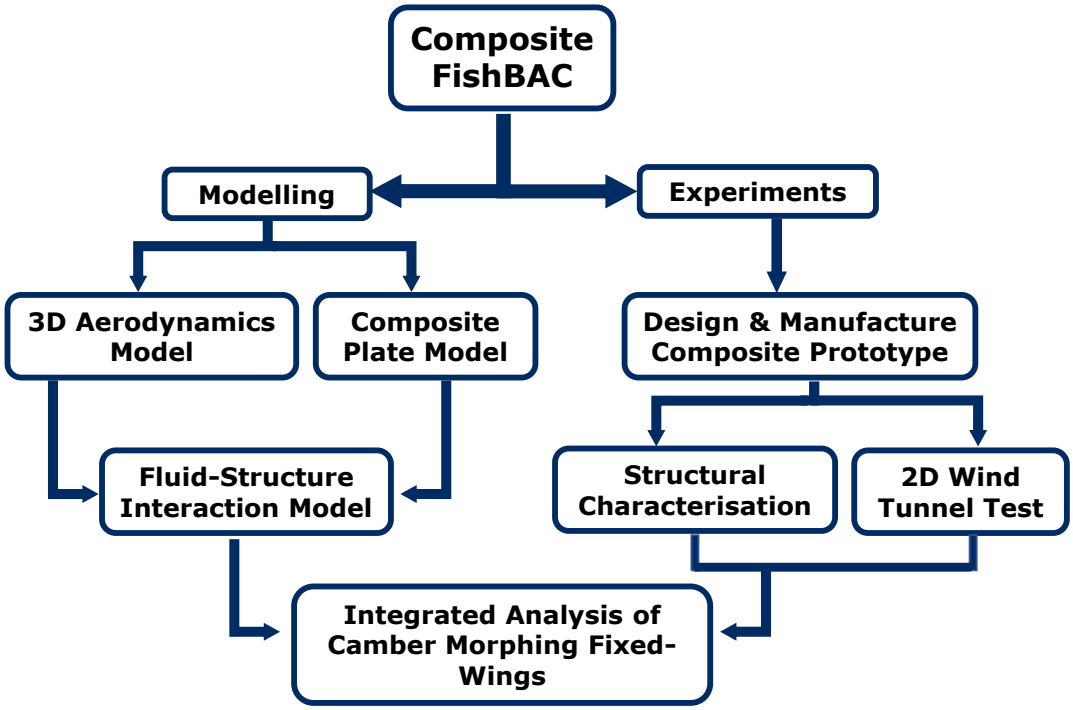

Figure 1.4: Schematic of main research outputs presented in this thesis

2. To develop a Fluid-Structure Interaction (FSI) analysis to couple both structural and aerodynamic modelling of the FishBAC. Specifically, this routine should:

    a) Couple structural and aerodynamic analysis of the FishBAC into a single routine

    b) Model three-dimensional aerodynamic effects (i.e. downwash)

    c) Capture the impact of non-uniform changes in camber along the span

3. To design, manufacture and test a composite FishBAC wind tunnel wing model. The following tests are to be performed on the completed model:

    a) Static structural testing for validation of the developed structural model

    b) Wind tunnel test for both understanding the aerodynamic benefits of the FishBAC

1.3 Chapter Outline

This thesis is outlined as follows:

- Chapter 2: introduces a literature review on morphing wings concepts, including planform, out-of-plane and aerofoil morphing. Furthermore, it introduces variable camber and its evolution throughout the past century. Finally, it reviews relevant modern camber morphing concepts, including the FishBAC device.
- Chapter 3: develops a discontinuous plate-based structural model of the FishBAC. The model is based on Kirchhoff-Love Plate Theory, and the Rayleigh-Ritz Method is used as the solution technique. This model successfully captures the static behaviour of the FishBAC, except when transverse shear stresses exist.
- Chapter 4: introduces a structural model that addresses the limitations of the Kirchhoff-Love model presented in Chapter 3. To account for transverse shear stresses, this model is based on Mindlin-Reissner Plate Theory. The model successfully addresses the limitations of the Kirchhoff-Love model and can accurately predict the FishBAC static behaviour under any actuation load case. Additionally, experimental validation is presented in this chapter.
- Chapter 5: describes the design, manufacture and structural tests of the composite FishBAC wind tunnel wing model. This includes material and actuator characterisation and calibration of the actuation system.
- Chapter 6: presents 2D wind tunnel tests results of the composite FishBAC wind tunnel wing model. To directly compare the aerodynamic behaviour of the FishBAC, a hinged flap device was also tested using the same equipment and setup. The performed tests include force balance and wake survey—to measure aerodynamic forces and moments—Particle Image Velocimetry (PIV) and stereo displacement point tracking videogauge.

- Chapter 7: proposes an FSI analysis that couples the Mindlin-Reissner plate model with a nonlinear viscous-corrected Lifting-Line Theory (aerodynamic model). The model is capable of analysing both structural and aerodynamic behaviour of the FishBAC in a coupled manner. Also, the chapter presents a brief study on the variation of the aerodynamic performance of a generic wing geometry with varying actuation inputs and angles of attack.
- Chapter 8: summarises the major findings of this thesis, highlights its novelty, and suggests routes for future work.

Chapter 2

Literature Review

This chapter reviews the three main morphing classifications for fixed-wing applications: planform morphing, out-of-plane morphing and aerofoil morphing. Since the main objective of this thesis is to develop a variable camber morphing device, there is an emphasis on reviewing aerofoil morphing technologies.

2.1 Introduction

The advantages of modifying the wing geometry during flight were known since the beginning of flight. The concept of morphing wings dates from the early 1900s when the Wright Brothers created a 'wing warping' mechanism that directly twisted the biplane wings of the Wright Flyer to create asymmetric spanwise variations in lift to roll the aircraft [28]. Also, one of the first variable camber concepts was introduced by H.F. Parker in 1920 (Figure 2.1) [11], where a series of 'rib springs' were used to modify the camber distribution. This wing was then tested in a wind tunnel, and improvements in lift-to-drag ratios of 200% were recorded. Additionally, several variable camber patents were filed during the 1930s and 1940s [12, 13, 29], however, a common aspect among early variable camber concepts is that they all involved the use of complex actuation mechanisms that ended up adding significant structural weight. Consequently, they were not implemented and the aircraft design solidified around the simple and well-proven hinged trailing edge flap.

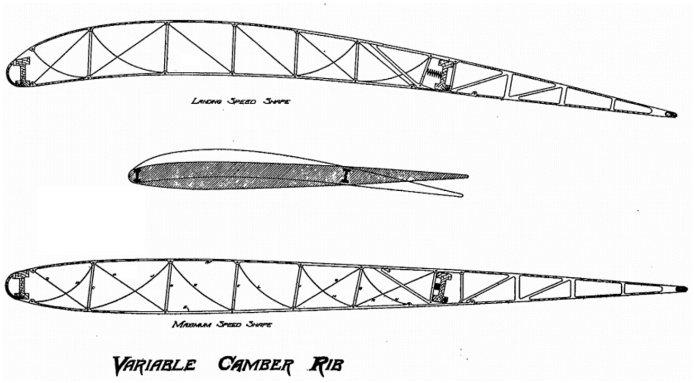

Figure 2.1: Parker variable camber wing. Reproduced from Parker (1920) [11]. No copyright applies.

In terms of 'morphing aircraft', the Pterodactyl IV and Makhonine Mak-10 were two of the first full-size morphing aeroplanes, introducing variable sweep and span, respectively. Also, the Nikitin-Shevchenko IS-1 fighter was able to transition from biplane to monoplane during flight [7]. Although capable of morphing during flight, these aircraft used heavy and complex mechanisms to change shape. The added structural complexity and weight, as well as additional costs and airworthiness concerns, led to these concepts not being fully implemented and their development stopped at the prototype stage.

However, due to advances in smart structures and composite materials, morphing aircraft have become a popular subject of study since the beginning of the 21st century. Significant research outputs have been generated in this subject, and they are summarised by several review articles [7, 8, 30–32]. The main objective of these 'newer' concepts is to address the weight and complexity penalties of 'traditional' morphing mechanisms so that the aerodynamic benefits of morphing wings can be fully observed and exploited. Also, these developments in lightweight morphing concepts have been accompanied by newer structural, aerodynamics and aeroelastic modelling techniques that have enhanced the understanding of morphing structures and the potential implications of full-scale applications.

According to Barbarino et al. (2011) [7], there are three main ways of achieving morphing in wings: changing the wing planform geometry (i.e. sweep, chord and span changes), its out-of-plane properties (i.e. twist, dihedral and spanwise bending) or its aerofoil geometry (i.e. aerofoil thickness and camber distribution). The work developed in this thesis lies in the variable aerofoil geometry area, specifically, in variable camber morphing aerofoils. However, the other two ways of achieving morphing are briefly introduced in the following subsections.

2.2 Planform Morphing

Planform morphing refers to modifying the planform (top-view) dimensions of the wing during flight. This can usually be achieved by either modifying the span of the wing, the chord length or a change in sweep angle. Early concepts were introduced in the 1930s; specifically, the MAK-10 (1931) is the first known flying example of telescopic span-morphing, whereas the Soviet LIG-7 (1937) was the first chord morphing introduced [7]. During the 1950s, several patents that involved telescoping span-morphing [33] and leading edge extensions [34] were filed.

2.2.1 Span Morphing

One of the most common approaches for planform morphing is span-morphing. The objective of span-morphing is to increase the aspect ratio of the wing by extending its length, which results in a reduction of induced drag. Specifically, one of the most common approaches is the telescoping wing approach, such as presented by Bloudeau and Pines (2007) [35], Leite et al. (2009) (Figure 2.2) [36] and Bye and McClure (2007) [37], among others.

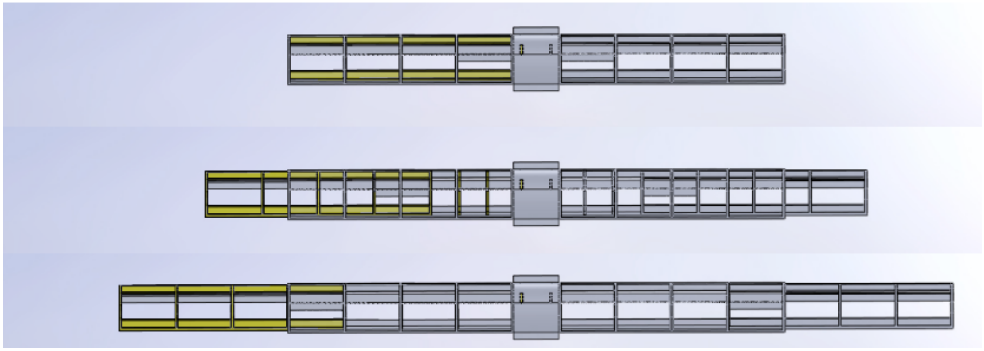

Figure 2.2: Span morphing concept developed by Leite et al. (2009). Reproduced from Leite et al. (2009) with Authors' permission [36].

Additionally, Henry and Pines (2007) [38] and Seigler et al. (2004) [39] investigated asymmetric span morphing for roll control. The former found that asymmetric span morphing provides significantly higher roll damping than ailerons, whereas the latter one concluded that even though this approach gives more control authority in roll, the dynamic properties of the vehicle change significantly and thus adds unnecessary complexity to the stability of the system. For example, when spanwise morphing is performed asymmetrically, the centre of gravity can no longer be assumed to be fixed. Lastly, another common approach to achieve span morphing is by folding wing and wingtips [40–42], which has been of interest not only for extending wings during flight but mostly to accommodate aircraft in reduced parking spaces such as airport gates and aircraft carriers.

One conceptual disadvantage of span morphing is the increasing bending moments due to added length. Bae et al. (2005) [43] performed an aeroelastic study on a variable span morphing wing and concluded that the overall flexibility of the wing increases with increasing span, which requires additional bending stiffness in the design. Overall, it can be concluded that the induced drag reduction due to span morphing is at the expense of extra structural weight and stiffness.

2.2.2 Chord Morphing

Adding chord length to a wing has the benefits of increasing the amount of lift that can be generated due to an increase in surface area. Most fixed-wing aircraft currently achieve this by having trailing edge extensions (e.g. fowler flaps), which are usually hinged to the main wing.

However, the use of smart materials and compliant structures to achieve chord morphing without the use of hinged extensions has not attracted significant attention [7]. In many fixed-wing aircraft designs, the internal chordwise configuration of the wing is very complex due to the presence of fuel tanks, which reduces the effective space for any chord morphing mechanisms.

Some of the concepts that have been investigated involved using a series of chordwise rib partitions actuated by DC motors [44] and Dynamic Modular Foams [45]. The former one was successful but with a significant weight penalty added by the actuation mechanism, whereas the latter one had issues with achieving uniform heat transfer to actuate the Dynamic Modular Foam, which has a similar actuation behaviour to a Shape Memory Alloy.

2.2.3 Variable Sweep

Swept wings were introduced as a way to increase the critical Mach number of fixed-wing aircraft, allowing for transonic flight and delaying drag divergence due to supersonic flow. However, sweeping the wings comes at the expense of a reduction in lift generated, and thus, a reduction in lift-to-drag ratio [46]. The motivation behind variable sweep in fixed-wings is to give the aircraft the ability to perform the lower speed stages of flight—takeoff, climb, approach and land—with an unswept wing configuration, and as the aircraft approaches transonic (or even supersonic) cruise speeds, the wings can be swept to increase the critical Mach number in transonic flight or reduce the wave drag in supersonic flight. This feature would increase the overall efficiency of the aeroplane as higher lift-to-drag ratios could be achieved during the slowest portions of the flight.

The first aircraft prototype that was able to fully vary the sweep angle was the Bell X-5, which had its maiden flight in 1951. Despite its successful variable sweep mechanism, this aircraft tended to have control and stall issues during flight. During the 1970s and 1980s, variable sweep wings became popular in military aircraft. Some of the designs that offered this mechanism are: the General Dynamics F-111, the Grumman F-14, the Mikoyan-Gurevich MiG-23 and the Sukhoi Su-24, among others. One common characteristic of these aircraft is the significant extra weight that the variable sweep mechanism adds to the vehicle, having a negative impact on the vehicle's fuel efficiency and maximum payload [7].

In response to these heavy mechanisms, the use of smart materials and lightweight structures for variable sweep has been investigated by several research groups. For example, de Marmier and Wereley (2003) (Figure 2.3) [47] looked into using inflatable actuators for UAV wings, whereas Yu et al. (2007) [48] looked at temperature-induced morphing by deforming a scissor mechanism using Shape Memory Polymers (SMP). Furthermore, Mattioni et al. (2006) [49] proposed a variable sweep mechanism using bistable composite laminates in a two-spar wing in which residual stresses after curing acted as an elastic hinge. However, this previous concept did not include a skin, and therefore the feasibility of the proposed design was not thoroughly tested.

Variable sweep concepts have two conceptual disadvantages: they inherently vary the position of the centre of gravity of the aircraft during flight—representing a challenge in terms of stability and control—and the actuating pivot point is usually at the wing root—location where the wing experiences its highest bending moments.

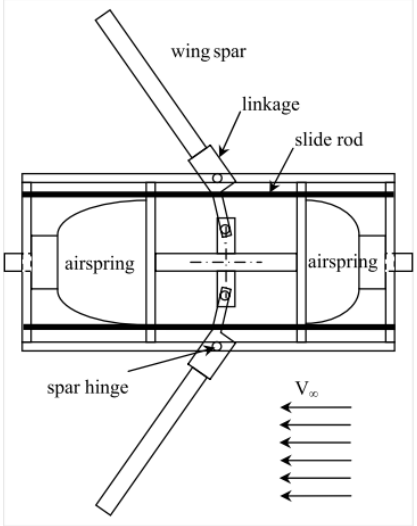

Figure 2.3: Variable sweep morphing concept developed by de Marmier and Wereley (2003). Reproduced from de Marmier and Wereley (2003) [47]. Reproduced with Authors' permission.

2.3 Out-of-Plane Morphing

Out-of-plane morphing refers to shape-changing mechanisms that focus on varying the wing's incidence angle with respect to the freestream flow. There are three main out-of-plane parameters that can be modified during flight that could positively impact the performance of aeroplanes: wing twist, dihedral and spanwise bending [7].

2.3.1 Variable Twist

The twist of a wing corresponds to the local change in incidence angle along the span, measured with respect to the root's angle of attack. A wing is usually twisted for three main reasons: to keep the entire wing from stalling at the same time, to reduce induced drag due to lift and to vary the spanwise load distribution. Besides induced drag reduction, twist morphing has two additional applications: roll control—as the Wright Brothers implemented in their wing warping mechanism—and load alleviation.

Two of the first concepts that introduced morphing wing twist were developed by Rockwell's Active Flexible Wing (1998) [50] and by the USAF/NASA Active Aeroelastic Wing framework (2000) [51]. These projects introduced the use of conventional control surfaces as 'aerodynamic tabs' that can modify the twist of a wing for roll control purposes. These authors showed not only potential improvements in performance but also on preventing the risk of aileron reversal—an undesired phenomenon where the aeroplane rolls in the opposite direction to the control input. Aileron reversal normally occurs on aeroplanes with twisted wings flying at high speeds.

When ailerons deflect downward, a nose-down pitching moment that reduces the effective angle of attack is induced. If the torsional stiffness of the wing is not sufficient, this reduction in angle of attack could result in the wing generating negative lift, which would roll the aeroplane in the opposite direction [52, 53].

Moreover, Griffin and Hopkins (1997) [54] introduced one of the first variable twist concepts: a Variable Stiffness Spar (VSS) that can switch from a low stiffness configuration—enhancing roll performance—to a high stiffness configuration that prevents aileron reversal at high speeds. Inspired by Griffin and Hopkins (1997), Chen et al. (2000) [55] focused on showing the potential of this spanwise variable stiffness concept by optimising for maximum roll rate. They proposed a 'torsion-free' modification, which combines two 'very stiff' spars near the quarter-chord of the wing with two VSS spars at both leading and trailing edges. This configuration showed an increase in roll rate without sacrificing any static and flutter stability.

Further studies on how variable stiffness can be exploited for morphing twist purposes is summarised by Cooper (2006) [56], where the idea of a pneumatic device for translating and internally rotating the spars in the chordwise direction is introduced. The main objective of this pneumatic device is to minimise drag by varying twist during flight. Other concepts that focused on varying the internal configuration of the wing or the stiffness of the main load-bearing members for roll control were presented by Garcia et al. (2003) (Figure 2.4), Stanford et al. (2007) and Ajaj et al. (2011) [57–59].

However, one disadvantage of these active twist concepts that were previously presented is that they may not offer a weight-effective design. Some of them involve the presence of additional actuation mechanisms, whereas others present additional structural members. As an alternative, some researchers have attempted to embed actuation to the main load-bearing members by using Piezoelectrics [60–63] and Shape Memory Alloys (SMAs) [64–67]. Although lighter, these concepts can see their effectiveness limited due to the well-known actuation limitations of Piezoelectrics (e.g. low strains, hysteresis and limited tensile strengths [68, 69]) and SMAs (e.g. low usable strains, fatigue, low actuation frequency and low controllability [70]).

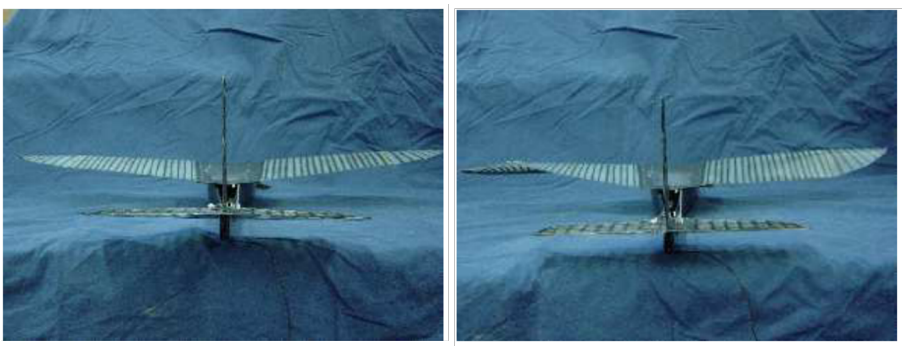

Figure 2.4: Variable twist morphing concept for roll control, by Garcia et al. (2003). Reproduced from Garcia et al. (2003) with Authors' permission [57].

One important concept that is worth highlighting is the DARPA Smart Wing project, which combined a series of 'smart' concepts that combine compliance-based control surfaces with novel actuation systems such as standard piezoelectric, SMAs and ultrasonic piezoelectric motors. This last one—the ultrasonic piezoelectric motors—are implemented using an 'innovative' eccentuator approach, i.e. a beam that converts rotation at one end into translation on the other. When implemented in pairs, this approach allows for variations in wing bending (actuation in series) or twist (asymmetric actuation). This actuation configuration is only possible due to the compliant nature of the aerostructure, which combines different materials and structural elements to simultaneously reduce the actuation energy requirements and provide sufficient stiffness to resist aerodynamic loads [22, 71].

Lastly, during the past decade, the concept of passive morphing and load alleviation has been studied by several research groups. By exploiting material anisotropy and coupling between bending and torsion of composite laminates, the stiffness of a structure can be tailored to control structural deflections, such as the amount of twist due to aerodynamic loads [72–74]. The main advantage of this approach is that it does not require additional actuation mechanisms, but just needs an adequate fibre-placement technique within a composite laminate. Controlling the amount of twist at the outboard sections of wings can lead to a reduction in induced drag due to local reduction in induced angle of attack.

2.3.2 Dihedral

In aircraft design, dihedral refers to the upward angle that the wings form with respect to the horizontal plane when viewed from the front. Varying this angle during flight may lead to a potential positive impact in performance, specifically by varying the stability/agility of the vehicle, the stall properties and by targeting a reduction in induced drag [7].

In terms of morphing concepts, there have been significant research efforts on the use of a series of active winglets that are actuated between 'retracted' and 'extended' position. These active winglets can be used to vary the local dihedral angle [75–77]. However, these changes in dihedral are localised at the wingtips. Conversely, global morphing dihedral concepts are not as common due to the need to directly actuate against the very large root bending moments and the associated large energy requirements. However, these concepts do exist in the literature, as introduced by Bye and McClure's (2007) folding wing prototype [37].

2.3.3 Spanwise Bending

The objective of spanwise bending morphing is to mimic the flying mechanics of several birds, capable of 'furling down' their wings during flight, by continuously bending the wings along the transverse direction (Figure 2.5). It is argued that this ability allows for the reduction of induced drag and the increase of the lift-to-drag ratio by of around 15% due to a reduction in trailing edge vortices when compared to an elliptical wing planform.

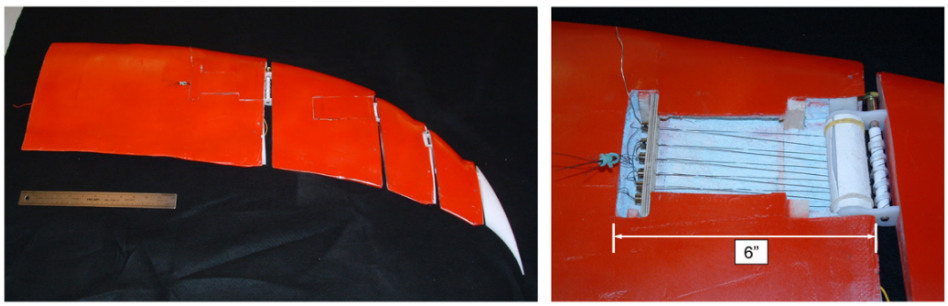

Figure 2.5: Spanwise bending morphing concept for spanwise load alleviation and induced drag reduction. Reproduced from Manzo and Garcia (2010) with Authors' permission [78].

The most studied spanwise bending concept is known as the NASA Hyper Elliptical Camber Span (HECS) wing [16, 78], which observed a drag reduction of 50% at high angles of attack. However, one disadvantage of this spanwise bending morphing is the reduction in aspect ratio when the wing is in the 'furled' configuration, which reduces the overall efficiency of the wing due to an increase in induced drag.

2.4 Aerofoil Morphing

In the context of morphing aircraft, aerofoil morphing—specifically variable camber—is one of the topics that has been broadly studied. Even though variable thickness devices exist in the literature, these normally induce changes in camber distribution as well. Therefore, these are not reviewed individually in this chapter. Since camber morphing is the main subject of study of this thesis, a comprehensive review is presented in the following section.

2.4.1 Variable Camber

As described in Chapter 1, conventional fixed-wing aircraft are controlled by varying the amount of forces and moments that the wings generate. These changes are generated by variations in aerofoil camber distribution, which are achieved by actuating a series of hinged structures commonly known as trailing edge flaps. Depending on the location and purpose of trailing edge flaps, they are called elevators (pitch control), rudders (yaw) or ailerons (roll) and they are used throughout flight to manoeuvre and trim the aircraft [46]. Although the deflection of these hinged flaps causes an effective variation in aerodynamic forces, the sharp and discontinuous change in aerofoil camber due to the hinged configuration comes with a significant drag penalty. While the drag associated with manoeuvres does not typically make a significant impact on fuel burn over a mission, the significant drag penalty of traditional plain flaps makes them an unattractive option for more ambitious attempts to actively and continuously morph the wing geometry of the entire wing for aerodynamic efficiency gains.

An ideal solution to this issue is to generate smooth and continuous changes in camber distribution, with similar aerodynamic control authority but with a lower drag penalty. Consequently, there has been a significant motivation to develop these camber morphing technologies, and the most relevant concepts are reviewed in the following subsections.

2.4.2 Early Years

As mentioned in Section 2.1, the first camber morphing concepts were introduced in the early 20th century. In 1920, H.F. Parker of the National Advisory Committee for Aeronautics (NACA) highlighted that fixed-wing aircraft flying at high speeds would be forced to fly at inefficient conditions—at slightly negative angles of attack—if the wing geometry could not be modified from the takeoff and landing configurations to a cruise one. As a solution, Parker (1920) mentioned that varying the aerofoil camber distribution would give the wing sufficient adaptability to sustain efficient flight at different flight stages. He proposed a variable camber rib mechanism that was wind tunnel tested. Results showed maximum achievable lift coefficient of $C_L = 0.76$ and minimum lift coefficient of $C_D = 0.007$ [11].

Herbert Hogan [12] filed a US Patent of a variable camber wing in 1931, which consisted of a rigid central aerofoil with an adjustable 'front' and 'rear' sections. The leading and trailing edge sections of the aerofoil are discretised in individual structural units that pivot about central points and are actuated using a system of gears and linkage bars. The moving sections allow for camber distribution modifications at multiple locations at both leading and trailing edges, resulting in smooth and continuous changes in camber. Similarly, Charles Grant (1939) designed and patented a variable camber wing that only morphed at the trailing edge. The mechanism consisted of a series of hinged panels actuated by a set of external pivot arms [29]. In 1938, Roland Chilton patented a wing capable of varying both camber and surface area. This design implemented a series of leading and trailing edge panels that slid on guide tracks. It was meant to be used in a 'multi-part' wing, where fixed, rigid sections are alternated with auxiliary morphing sections [13]. Although impractical due to the complexity of the mechanisms and the added weight they represented, these preliminary concepts demonstrated remarkably well the potential of variable camber. These early designs highlight a common aspect that is still observed in many more modern camber morphing concepts, i.e. the changes in camber are localised at the leading and trailing edges of the aerofoil section and not at the central portions.

The complexity and weight penalty of these morphing concepts was a significant disadvantage and therefore they were not implemented in full-scale applications. It was not until the 1990s, when advances in smart materials and actuation systems—such as the use of Piezoelectric and Shape Memory Alloys (SMAs)—along with the use of composite materials, that camber morphing became a topic of interest in the aircraft design research community again.

2.4.3 Camber Morphing: Modern Concepts

The main objective of 'modern' camber morphing concepts is to address the weight penalty and complexity of earlier morphing mechanisms so that real aerodynamic benefits can be observed. As mentioned in Section 2.1, advances in smart materials and lightweight structures have led to lighter and less complex morphing mechanisms. For example, developments in piezoelectric materials [14, 15] and Shape-Memory Alloys (SMA) [16, 17] have focused on exploring alternative actuation mechanisms, whereas the further understanding of composite laminates has led to exploiting structural instabilities for shape-changing [18–20]. Furthermore, some concepts achieved variable camber by embedding actuators within the wing skin [14, 23], whereas others focused on active actuation of the internal load-bearing structural members [17, 79–81].

Despite the actuation mechanisms, a common aspect among the majority of these morphing concepts is that the change in shape does not occur across the entire aerofoil section, but is mainly localised on the trailing edge, where the aerodynamic loads are relatively low. However, there are concepts that have developed morphing leading edge devices, such as a compliant "droop-nose" morphing leading edge using superelastic materials [82], whereas others have combined both leading and trailing edges morphing devices [83]. Similarly, Werter et al. (2016) [84] proposed leading and trailing edge morphing devices that combined skin warping and bending to induce shape change. This research effort focused on developing a morphing mechanism that could be retrofitted to an existing aircraft using as many off-the-shelf components as possible.

Some research efforts have focused on studying the benefits of morphing from a fixed-wing aircraft systems-level perspective. Some examples are the NASA Ames F-111 Mission Adaptive Wing, where a variable camber wing is implemented to optimise aerodynamic performance at different flight scenarios [21]; the DARPA Smart Wing project [22] (Figure 2.6); and the NASA-Boeing Variable Camber Continuous Trailing Edge Flap (VCCTEF) [85] concept. This latter concept focused on variable camber morphing with spanwise variations by using a series of panels that were individually hinged to each other, providing significantly higher degrees of freedom than a traditional plain flap and allowing for continuous changes in camber. Even though this concept successfully showed through analysis the potential aerodynamic benefits of gradual chances in camber along the span, the design would add significant structural complexity to the wing. Similarly, Flexsys Flexfoil [86] morphing device is capable of generating camber variations along the span, reducing both induced drag and wing root bending moments simultaneously. This concept has been successfully flight tested and is currently being commercialised for large-scale applications [87].

To successfully implement camber morphing concepts in fixed-wing applications, it is necessary to simultaneously address both the two-dimensional lightweight aerofoil morphing concept design and its integration into three-dimensional wings. However, there is a current lack of these combined efforts in the literature, which is being addressed by this thesis.

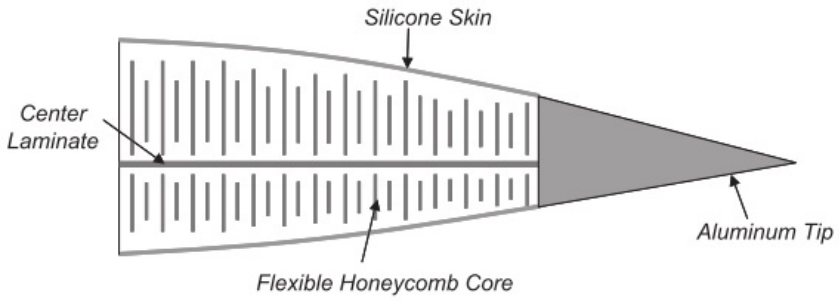

Figure 2.6: DARPA smart wing variable camber concept. Reproduced from Kudva (2004) [22], with Author's permission.

The specific morphing concept that is developed in this thesis is the Fish Bone Active Camber (FishBAC) concept, which is a compliance-based morphing device capable of generating large, smooth and continuous changes in camber distribution [24, 25]. Initial wind tunnel testing of a 3D printed plastic version of this concept measured a 20-25% improvement in lift-to-drag ratios when compared to a traditional trailing edge flap configuration [25]. These significant aerodynamic efficiency improvements can directly translate into fuel efficiency gains in fixed-wing aircraft.

2.5 Fish Bone Active Camber (FishBAC) Concept

The FishBAC device is a compliance-based morphing aerostructure that is highly orthotropic as it has been carefully engineered to allocate stiffness along the span while remaining compliant along the thicknesswise bending direction.

The FishBAC's main load-bearing member is a central bending plate (spine) that follows the aerofoil camber line. Attached to it, a series of perpendicular spanwise stringers of varying height support the skin, maintain the aerofoil thickness distribution and also increase the spanwise stiffness, without adding significant stiffness in the chordwise direction (Figure 2.7). The structure is actuated by a set of servo actuators that drive antagonistic tendons through a spooling-pulley mechanism. These tendons are clamped to each spooling-pulley in one end and then anchored to the top and bottom surfaces of a rigid strip at the extreme trailing edge of the device. Therefore, when the pulley is rotated by the actuators, the tendon tensions, converting actuation torque and rotation into bending moments on the FishBAC. Depending on the direction of these actuation inputs, the FishBAC bends upwards or downwards. Another feature of the FishBAC is the number of actuation points along the span is an open design variable; thus, gradual changes in camber along the span can be achieved if these actuators apply different loads. Having this spanwise deflection 'control' gives the FishBAC the ability to potentially optimise spanwise lift distributions and to reduce induced drag and spanwise bending moments. Lastly, a pre-tensioned elastomeric sheet skin is bonded to the stringers, and acts as the aerodynamic

surface of the FishBAC [24]. The FishBAC trailing edge device integrates readily with the rigid wing that carries the majority of the aerodynamic loads.

The large camber deflections that the FishBAC can achieve are mainly due to its thicknesswise bending compliance along the chordwise direction. This bending compliance is achieved by reducing the bending stiffness contribution of the stiffest structural element (i.e. bending spine) by locating it near the neutral axis, whereas the structural elements furthest away from the neutral axis (i.e the skin sheets) have a Young's Modulus three to four orders of magnitude lower than the spine's. Moreover, as previously mentioned, the spanwise stringers do not significantly contribute to the chordwise bending stiffness. This structural design gives the FishBAC the ability to achieve large changes in camber distribution without any surface discontinuities, while still having sufficient spanwise rigidity to sustain spanwise bending moments.

The FishBAC is proposed as an alternative to plain flaps—i.e. defined as when the flap is hinged to the wing without a structural gap. Since neither the FishBAC nor plain flaps have structural gaps in the wing surface, similar maximum lift coefficients will be achieved by both devices. However, most general aviation and commercial airliners have slotted flaps—i.e. flaps with a structural gap between the rigid wing and the moving elements. As previously mentioned, unlike hinged slotted flaps, the FishBAC has no structural gaps between the main wing and the morphing device. These gaps in slotted flaps increase lift as they allow flow from the pressure side to go to the suction side, which prevents boundary layer separation and increases the maximum lift coefficients [88]. Therefore, the absence of these structural gaps in the FishBAC comes at the expense of a reduction in maximum lift coefficient ($C_{L_{\max}}$), if compared against slotted flaps. However, this reduction in maximum lift coefficient is offset by both its large lift control authority and its increase in aerodynamic efficiency. In summary, it can be stated that the FishBAC is more suitable to be used for aerodynamic optimisation and control purposes than as a high lift device.

The initial structural design and analysis of this concept was performed using an analytical model based on Euler-Bernoulli beam theory [26], and the first prototypes were 3D printed using Acrylonitrile Butadiene Styrene (ABS) plastic. Also, significant modelling and experimental work was performed in terms of developing these first-generation FishBAC devices. These efforts

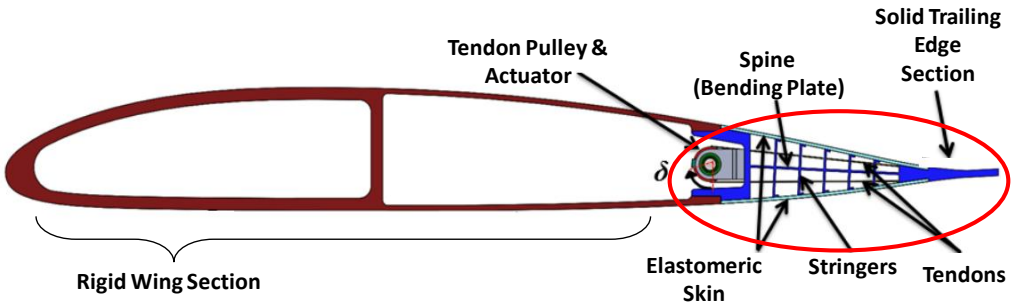

Figure 2.7: Schematic of the structural configuration of the Fish Bone Active Camber morphing trailing edge concept [26].

include the development of an XFOIL-based FSI analysis [27], a preliminary wind tunnel test of an ABS plastic 3D printed prototype [25]—where a drag reduction of $20-25\%$ was achieved when compared to a hinged control surface—and a multi-objective optimisation routine for optimising the FishBAC's geometry and structural configuration [89]. This preliminary work successfully demonstrated the capabilities of the FishBAC as a morphing technology, motivating further development.

2.5.1 Limitations of Previous Work

Even though the initial modelling, design, manufacture and wind tunnel test of the FishBAC successfully demonstrated its aerodynamic benefits, the work was limited to developing the 2D aerofoil device. To scale-up the FishBAC technology and implement it in fixed-wing applications, the FishBAC must be analysed, designed and manufactured as a three-dimensional structure, with the coupling between structural and aerodynamic response that is so intrinsic to compliance-based morphing being considered from the start. Also, the use of aerospace grade materials, such as composite laminates, is of extreme importance for scaling-up this technology towards industrial applications.

Specifically on the modelling side, the already developed Euler-Bernoulli-based FishBAC structural model [26] can neither model composite laminates nor capture spanwise deflections. Also, the existing aerodynamic solver is based on XFOIL, a 2D-viscous corrected panel method incapable of capturing 3D aerodynamic effects [27]. Therefore, new structural and aerodynamic tools must be developed and coupled in a 3D FSI routine. Also, these modelling tools must be computationally efficient and with the right level of fidelity, so that they can be used for multiple design iterations and structural optimisation.

Besides developing new modelling techniques, it is crucial to manufacture a working FishBAC prototype with a carbon fibre spine to both demonstrate that it is possible and to validate the new structural, aerodynamic and FSI models. Also, this wing model will be used to obtain additional wind tunnel data to both corroborate the aerodynamic efficiency gains observed in preliminary wind tunnel tests, and to further understand the aerodynamic benefits of variable camber morphing.

In summary, these new modelling techniques, along with a complete set of experimental data, will create a robust framework for future design, optimisation and manufacture of future composite FishBAC devices, as well expanding the overall knowledge on how camber morphing wings can benefit fixed-wing aircraft.

Chapter 3

Discontinuous Composite Kirchhoff-Love Plate Model

This chapter presents a parametric structural model for simulating the static behaviour of a composite FishBAC. It addresses the limitations of a previously developed 1-dimensional Euler-Bernoulli FishBAC beam model where, by definition, only isotropic materials and displacements in the thicknesswise dimension can be modelled. Specifically, these limitations are addressed by implementing a 2-dimensional structural model based on Kirchhoff-Love Plate Theory and by using Classical Laminate Theory to obtain the material properties of the composite laminates.

3.1 Introduction

As mentioned in Chapter 2.5, the initial analysis, design and sizing of the first FishBAC prototypes were performed using an analytical structural model based on Euler-Bernoulli beam theory [26]. This model accounts for chordwise changes in stiffness due to structural discontinuities (spanwise stringers), by varying the bending stiffness distribution (i.e. $EI(x)$) across the chord length. One advantage of modelling the out-of-plane behaviour with a beam model is that a 1-D net aerodynamic pressure distribution can be directly integrated and the actuation loads can be accounted for by adding local point forces and moments. However, as also mentioned in Chapter 2.5, a beam model is not capable of capturing any displacement variations along the span, as the spanwise dimension is neglected in a 1-D beam model. Consequently, the spanwise aerodynamic pressure distribution cannot be captured, which is crucial to analyse the aerodynamic behaviour of 3D wings.

It is precisely these sorts of spanwise varying deformations that are of great interest, as they provide the ability to actively change the spanwise loading of the wing. As explained in Chapter 1, the ability to have significant control over the spanwise distribution of lift on a 3D wing would provide a number of potential drag, structural, control, and aeroelastic benefits. The presented model addresses these shortcomings by modelling the FishBAC using a two-dimensional structural formulation based on Kirchhoff-Love Plate Theory. This approach is more suitable for the intended application as variations in out-of-plate displacement due to several factors, such as bend-twist coupling, non-uniform actuation inputs and 3D aerodynamic effects [90] can be captured and eventually be exploited to optimise lift distributions in both chord and spanwise directions.

Also, another advantage of modelling the structure using Plate Theory is to allow for the exploitation of the high degree of material anisotropy achievable with composite materials, which is captured within the model by including Classical Laminate Theory (CLT) formulations within the plate's differential equation. Derivations of the equations of motions and strain energy of composite laminated plates are well established [91], and consequently, they can be implemented to analyse and design a composite FishBAC prototype.

The objective of this chapter is to develop a semi-analytical model of the FishBAC concept that captures the in-plane and out-of-plane displacement due to both aerodynamic pressure (i.e. transverse loading distribution) and actuation loads (i.e. distributed moments at the trailing edge). This model can analyse the discontinuous geometry of the FishBAC by modelling its variable stiffness as multiple individual plates that are joined by penalty springs, capturing its complexity within a single system of linear equations. The scope of this effort represents a significant advance beyond existing semi-analytical plate models for discontinuous structures in the literature (for any structure) and a significantly more capable approach to modelling the FishBAC. Currently, there is evidence in the literature of neither the use of penalty springs to join a significant number of individual plate partitions (115 in this case) nor the use of Rayleigh-Ritz Method to model static deflections under transverse pressure and distributed moments of such a complex structure, where several drastic changes in stiffness exist. Therefore, there is significant novelty in the ambition of what is desired and realised, with this work.

The semi-analytical nature of the model not only allows local stiffness properties to be defined for each individual plate 'partition', but also to rapidly modify the geometric parameters (e.g. stringer spacing, spine and skin thickness, wing dimensions, among others) and material properties. Lastly, unlike in FEM, the semi-analytical model is 'mesh-independent', which means that its convergence only depends on the number of the assumed shape functions that are used.

This chapter is outlined as follows: first, an introduction of the Kirchhoff-Love plate model and the relevant modelling parameters for this problem are presented, followed by a brief description of the Rayleigh-Ritz Method, assumed shape functions, boundary conditions and model implementation. Lastly, a convergence study and comparison with FEM results is introduced as a validation to the developed semi-analytical model.

3.2 Discontinuous Kirchhoff-Love Plate Model

The following section introduces the fundamentals of the plate theory that are used to model the behaviour of the FishBAC, as well as the specific procedure that is followed to obtain the displacement fields, including an introduction to the Rayleigh-Ritz Method for structural analysis [91]. Also, this section introduces the assumed shape functions and the global boundary conditions that are implemented in the semi-analytical formulation.

3.2.1 Kirchhoff-Love Plate Theory

Kirchhoff-Love plate theory is a two-dimensional mathematical model that can be used to analyse stresses and strains of thin plates when subjected to external forces and moments. It assumes that through-thickness stresses and strains, as well as transverse shear strains, are negligible. Thus, this theory is only valid for thin plates with thickness-to-length and thickness-to-width ratios of less than 1/20 (preferably 1/30). Kirchhoff-Love plate theory is analogous to Euler-Bernoulli beam theory, where through-thickness stresses and strains are also neglected [91].

3.2.2 Rayleigh-Ritz Method

The Rayleigh-Ritz Method is a variational method that can be used to approximate solutions to partial differential equations based on energy formulations. Its foundation lies in the principle of conservation of total energy in a closed system. From a mechanics point of view, this implies that the sum of the strain energy of the body and the kinetic and potential energies due to external loads is a stationary value [91, 92]. This approach assumes that no frictional losses exist, which is a reasonable simplifying assumption for many types of structures.

For an initially flat plate, these energy formulations can be written in terms of a total energy expression that is a function of the plate displacement's v^0, v^0 and w

$$\Pi(v^0, v^0, w) = U + W + V - T = \text{constant}, \tag{3.1}$$

where U refers to the strain energy of the body, V and W are the potential energies due to transverse and in-plane loads, respectively, and T is the kinetic energy. Since the scope of this work is to analyse the static displacement of composite FishBAC structures, kinetic energy is neglected for the time being, although it can still be added in later if dynamics are of interest.

3.2.3 Strain Energy

For an elastic body, the total strain energy is defined as the integral of the sum of the products of stresses and strains across the volume of the body, as described by

$$U = \frac{1}{2}\iiint (\sigma_x\epsilon_x + \sigma_y\epsilon_y + \sigma_z\epsilon_z + \tau_{xz}\epsilon_{xz} + \tau_{yz}\epsilon_{yz} + \tau_{xy}\epsilon_{xy})dxdydz\,. \tag{3.2}$$

Since the semi-analytical model is based on Kirchhoff-Love Plate Theory, through-thickness and transverse shear strains are neglected (i.e. $\epsilon_z = \epsilon_{xz} = \epsilon_{yz} = 0$), as stated by Whitney (1987) [91]. Furthermore, the in-plane strains of the laminate can be obtained in terms of the plate's displacements and their derivatives:

$$\begin{aligned}\epsilon_x &= \frac{\partial v^0}{\partial x} - z\frac{\partial^2 w}{\partial x^2} \\ \epsilon_y &= \frac{\partial v^0}{\partial y} - z\frac{\partial^2 w}{\partial y^2} \\ \epsilon_{xy} &= \frac{\partial v^0}{\partial y} + \frac{\partial v^0}{\partial x} - 2z\frac{\partial^2 w}{\partial x \partial y}\ .\end{aligned} \tag{3.3}$$

These strain definitions (Equation 3.3) yield to a mathematical expression in terms of the plate's displacements and their derivatives and the stiffness terms. These stiffness terms are expressed in terms of the *ABD* Matrix, obtained from CLT. The expression represents the total strain energy of the laminate, such that

$$\begin{aligned}U_{ij} = \frac{1}{2}\iint & A_{11}\left(\frac{\partial u^0_{ij}}{\partial x}\right)^2 + 2A_{12}\frac{\partial u^0_{ij}}{\partial x}\frac{\partial v^0_{ij}}{\partial y} + A_{22}\left(\frac{\partial v^0_{ij}}{\partial y}\right)^2 + 2\left(A_{16}\frac{\partial u^0_{ij}}{\partial x} + A_{26}\frac{\partial v^0_{ij}}{\partial y}\right)\left(\frac{\partial u^0_{ij}}{\partial y} + \frac{\partial v^0_{ij}}{\partial x}\right) \\ & + A_{66}\left(\frac{\partial u^0_{ij}}{\partial y} + \frac{\partial v^0_{ij}}{\partial x}\right)^2 - 2B_{11}\frac{\partial u^0_{ij}}{\partial x}\frac{\partial^2 w_{ij}}{\partial x^2} - 2B_{22}\frac{\partial v^0_{ij}}{\partial y}\frac{\partial^2 w_{ij}}{\partial y^2} - 2B_{12}\left(\frac{\partial v^0_{ij}}{\partial y}\frac{\partial^2 w_{ij}}{\partial x^2} + \frac{\partial u^0_{ij}}{\partial x}\frac{\partial^2 w_{ij}}{\partial y^2}\right) \\ & -4B_{66}\frac{\partial^2 w_{ij}}{\partial x \partial y}\left(\frac{\partial u^0_{ij}}{\partial y} + \frac{\partial v^0_{ij}}{\partial x}\right) - 2B_{16}\left[\frac{\partial^2 w_{ij}}{\partial x^2}\left(\frac{\partial u^0_{ij}}{\partial y} + \frac{\partial v^0_{ij}}{\partial x}\right) + 2\frac{\partial u^0_{ij}}{\partial x}\frac{\partial^2 w_{ij}}{\partial x \partial y}\right] - 2B_{26}\left[\frac{\partial^2 w_{ij}}{\partial y^2}\left(\frac{\partial u^0_{ij}}{\partial y} + \frac{\partial v^0_{ij}}{\partial x}\right) + 2\frac{\partial v^0_{ij}}{\partial y}\frac{\partial^2 w_{ij}}{\partial x \partial y}\right] \\ & + D_{11}\left(\frac{\partial^2 w_{ij}}{\partial x^2}\right)^2 + D_{22}\left(\frac{\partial^2 w_{ij}}{\partial y^2}\right)^2 + 4D_{66}\left(\frac{\partial^2 w_{ij}}{\partial x \partial y}\right)^2 + 2D_{12}\frac{\partial^2 w_{ij}}{\partial x^2}\frac{\partial^2 w_{ij}}{\partial y^2} + 4\left(D_{16}\frac{\partial^2 w_{ij}}{\partial x^2} + D_{26}\frac{\partial^2 w_{ij}}{\partial y^2}\right)\frac{\partial^2 w_{ij}}{\partial x \partial y}\,dx\,dy\,.\end{aligned} \tag{3.4}$$

The *ABD* Matrix describes the stiffness of the composite laminate; it combines both material and geometric stiffness in a single expression [93].

3.2.4 Potential Energy due to External Loads

There are two external loads acting on the FishBAC: the aerodynamic pressure distribution and the actuation loads. The aerodynamic pressure—found separately using an aerodynamic solver, e.g. panel methods or CFD—can be treated as a transverse pressure distribution acting on the plate, with both variations in x and y. The potential energy due to transverse pressure distributions (i.e. force per unit area) is defined as the integral of the pressure times the transverse displacement across the surface area [91]

$$V_{ij} = -\iint q_{ij}(x,y)\, w_{ij}(x,y)\, dx\, dy\,. \tag{3.5}$$

Additionally, if frictional losses in the actuation mechanism are neglected, the actuation torque inputs can also be introduced to the Rayleigh-Ritz formulation as potential energy acting on the plate. The composite FishBAC device is actuated at two locations along the span of the wing, which are equidistant from the centre. This actuation is currently performed by a set of servo actuators that drive a tendon-based spooling pulley mechanism (see Chapter 2.5).

This pulley is connected to a Kevlar-tape tendon that travels through slots in the stringers until reaching the trailing edge portion of the spine (where they are stitched and bonded). In this way, torque and rotation input to the spooling pulley is transformed into force and displacement of the tendons, before being converted back into a bending moment at the trailing edge. It is this bending moment which drives the morphing deformation. To capture the impact of this actuation method within this analysis, the external actuation loads are then modelled as applied distributed moments over each short actuated segment of the FishBAC, such that

$$W_{ij} = -\int M_{x_j}\, \psi_{x_{ij}}(a_i, y)\, dy \ , \tag{3.6}$$

where a_i is the location where the distributed moment is applied, and ψ_x is the plate rotation about the $y-$axis. Since transverse shear strains are neglected, Kirchhoff-Love plate theory assumes that $\psi_x = \partial w/\partial x$. Note that this potential energy formulation neglects any friction on the pulley-tendon system.

3.2.5 Displacement Fields and Shape Functions

The energy definitions presented in Section 3.2.3 are all in terms of the plate's displacements and their derivatives, the material and geometric stiffness represented by the ABD matrix terms (Equation 3.4) and external loads (Equations 3.5-3.6). In this case, both material properties and external loads are known and treated as inputs, whereas the displacements are unknown and, therefore, their shapes need to be determined. Within the context of Rayleigh-Ritz Method, all three displacements (i.e. v^0, v^0 and w) are normally defined in the form of three sets of double summations of terms in the x- and y-direction that satisfy compatibility conditions

$$u^0_{ij} = \sum_{m=0}^{M} \sum_{n=0}^{N} L^{ij}_{mn} X^i_m(x) Y^j_n(y) \tag{3.7a}$$

$$v^0_{ij} = \sum_{m=0}^{M} \sum_{n=0}^{N} O^{ij}_{mn} X^i_m(x) Y^j_n(y) \tag{3.7b}$$

$$w_{ij} = \sum_{m=0}^{M} \sum_{n=0}^{N} P^{ij}_{mn} X^i_m(x) Y^j_n(y), \tag{3.7c}$$

where L_{mn}, O_{mn} and P_{mn} are the displacement amplitudes (unknown constants) and $X_m(x)$ and $Y_n(y)$ are the assumed shape functions, in x- and y- directions, respectively. Note that, since the semi-analytical model performs the energy balance in each one of the plate's partitions individually, different sets of shape functions need to be defined for each one of the partitions. The subscripts i and j in Equation 3.7 refer to the individual partitions in the chordwise and spanwise directions, respectively.

Previous studies have considered several types of shape function. A common approach in plate mechanics is to assume that the displacement occurs in a periodic form, which makes the use of cosine and sine Fourier series expansions convenient as it allows for closed-form solutions to the differential equation. Several examples of using periodic functions are presented in the literature [94–97].

Another alternative to periodic functions is using orthogonal polynomials. They present better convergence rates when deflections do not occur in a periodic way as they can capture localised features using fewer expansion terms [92]. In the context of plate mechanics, successful examples of implementing generic orthogonal polynomials can also be found in the literature [98], specifically in the field of static analysis of fibre-reinforced composite plates using orthogonal polynomials [99].

Furthermore, a specific set of polynomials, known as the 'Jacobi family', are commonly used in structural mechanics. This 'family' includes the Gegenbauer polynomials, which is a special case of the Jacobi polynomials and the Chebyshev and Legendre polynomials, which themselves are a special case of the Gegenbauer set [100, 101].

From the mechanics point of view, Legendre polynomials have been successfully implemented in several cases, for example, in predicting buckling of highly anisotropic plates [102] and discontinuous panels with variable stiffness [103], analysing displacements of variable stiffness beams and plates under transverse pressure loading [104] and also in capturing step changes in thickness [105]. However, their integrals have an exact value of zero when integrated across their normalised domain. This would imply that there is zero net work when a uniform transverse pressure distribution and external moments are applied (Equations 3.5-3.6), which is not physically correct. On the other hand, Chebyshev polynomials do not integrate to zero in a normalised domain. These non-zero integrations, along with their fast convergence rate [92], were the two main reasons why Chebyshev Polynomials of the First Kind (Figure 3.1) were selected as shape functions. These polynomials are defined as

$$T_n(\zeta) = \frac{1}{2}\left[\left(\zeta - \sqrt{\zeta^2 - 1}\right)^n + \left(\zeta + \sqrt{\zeta^2 - 1}\right)^n\right], \tag{3.8}$$

where n corresponds to the polynomial order.

One crucial aspect to consider during this analysis is that, since Chebyshev polynomials are normalised and defined from $[-1,1]$, the numerical analysis must be performed within this domain. Consequently, two non-dimensional variables (ζ and $\eta \in [-1,1]$) are defined to relate the physical dimensions of each plate to a normalised frame, such that

$$\zeta_i = \frac{2x_i}{a_i} \quad \text{and} \quad \eta_j = \frac{2y_j}{b_j}. \tag{3.9}$$

These two non-dimensional variables are used to replace x and y in Equations 3.4, 3.5, 3.6 and 3.7, which changes the integration bounds from physical boundaries to the normalised ones ($[-1,1]$). Figure 3.2 shows the relationship between physical and normalised frames.

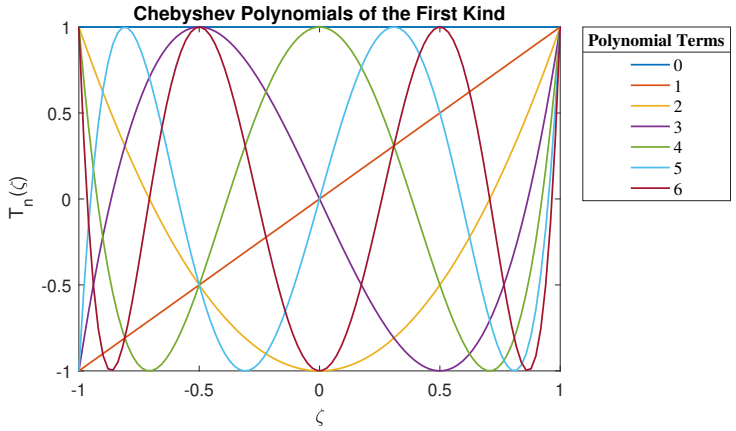

Figure 3.1: Chebyshev Polynomials of the First Kind in a normalised domain

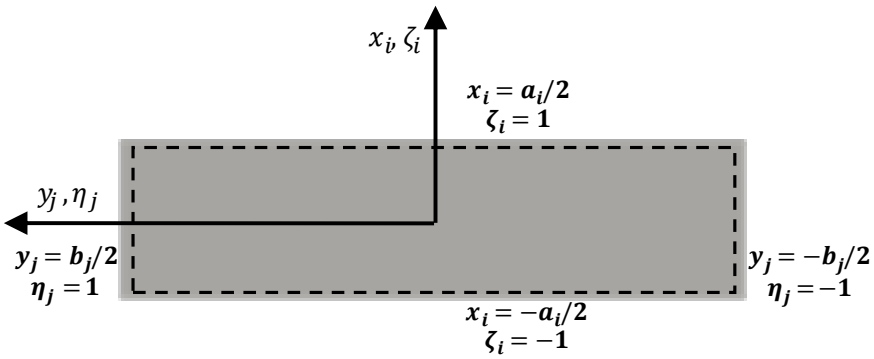

Figure 3.2: Coordinate transformation, from physical x_i,y_j to normalised ζ_i,η_i coordinate frames, performed in each one of the partitions.

3.2.6 Global Boundary Conditions

The FishBAC morphing trailing edge section is modelled as a cantilever plate (Figure 3.3) clamped to the rigid forward section of the wing . This constraint implies that displacements and rotations must be zero at the FishBAC's root. Since the Chebyshev polynomials do not naturally meet this condition (see Figure 3.1), the expansion in the chordwise polynomial functions must be modified to enforce the clamped boundary at the root. Jaunky et al. (1985) [106] introduced the concept of using a circulation function to enforce boundary conditions at any location ζ_c

$$\Gamma_x(\zeta) = (\zeta - \zeta_c)^{n_{\text{bc}}}, \tag{3.10}$$

where the value of n_{bc} is set depending on the nature of the boundary condition of the ζ_c location (Table 3.1). Note that, as long as the circulation term is multiplied to every term of the Chebyshev polynomial expansion, the polynomial expansion remains orthogonal.

Table 3.1: Boundary Conditions as implemented by circulation function in Equation 3.10 [107].

Boundary Condition at ζ_c	n	Displacement	Rotation
Free Edge (F)	0	Free	Free
Simply Supported (SS)	1	0	Free
Clamped (C)	2	0	0

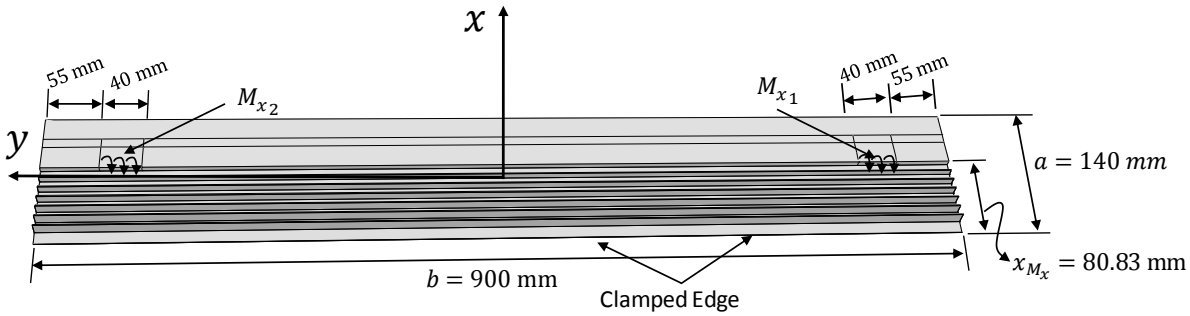

Figure 3.3: Global coordinate frame of the FishBAC, as well as global dimensions and locations where actuation moments are applied. These actuation loading points correspond to the tendon-spine points of contact (tendons not shown).

3.2.7 Stiffness Discontinuities and Local Boundary Conditions

The stiffness of the FishBAC is inherently discontinuous due to the presence of the stringers, which implies that the energy balance presented in Equation 3.1 has to be calculated in each section of uniform stiffness as the ABD Matrix terms in Equation 3.4 vary significantly between regions with and without stringers. Note that, since independent shape functions are used for each individual section (Equation 3.7), a coordinate transformation from the physical to the normalised frame has to be performed in each partition, individually. Hence, a local coordinate system is defined at the centre of each element, and then individually mapped to local ζ_i and η_j variables (Equation 3.9) as observed in Figure 3.2.

In structures with stiffness discontinuities, shear force and bending moments at each 'joint' must be continuous when approached from either side of the boundary. However, due to the 'step' change in both geometric and material stiffness, curvatures are not continuous. These types of structures are known as 'C^1-continuous', where displacement and rotations at local boundaries must be continuous, but higher-order derivatives do not. Since Chebyshev polynomials do not inherently meet this type of structural continuity at local boundaries, these have to be enforced by other means [107].

There are two common approaches for ensuring displacement and rotation continuities: Lagrange Multiplier Method or Courant's Penalty Method [92]. The former one consists of deriving a set of constraint equations that are scaled by unknown coefficients—known as Lagrange Multipliers—that represent the exact value that the constraints need to be weighted by to enforce continuity. The latter approach consists of using a penalty energy term, analogous to joining each section with a torsional/displacement springs and accounting for the spring energy that is needed to enforce displacement and rotation compatibility. Due to the number of equations and separate Lagrange Multipliers that would need to be solved for in this application, the Courant's Penalty Method, in the form of spring penalty energies, is a more suitable approach. It is worth noting that, while these are not the only methods to enforce the 'C^1-continuity'—for example, each individual polynomial set could be modified so they naturally meet this condition—these two approaches are by far the most common in the literature as modifying each polynomial set would be difficult to set up and computationally expensive.

3.2.8 Courant's Penalty Method

As mentioned in the previous subsection, each one of the plate's sections is assumed to be joined with an artificial penalty spring with a stiffness equal to k_k. Given the relevant degrees of freedom between partitions in this analysis, a set of penalty equations for displacements and out-of-plane rotations are defined as

$$U_{pu,kl} = \frac{k_k}{2}\int_{-b_j/2}^{b_j/2}(u_k(x_{kl}^{(+)},y_j) - u_l(x_{kl}^{(-)},y_j))^2 dy \tag{3.11a}$$

$$U_{pv,kl} = \frac{k_k}{2}\int_{-b_j/2}^{b_j/2}(v_k(x_{kl}^{(+)},y_j) - v_l(x_{kl}^{(-)},y_j))^2 dy \tag{3.11b}$$

$$U_{pw,kl} = \frac{k_k}{2}\int_{-b_j/2}^{b_j/2}(w_k(x_{kl}^{(+)},y_j) - w_l(x_{kl}^{(-)},y_j))^2 dy \tag{3.11c}$$

$$U_{pw_x,kl} = \frac{k_k}{2}\int_{-b_j/2}^{b_j/2}\left(\frac{\partial w_k(x_{kl}^{(+)},y_j)}{\partial x} - \frac{\partial w_l(x_{kl}^{(-)},y_j)}{\partial x}\right)^2 dy \tag{3.12a}$$

$$U_{pw_y,kl} = \frac{k_k}{2}\int_{-b_j/2}^{b_j/2}\left(\frac{\partial w_k(x_{kl}^{(+)},y_j)}{\partial y} - \frac{\partial w_l(x_{kl}^{(-)},y_j)}{\partial y}\right)^2 dy, \tag{3.12b}$$

where k and l correspond to two adjacent partitions with different stiffness and x_{kl} to the location where they meet. When the spring stiffness k_k is 'large', the energy is minimised when the differences in displacements and rotations in Equations 3.11 and 3.12 are minimal. Additionally, a similar set of penalty expressions are implemented for spanwise discontinuities, where integration with respect to x at locations y_{kl} is performed, instead of with respect to y at x_{kl}.

As previously mentioned, the values of k_k need to be 'large' to enforce continuity. However, if these values are 'too large', numerical errors arise due to ill-conditioning of the coefficient matrix.

The condition number of a matrix is defined as the product of the Euclidean norm of the matrix and its inverse, expressed as

$$K(A) = \|A\|\|A^{-1}\|. \tag{3.13}$$

The resulting condition number is a measure of how close to singular the matrix is. A low condition number represents that the matrix is 'well-conditioned' and hence, its inversion is stable, whereas a high condition number indicates 'ill-conditioning'. An ill-conditioned system is much more sensitive to changes in response due to small changes in input [108, 109], introducing numerical error and decreasing solution stability.

Previous studies have selected the stiffness of penalty springs based on convergence studies of their models. Coburn (2015) [107] performed a convergence study based on percentage difference with respect to FEM and estimated that the model was accurate for a penalty stiffness between $k = 1 \times 10^5 - 1 \times 10^{12}$ N/m. Similarly, Vescovini and Bisagni (2012) [105] estimated that a penalty stiffness of $k = 1 \times 10^8$ N/m was 'sufficient' for convergence.

Convergence studies for selecting the magnitude of both chordwise and spanwise penalty springs were performed using the FishBAC's geometry. These studies showed that, for four different spine composite ply stacking sequences, a value of $k = 1 \times 10^8$ N/m provides stable results. Figure 3.4 shows an example of these convergence studies for a $[45/45/45]_S$ spine stacking sequence. To mitigate numerical errors due to high condition number, the coefficient matrix is normalised by dividing each individual row K_T by its root mean square, such that [109]

$$\widetilde{K_T} = \frac{K_{T_j}}{\sqrt{\sum K_{T_j}^2}}. \tag{3.14}$$

In this particular application, this normalisation reduces the condition number of the coefficient matrix by at least four orders of magnitude.

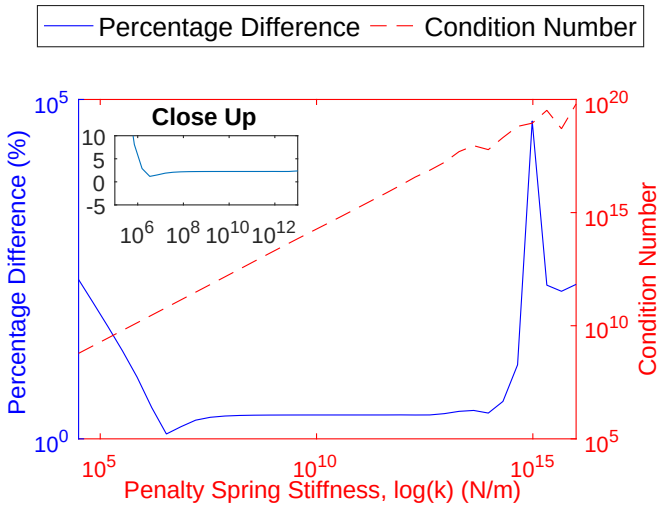

Figure 3.4: Convergence study for selecting the magnitude of the penalty springs for Chebyshev Terms of $M = N = 5$. Primary axis (solid) presents the RMS percentage error with respect to FEM, whereas the secondary axis (dashed) presents the condition number of the coefficient matrix.

3.2.9 Principle of Minimum Potential Energy

As previously stated in Section 3.2.2, the Rayleigh-Ritz method is based on the assumption of conservation of total energy in a closed system. This approach implies that the sum of energies defined in Equation 3.1 has a stationary value. Therefore, differentiating the total energy formulation with respect to any of the unknown constant shape function amplitudes, L_{mn}, O_{mn} and P_{mn}, leads to a state of minimum energy [92, 107]. Note that, to have a state of stable minimum energy, static equilibrium must exist. From a mathematical point-of-view, a state of stable equilibrium exists when *(a)* the first derivatives of the total potential energy equation (Equation 3.1) are equal to zero and *(b)* the second derivatives are greater than zero (i.e. positive definite). This condition is readily met by linear elastic bodies under small deformations as long as the materials are also linearly elastic (i.e. $E > 0$ and $-1 < \nu < 0.5$) [110]. For this application, all three types of materials are defined as linear elastic, hence, the second derivatives of Equation 3.1 with respect to the unknown amplitudes L_{mn}, O_{mn} and P_{mn} are positive definite. Since the total potential energy is quadratic in terms of the unknown coefficients [91], a system of $3 \times (M \times N) \times (i \times j)$ linearly independent equations can be constructed by

$$\frac{\partial \Pi}{\partial L_{mn}^{ij}}, \frac{\partial \Pi}{\partial O_{mn}^{ij}}, \frac{\partial \Pi}{\partial P_{mn}^{ij}} = 0 \quad \begin{cases} m = 1,2,...,M \\ n = 1,2,...,N \end{cases}, \tag{3.15}$$

where $i \times j$ refers to the total number of partitions in chord and span directions. Consequently, a single system of linear equations is solved to estimate the value of all the unknown amplitudes of the entire structure, regardless of the number of individual partitions that are used to ap-

proximate the FishBAC geometry. This approach is computationally convenient, as the static behaviour of the highly discontinuous geometry can be captured with a single coefficient matrix.

3.3 Modelling Assumptions: Geometry and Materials

One of the initial assumptions is that deflections of the non-morphing section of the wing are negligible. Consequently, the semi-analytical model presented in this chapter only focuses on the deformation of the compliant morphing trailing edge device, which is assumed to be 'clamped' (i.e. cantilever boundary condition) to this rigid front portion of the wing. Therefore, the FishBAC is modelled as a cantilever plate with three free edges.

Furthermore, the semi-analytical model developed in this chapter assumes that the spine's initial geometry (Figure 3.5a) is a flat plate with no initial curvature (Figure 3.5b). For symmetric aerofoils, this assumption has no effect, but for cambered aerofoils, it flattens out the small amount of curvature that exists in the camber line over the morphing region. Due to this initial assumption, a number of 'simplifications' are applied to the geometry, such as: within each spine section bounded by two stringers, the skin is flat and parallel to the spine, and each skin section is located at an equivalent height (from the spine) that is calculated by estimating the equivalent contribution in second moment of area of the curved skin in the original design. Lastly, the solid, tapered trailing edge section is 'discretised' into sections of constant thickness.

To capture the significant stiffness discontinuities caused by the stringers, the structure is divided into several partitions of uniform thickness distribution and composite stacking sequence and the plate's energy balance is solved in each partition, individually. Each one of these individual 'plates' are then joined together by artificial penalty springs at each local boundary, as explained in Section 3.2.8. Lastly, the stiffness of each partition is 'condensed' to its mid-plane (Figure 3.5c) by using CLT. This means that displacement and rotation compatibility is only enforced at the midplane and not at the stringers-skin joints. This assumption is reasonable and expected to be valid for the FishBAC due to the compliance of the skin. As the materials used for the stringers and spine are at least three orders of magnitudes stiffer than the elastomeric skin, there is no risk of structural penetration (i.e. the skin perforating through a stringer in the in-plane direction) at the skin-stringer contacts if compatibility is not enforced at these locations.

Figure 3.5 shows a comparison between the FishBAC's actual geometry (Figure 3.5a), the assumed geometry in the semi-analytical model (Figure 3.5b) and the 'condensed' stiffness assumption at the mid-plane (Figure 3.5c). Note that the geometry of the FEM model that is used to validate the semi-analytical model corresponds to the actual geometry (Figure 3.5a), which allows for the validation of the underlying geometry assumptions and the implementation of the modelling methods. Further details about the FEM model and the validation process are discussed in Section 3.5.

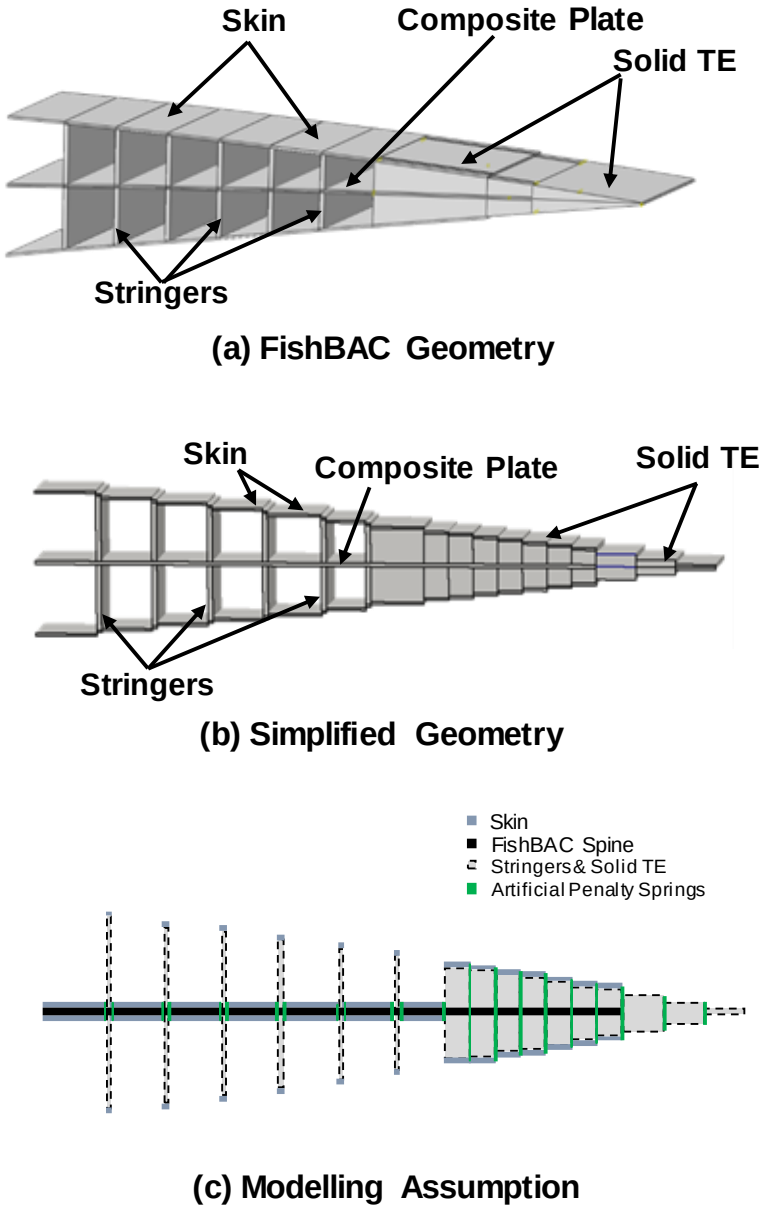

Figure 3.5: FishBAC's geometry (a), simplified geometry (b) and modelling assumption (c). In the FishBAC geometry (a), the spine follows the camber line of the aerofoil section, whereas in the simplified geometry (b), the spine has no curvature. Moreover, the stiffness of each partition is 'condensed' at the local midplane, and each partition is joined using a series of artificial penalty springs (c).

Three types of materials are used throughout this analysis: High-Strength Carbon Fibre-Reinforced Polymer (CFRP), Acrylonitrile Butadiene Styrene (ABS) 3D printed plastic and silicone sheets. The stringers and solid trailing edge sections are modelled using isotropic ABS plastic, whereas the skin is modelled as isotropic silicone. This material selection for stringers, solid trailing edge and skin was performed based on the materials that were used for manufacturing the isotropic FishBAC wind tunnel prototype [26] and also because they are relevant to the first FishBAC composite prototype, to be shown in forthcoming chapters. Finally, the composite spine is modelled using High-Strength Carbon Fibre-Reinforced Polymer. Table 3.2 presents the stiffness values of each one of the material definitions.

It is important to mention that all integrals were performed in the non-dimensional reference frame, defined from $[-1, 1]$ in both in-plane directions. Since each plate partition is rectangular and it is also assumed that the relationship between the normalised and physical frames (Equation 3.9) does not vary with increasing displacements, the normalised-to-physical scaling of the integrals can be performed 'outside' the integrals. This assumption is valid as the Jacobian matrix of each partition is constant, and can therefore be factored outside the integral. There are two reasons why this is important: first, the integrals do not need to be calculated for every individual partition as they can be later scaled for each individual element, and second, this approach allows the computation and storage of all integrals of interest before performing the structural analysis, which has a significant positive impact on both computation times and RAM memory use.

The FishBAC was then divided into a total of 115 partitions: 23 in the chordwise direction, and 5 in the spanwise direction. This allows all stiffness discontinuities due to stringers to be captured and also to 'discretise' the solid trailing edge section in five partitions to avoid steep changes in thickness. In terms of physical dimensions, the spine has a uniform thickness of 0.75 mm, whereas each stringer's height varies in accordance to the aerofoil thickness distribution, having values that range from 14 mm to 7 mm. Finally, a uniform skin thickness of 0.5 mm maintains the aerofoil section's shape. It is important to mention that, even though this structural model was developed around the FishBAC concept, it can be easily adapted to model any plate-based

Table 3.2: Material properties of CFRP [111], ABS [112] and Silicone [113] used in this chapter. The shear modulus of both ABS and Silicone are obtained using the isotropic Young's modulus and Poisson's ratio.

Material	CFRP	ABS	Silicone
E_{11}	140 GPa	2.9 GPa	3.18 MPa
E_{22}	10 GPa		
G_{12}	5 GPa	N/A	N/A
ν_{12}	0.3	0.35	0.425
t	0.125 mm	N/A	N/A

structure regardless of its level of discontinuity, stiffness properties, boundary conditions or dimensions.

Lastly, it is considered that a targeted accuracy between 5 and 10% is acceptable for initial design and elastic tailoring. However, this target may need to change depending on the sensitivity of the aerodynamics to structural deflections. Future wind tunnel tests and FSI models will give a better insight into the required accuracy for modelling this morphing device.

A top view diagram of the partitions, with their respective dimensions, can be found in Figure 3.6. It is important to mention that the number of partitions, dimensions and stringer spacing can be easily modified by manually changing the input parameters of the MATLAB script file. Also, since the integrals are not computed for each partition individually, increasing the number of partitions does not have a significant impact on the computational cost of the simulation.

3.4 Model Implementation

The structural model described in the previous sections was implemented using MATLAB® R2016a, on an Intel® Core™ i7-4790 3.60 GHz CPU processor, using a 64-bit OS with 16 GB of physical memory. The geometric dimensions of the model were selected based on a 600 mm × 900 mm NACA 2510 wing tunnel wing model that was used for previous experiments. Out of those 600 mm of chord length, the last 140 mm correspond to the FishBAC, which implies that the morphing device starts at 76.6 % of chord length.

The derivatives of the shape functions that are needed to calculate both potential energy and external work were computed analytically, whereas the integrals in Equations 3.4 and 3.5 were computed using *'integral2'*—a two-dimensional adaptive quadrature MATLAB built-in function.

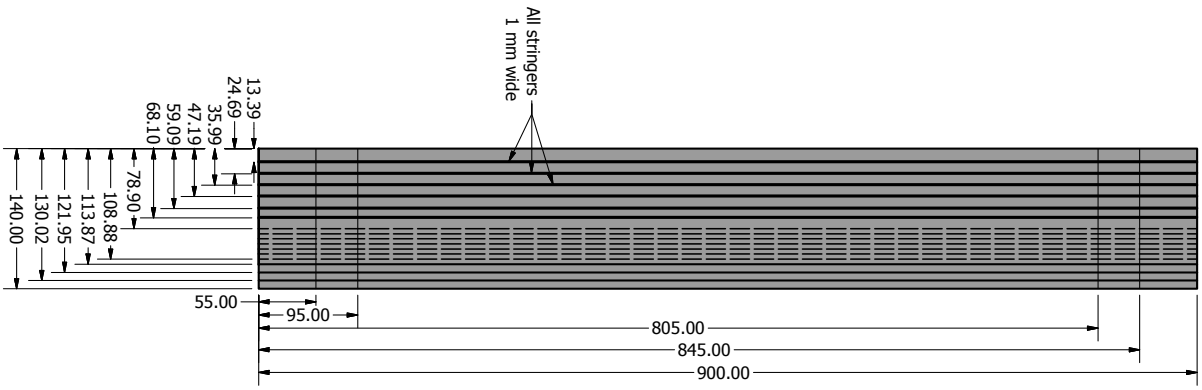

Figure 3.6: Top view of the semi-analytical model geometry (with local dimensions). A total of 23 chordwise and 5 spanwise partitions, respectively, are used to model the complex geometry of the FishBAC. Note that the bottom edge of this drawing is the trailing edge of the aerofoil. All dimensions in mm.

Furthermore, the integrals at the partition boundaries are needed for calculating the work due to actuation moments (Equation 3.6) and penalty energy terms (Equations 3.11 and 3.12). However, the analytical derivative of the Chebyshev polynomial recurrence formula (Equation 3.8) cannot be directly integrated at these locations as it is indeterminate due to a zero denominator. This problem was solved by calculating the analytical limit of the Chebyshev polynomial at its two boundaries (i.e. at $\zeta, \eta = -1$ and 1), followed by integrating the resulting expressions along the reference length using *'integral'*—a one-dimensional adaptive quadrature MATLAB built-in function.

3.5 Validation: Finite Element Model

A FEM model of the FishBAC was developed—using *ABAQUS/CAE*® version 6.14-1—to validate the semi-analytical model. As this FEM model is based on the true FishBAC geometry, comparing the semi-analytical model to it will simultaneously test both the simplified geometry assumptions (Figure 3.5) and the implementation of the many different mathematical components of the semi-analytical method. The FEM model consists of a combination of shell, continuum shell and solid elements that are joined together as a single part. The composite plate, stringers and the skin of the compliant section are modelled using 4-node shell (S4R) elements. The spine's material is defined as a composite laminate—i.e. shell elements with material defined on a ply-by-ply basis—whereas both the skin and the stringers are modelled as isotropic shells (see Table 3.2 for material properties).

The non-morphing trailing edge strip is modelled using a combination of solid 8-node (C3D8R) elements, for the isotropic parts, and continuum shell (SC8R) elements, for the laminated composite parts (Figure 3.7). This is due to the fact that this region contains a section of the composite spine that is located in between solid isotropic material. A geometrically non-linear analysis was performed for several different spine stacking sequences under a range of uniform pressure distributions, ranging from 20 Pa to 500 Pa. The nodal displacements along the free edges were tracked and extracted to allow for comparison to the semi-analytical model. A fully clamped boundary condition was applied to the root of the FishBAC. Also, the FishBAC's skin is pre-strained by 10% to minimise out-of-plane deflections under aerodynamic loading and to avoid buckling in compression. To simulate this pre-strain, the skin was prestressed by applying a prescribed uniform, in-plane predefined stress field equal to the Young's modulus of the skin times 10% strain in the chordwise direction. Spanwise stress/strain due to Poisson's ratio effect is not considered, as during the manufacture of actual FishBAC skins, the skin is free to contract in the spanwise direction before it is bonded to the structure. A convergence study was performed to set the element size used for comparison by varying the global element size of the mesh and calculating the percentage difference for each increment.

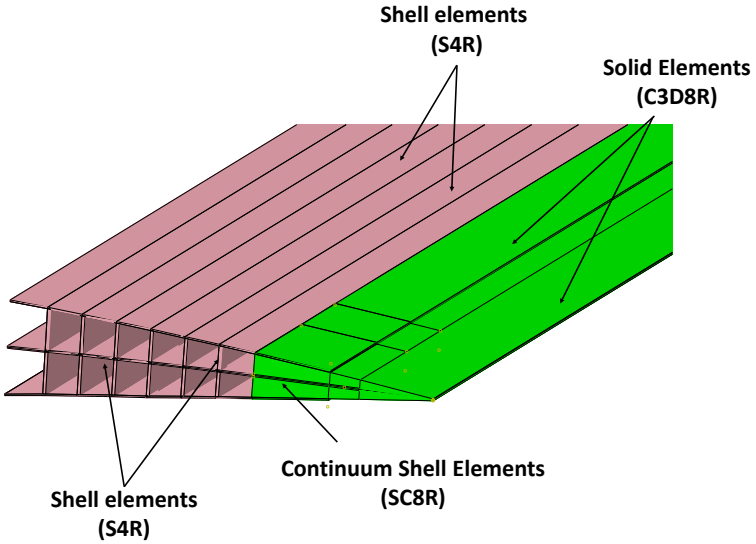

Figure 3.7: Schematic of the type of elements that are used to model the behaviour of the FishBAC's static displacement. Solid and continuum shell elements are displayed in 'green' colour, whereas shell elements are displayed in 'pink' colour.

In this study, convergence is said to have been achieved when the average percentage difference in tip displacements vary less than 0.5% for two consecutive increments in mesh density.

3.6 Load Cases

One of the assumptions in the structural analysis of the FishBAC is that the aerodynamic pressure distributions on the upper and lower skins are translated directly to the spine. This equivalent pressure is found by subtracting the top surface pressure distribution from the bottom one. This approach has one disadvantage: it does not allow the out-of-plane deformation of the skin under aerodynamic loads to be modelled. However, for the level of fidelity and purpose of this tool (i.e. a robust and efficient FSI routine for design and optimisation), the impact of these skin deformations on the aerodynamic response would not be accurately captured anyway, and so not having them is a reasonable trade-off. A high-fidelity coupled CFD-FEM analysis would be needed to estimate the skin deformation between stringers, the complexity and computational expense of which would explicitly go against the objectives of this work. Lastly, as previously mentioned, pre-tensioning the skin mitigates the effects of skin deformation on the aerodynamic loads, as it increases its effective stiffness, reduces out-of-plane skin deflections and prevents buckling when in compression.

Figure 3.8 displays the type of loading applied in both semi-analytical and FEM models, whereas Figure 3.3 shows the locations where the distributed moments are applied, as well as their moment arms with respect to the clamped edge.

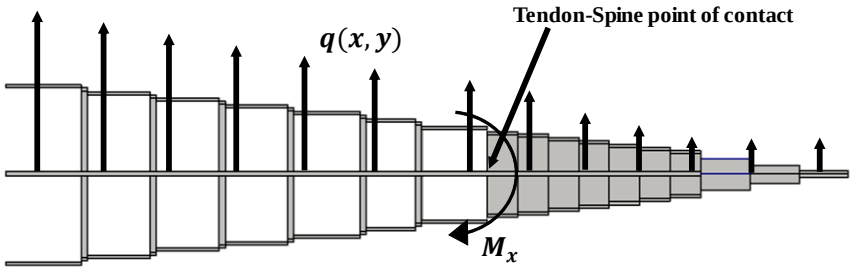

Figure 3.8: External loads applied in both semi-analytical and Finite Element models in the global in the global x-y coordinate frame. Dimensions and specific locations of the moment loads are presented in Figures 3.3 and 3.6.

For the purpose of this initial investigation, $P_{\text{down}}(x,y)$ and $P_{\text{up}}(x,y)$ are assumed to be uniform, which results in a net positive uniform pressure distribution acting on the spine, obtained by the expression

$$q_{\text{net}}(x,y) = \left(P_{\text{down}}(x,y) - P_{\text{up}}(x,y)\right). \tag{3.16}$$

Using uniform pressure distributions facilitates the direct comparison between the semi-analytical and FEM models, without having to interpolate to match the location of the FEM nodes and the semi-analytical model partitions.

The magnitude of the transverse pressure loadings were selected based on preliminary FEM simulations, targeting similar maximum deflections between 4 mm and 5 mm for all four spine material configurations, allowing for direct error comparison between all four cases. Note that the highest pressure value applied to each case is similar or higher to the values that the composite wind tunnel wing model of similar dimensions would experience at the design speed of Mach 0.15.

3.7 Results and Discussion

The semi-analytical model presented in this chapter is compared against a non-linear FEM model of the FishBAC under uniform pressure distribution and actuation moments. In addition to the resulting displacement fields, a convergence study in terms of Chebyshev Polynomial terms is presented. In these sets of results, two types of errors are reported: the maximum absolute value percentage difference and the root mean square (RMS) percentage difference between semi-analytical and FEM results.

3.7.1 Polynomial Term Convergence

A convergence study of Chebyshev polynomial terms against the converged FEM results is presented for four different spine material configurations: isotropic ABS, $[0/90/0]_S$ CFRP, $[45/45/45]_S$ CFRP and $[90/90/90]_S$ CFRP (where 0 degrees is aligned with the global x-axis). The spine's thickness was kept constant at $t = 0.75$ mm for all four cases, and the dimension, position and material properties of the stringers and skin remained constant. The structure is loaded under uniform transverse pressure and maximum absolute and RMS percentage errors were computed. Also, the study involved comparing these errors with both computation time and condition number, as observed in Figure 3.9. Table 3.3 shows a summary of the convergence study.

Table 3.3: Comparison of semi-analytical and geometrically non-linear FEM results as a function of Chebyshev Polynomials terms (polynomial order).

Laminate	Material	Polynomial Terms (M=N)	Max. Err. (Abs. Value) [%]	RMS Err. [%]	DOF
Isotropic	ABS Plastic	2	7.978	7.847	3015
		3	7.141	7.846	5520
		4	5.054	4.912	8625
		5	2.332	2.185	12420
		6	0.791	0.732	16905
		7	3.634	3.570	22080
$[0/90/0]_S$	CFRP	2	7.814	7.711	3015
		3	6.973	6.874	5520
		4	4.150	4.039	8625
		5	0.691	0.580	12420
		6	3.308	3.129	16905
		7	6.933	6.745	22080
$[45/45/45]_S$	CFRP	2	14.27	9.927	3015
		3	13.28	9.136	5520
		4	10.80	6.903	8625
		5	7.757	4.864	12420
		6	7.753	4.702	16905
		7	11.48	6.675	22080
$[90/90/90]_S$	CFRP	2	7.825	7.691	3015
		3	7.077	6.974	5520
		4	4.675	4.530	8625
		5	1.730	1.578	12420
		6	1.642	1.575	16905
		7	4.715	4.644	22080

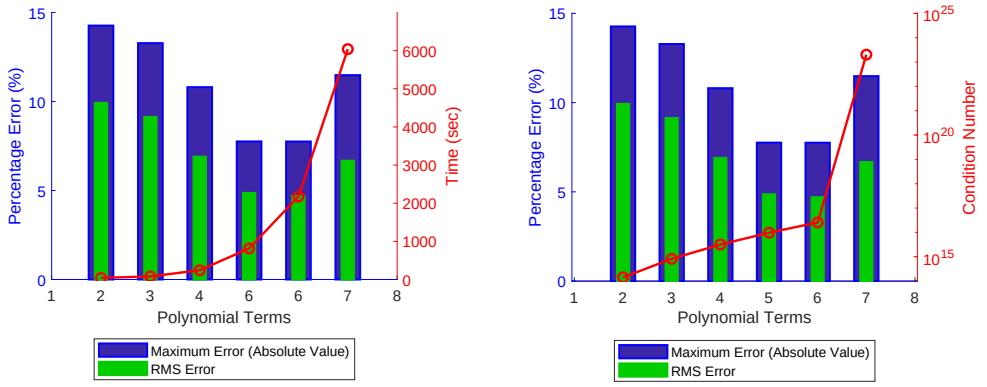

Figure 3.9: Convergence study: comparison between semi-analytical and geometrically non-linear FEM results for a spine's stacking sequence of $[45/45/45]_S$.

Results show that, for all four spine configurations, a root mean square error of less than 4.9% can be achieved when five Chebyshev Polynomial terms in both chordwise and spanwise direction (i.e. $M = N = 5$) are used. In general, it is observed that adding a sixth term has a positive effect in further reducing the RMS percentage error, at the expense of doubling the computation time. Conversely, there is a significant increase in error when adding a seventh polynomial term. This also corresponds to an increase in condition number of about 7 orders of magnitude in all four cases, as observed in Figure 3.9. It can be concluded that the proposed semi-analytical model has a limit of six Chebyshev polynomial terms, as further increasing the number of polynomial terms yields severe ill-conditioning. This finding is consistent with results reported by Ilanko et al. (2015) [92], where it is stated that although orthogonal polynomials offer fast convergence, they are prone to ill-conditioning when high-order terms are used. These numerical instabilities are attributed to rounding errors when high-order terms (and their derivatives) are integrated. Additionally, Ilanko et al. (2015) recommend that, to ensure numerical stability when orthogonal polynomials are selected as shape functions, the minimum possible number of polynomial functions with the lowest possible order should be used. Lastly, it can be observed that results within $\approx 7\%$ RMS error can be obtained when four polynomial terms are used, which represents an attractive scenario for future optimisation studies as this case represents a 66% reduction in computational time than when five terms are used. It is also attractive in terms of computational effort with respect to the FEM, as it requires less than 8% of the total number of DOFs than converged FEM. These computational benefits are in addition to the benefits of simple, parameter-driven geometry/material definition (ideal for optimisation and aeroelasticity studies) provided by the proposed method.

Regarding the type of error, it is observed that the RMS and the maximum absolute value percentage error in the isotropic, $[0/90/0]_S$ and $[90/90/90]_S$ are very similar, for each material layup case and for a given polynomial term expansion. However, these two significantly differ from the most anisotropic case (i.e. $[45/45/45]_S$). This implies that the maximum absolute value percentage error in this last case is driven by differences in localised deformation, rather than from the global ones. Since the application of this structural model is to predict deformations due to aerodynamic loads, which are mainly dependent on global deformations, the root mean square error is more useful for comparing the model with FEM results and is used subsequently as a measure of comparison for the remaining of this chapter. Lastly, the difference in percentage error (Table 3.3) among the four material configuration cases is not caused by non-linearities, but by the degree of material anisotropy and the presence of transverse shear in the $[45/45/45]_S$ material configuration. A comparison between linear and non-linear FEM was performed, showing no significant differences between the two cases.

3.7.2 Uniform Pressure Loading

Uniform transverse pressure was applied to the same four laminates presented in the previous subsection. The RMS percentage difference along the spanwise $x = a/2$ edge is used to measure the difference between the semi-analytical and FEM results. Table 3.4 shows that the RMS error remains stable as the load increases. Also, it is observed that the most anisotropic layup (i.e. $[45/45/45]_S$) consistently presents a higher error than the other three cases. The corresponding displacement field is displayed in Figure 3.10, whereas Figures 3.11 and 3.12 show a comparison between semi-analytical and FEM results along the spanwise $x = a/2$ and chordwise $y = -b/2$ edge, respectively. Even though localised discrepancies can be observed along the spanwise edge, the global deformation of the FishBAC is properly captured (Figure 3.10). As mentioned earlier, properly capturing the global deformation is a priority for this application, as this would drive any change in aerodynamic loads.

It is observed that the $[0/90/0]_S$ case consistently presents the lowest percentage error out of all four cases. Figure 3.13 displays the 2-dimensional displacement field, whereas Figures 3.14 and 3.15 show a comparison between semi-analytical and FEM results along the chordwise $y = -b/2$ and spanwise $x = a/2$ edge, respectively. In this case, both local and global features are well captured by the semi-analytical model. Unlike in the $[45/45/45]_S$ case (Figure 3.11), it can be observed that there is no significant spanwise variation in out-of-plane displacement in the $[0/90/0]_S$ (Figure 3.14), which is expected as cross-ply laminates present no bend-twist coupling, as the D_{16} and D_{26} terms in the ABD Matrix are zero.

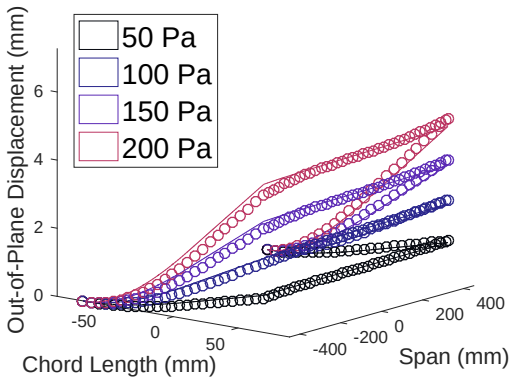

Figure 3.10: Comparison between semi-analytical (solid) and FEM (∘) displacement field for a $[45/45/45]_S$ spine's stacking sequence under uniform transverse pressure.

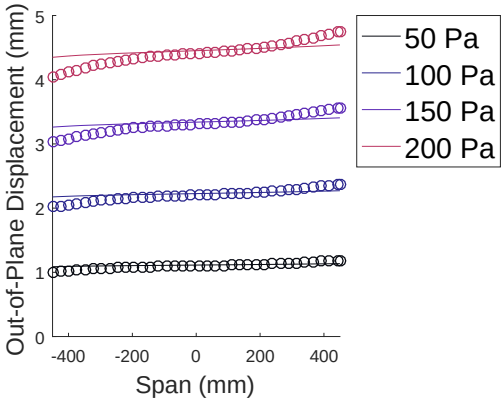

Figure 3.11: Semi-analytical (solid) vs FEM (∘) displacement along the spanwise edge $x = a/2$ for a $[45/45/45]_S$ spine's stacking sequence under uniform transverse pressure.

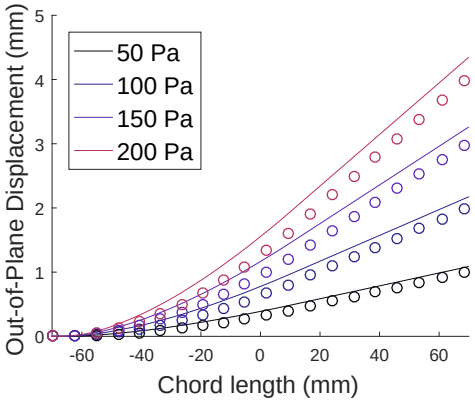

Figure 3.12: Semi-analytical (solid) vs FEM (∘) displacement along chordwise edge $y = -b/2$ for a $[45/45/45]_S$ spine's stacking sequence under uniform transverse pressure.

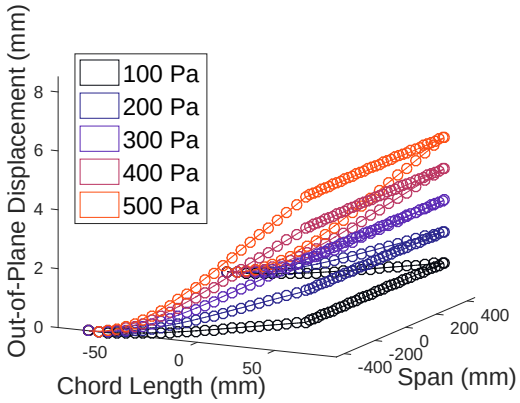

Figure 3.13: Comparison between semi-analytical (solid) and FEM (∘) displacement field, for a $[0/90/0]_S$ spine's stacking sequence, under uniform transverse pressure.

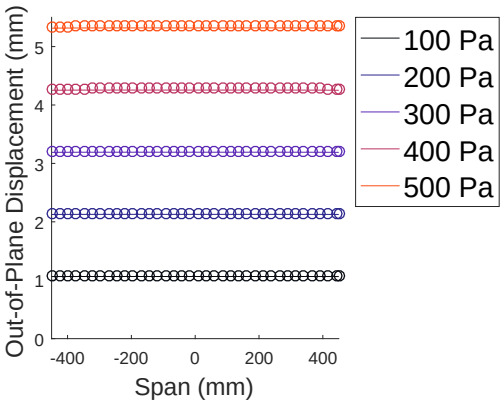

Figure 3.14: Semi-analytical (solid) vs FEM (∘) displacement along the spanwise edge $x = a/2$ for a $[0/90/0]_S$ spine's stacking sequence under uniform transverse pressure.

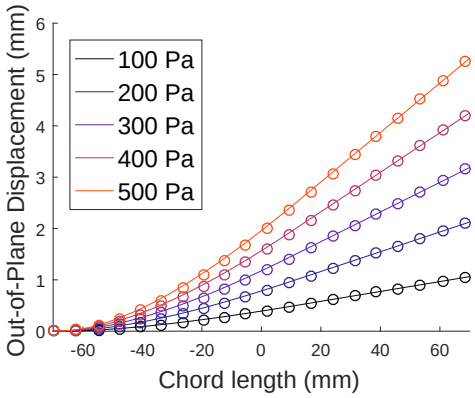

Figure 3.15: Semi-analytical (solid) vs, FEM (∘) displacement along the chordwise edge $y = -b/2$ for a $[0/90/0]_S$ spine's stacking sequence under uniform transverse pressure.

Table 3.4: Comparison, in terms of RMS percentage difference between semi-analytical ($M = N = 5$ terms) and FEM, of the four different configurations under uniform transverse pressure loading.

Laminate	Material	Pressure [Pa]	RMS Error [%]
Isotropic	ABS Plastic	20	1.815
		40	1.929
		60	2.047
		80	2.165
$[0/90/0]_S$	CFRP	100	0.518
		200	0.536
		300	0.553
		400	0.567
		500	0.580
$[45/45/45]_S$	CFRP	50	4.798
		100	4.823
		150	4.846
		200	4.864
$[90/90/90]_S$	CFRP	20	1.224
		40	1.308
		60	1.398
		80	1.488
		100	1.577

3.7.3 Actuation Moments

A comparison of semi-analytical vs FEM displacements, under input moments, was performed for the two most compliant laminates in the chordwise direction (i.e. isotropic and $[90/90/90]_S$). The magnitudes of the maximum applied moments were selected based on preliminary nonlinear FEM results, such that the deflections in both stacking sequence cases had similar values. Three different scenarios were analysed: the first one consisted of applying two positive moments of the same magnitude, the second one, applying moments of equal magnitude but opposite directions, and the third one, applying a negative moment to just one of the actuators. The RMS percentage difference between semi-analytical and FEM results is computed at the spanwise $x = a/2$ edge, and results are summarised in Tables 3.5 and 3.6 for the isotropic and $[90/90/90]_s$ spine laminates, respectively.

When comparing displacement fields, it is observed that Case 1 and Case 3 show similar behaviours to FEM, in terms of chordwise and spanwise edge displacement and slopes, with an overall RMS error of less than 8.6%. Figure 3.16 shows the displacement field of the $[90/90/90]_S$ spine under uniform actuation, whereas Figure 3.17 shows the same laminate under single actuation. Unlike Cases 1 and 3, Case 2 (i.e. differential moment inputs) show significant discrepancies, in terms of RMS error along the spanwise free edge and the deformed shape. Tables 3.5 and 3.6 show RMS errors as high as 44%, for the isotropic and $[90/90/90]_S$ cases. In terms of displacement magnitudes, it is observed that the semi-analytical model is stiffer than the FEM model (Figure 3.18) by a factor of approximately 2. After further interrogation of the results, it was concluded that these discrepancies are caused by the presence of significant transverse shear deformations along the y-z plane. Since the stringers divide the plate into several partitions, the effective chordwise in-plane global dimension of the FishBAC is reduced; hence, local thickness-to-width ratios of approximately $t/a \approx 1/13$ exist. Consequently, through-thickness normal planes rotation can no longer be neglected.

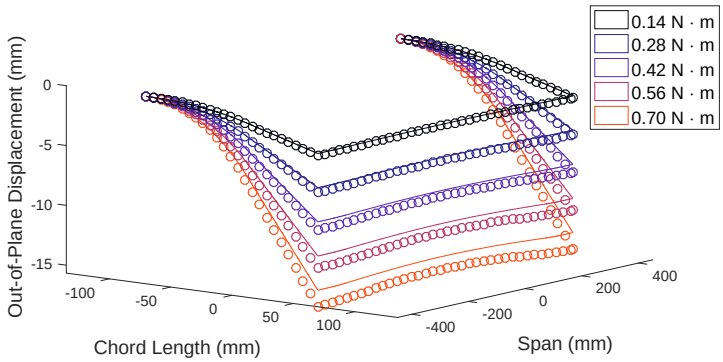

Figure 3.16: Semi-analytical (solid) vs FEM (∘) for a $[90/90/90]_S$ spine's laminate under uniform positive actuation inputs.

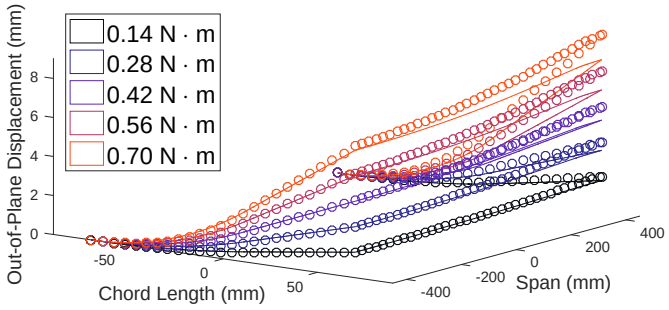

Figure 3.17: Semi-analytical (solid) vs FEM (∘) for a $[90/90/90]_S$ spine's laminate under a single negative M_{x_2} input. Legend corresponds to the moment magnitude of the right actuator.

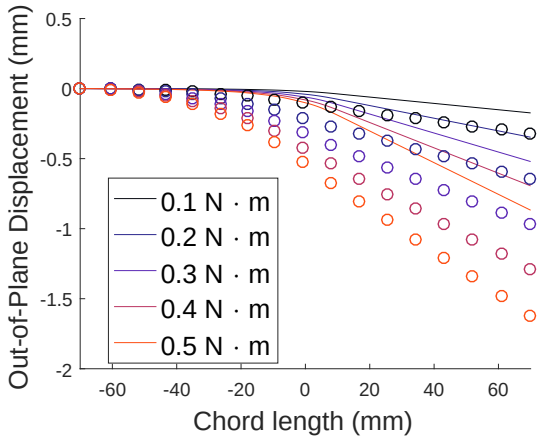

Figure 3.18: Semi-analytical (solid) vs FEM (∘) deflection along chordwise edge $y = -b/2$, for a $[90/90/90]_S$ spine's laminate, under differential moment inputs.

Table 3.5: Comparison, in terms of RMS percentage difference, between semi-analytical ($M = N =$ 6 terms) and FEM for the isotropic spine configuration under all three moment loading scenarios.

Case	M_{x_1}[N · m]	M_{x_2} [N · m]	RMS Error [%]
Case 1 (Symmetric Input)	0.14	0.14	3.927
	0.28	0.28	5.098
	0.42	0.42	6.204
	0.56	0.56	7.236
	0.7	0.7	8.187
Case 2 (Differential Input)	0.1	-0.1	43.74
	0.2	-0.2	43.74
	0.3	-0.3	43.72
	0.4	-0.4	43.70
	0.5	-0.5	43.38
Case 3 (Single Input)	0	-0.14	5.550
	0	-0.28	6.371
	0	-0.42	7.342
	0	-0.56	8.406
	0	-0.70	9.526

Table 3.6: Comparison, in terms of RMS percentage difference, between semi-analytical ($M = N =$ 6 terms) and FEM of the CFRP $[90/90/90]_s$ spine configuration under all three moment loading scenarios.

Case	M_{x_1}[N · m]	M_{x_2}[N · m]	RMS Error [%]
Case 1 (Symmetric Input)	0.14	0.14	3.252
	0.28	0.28	4.110
	0.42	0.42	4.946
	0.56	0.56	5.755
	0.7	0.7	6.534
Case 2 (Differential Input)	0.1	-0.1	44.09
	0.2	-0.2	44.08
	0.3	-0.3	44.07
	0.4	-0.4	44.05
	0.5	-0.5	44.02
Case 3 (Single Input)	0	-0.14	6.028
	0	-0.28	6.356
	0	-0.42	6.812
	0	-0.56	7.370
	0	-0.70	8.008

Unlike in the other load cases that have been analysed, the differential moment input case does present significant transverse shear strains as these moment inputs generate a net torque along the spine's x-axis. As a consequence, shear flow is induced, resulting in transverse shear stresses and strains (i.e. τ_{yz} and γ_{yz}, respectively) that cannot be captured using Kirchhoff-Love Plate Theory. Further FEM estimations were performed to analyse this case, and they confirm this limitation. A comparison between the original FishBAC model and a case in which transverse shear in the y-z direction is artificially 'suppressed' by increasing the CFRP's G_{yz} shear modulus by four orders of magnitude, is performed. Figure 3.19 shows the variation along the span of the transverse shear stress τ_{yz} between stringers four and five. It is observed that, for the case of realistic G_{xz}, transverse shear stress does exist and varies along the span. Lastly, to verify that transverse shear is the source of discrepancy in deformed shapes, the displacement along the chordwise edge $y = -b/2$ of the semi-analytical model is compared with the FEM 'suppressed' transverse shear case. It is observed that similar deformations are achieved, with an error of less than 3% (Figure 3.20). A potential solution to this limitation is to expand the semi-analytical model to account for transverse shear deformation using First-Order Shear Deformation Theory (FSDT), also known as Mindlin-Reissner Plate Theory in the context of plate mechanics—this will be pursued in the next chapter.

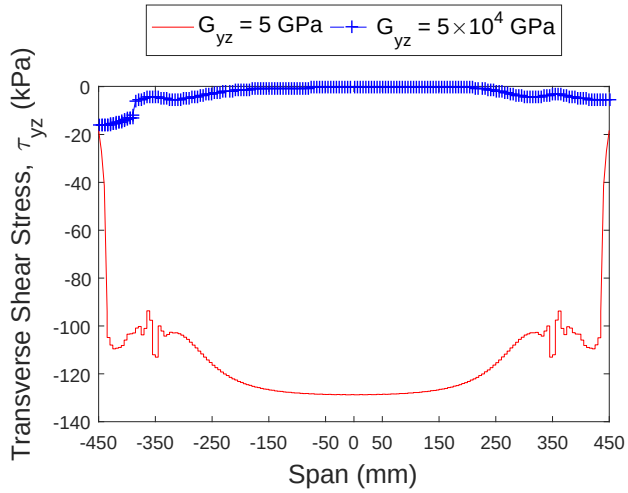

Figure 3.19: Transverse shear stress τ_{yz} between stringers four and five and along the span. The solid line corresponds to the FishBAC with 'real' material properties, whereas the line with cross markers (+) is obtained when transverse shear deformation in the y-z plane is artificially suppressed.

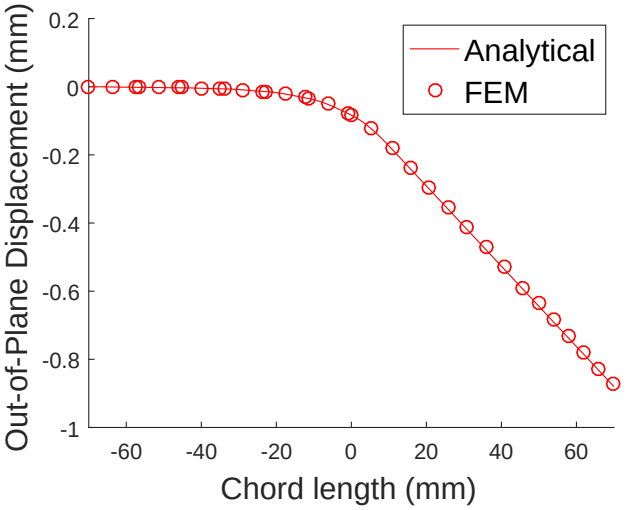

Figure 3.20: Semi-analytical (solid) vs FEM (o) displacement along chordwise edge $y = -b/2$, when transverse shear deformations in FEM are 'artificially' suppressed.

3.7.4 Computational Comparison: Model Size and Convergence Study

A final comparison, in terms of DOFs between semi-analytical and FEM model, is presented in this section (Table 3.7). The FEM's DOFs correspond to a converged mesh, and include all boundary conditions and constraints applied during the analysis. It is observed that, among all cases, the semi-analytical model reduces the DOF that need to be solved by at least 84%, compared to a FEM converged mesh. Note that, for the $[45/45/45]_S$ case, the FEM model presents about seven times more DOFs than the other three cases. This means that a finer mesh was needed for FEM convergence, which is consistent with the fact that this is the most anisotropic case and experiences more localised displacement features and variations along the span than the isotropic or orthotropic cases.

A reduction in DOFs is not only a measure of the efficiency of the semi-analytical model, as it can obtain converged solutions (except when transverse shear due to differential moment inputs exist) with a smaller linear system, but also significantly decreases the amount of RAM memory required to obtain static deformations.

Table 3.7: Semi-analytical vs FEM DOFs. FEM results correspond to converged meshes and include all applied boundary conditions and constraints.

Laminate	Semi-analytical [DOF] (Chebyshev Terms)		FEM [DOF]
	$M,N=5$	$M,N=6$	
Isotropic	12420	16905	109346
$[0/90/0]_S$	12420	16905	109346
$[45/45/45]_S$	12420	16905	821906
$[90/90/90]_S$	12420	16905	109346

3.8 Conclusions

An efficient and mesh-independent two-dimensional semi-analytical model for predicting the static behaviour of complex composite plate-based structures with large stiffness variations in general, and the FishBAC device in particular, has been developed. The model is capable of analysing fully anisotropic FishBAC geometry and material configurations and predicting the in-plane and out-of-plane displacement fields under two-dimensional transverse pressure loading and applied actuation moments. It achieves the static modelling by condensing all of the geometric and material features of the FishBAC into a single system of linear equations, obtained using the Rayleigh-Ritz Method.

Results show that, under uniform pressure loading, the semi-analytical model converges in five Chebyshev polynomial terms, with a percentage error under 4.8% with respect to FEM, while using 84% fewer degrees of freedom. Furthermore, errors in predicting large deflections due to actuation loads range from 3% to 8%, except when a differential moment input is applied. This load case results on a net torque on the FishBAC's spine, causing transverse shear deformations along the y-z plane. Significant discrepancies exist in this specific load case, and they are due to Kirchhoff-Love Plate Theory's inability to capture any through-thickness strains.

Although the semi-analytical model has been developed around the FishBAC morphing trailing edge concept, this approach can be used to model any plate structure, regardless of its level of discontinuity or material properties. Additionally, this model opens the design space for future design iterations of the FishBAC, not only allowing for the use of composite laminates, but also of core materials (e.g. sandwich configuration). Also, since it is built around the Rayleigh-Ritz Method, dynamic analysis can be introduced by accounting for kinetic energy, which will be required in the near future to model deflections under unsteady aerodynamic load cases.

In summary, this Kirchhoff-Love semi-analytical model represents a powerful, robust and fast tool for future design and optimisation of the FishBAC as the structural and material parameters can be easily modified. However, its limitations in modelling load cases that result in transverse shear must be addressed. A potential path forward is to implement the FSDT by using Mindlin-Reissner Plate Theory, which allows the rotation of through-thickness planes.

Chapter 3 presented a novel structural modelling tool for predicting the static displacement of discontinuous plate structure under bending loads. However, due to the presence of transverse shear strains, the Kirchhoff-Love-based discontinuous plate model fails to predict the FishBAC's torsional response under asymmetric actuation loading. To fully exploit the FishBAC's potential on controlling spanwise aerodynamic loads, these asymmetric actuation load cases need to be appropriately modelled. Consequently, a modelling definition that allows capturing transverse shear strains needs to be implemented.

Chapter 4

Modelling and Experimental Validation of a composite FishBAC device under Transverse Shear Loading

The objective of this chapter is to address the limitations of the Kirchhoff-Love Plate Model (Chapter 3) on modelling transverse shear deformations. This limitation is successfully addressed by applying Mindlin-Reissner Plate Theory, which models transverse shear by incorporating first-order shear effects. Additionally, besides validating this new model against FEM, experimental validation was performed and is also presented in this chapter.

4.1 Introduction

Chapter 3 introduced a Kirchhoff-Love plate-based formulation to analytically model the static behaviour of a composite FishBAC under transverse pressure and actuation loads. Although successful in predicting deflections under uniform transverse pressure and uniform actuation loads, the model failed to accurately predict deflections when the FishBAC is subject to spanwise twist due to asymmetric actuation loads. Chapter 3 concluded that this limitation is caused by the existence of transverse shear strains due to torsion, which cannot be predicted using Kirchhoff-Love Plate Theory because this theory neglects transverse shear strains.

Therefore, the objective of this chapter is to address these limitations by enhancing the modelling technique proposed in Chapter 3. This goal is achieved by replacing the Kirchhoff-Love plate model with a Mindlin-Reissner-based formulation, which models transverse shear deformations by applying a First-Order Shear Deformation Theory (FSDT) and assumes that transverse shear displacements vary linearly across the thickness of the structure [103]. This enhanced semi-analytical structural model, implemented in MATLAB®R2016a, is validated both numerically and experimentally. The numerical validation was performed by comparing results to static displacements obtained using a FEM model—developed in ABAQUS/CAE®6.14-1—and the experimental validation was performed using a composite FishBAC prototype developed for wind tunnel testing (thoroughly discussed in Chapter 5).

The novelty of this work resides in the ability of this model to capture displacements of a highly discontinuous plate structure subjected to different load cases—including transverse shear loads—using a series of individual plates that are joined together using artificial penalty springs.

This model will become a key element in future design, optimisation and fluid-structure interaction analysis of the FishBAC. Moreover, its use is not exclusive to the FishBAC device; any continuous or discontinuous composite plate-type structure can be modelled with this technique.

This chapter will first introduce the modelling technique, including the solution method, boundary conditions and assumptions. It then describes the FEM model used for validation purposes, followed by a summary of results and a brief analysis on the numerical performance of the model.

4.2 Mindlin-Reissner Plate Model

The semi-analytical structural model that is developed in this chapter is based on the Rayleigh-Ritz Method, which is used to solve the plate differential equation using a weak formulation. Additionally, CLT extended for Mindlin-Reissner plates is used to calculate the stiffness terms [91]. This solution technique requires the use of assumed shape functions and, in this case, Chebyshev Polynomials of the First Kind were selected. Lastly, to account for the large number of chordwise and spanwise stiffness discontinuities created by the presence of stringers and discrete actuation inputs, the structure is discretised in sections of uniform stiffness that are joined together using the Courant's penalty method in the form of artificial penalty springs [92].

4.3 Semi-analytical Formulation

In beam analysis, Euler-Bernoulli Beam Theory is unable to accurately predict deflections of thick beams. This limitation is due to its inability to represent transverse shear deformations. In response to this, Timoshenko developed his famous transverse shear deformation theory of beams [114]. Similarly, Kirchhoff-Love Plate Theory is analogous to Euler-Bernoulli beam theory and is likewise unable to model the behaviour of thick plates as it assumes no through-thickness shear deformations. Therefore, Mindlin-Reissner Plate Theory extends Kirchhoff-Love Plate Theory to include the effects of transverse shear deformation by allowing the rotation of the through-thickness normal planes. It assumes that transverse shear displacements vary linearly across the thickness of the plate, which is why it is also known as the First-Order Shear Deformation Theory of Plates [115].

In order to solve the Mindlin-Reissner equations with the Rayleigh-Ritz Method, a strain energy formulation of the plate's differential equation is needed. This equation considers total strain energy in the plates as the summation of strain energies due to stretching and bending [91, 107]

$$U_{ABD} = \frac{1}{2}\iint A_{11}\left(\frac{\partial u^0_{ij}}{\partial x}\right)^2 + 2A_{12}\frac{\partial u^0_{ij}}{\partial x}\frac{\partial v^0_{ij}}{\partial y} + A_{22}\left(\frac{\partial v^0_{ij}}{\partial y}\right)^2 + 2\left(A_{16}\frac{\partial u^0_{ij}}{\partial x} + A_{26}\frac{\partial v^0_{ij}}{\partial y}\right)\left(\frac{\partial u^0_{ij}}{\partial y} + \frac{\partial v^0_{ij}}{\partial x}\right)$$
$$+ A_{66}\left(\frac{\partial u^0_{ij}}{\partial y} + \frac{\partial v^0_{ij}}{\partial x}\right)^2 - 2B_{11}\frac{\partial u^0_{ij}}{\partial x}\frac{\partial \psi_{x_{ij}}}{\partial x} - 2B_{22}\frac{\partial v^0_{ij}}{\partial y}\frac{\partial \psi_{y_{ij}}}{\partial y} - 2B_{12}\left(\frac{\partial v^0_{ij}}{\partial y}\frac{\partial \psi_{x_{ij}}}{\partial x} + \frac{\partial u^0_{ij}}{\partial x}\frac{\partial \psi_{y_{ij}}}{\partial y}\right)$$
$$- 2B_{66}\left(\frac{\partial u^0_{ij}}{\partial y} + \frac{\partial v^0_{ij}}{\partial x}\right)\left(\frac{\partial \psi_{x_{ij}}}{\partial y} + \frac{\partial \psi_{y_{ij}}}{\partial x}\right) - 2B_{16}\left[\frac{\partial \psi_{x_{ij}}}{\partial x}\left(\frac{\partial u^0_{ij}}{\partial y} + \frac{\partial v^0_{ij}}{\partial x}\right) + \frac{\partial u^0_{ij}}{\partial x}\left(\frac{\partial \psi_{x_{ij}}}{\partial y} + \frac{\partial \psi_{y_{ij}}}{\partial x}\right)\right]$$
$$- 2B_{26}\left[\frac{\partial \psi_{y_{ij}}}{\partial y}\left(\frac{\partial u^0_{ij}}{\partial y} + \frac{\partial v^0_{ij}}{\partial x}\right) + \frac{\partial v^0_{ij}}{\partial y}\left(\frac{\partial \psi_{x_{ij}}}{\partial y} + \frac{\partial \psi_{y_{ij}}}{\partial x}\right)\right] + D_{11}\left(\frac{\partial \psi_{x_{ij}}}{\partial x}\right)^2 + D_{22}\left(\frac{\partial \psi_{y_{ij}}}{\partial y}\right)^2 + D_{66}\left(\frac{\partial \psi_{x_{ij}}}{\partial y} + \frac{\partial \psi_{y_{ij}}}{\partial x}\right)^2$$
$$+ 2D_{12}\left(\frac{\partial \psi_{x_{ij}}}{\partial x}\frac{\partial \psi_{y_{ij}}}{\partial y}\right) + 2D_{16}\frac{\partial \psi_{x_{ij}}}{\partial x}\left(\frac{\partial \psi_{x_{ij}}}{\partial y} + \frac{\partial \psi_{y_{ij}}}{\partial x}\right) + 2D_{26}\frac{\partial \psi_{y_{ij}}}{\partial y}\left(\frac{\partial \psi_{x_{ij}}}{\partial y} + \frac{\partial \psi_{y_{ij}}}{\partial x}\right) dx\,dy \quad (4.1)$$

and transverse shear

$$U_H = \frac{1}{2}\iint \left[H_{44}\left(\frac{\partial w_{ij}}{\partial y} - \psi_{y_{ij}}\right)^2 + 2H_{45}\left(\frac{\partial w_{ij}}{\partial y} - \psi_{y_{ij}}\right)\left(\frac{\partial w_{ij}}{\partial x} - \psi_{x_{ij}}\right) + H_{55}\left(\frac{\partial w_{ij}}{\partial x} - \psi_{x_{ij}}\right)^2\right] dx\,dy, \quad (4.2)$$

where A_{fg}, B_{fg},D_{fg} and H_{fg} matrices are the plate's material and geometric stiffness, u^0, $v^0$and w are the plate displacements, and ψ_x and ψ_y are the plate rotations. Note the subscript ABD in Equation 4.1 denotes the strain energy terms present in Kirchhoff-Love theory, whereas the subscript H in Equation 4.2 denotes the additional term added by Mindlin-Reissner theory to capture the transverse shear energy. These plate rotations include transverse shear strains, such that

$$\psi_x = \frac{\partial w}{\partial x} - \gamma_{xz} \qquad \text{and} \qquad \psi_y = \frac{\partial w}{\partial y} - \gamma_{yz} \quad . \quad (4.3)$$

The A_{fg},B_{fg} and D_{fg} terms in Equation 4.1 —commonly known as the ABD matrix— are, respectively, the extension, bending-coupling and bending material and geometric stiffnesses of the laminate, and these are obtained using CLT [93]. Furthermore, the H_{fg} terms in Equation 4.2 correspond to the transverse shear stiffness, and are derived as

$$H_{ij} = \frac{1}{\kappa}\int_h \overline{Q}_{ij}\,dz = \frac{1}{\kappa}\sum_{k=1}^{K}\overline{Q}_{ij,k}(z_k - z_{k-1})dz\,, \quad (4.4)$$

where $i,j = 4,5$ and κ is known as the Timoshenko Shear Correction Factor, which has an approximate value of 6/5 for rectangular cross-sections. Although this approximation is valid for isotropic plates, it has been shown to provide accurate results when used to model composite laminates [107]. Therefore, a value of $\kappa = 6/5$ is used throughout this study. Lastly, the $\overline{Q}_{ij}$ terms correspond to the stiffness of each ply in the global coordinate frame, which are a function of fibre orientation angle and the following material properties: E_{11}, E_{22}, ν_{12}, G_{12}, G_{13} and G_{23}, in which the subscripts $i,j = 1, 2, 3$ refer to the fibre, transverse and trough-thickness directions, respectively.

4.3.1 Shape Functions and Boundary Conditions

As described in Chapter 3.2.5, when solving the plate equation by minimising total energy (i.e. by using Rayleigh-Ritz Method), the displacements and transverse rotations of the plate are unknown and thus become the independent variables of the problem. Therefore, the underlying shape functions of the displacements and transverse rotations need to be assumed, such that the corresponding amplitudes can be solved for. Commonly, when in 2-dimensions, these are assumed in the form of a double summation in x and y. The main difference between the shape functions derived in Chapter 3.2.5 is that only three shape functions are needed when using Kirchhoff-Love Plate Theory (i.e. one out-of-plane and two in-plane displacements, respectively), whereas two additional assumed shape functions are required for the additional DOFs in Mindlin-Reissner Plate Theory (i.e. the two transverse plane rotations). Thus, the three displacements have the same form as in Chapter 3.2.5

$$u_{ij}^0 = \sum_{m=0}^{M}\sum_{n=0}^{N} L_{mn}^{ij} X_m^i(x) Y_n^j(y) \ , \quad v_{ij}^0 = \sum_{m=0}^{M}\sum_{n=0}^{N} O_{mn}^{ij} X_m^i(x) Y_n^j(y) \quad \text{and} \quad w_{ij} = \sum_{m=0}^{M}\sum_{n=0}^{N} P_{mn}^{ij} X_m^i(x) Y_n^j(y) \ , \tag{4.5}$$

and the new transverse plane rotations are defined as

$$\psi_x = \sum_{m=0}^{M}\sum_{n=0}^{N} R_{mn}^{ij} X_m^i(x) Y_n^j(y) \quad \text{and} \quad \psi_y = \sum_{m=0}^{M}\sum_{n=0}^{N} S_{mn}^{ij} X_m^i(x) Y_n^j(y) \ . \tag{4.6}$$

These shape functions described in Equations 4.5 and 4.6 have two main components: the assumed shape functions $X(x)$ and $Y(y)$ and the unknown amplitudes L_{ij}, O_{ij}, P_{ij}, R_{ij} and S_{ij}. Similarly as in Chapter 3, the shape functions implemented in this Mindlin-Reinsser model are orthogonal polynomials, specifically Chebyshev Polynomials of the First Kind. Reasons behind this shape function selection are thoroughly described in Chapter 3.2.5, where it is explained that these polynomials allow for direct integration in a normalised domain without leading to values of zero. The recurrent relation that describes Chebyshev Polynomials of the First Kind is derived by Equation 3.8. Furthermore, it is important to recall that these polynomials are defined in a normalised domain; therefore, the global coordinate system is transformed into a local coordinate system as described by Equation 3.9 in Chapter 3.2.5.

Lastly, it is necessarily to implement the correct boundary conditions. In this particular application, the FishBAC is modelled as a cantilever plate that is clamped at one of its chordwise edges. It can be observed in Figure 3.1 that Chebyshev Polynomials do not naturally meet this condition, as they have non-zero displacements at the boundaries. Therefore, the clamped condition needs to be enforced separately. As introduced in Chapter 3.2.6. a circulation function [106]

$$\Gamma_x(\zeta) = (\zeta - \zeta_c)^n \, , \tag{4.7}$$

can be added as a multiplier to the displacement and transverse shear functions (i.e. Equations 4.5 and 4.6).

This condition forces certain boundary condition at a location ζ_c and the type of boundary condition is set by choosing the value of n. The relevant values for different conditions when transverse shear is considered are given in-depth in Table 4.1. Furthermore, it is important to note again that using this circulation function does not affect the orthogonality of the Chebyshev Polynomials, as long as every polynomial term in the expansion is multiplied by it.

As the FishBAC structure is modelled as a clamped plate, all three translations $u^0, v^0$and w and two rotations ψ_x, ψ_y must be equal to zero at the root. However, the transverse shear strains γ_{xz}, γ_{yz} need not be zero, as transverse shear straining at the root is a likely deformation mode [116]. Hence, for a clamped edge, a value of $n = 1$ must be used in Equation 4.7, as this yields zero displacement and rotations at the root, while still allowing for non-zero transverse shear strains at this location.

The derivatives of the Chebyshev Polynomials that are required to solve Equation 4.1 are computed analytically, whereas all of the required integrations in this semi-analytical model are calculated numerically using MATLAB's adaptive quadrature functions 'integral' and 'integral2', for 1D and 2D integrals, respectively. Because all integrals are computed in a normalised coordinate system, these can be calculated beforehand and their values can be stored and then transformed to the physical coordinate system, as long as the relationship between the normalised and physical coordinate systems is assumed to be constant (i.e. constant Jacobian). This property allows for significantly reducing the computational cost of running this semi-analytical model as the integrals have to be performed only once "up front" for each set of boundary conditions.

4.3.2 Stiffness Discontinuities

As described in Chapter 2.5, the stiffness of the FishBAC structure is highly discontinuous due to the presence of stringers, the chordwise taper of the aerofoil thickness, and the presence of localised actuation sections along the span. To account for these discontinuities, the FishBAC structure is modelled in this work as individual plate units of uniform stiffness that are joined together using a series of artificial penalty springs. These penalty springs act by enforcing displacement and rotation continuity at the joints of each partition.

Table 4.1: Boundary Conditions as implemented by circulation function in Equation 4.7 [107, 116]

Boundary Condition at ζ_c	n_{disp}	n_{rot}	u^0, v^0, w	ψ_x, ψ_y	Transverse Shear Strain (γ_{xz}, γ_{yz})
Free Edge (F)	0	0	Free	Free	Free
Simply Supported (SS)	1	0	0	Free	Free
Clamped (C)	1	1	0	0	Free

To implement this approach within the Rayleigh-Ritz Method, the strain energy of these artificial springs need to be minimised to enforce displacement and rotation compatibility at joints. The penalty spring energies to enforce displacement compatibility have the form

$$U_{pu,kl} = \frac{k_k}{2}\int_{-b_j/2}^{b_j/2}(u_k(x_{kl}^{(+)},y_j)-u_l(x_{kl}^{(-)},y_j))^2dy \ , \quad U_{pv,kl} = \frac{k_k}{2}\int_{-b_j/2}^{b_j/2}(v_k(x_{kl}^{(+)},y_j)-v_l(x_{kl}^{(-)},y_j))^2dy$$
$$\text{and} \qquad U_{pw,kl} = \frac{k_k}{2}\int_{-b_j/2}^{b_j/2}(w_k(x_{kl}^{(+)},y_j)-w_l(x_{kl}^{(-)},y_j))^2dy \tag{4.8}$$

where k and l refer to two adjacent plate partitions and + and − signs represent the right- and left-hand sides of the discontinuity (Figure 4.1), respectively. Similarly, artificial spring energies to enforce rotation compatibility are defined as

$$U_{prx,kl} = \frac{k_k}{2}\int_{-b_j/2}^{b_j/2}(\psi_{x_k}(x_{kl}^{(+)},y_j)-\psi_{x_l}(x_{kl}^{(-)},y_j))^2dy \quad \text{and}$$
$$U_{pry,kl} = \frac{k_k}{2}\int_{-b_j/2}^{b_j/2}(\psi_{y_k}(x_{kl}^{(+)},y_j)-\psi_{y_l}(x_{kl}^{(-)},y_j))^2dy \ . \tag{4.9}$$

These expressions (Equations 4.8 and 4.9) correspond to penalty springs in the chordwise direction (i.e. along the x-direction). For spanwise partitions along the y-direction, similar equations apply but the integration is performed along the x-direction at $y_k^{(+)}$ and $y_l^{(-)}$ locations.

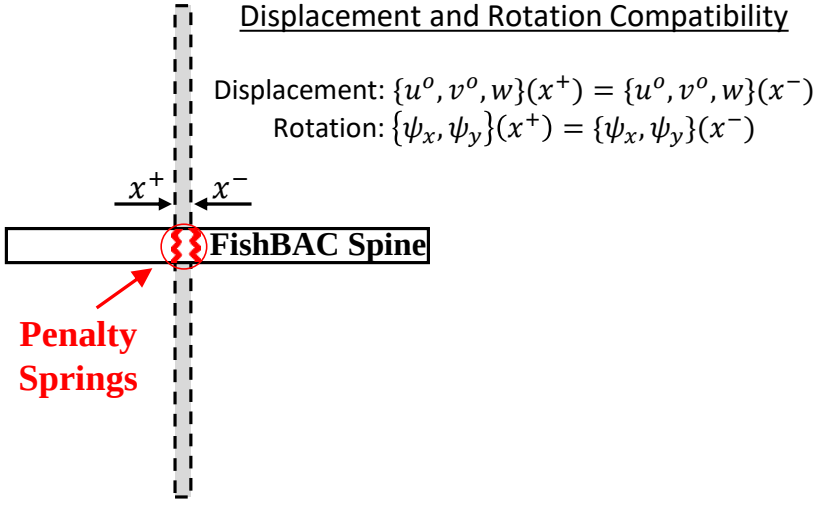

Figure 4.1: Displacement and Rotation compatibility enforced at each plate-stringer joint using artificial penalty springs.

4.3.3 Actuation Loads

Similarly, as in Chapter 3, the actuation loads are incorporated to the model as external potential energy (see Equation 3.6). A detailed explanation of how these actuation loads are applied can be found in Chapter 3.2.4.

4.3.4 Rayleigh-Ritz Method: Minimum Potential Energy

As mentioned in Section 4.2, the solution method that this structural model is based upon is the principle of conservation of energy. In this work, there are no non-conservative energy losses (such as friction), and so the total energy of the system is constant. Differentiating with respect to any of the unknown amplitudes leads to a state of minimum potential energy [117] (see Chapter 3.2.9 for details). If the total energy is defined as the sum of strain energy and potential energy due to external loads, described as

$$\Pi(u^0, v^0, w, \psi_x, \psi_y) = U_{ABD} + U_H + U_{penalty} + W = \text{constant} \quad , \tag{4.10}$$

differentiation with respect to the unknown amplitudes O_{mn}^{ij}, P_{mn}^{ij}, R_{mn}^{ij}, S_{mn}^{ij} and V_{mn}^{ij} leads to a state of minimum potential energy— where the right-hand side of Equation 4.10 is equal to zero. This feature allows generating a system of $5 \times (M \times N) \times (i \times j)$ independent linear equations

$$\frac{\partial \Pi}{\partial O_{mn}^{ij}}, \frac{\partial \Pi}{\partial P_{mn}^{ij}}, \frac{\partial \Pi}{\partial R_{mn}^{ij}}, \frac{\partial \Pi}{\partial S_{mn}^{ij}}, \frac{\partial \Pi}{\partial V_{mn}^{ij}} = 0 \quad \begin{cases} m = 1, 2, ..., M \\ n = 1, 2, ..., N \end{cases} \quad . \tag{4.11}$$

Due to the multi-plate assembly procedure and its mesh-independence, this model is suitable for simple, fast, parameter-driven analysis of new FishBAC configurations. This approach can be used to automate the generation of completely different FishBAC geometries from simple vectorised inputs of geometry and material properties. This allows for easy modification of the dimensions, aerofoil, detailed component geometries, material properties and laminate stacking sequences. Note that these changes in parameters do not significantly impact the convergence of the model.

4.4 Numerical Validation: Finite Element Method

In order to provide a reference for validation and comparison, a FEM model of the composite FishBAC was created in Abaqus/CAE 6.14 as described in Chapter 3.5. A fully clamped boundary condition is applied at the root of the FishBAC, and the actuation loads are introduced as distributed moments at the tendon-spine anchor points. To transfer these actuation loads to the solid elements, two external reference points are created and coupled via *Kinematic Coupling* to the node sets that correspond to the anchor points.

This coupling allows transferring rotation to the solid elements. Transverse displacements are tracked along all three free edges of the FishBAC at the nodes located at the centre of the spine (in the through-thickness direction), and are then used to validate the semi-analytical model.

Finally, a mesh-convergence study was performed by tracking tip displacements when the overall element size was reduced from 10 mm to 2.5 mm (in increments of 2.5 mm). The mesh was considered to be converged when both tip displacements varied by less than 0.5%, with respect to the previous meshing iteration.

4.5 Experimental Validation: FishBAC Composite Wind Tunnel Model

This section introduces the characteristics of a composite FishBAC wind tunnel wing model, which is the structure that is modelled in this study. The main structure corresponds to the first-ever composite-spine carbon fibre FishBAC, which has been designed and manufactured for wind tunnel testing. The wind tunnel model is a rectangular planform NACA 23012 wing with a chord of 270 mm and a span of 1000 mm, with the FishBAC occupying the aft 69 mm of the chord. It has two actuation points with tendons mounted 415 mm in either direction from the centre of the wingspan: one on the left-hand side (M_{x_2}) and one on the right-hand side (M_{x_4}), when viewed from above. Figure 4.2 shows a schematic diagram of this structural configuration and its primary dimensions.

4.5.1 Wind Tunnel Model

The wind tunnel wing model was designed and manufactured using a combination of metallic and 3D printed plastic parts, with silicone sheet skins and a carbon fibre spine. The spine was manufactured using Hexcel®'s 8552/IM7 carbon fibre prepreg under vacuum bag and autoclave pressure curing. With a total cured ply thickness of 0.39 mm, this composite spine provides another level of anisotropy as it has a layup ($[90/0/90]_T$), which results on the spanwise bending rigidity being around 3 times higher than the chordwise bending rigidity.

A series of 3D printed plastic (Digital ABS Plus by Stratasys) stringers and trailing edge sections were bonded to the cured composite spine using Cyanoacrylate adhesive. Although the use of plastic for the stringers implies that the spanwise bending stiffness of this FishBAC is significantly lower than a fully composite version, this choice was made to reduce the complexity and risk of this first attempt to manufacture a composite FishBAC device. The use of unreinforced polymer stringers significantly increases the amount of elastic washout—i.e. the reduction in camber deflection towards the midspan due to actuating the wing at discrete points along the span and the low spanwise bending stiffness of the wing model—of deformation which occurs along the span (particularly for more highly loaded cases), but can be readily addressed in future designs. The structure is actuated at two locations using a total of four KST X10 HV servo

actuators—two in each location [118]. As mentioned in Section 4.5.1, the actuation loads are transferred to the spine by a pulley-tendon system using a Kevlar-tape tendon that is stitched to the carbon plate. Finally, a pre-tensioned elastomeric silicone sheet covers the FishBAC structure and provides the aerofoil shape. Figure 4.3 shows a close-up view of the composite FishBAC morphing device—note that the fairing that covers the very rear of the trailing edge has been removed. This composite FishBAC prototype is used to validate the structural model presented in this chapter.

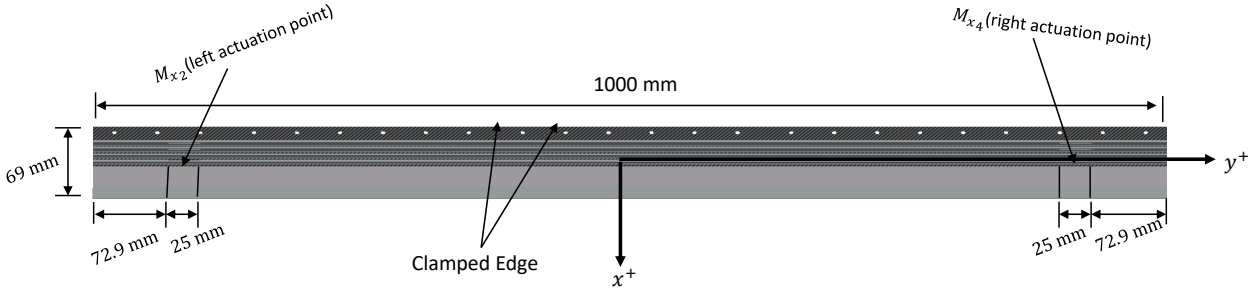

Figure 4.2: FishBAC wind tunnel model global dimensions and actuation points

Figure 4.3: Composite FishBAC device used for experimental validation of the semi-analytical structural model.

4.5.2 Material Characterisation

To accurately predict the deflections of the FishBAC, a material characterisation was performed to obtain experimental stiffness and Poisson's ratio values. The carbon fibre used for this material characterisation was cured in the same vacuum bag as the FishBAC spine and underwent the same curing cycle.

The carbon fibre's 0° and 90° Young's modulus were determined in accordance with ASTM D3039 test standard [119], whereas the in-plane shear modulus was determined using ASTM D3518's test standard [120]. Additionally, the ABS 3D printed plastic was tested by following ASTM D638's test standard guidelines [121]. Finally, the silicone skin was tested using 25 mm × 150 mm samples, which where bonded to 3D printed ABS end tabs to not only test the Young's modulus of the silicone skin, but also to test the adhesive that was used to bond the skin on the FishBAC wing. Tables 4.2 and 4.3 present the results of these material tests, which are the material properties that are used in both semi-analytical and FEM models.

As mentioned in Section 4.3, the material properties that are needed to model composite materials using Mindlin-Reissner Plate Theory are: E_{11}, E_{22}, G_{12}, G_{13} and G_{23} and ν_{12}. However, the material properties obtained via material testing (Table 4.2) do not include G_{13} or G_{23}. Additionally, the composite 3D solid elements in the FEM model (see Section 3.5) require E_{33}, ν_{13} and ν_{23} to be defined. A common assumption in composite analysis is to assume transverse isotropic behaviour, which states that the in-plane matrix direction is identical to the transverse direction. For this situation,

$$G_{12} = G_{13}\,, \quad E_{22} = E_{33} \quad \text{and} \quad G_{12} = G_{13}\,. \tag{4.12}$$

Additionally, the transverse shear modulus G_{23} can be estimated using the isotropic relationship

$$G_{23} = \frac{E_{22}}{2(1+\nu_{23})}\,. \tag{4.13}$$

where $\nu_{23} \approx 0.45$ is a common assumption in composite analysis [93].

Table 4.2: Material properties of the 8552/IM7 carbon fibre prepreg. Properties obtained via tensile tests.

Material	E_{11} [GPa]	E_{22} [GPa]	G_{12} [GPa]	ν_{12}
8552/IM7 Carbon Fibre	169.50	8.58	5.03	0.28

Table 4.3: Material properties of Isotropic silicone sheet and ABS plastic. Properties obtained via tensile tests.

Material	E [MPa]	G [MPa]	ν
40° Shore Silicone	1.22	0.44	0.39
ABS Plastic	2010	728	0.38

4.5.3 Static Displacement Measurements

To validate both the discontinuous Mindlin-Reissner analysis and the FEM model, a series of experimental displacement measurements were performed on the composite FishBAC wind tunnel wing model under actuation loads. Displacements were measured at several chordwise and spanwise points using an Imetrum® 3D Precision Displacement Tracker (Stereo Videogauge). The system consists of two-5 megapixel cameras in a stereo configuration, measuring at a 117 Hz frequency rate. These two cameras are mounted to a 3D measurement head (ICA-3D-0500-03), a pre-calibrated frame where both cameras are installed at a fixed angle and distance from each other (Figure 4.4). For the selected 3D measurement head, a measurement area of 600 mm × 600 mm with a 14 µm resolution is achieved [122].

The actuation torque inputs can be estimated by measuring current in each actuator, and then using the DC motor's torque-current linear relationship [123]

$$T = \epsilon k_t I\,, \tag{4.14}$$

where ϵ is the mechanical efficiency factor of the actuation mechanism and k_t is the torque constant, which links the mechanical torque and current. The torque constant depends on the servo's magnetic circuit design and coil winding and can be calculated experimentally by performing a torque-current test. The torque constant of the KST X10 servos was obtained via torque cell test (see Chapter 5.7.2), and it has an estimated value of $k_t = 0.82\,\text{N/A}$ for a constant voltage of 6 V, used throughout the experiment. Moreover, the mechanical efficiency factor ϵ was obtained experimentally by comparing semi-analytical vs experimental displacements. This efficiency factor accounts for frictional losses and energy loss due to tendon-pulley slack.

To measure current, four (one per actuator) LEM® 6 A CASR 6-NP Hall Effect current sensors (Figure 4.5) are used. These sensors measure the strength of the magnetic field induced by the current flow through the actuator leads and generate an output voltage that is directly proportional to the magnitude of current—at a rate of 312.6 mA/V. A series of 5 mm diameter bullseye stickers were used as target points, and voltage and current measurements were recorded using a National Instruments® USB-6211 data acquisition card. Finally, chordwise and spanwise displacements were measured using the stereo Precision Displacement Tracker.

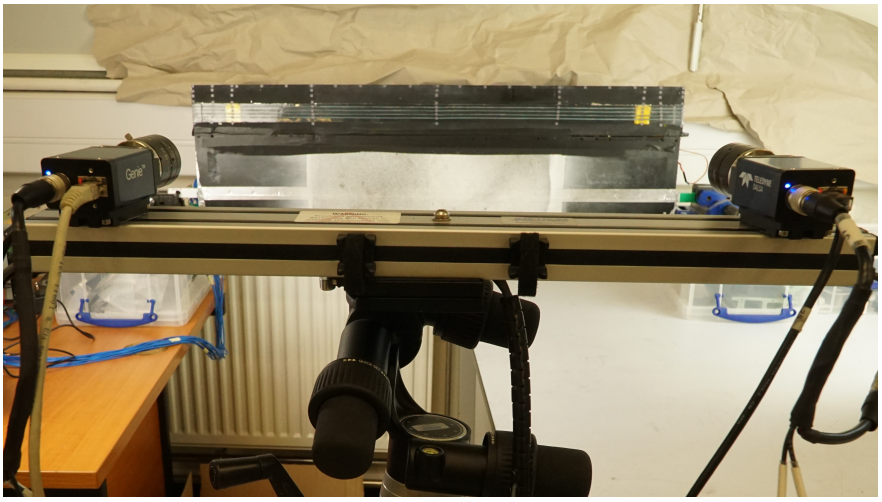

Figure 4.4: Imetrum's 3D Precision Displacement Tracker system for in-plane and out-of-plane displacement measurements.

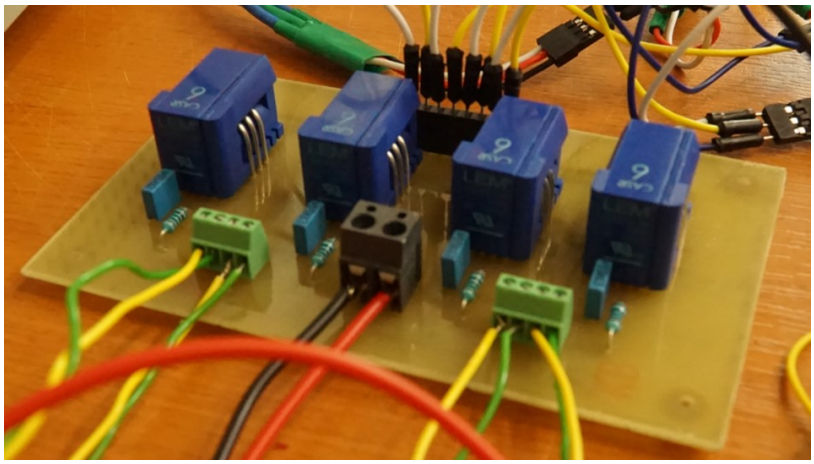

Figure 4.5: Hall Effect actuator current sensor for measuring torque inputs

4.6 Results and Model Improvements

The Mindlin-Reissner discontinuous plate model was first validated against FEM. This comparison was performed in terms of the percentage error difference along the spanwise free edge. Besides obtaining displacement fields under several load cases, two convergence studies were performed: the first one to estimate the required number of polynomial terms to achieve convergence and the second one to determine the stiffness of the artificial penalty springs. The stacking sequence and geometrical dimensions used correspond to the manufactured FishBAC wind tunnel model (i.e. stacking sequence of $[90°/0°/90°]_T$ and spine thickness of $t = 0.39\,\text{mm}$).

The FishBAC structure is discretised into 16 chordwise and 5 spanwise partitions of uniform thickness. These 16 chordwise partitions capture the presence of the stringers and the geometric taper of the aerofoil. This chordwise partitioning is different from the one performed in Chapter 3.3 since the FishBAC geometry modelled in this chapter has 4 stringers only, whereas the FishBAC geometry in Chapter 3 has 6 stringers.

The tapered trailing edge is modelled as 7 sections of constant average height. While the trailing edge could be discretised into more partitions, this region of the aerofoil is relatively rigid and adding partitions increases the size of the system of equations (Equation 4.11), and so 7 partitions were found to be sufficient for convergence.

4.6.1 Semi-analytical Model: Polynomial Term Convergence

A convergence study was performed to determine the number of Chebyshev Polynomial terms needed to capture the deformed shapes with sufficient accuracy while avoiding unnecessary computational cost. For simplicity purposes, the number of chordwise and spanwise terms in each plate segment are equal to each other (although more plate segments are used along the chord than along the span). To assess convergence, both maximum and RMS percentage errors are calculated along the free spanwise edge. The chosen load case for this convergence study is a differential moment input of $M_{x_2} = -1\,\mathrm{N\,m}$ and $M_{x_4} = 1\,\mathrm{N\,m}$, respectively. These inputs correspond to the load case that the Kirchhoff-Love formulation was unable to model, while the selected moment magnitudes yield to deflections that are similar to the maximum ones that can be achieved by the composite wind tunnel prototype.

Table 4.4 shows a summary of the corresponding percentage errors, whereas Figure 4.6 also shows the stability of the system of equations in terms of the condition number—defined in Chapter 3.2.8—and the total computational time per iteration. It is important to note that all results were computed on a single Intel® Core™ i7-4790 3.60 GHz CPU processor, using a 64-bit OS with 32 GB of physical memory.

Results show convergence with as few as three polynomial terms (in each direction), with a 4.2% and 2.7% maximum and RMS percentage errors, respectively. It can also be observed that increasing the number of terms only reduces both errors by a maximum of $\approx 1\%$. Furthermore, results show that the maximum error has a minimum value at five polynomial terms, and then increases with additional terms. This is due to the increase in the condition number of the coefficient matrix when the number of polynomial terms is increased, as the system becomes more sensitive to small changes in input. It can be concluded from this convergence study that this model converges at five Chebyshev Polynomial terms, for this combination of material and geometrical properties.

Table 4.4: Comparison of semi-analytical and geometrically linear FEM results as a function of Chebyshev Polynomials terms (polynomial order).

Laminate	Material	Polynomial Terms (M=N)	Max. Error (Abs. Value) [%]	RMS Error [%]	DOF
$[90°/0°/90°]_T$	8552/IM7 Carbon Fibre	2	99.90	43.00	1600
		3	4.172	2.688	3600
		4	3.478	1.879	6400
		5	3.287	1.686	10000
		6	5.740	1.645	14400
		7	5.728	1.618	19600
		8	5.097	1.465	25600

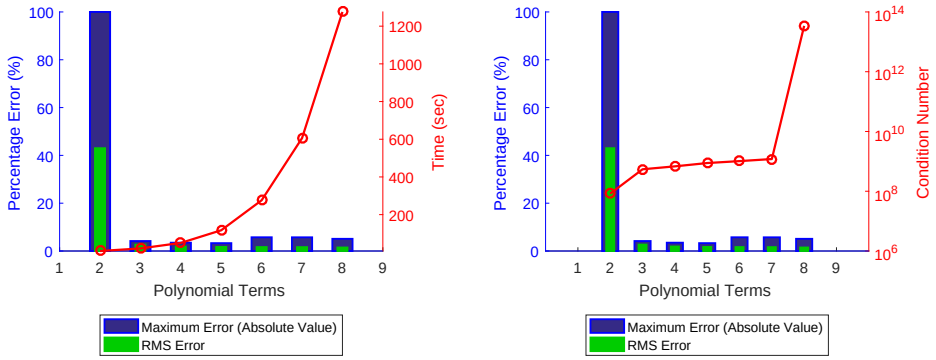

Figure 4.6: Convergence study of semi-analytical Mindlin-Reissner plate model versus Finite Element Method. Study also analysed the stability of the system—in terms of the condition number—and the total computation time of each iteration.

4.6.2 Penalty Stiffness Convergence

A second convergence study was performed to determine the impact that the penalty spring stiffness values have on the stability of the solution. To assess this impact, the spanwise RMS error and the condition number are calculated for different penalty stiffness values. Figure 4.7 shows the results of this convergence study, where it can be seen that the solution remains stable in terms of percentage error for a penalty spring stiffness between $k = 10^6$ $\mathrm{N\,m^{-1}}$ and $k = 10^{13}$ $\mathrm{N\,m^{-1}}$. This is consistent with results presented in Chapter 3.2.7, as well as with results presented by other authors [105, 107]. A minimum percentage error is observed when the penalty stiffness is $k = 10^6$ $\mathrm{N\,m^{-1}}$; however, this value may be too 'low' to guarantee convergence when the structure is subjected to higher loads. Consequently, is considered that $k = 10^7$ $\mathrm{N\,m^{-1}}$ is a more suitable value to ensure convergence throughout this study, as it presents a higher stiffness value, a stable condition number and a low percentage error. Therefore, a value of $k = 10^7$ $\mathrm{N\,m^{-1}}$ is used throughout the rest of this study.

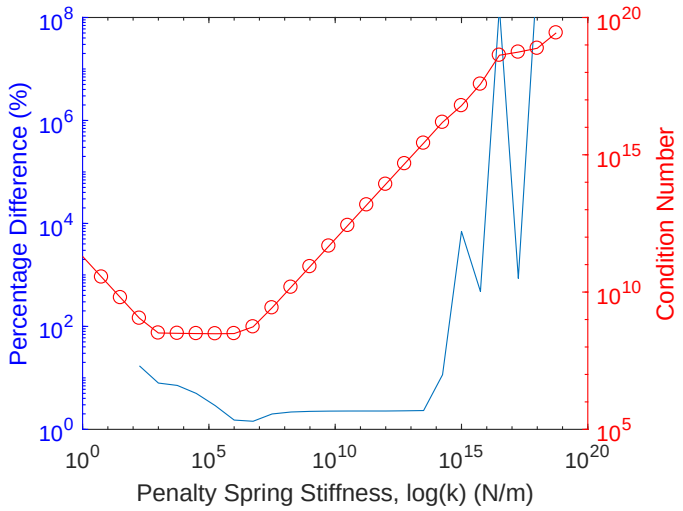

Figure 4.7: Root-mean-square error—along the spanwise edge—and condition number, as a function of penalty spring stiffness. Note that, for values lower than $k = 10^2$, there is no solution as the coefficient matrix is singular.

4.6.3 Kirchhoff-Love vs Mindlin-Reissner Models

The presented discontinuous Mindlin-Reissner model was primarily developed to address the inability of a discontinuous Kirchhoff-Love Plate Theory to capture deflections when differential actuation loads are applied (i.e. actuation moment loads with opposite direction). It was determined that this inability was due to the presence of transverse shear, as the structure reacts this load case by twisting, which induces transverse shear on the yz-plane. Since Kirchhoff-Love models cannot capture transverse shear deformations, an FTSD approach was implemented to address these limitations. Figure 4.8 shows a direct comparison between Kirchhoff-Love, Mindlin-Reissner and FEM models, when the FishBAC is loaded under differential actuation (i.e. equal magnitude but opposite direction). On the one hand, it can be observed that the Kirchhoff-Love model fails to predict the FishBAC displacement (compared to FEM), presenting an RMS percentage error—along the spanwise edge—of 35 %. On the other hand, it can be observed that the Mindlin-Reissner model successfully captures the displacement of the FishBAC, presenting an RMS percentage error of less than 2%. This result highlights the importance of developing this new model, which will be used for further design, optimisation and FSI analysis of this morphing concept.

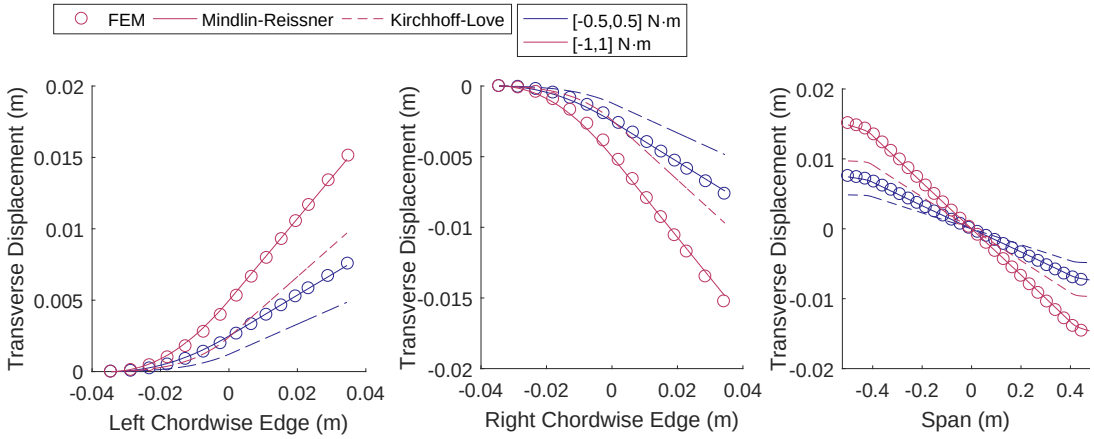

Figure 4.8: Comparison between Kirchhoff-Love and Mindlin-Reissner discontinuous plate models and Finite Element Method

4.6.4 Comparison Study: Mindlin-Reissner vs FEM

A more thorough comparison study of FEM vs semi-analytical displacement fields was also performed. Three different load cases are considered: uniform actuation (i.e. equal magnitude and direction), differential actuation (i.e. equal magnitude, but opposite direction) and single input (i.e. only one actuation input instead of two). The following subsection presents these results.

4.6.4.1 Uniform Actuation

The uniform actuation case corresponds to equal actuation inputs—in magnitude and direction—at both spanwise actuation points. Figures 4.9 and 4.10 show a comparison between semi-analytical and FEM results, showing an agreement with a maximum and RMS percentage error along the spanwise edge of 12.94% and 7.485%, respectively. An important characteristic of these displacement fields is the significant elastic washout along the span, which both models are able to capture. As mentioned in Section 4.5.1, this is due to the use of plastic instead of carbon fibre composite for the stringers in the wind tunnel wing model. While future designs will most likely be stiffer in the spanwise direction, the ability to capture the washout created by spanwise compliance is still crucial to the efficacy of this model, as washout will significantly impact the aerodynamic performance.

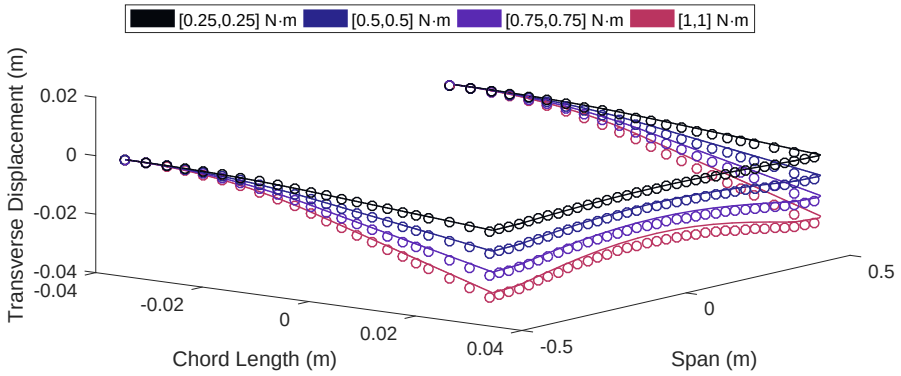

Figure 4.9: Mindlin-Reissner discontinuous plate model (solid) vs FEM (circle) under uniform actuation loads (trailing edge down).

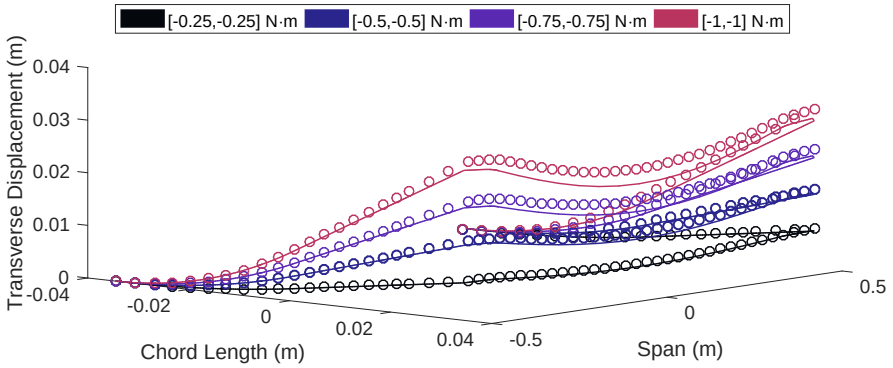

Figure 4.10: Mindlin-Reissner discontinuous plate model (solid) vs FEM (circle) under uniform actuation loads (trailing edge up).

4.6.4.2 Single Actuation Input

This load case corresponds to applying actuation input to only one actuation point. To simulate this case, negative actuation inputs between $M_{x_4} = -0.25\,\mathrm{N\,m}$ and $M_{x_4} = -1\,\mathrm{N\,m}$ were applied at the right-end actuation point, while the left-end actuation input was set to zero (i.e. $M_{x_2} = 0$). Figure 4.11 shows these results, which present a maximum and RMS error along the spanwise edge of 13.70% and 9.132%, respectively. This actuation case is primarily reacted as bending in the chordwise direction, with significant displacement variations along the span. This type of actuation case could potentially be useful for controlling spanwise aerodynamic loads, as different lift distributions along the span would be obtained.

4.6.4.3 Differential Actuation

The differential actuation case consists of applying torque inputs of equal magnitude but opposite sign to the two actuation points. In addition to chordwise bending moments, this creates a net torque on the FishBAC structure, inducing transverse shear. Consequently, this is the scenario that cannot be accurately captured using Kirchhoff-Love Plate Theory.

Actuation inputs of magnitudes between M_x =0.25 N m and M_x =1 N m, in increments of 0.25 N m, are applied. Figure 4.12 shows the displacement fields obtained using both FEM and the semi-analytical model. It can be observed that the FEM and semi-analytical results agree with each other (Figure 4.12), with a maximum and RMS percentage error along the free spanwise edge of 3.28% and 2%, respectively. This is a significant improvement from the Kirchhoff-Love model, which presents an RMS percentage error of 33% for this load case.

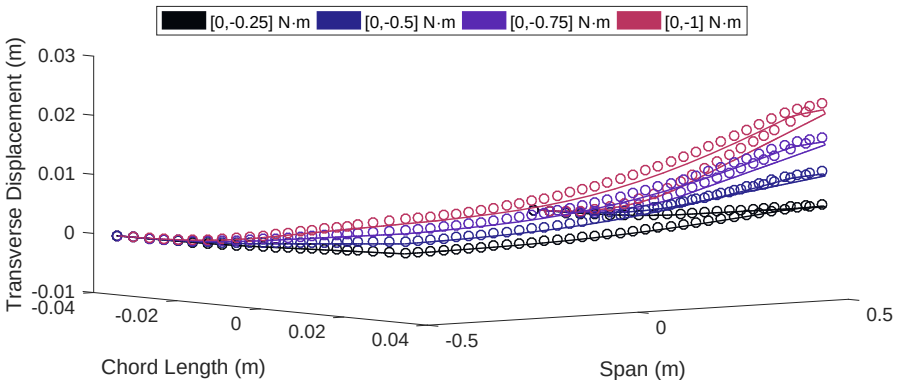

Figure 4.11: Mindlin-Reissner discontinuous plate model (solid) vs FEM (circle) under a single actuation load.

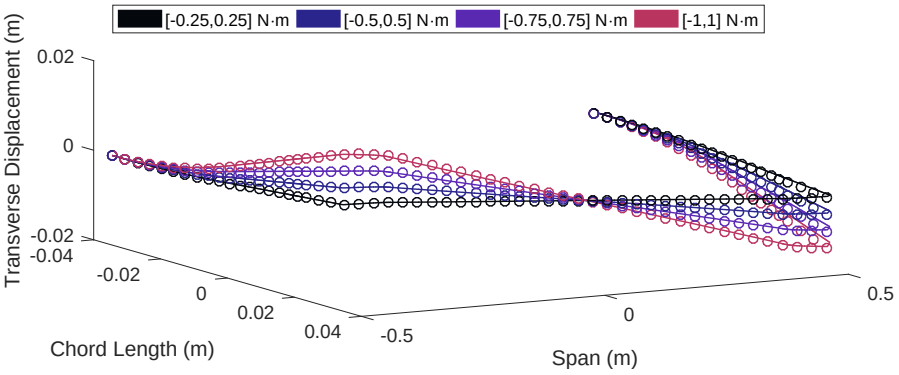

Figure 4.12: Mindlin-Reissner discontinuous plate model (solid) vs FEM (circle) under differential actuation loading (i.e. equal moment magnitude but opposite directions).

4.6.5 Numerical Efficiency

This subsection summarises the presented work by evaluating the total percentage errors of the Mindlin-Reissner model—with respect to FEM—and by estimating the total number of DOFs that each approach requires to achieve convergence. It is observed in Table 4.5 that the number of DOFs increases by 66% when transverse shear is analytically modelled; however this approach still needs only a very small fraction (around 1%) of the DOFs' that FEM requires to converge. A summary of the comparison study between the Mindlin-Reissner discontinuous plate model and FEM is presented in Table 4.6. These results show that the maximum RMS error occurs when a single actuation input is applied. This maximum percentage error of $\approx 9\%$ is a significant improvement from the errors between 35% and 45% obtained using the Kirchhoff-Love discontinuous plate model presented in Chapter 4.2.

Table 4.5: Efficiency study, in terms of required degrees of freedom for convergence

Model	DOFs	RMS Error [%]
FEM	1,086,426	–
Kirchhoff-Love	6,000	35.42
Mindlin-Reissner	10,000	9.13

Table 4.6: Maximum RMS error of Mindlin-Reissner discontinuous plate model, under different load cases. Errors are calculated with respect to Finite Element Method.

Load Case	RMS Error [%]	Maximum Error[%]
Symmetric	7.485	12.94
Single-Input	9.132	13.70
Differential	2.128	3.28

4.6.6 Experimental Validation

As explained in Section 4.5.3, the first step of the experimental validation is to estimate the efficiency factor ϵ of the actuation mechanism. A comparison between the semi-analytical and experimental tip deflections (measured using the Stereo Videogauge system) was performed, and the efficiency factor is calculated using a linear fit. As observed in Figure 4.13, the estimated mechanical efficiency factor is $\epsilon = 0.503$.

Once the efficiency factor is estimated, direct displacement comparisons can be established. First, the displacements along the spanwise edge are compared, as seen in Figure 4.14. Note that, due to restrictions on the measurement area of the video gauge system (the achievable window was 600 mm $\times$ 600 mm), only half of the span can be measured. Two different load cases are considered: positive (i.e. trailing edge up) and negative (i.e. trailing edge down) actuation. It is observed that the model predicts the downward displacements reasonably well (Figure 4.14).

The upward trailing edge deflections are not predicted as well, as there appears to be a displacement offset. In this case, the structural model slightly overpredicts the transverse displacements. While the exact cause of this overprediction is not currently known, it is possible that there are errors in the experimental measurements. Glare and light reflections off of the silicone skin, compounded by resolution and focus issues, did make point tracking more difficult for the positive displacements. After calculating the percentage difference error at three different locations—mid-span, three-quarter-span and wintip—a total RMS error of 10.4 % was obtained for all six measured displacements.

Additionally, transverse displacements were also tracked along the chordwise direction at two different spanwise locations. Figure 4.15 shows the transverse displacements measurements along the chord, at midspan (left) and three-quarter-span (right). These results are consistent with those observed in Figure 4.14: over-predicted positive deflections at mid-span, and good agreement at three-quarter-span.

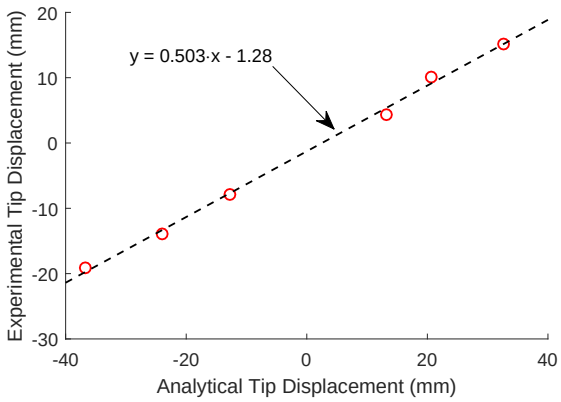

Figure 4.13: Experimental vs semi-analytical tip deflection. Results are used to estimate the actuation mechanism efficiency factor.

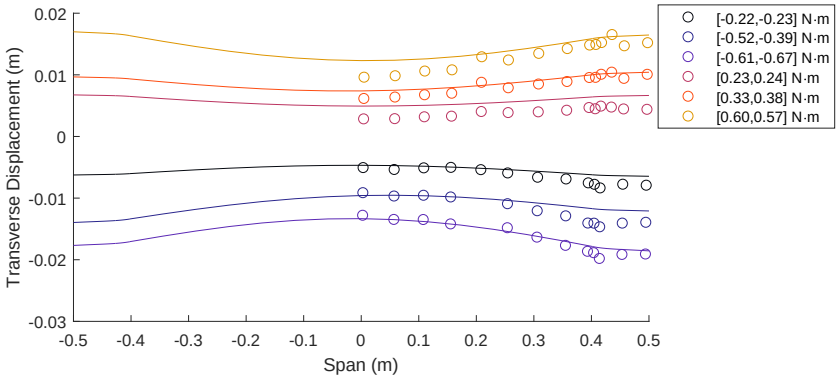

Figure 4.14: Experimental (circle) vs semi-analytical (solid) tip deflection along the FishBAC's spanwise edge. Results are used to estimate the actuation mechanism efficiency factor.

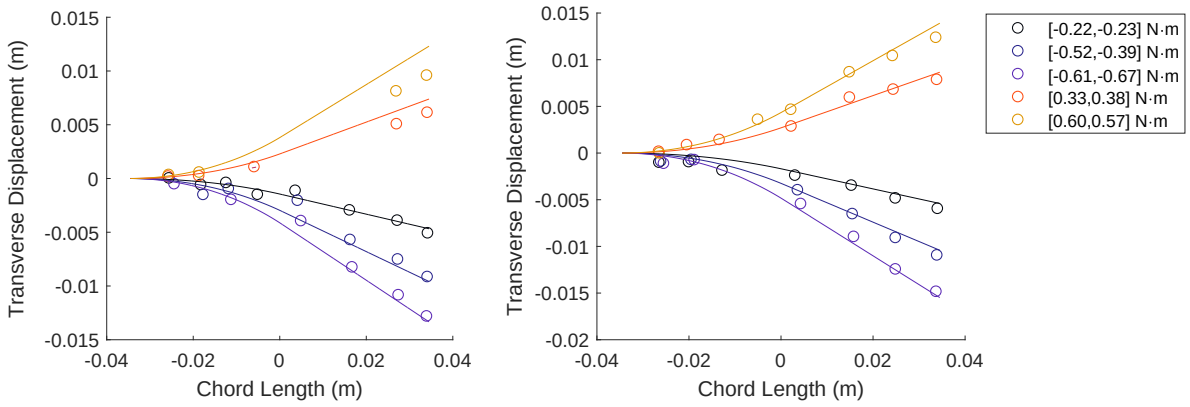

Figure 4.15: Experimental (circle) vs semi-analytical (solid) transverse deflection, along chordwise direction, at two spanwise locations: mid-span (left) and three-quarter-span (right).

4.7 Conclusions

A discontinuous, mesh-independent Mindlin-Reissner plate model was developed to model the structural behaviour of the highly anisotropic composite FishBAC morphing device. The novelty of this model lies in its ability to fully capture both chordwise and spanwise transverse shear displacements of the FishBAC using only around 1% of the DOFs when compared to a FEM model. This model addresses the limitations of a previously developed Kirchhoff-Love plate model presented in Chapter 3, which failed to predict the FishBAC's behaviour at certain important load cases due to its inability to account for transverse shear strains.

Some of the main advantages of this model are that it converges on a fixed number of equations (DOFs), it does not require meshing, and all the polynomial integrals can be calculated once up-front. These up-front polynomial integrations are performed and saved before the structural model is executed. Once the model is run, the required integrals are simply retrieved from a lookup table, meaning that all the computationally expensive steps are performed in advance. A summary of the main findings of this study is given as follows:

1. The Mindlin-Reissner Plate Theory-based model is able to accurately predict the out-of-plane displacement of the FishBAC when the structure is subject to twist, with a percentage error of $\approx 2\%$ when compared to FEM.

2. The worst-case RMS error between the Mindlin-Reissner plate model and the numerical (FEM) solution for all of the loading conditions considered is approximately 9%, with typical RMS error values of 2-7%.

3. The Mindlin-Reissner plate model converges using 99 % fewer DOFs than the FEM approach. It is mesh-independent, parametrically defined, computationally efficient and can

be used to model any continuous or discontinuous anisotropic plate structure subject to changes in thickness along either of the in-plane dimensions.

4. An overall RMS error of 10.4 % was obtained when validating the discontinuous Mindlin-Reissner plate model against experimental results.

This chapter successfully addresses the limitations of the Kirchhoff-Love plate model presented in Chapter 3, as it can predict the static behaviour of the FishBAC under any actuation load case. Therefore, this plate-based model will be used as the structural solver on the composite FishBAC's three-dimensional FSI analysis, which is later presented in Chapter 7.

Chapter 5

Design and Manufacture of a Composite FishBAC Wind Tunnel Wing Model

This chapter presents the design, manufacture and test of a composite carbon-fibre spine FishBAC device. The design was performed using the discontinuous Kirchhoff-Love plate model presented in Chapter 3, and this process consisted of sizing the composite spine, selecting the number of stringers and calculating the actuation energy requirements. The design process was completed by creating a Computer-Aided Design (CAD) model, which was then used to manufacture the wing model using a series of manufacturing techniques. Finally, a series of tests were performed to fully characterise materials and actuator properties, as well as the structural response of the FishBAC under static actuation loads.

5.1 Introduction

As discussed in Chapter 2.5, the first prototypes of the FishBAC morphing concept were manufactured using 3D printed plastic. This technique represents a low cost and quick solution for initial prototyping and testing. For example, these initial prototypes were crucial for obtaining preliminary experimental data that showed the potential benefits of the FishBAC concept—results which motivated the work in this thesis. Structural characterisation test results were used to validate a FishBAC's Euler-Bernoulli-based structural model [26] and the 3D printed prototypes were also used to obtain preliminary wind tunnel data. These wind tunnel test results showed promising lift-to-drag improvement of around 25% when the FishBAC was directly compared to a hinged trailing edge flap [25].

These preliminary results encourage further exploration, and one aspect of the concept that needs further development is the material selection and construction process. For example, the 3D printed plastic used on the first prototypes is not a viable material for full-scale applications and, therefore, aerospace grade materials need to be incorporated. Additionally, these materials are essentially isotropic, and thus elastic tailoring cannot be performed. Carbon fibre-reinforced polymer composites, on the other hand, hold much more promise as a material for FishBAC construction due to their excellent material properties, viability for commercial aviation, and their unique ability to be designed and tailored to provide high levels of anisotropic stiffness.

It is therefore important to consider composite-based FishBAC designs in order to scale-up this technology. Consequently, a composite-spine FishBAC wind tunnel wing model was designed using a series of analytical aerodynamic and structural tools that were custom-made for this application and then manufactured using a combination of different materials and manufacturing techniques. This final product (the carbon fibre prototype) not only demonstrated that it is possible to design and manufacture a composite FishBAC device, but the resulting wing model was also used to obtain experimental structural and aerodynamic data. These experimental results were used to both validate modelling techniques, and also to further analyse the aerodynamic benefits of camber morphing and the capabilities of the FishBAC device.

5.2 Design Objectives

A two-dimensional wind tunnel wing model was designed based on a NACA 23012 aerofoil profile, with a chord length of 270 mm and span of 1000 mm. The span was chosen based on the test section size of the chosen wind tunnel (Swansea University's subsonic wind tunnel) to provide as close to two-dimensional flow as possible, whereas the aerofoil and chord length were selected to match that of the Bo-105 helicopter, which is the baseline rotor system for a large morphing aircraft research program (SABRE—Shape Adaptive Blades for Rotorcraft Efficiency) running in parallel to this work [124]. By choosing to align with this research program, the impact of the research undertaken in this thesis was significantly increased. It is worth noting as an aside that the NACA 23012 is a commonly used aerofoil in a wide range of applications, and therefore provides a degree of general relevance to the work as well.

The design concept pursued for the wind tunnel wing model developed in this chapter consists of a modular wing, where both the leading and trailing edges can be detached from a central main section. This not only allows the installation of different FishBAC devices, but also fitting any other leading or trailing edge configurations/devices. A combination of high-strength carbon fibre prepreg, 3D printed ABS plastic, aluminium 6082T and silicone sheets were used to manufacture this prototype. Lastly, the wind tunnel wing model was designed for testing over a range of flow speeds up to a maximum freestream velocity of 50 m/s, corresponding to Reynolds numbers of up to $Re = 1 \times 10^6$.

The focus on this first composite FishBAC is the composite spine, as this is the primary structural member where most of the loads are reacted. For the time being and with the exception of the wing skin and an aluminium spar, the other structural components will still be 3D printed. This decision was made to reduce the complexity and mitigate the risk of this first attempt to manufacture a composite FishBAC. However, future design iterations should consider replacing 3D printed parts by fully composite components.

5.3 Initial Sizing

The sizing of the FishBAC morphing device is driven primarily by the thickness and material stiffness of the spine, which drives the maximum achievable deflection of the FishBAC for a given actuation system. To achieve a sufficiently high lift control authority, a maximum transverse deflection of $y/c = 0.1$ (i.e. 27 mm in this case) was targeted based on previous aerodynamic studies. Consequently, the spine thickness and material layup were selected to achieve this target deflection within certain limits of actuation torque. An intermediate modulus carbon fibre prepreg (Hexcel® 8552/IM7) was chosen as the spine's material. For ease of manufacturing, the ply angle orientation was restricted to cross-ply configurations (i.e. 0° or 90° plies). A two-step analysis was performed: first, the semi-analytical model was run under actuation loads, followed by superimposing representative aerodynamic pressure distributions obtained using an existing 2D FSI analysis [113] with the new two-dimensional plate model. Although this analysis is not a fully coupled FSI routine, it considers aerodynamic loads in the sizing process. Also, even though the Kirchhoff-Love plate model showed limitations in modelling the FishBAC's response under asymmetric actuation loads (see Chapter 3), this technique is appropriate to model the quasi-2D wind tunnel test load scenario as only symmetric actuation inputs are applied for this quasi-2D case.

5.3.1 Actuation Loads Without Aerodynamics

The first actuation requirement estimates were performed by comparing static deflections, in the absence of aerodynamic loads, between the one-dimensional Euler-Bernoulli beam model by Woods and Friswell (2014) [26] and the two-dimensional Kirchhoff-Love plate model introduced in Chapter 3. This comparison allows contrasting the two models against each other. The material properties used during the design stage for the relevant materials—carbon fibre prepreg, silicone and 3D printed ABS plastic—were directly obtained from manufacturers' datasheets and are summarised in Table 5.1. However, for more robust validation of the modelling methods, all three materials were later characterised by performing a series of material tests, which are presented in Section 5.6.

As mentioned in Chapter 2.5, due to the presence of spanwise stringers, the FishBAC is highly orthotropic as it is stiffer along the span than along the chord. This configuration allows for the minimisation of the actuation energy needed to achieve certain camber deflection, while still providing sufficient spanwise stiffness to resist spanwise bending moments due to aerodynamic loads. Additionally, the use of carbon fibre on the bending spine can further increase the degree of anisotropy by reducing the number of plies aligned with the chordwise direction. Therefore, an initial spine layup of $[90/0/90]_S$—where 0° direction is aligned with the chordwise direction—was analysed.

A total of 6 plies were considered based on the spine thickness of the FishBAC geometry modelled in Chapter 3. However, this stacking sequence resulted in an actuation torque requirement of at least $6.5\,\mathrm{N}\cdot\mathrm{m}$. Considering the size of the aerofoil, there were no off-the-shelf actuators that could provide the required torque that can fit inside the aerofoil dimensions. Also, it is important to note that frictional losses and aerodynamic loads are not included in these estimations and, therefore, these torque requirements are expected to increase. These results suggest that a spine of six carbon fibre plies is over-designed for this structural dimensions.

Based on these preliminary estimates, reducing the spine thickness was the most feasible option to reduce the actuation energy requirements. To achieve this thickness reduction, the spine thickness was reduced in half by having a layup of $[90/0/90]_T$, which not only has a lower thickness value, but also presents lower stiffness in both membrane and bending modes. A positive and negative moment input sweeps were applied to the structure, and the behaviour of both beam and plate models were compared. Since the beam model is not capable of analysing composite laminates, an effective Young's modulus in the chordwise direction is calculated by 'homogenising' the bending stiffness along the chordwise direction, as defined by

$$E_x^b = \frac{12}{d_{11}t^3}\,, \tag{5.1}$$

where d_{11} is the laminate's bending compliance along the chordwise direction and corresponds to the $i = 4, j = 4$ term in the abd laminate compliance matrix. The abd compliance matrix is obtained by calculating the inverse of the ABD laminate stiffness matrix, which is itself obtained from CLT analysis [93].

Results show that the one-dimensional beam model and two-dimensional plate model agree within 14% (Figure 5.1), when comparing the average edge displacements. Note that this percentage difference corresponds to the average error along the spanwise free edge, and consequently, this percentage difference estimate is significantly affected by the spanwise elastic washout that the 1D beam model cannot capture. These results highlight the importance of using a two-dimensional structural modelling approach to analyse a three-dimensional FishBAC device. Results also show that transverse deflections of approximate 8%-chord can be obtained by applying a total moment input of approximately $2.84\,\mathrm{N}\,\mathrm{m}$, which can be achieved from off-the-shelf actuators. However, it is important to remind that these torque requirements will increase when aerodynamic loads are considered. Details on the actuator selection will be addressed in the next subsection.

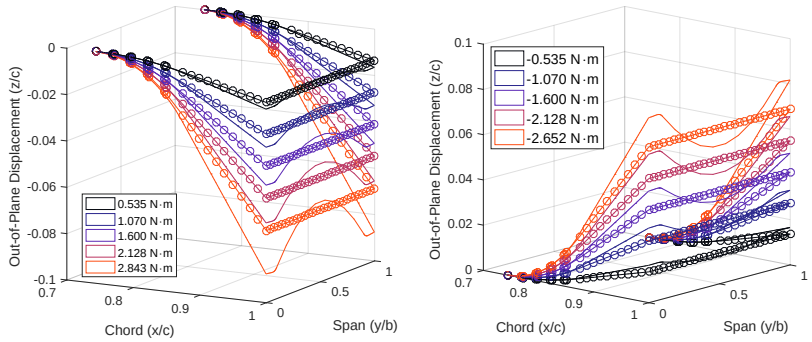

Figure 5.1: Two-dimensional plate model (solid) vs one-dimensional beam model (∘) actuation moment sweep in absence of aerodynamic loads. Moments correspond to total moment input.

Table 5.1: Material properties of CFRP, ABS and Silicone [112, 113]. Note that the shear modulus of both ABS and Silicone are obtained using the isotropic Young's modulus and Poisson's ratio.

Material	CFRP	ABS	Silicone
E_{11}	161 GPa	2.9 GPa	3.18 MPa
E_{22}	11.4 MPa		
G_{12}	5.17 MPa	N/A	N/A
ν_{12}	0.34	0.35	0.425
t	0.125 mm	N/A	N/A

5.3.2 Deflections Under Aerodynamic Loads

There is one key factor that must be considered when a compliance-based morphing device is subject to a freestream flow: the strong coupling between structural and aerodynamic loads, which directly impacts the actuation requirements. When these camber morphing devices are used to increase lift under attached flow regimes (e.g. when deflected downwards at typical operating positive angles of attack), the actuation loads required to achieve the desired camber deflections are higher than when there is no aerodynamic loading, thus, failing to consider aerodynamic forces and moments may lead to incorrect actuation sizing. Additionally, large changes in camber produce substantial changes in aerodynamic forces and therefore, the structural and aerodynamic analyses cannot be performed independently as they are continuously affecting each other. Consequently, FSI routines are implemented to properly model compliant structures subjected to fluid flows.

Even though the aerodynamic and structural analysis are not fully coupled in this design study, the aerodynamic pressure distributions from a one-dimensional FishBAC FSI [113] were extracted and then applied to the plate model. As mentioned in Section 5.1, this 1D FishBAC FSI is based on Euler-Bernoulli beam theory and XFOIL. The material properties and structural dimensions of the Euler-Bernoulli model were maintained from the analysis without aerodynamic loads (Section 5.3.1).

Moreover, a freestream flow velocity of Mach 0.15 (i.e. 50 m/s at room temperature), and an angle of attack of 5° were used to obtain a representative pressure distribution at maximum test speed and at a representative operating angle of attack where flow is fully attached, respectively. Ten different moment inputs were applied, with their respective aerodynamic pressure distributions previously obtained from the 1D FSI.

Since 1D FSI model cannot capture spanwise variations in deflection, spanwise pressure uniformity must be assumed. Consequently, this technique would not capture any pressure distribution changes due to spanwise elastic washout, however, the applied pressure distributions are still roughly representative of quasi-2D wind tunnel tests scenarios, and since the objective of this current analysis is to design the device and size the actuators (as opposed to validate structural or aerodynamic models), roughly representative loadings are still usable. Figure 5.2 shows a comparison between the 1D fully coupled FishBAC FSI and the 2D Kirchhoff-Love plate model loaded with the representative pressure distributions extracted from this 1D FishBAC FSI.

It is observed that the two-dimensional plate and one-dimensional beam models agree within an average error of 15%, when displacement percentage difference is calculated along the spanwise free edge. Similarly, as in Section 5.3.1, the main contributor to this percentage difference is the spanwise variation in displacement due to elastic washout that the plate model captures and the beam model cannot capture.

It is also observed that the actuation requirements to generate a transverse tip deflection between 8% and 10% chord increased by approximately 50% when compared to the zero freestream velocity case (Section 5.3.1). As previously mentioned, even though the two-dimensional plate model is not fully coupled with an aerodynamic modelling tool, these results are still meaningful as the pressure distributions that were applied were obtained from a separate (converged) FSI analysis. Lastly, these results show that a spine thickness of 0.375 mm, with a stacking sequence of $[90/0/90]_T$ is suitable for the composite wind tunnel wing model, and will be able to achieve the targeted camber deflections between 8% and 10%.

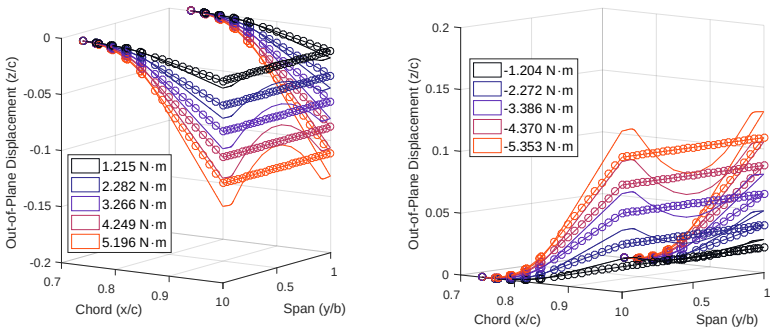

Figure 5.2: Two-dimensional plate model (solid) vs one-dimensional beam model (∘) actuation moment sweep under a freestream flow of Mach number of M = 0.15 and 5° angle of attack. Moments correspond to total moment input.

5.4 Detailed Design

As mentioned in Section 5.2, a modular approach is implemented in the wind tunnel model design. This modularity means that the leading and trailing edge sections are detachable, simplifying installation, modification, and allowing for testing different leading and trailing edge devices (in future work). A 19.05 mm × 19.05 mm × 3.25 mm aluminium (6082T alloy) spar acts as the main load-bearing member of the wing. Furthermore, there are three main 3D printed sections: the leading edge, the central main section and a removable trailing edge section that clamps the FishBAC to the wing and also contains the servo actuators and the actuation pulleys. The leading edge section is mounted to a 15.88 mm × 6.25 mm stainless steel bar, which is itself attached to the central 3D printed section using a set of transverse screws. The actuators are mounted to the removable rigid trailing edge section that slides into the central part itself. Once in position, the trailing edge section is secured to the central part of the wing by using a series of transverse screws and nuts. Moreover, the FishBAC device is later clamped to this removable trailing edge section by also using a series of transverse screws. Once the FishBAC is clamped, the silicone skin sheet is bonded to the FishBAC using silicone adhesive. Lastly, a series of spanwise oriented carbon fibre pultruded tubes were added, in nine various locations, to increase the stiffness and strength of the non-morphing portion of the wing, which was designed to resist up to 150% of the worst-case aerodynamic load at the maximum test speed of 50 m/s. Figure 5.3 shows a profile view of the wind tunnel model and Figure 5.4 shows a picture of the composite FishBAC assembly.

Based on the results shown in Figures 5.1 and 5.2, and considering the available space defined by the aerofoil geometry, the actuation selection was performed. Because of its compact dimensions of (35.5 mm × 30 mm × 10 mm), the KST X10 wing servo actuator was selected based on its ability to generate sufficient torque while still fitting inside the aerofoil profile [118]. However, since each one of these actuators produce a maximum torque of 1.05 N m when running at maximum voltage, two actuators per tendon are needed to achieve the desired control authority, including some margin in consideration of the frictional losses neglected in both analytical structural models. Table 5.2 summarises the main results from the initial sizing study.

Table 5.2: Preliminary FishBAC and actuation sizing

Spine Nominal Thickness	Stacking Sequence	# of stringers	Actuators
0.375 mm	$[90/0/90]_T$	4	4 × KST X10 HV Servo

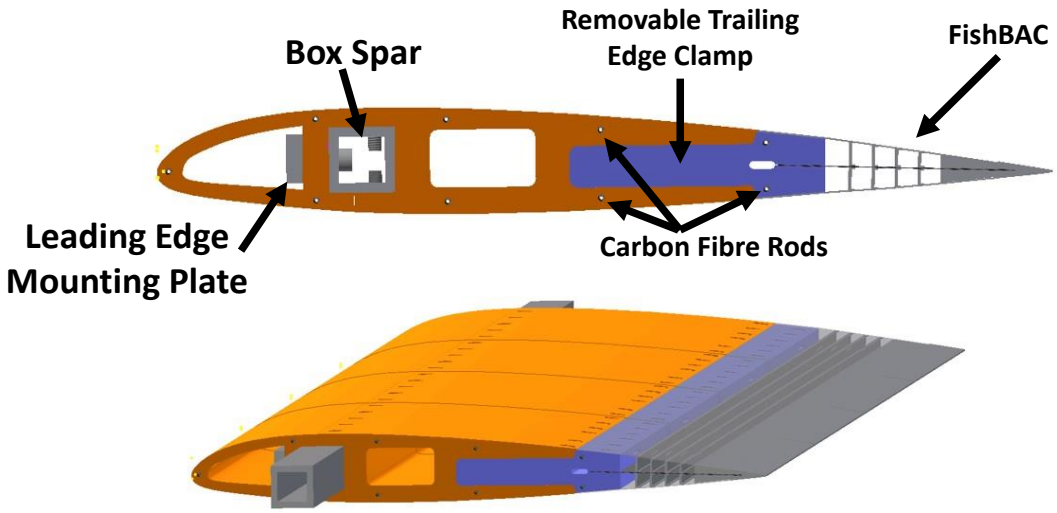

Figure 5.3: Profile view of the FishBAC wind tunnel wing model. Note that the tendons are missing in this CAD model.

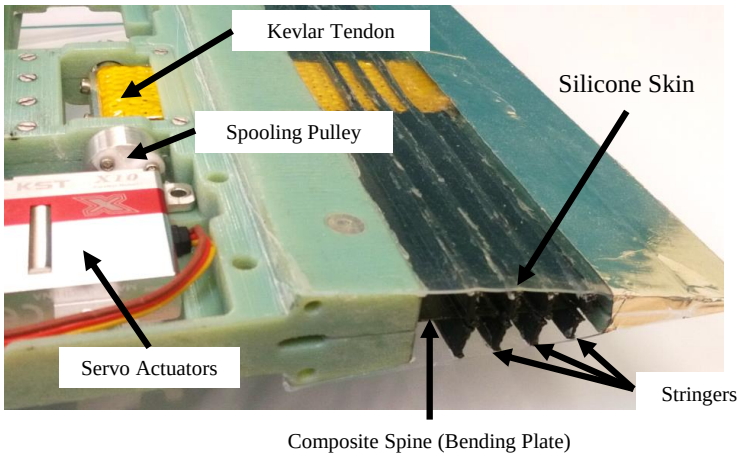

Figure 5.4: FishBAC structure and actuation mechanism

5.5 Manufacture

The first step of the wing manufacturing process was to create the carbon fibre spine. The composite lay-up was performed on a flat aluminium tooling plate, and cured under 8552/IM7's standard autoclave vacuum bag cure cycle—maximum temperature of 180 °C and autoclave pressure of 7 bar [125]. Additionally, three other plates of the same material were cured in the same vacuum bag. These plates were later used for material testing to experimentally characterise and calculate the fibre, matrix and shear modulus, as well as in-plane Poisson's ratio of the CFRP. Once cured, the composite spine was cut to size using a diamond saw, and its edges were finished by sanding. The spine was then attached to the plastic removable trailing edge clamp (see Figure 5.5) using a series of transverse screws. In order to fit the screws, holes were drilled into the spine using an end-mill, which was selected instead of a drill bit to avoid delamination. Unlike drill bits, end mills cut holes uniformly from the edges, preventing material peel-up. Note that this approach may not work on thick composite laminates.

The plastic parts of the wing, including the FishBAC stringers and solid trailing edge sections were 3D printed using a Stratasys® Objet^{TM} printer. This printer uses direct jetting of a liquid photopolymer and cures it under UV light. Once printed, the stringers were aligned using a series of laser-cut alignment jigs, and were finally bonded to the carbon fibre plate using a Cyanocrylate-based adhesive. Moreover, as explained in Chapter 2.5, the actuation loads are transferred from the actuators to the FishBAC's trailing edge end using a pair of antagonistic tendons. These tendons were pre-cut from a 25 mm-wide dry Kevlar-fibre tape roll and then coated with Kapton tape. The function of this Kapton tape is to both protect the dry fibres and to keep them together when the actuation loads are applied. The tendons spool around a machined aluminium drive pulley and, to attach them to each pulley, they are clamped using an aluminium clamp bar. The 'unclamped' ends of each tendon were hand-stitched onto the trailing edge and the carbon fibre spine using Kevlar tow. This stitching step was done after drilling a series of 2 mm holes into the composite spine. After stitching, each stitched region (Figure 5.6) was reinforced with epoxy resin, providing additional mechanical and adhesive strength at these tendon-spine attachment regions.

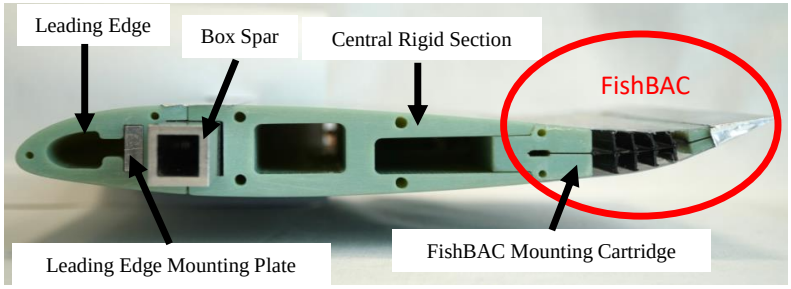

Figure 5.5: Composite FishBAC wind tunnel model (with upward FishBAC deflection)

Finally, a 0.5 mm thick 40° Shore silicone sheet (Silex Superclear from Silex Silicones LTD) was bonded to the FishBAC's mounting trailing edge clamping section, stringers and solid trailing edge strip using a fast cure silicone adhesive (NuSil MED3-4013). Note that, before bonding, the silicone sheet was pre-stretched by 30%.This pre-stretching increases the out-of-plane stiffness of the skin, reducing deformation under aerodynamic loading and preventing the skin from buckling when in compression. The pre-stretch was performed by first cutting the silicone sheet to size and then clamping both chordwise ends to two beam extrusions mounted to two fixed rails. Once this clamping was performed, the tension was adjusted by sliding the extrusion beams on the rails and then fixing them to the desire position using screws and nuts. After the desired tension was set, the silicone adhesive was applied to the stringers and then the skin was bonded by applying pressure (see Figure 5.6). To improve the external surface smoothness, the remaining solid parts of the wing (i.e. nose leading edge and mid-section) were sanded down by hand, and then attached to the main spar using a series of screws. A final layer of black paint was applied to the rigid wing parts, and all screw holes and joints on the wing surface were covered with aluminium tape.

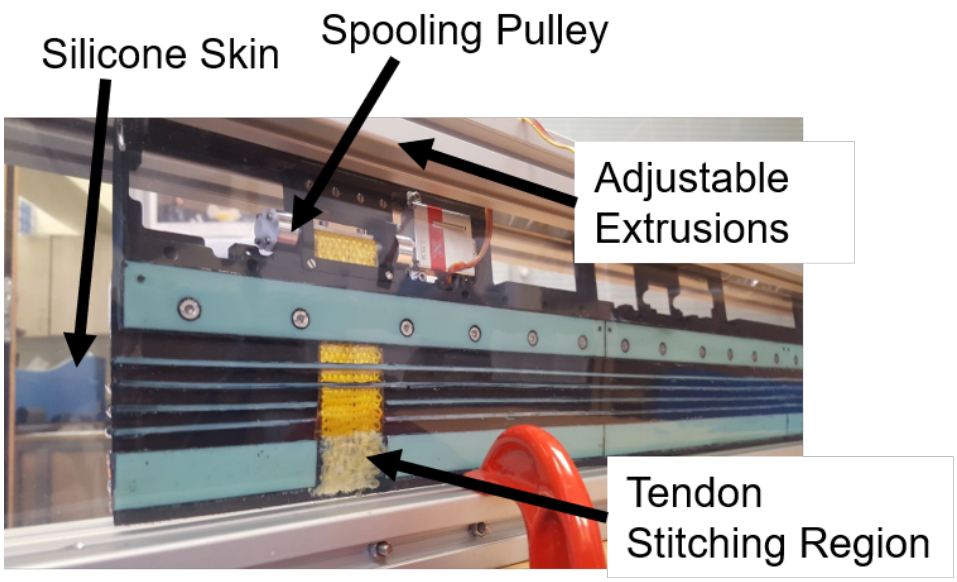

Figure 5.6: Kevlar tendon stitching region and skin pre-stressing rig

5.6 Material Characterisation

To properly model the structural behaviour of the composite FishBAC, the three materials that are used to build this wind tunnel wing model—ABS UV-cured 3D printed plastic, the carbon fibre prepreg and the silicone skin—are fully characterised to obtain their material properties. Each one of the experiments that were performed is presented in this section.

5.6.1 Hexcel® 8552/IM7 UD carbon fibre prepreg

The material properties of the carbon fibre UD prepreg were obtained in accordance with the ASTM D3039 [119] and ASTM D3518 [120] Standards for obtaining tensile and shear properties of fibre-reinforced polymers, respectively. Two different Instron® tensile machines—100 kN and 25 kN, respectively—were used depending on the nature of the specimens. An Imetrum® Video Gauge™ UVX Flexi point tracking camera system was used to measure both axial and transverse strains. Three types of tensile tests were performed: fibre-direction tension, matrix-direction tension and shear. Seven samples were tested in each test configuration. Table 5.3 shows a summary of the test specimen dimensions, stacking sequence and machine used.

The fibre-direction Young's modulus E_{11} and in-plane Poisson's ratio ν_{12} were calculated from the fibre tension specimens' stress-strain curves (Figure 5.7), whereas the matrix-direction Young's modulus E_{22} was obtained from the matrix-direction stress-strain curves (Figure 5.8). Since these stress-stress curves are linear, thus, E_{11}, E_{22} and ν_{12} are defined as

$$E_{11} = \frac{\Delta\sigma_{xx}}{\Delta\epsilon_{xx}}, \quad E_{22} = \frac{\Delta\sigma_{yy}}{\Delta\epsilon_{yy}} \quad \text{and} \quad \nu_{12} = \frac{-\Delta\epsilon_{yy}}{\Delta\epsilon_{xx}}. \tag{5.2}$$

Furthermore, the in-plane shear modulus G_{12} was obtained from the in-plane shear test specimens (Figure 5.9). This modulus was calculated by first estimating the in-plane shear stress on each specimen

$$\tau_{12} = \frac{P_{\text{load}}}{2A_{\text{cs}}}, \tag{5.3}$$

where P_{load} is the axial load applied by the tensile test machine and A_{cs} is the cross-sectional area of each specimen, followed by estimating the in-plane shear strains

$$\gamma_{12} = \epsilon_{xx} - \epsilon_{yy}. \tag{5.4}$$

Lastly, the in-plane shear modulus G_{12} can be calculated based on these in-plane shear stress and strain estimates, such that

$$G_{12} = \frac{\Delta\tau_{12}}{\Delta\gamma_{12}}. \tag{5.5}$$

It is important to note that all modulus and Poisson's ratio values were obtained by first performing linear fits on each individual stress-strain curve, then calculating the stiffness and Poisson's ratio values of each specimen and finally calculating average quantities across all specimens.

Table 5.3: CFRP specimen dimensions, thickness and stacking sequence. All dimensions correspond to average values across each set of specimens.

Test	Thickness	Stacking Sequence	Gauge Length	Width	Machine
Fibre Tension	1.03 mm	$[(0)_4]_S$	135.79 mm	19.80 mm	100 kN
Matrix Tension	2.04 mm	$[(90)_8]_S$	121.35 mm	25.35 mm	25 kN
In-Plane Shear	2.02 mm	$[(\pm 45)_4]_S$	161.00 mm	25.35 mm	25 kN

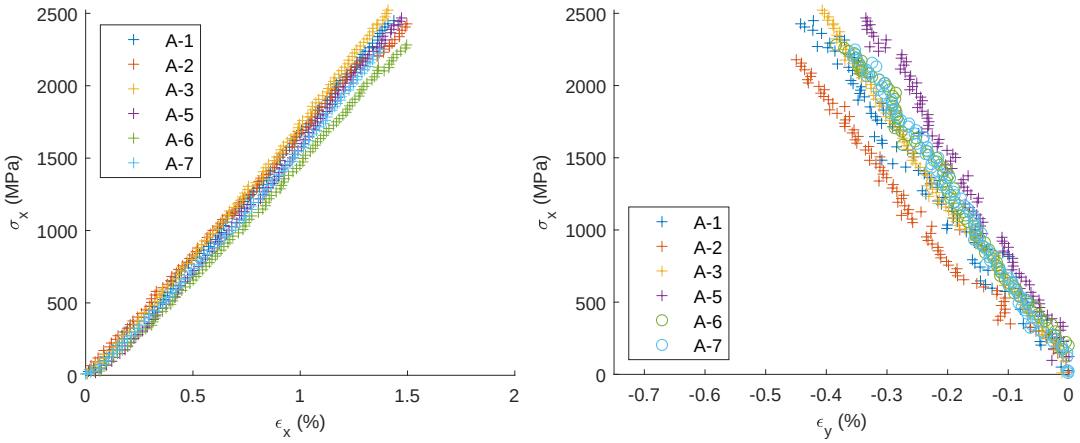

Figure 5.7: Stress-strain curves of the fibre-direction tensile CFRP specimens

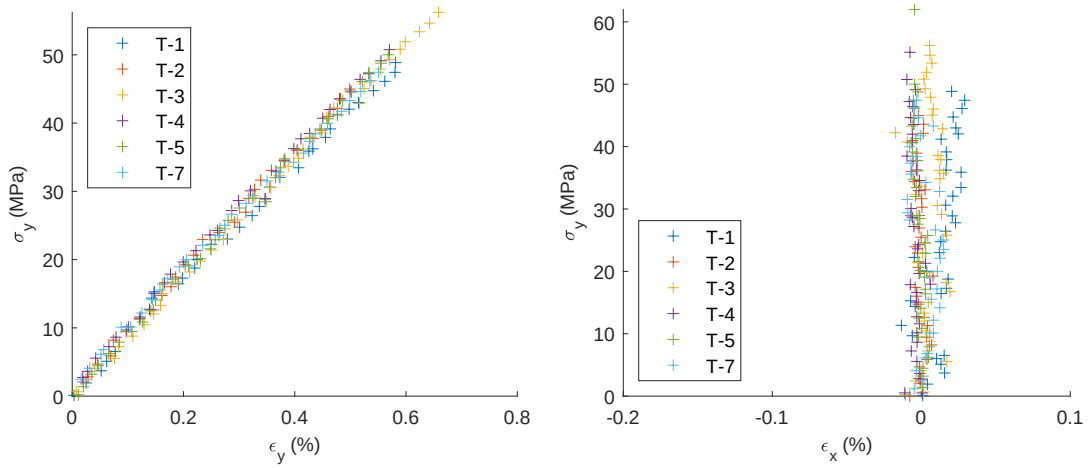

Figure 5.8: Stress-strain curves of the matrix-direction tensile CFRP specimens

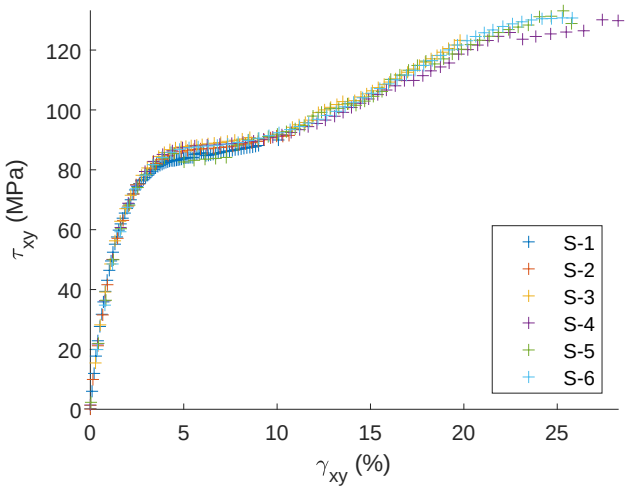

Figure 5.9: Stress-strain curves of the shear CFRP specimens

5.6.2 Silicone Skin

The Silex® 40° Shore 0.5 mm-thick skin material was tested under tension. The main objective of this test is not only to obtain the Young's modulus and Poisson's ratio, but also to test the strength of the fast cure silicone adhesive. Plastic ABS bonding tabs 50 mm × 25 mm in planform were 3D printed, and the specimens were created by cutting 200 mm × 25 mm silicone coupons and then bonding the plastic tabs onto each end to create single lap joints. Three of the six specimens had their tabs treated with a chemical primer (Momentive SS4004P) before bonding to determine whether this treatment increases the adhesive shear strength. Based on failure mode, results show that the primer contributed for a material failure (i.e. silicone breaking under tension), rather than adhesive failure. However, even without the primer, failure occurs at much higher strains than those the FishBAC sees during operation. Therefore, it was decided not to use primer to simplify the skin bonding process. One important aspect to point out is that the stress-strain curves (Figure 5.10) observe a significant amount of non-linearity, as would be expected for an elastomer such as silicone. Consequently, the Poisson's ratio varies with strain and was then calculated at a 30% strain, which corresponds to the amount of skin pre-strain applied to the silicone skin before bonding. The Young's modulus, in-plane Poisson's ratio and shear modulus at 30% strain were estimated as

$$E = \frac{\delta}{\sigma_{xx}}\epsilon_{xx}, \quad \nu = \frac{-\epsilon_{yy}}{\epsilon_{xx}} \quad \text{and} \quad G = \frac{E}{2(1+\nu)}. \tag{5.6}$$

5.6.3 ABS UV-cured 3D printed plastic

Finally, the 3D printed plastic was also tested under tension to determine its Young's modulus and Poisson's ratio (Figure 5.11). A set of dogbone specimens were 3D printed in accordance with ASTM D638 [121] Standard for tensile properties of plastic. A Shimadzu® tensile machine fitted with a 10 kN load cell was used, and strains are measured using an Imetrum UVX Flexi Video Gauge camera system. Young's modulus, Poisson's ratio and Shear modulus were calculated using Equation 5.6. A summary of all the experimentally measured material properties can be found in Table 5.4.

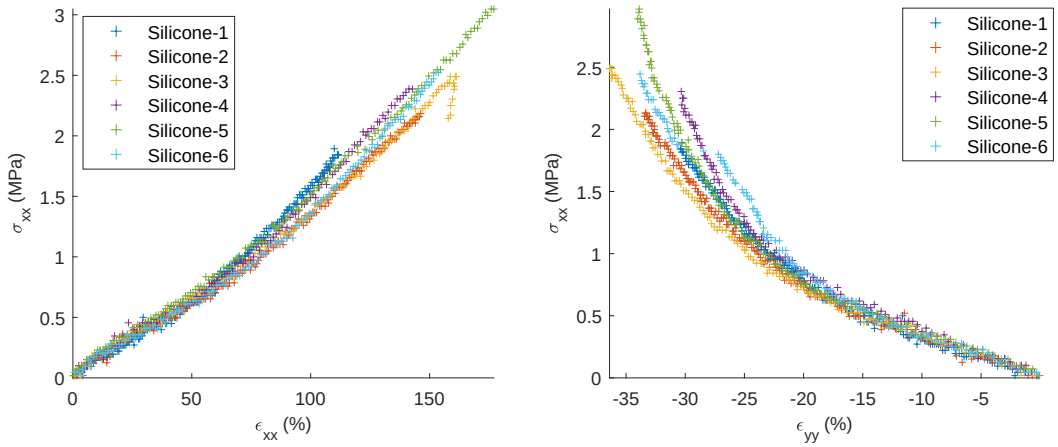

Figure 5.10: Stress-strain curves of the 40° Shore silicone skin. Specimens 1-3 were bonded to plastic tabs after applying primer, whereas specimens 4-6 were bonded in absence of primer.

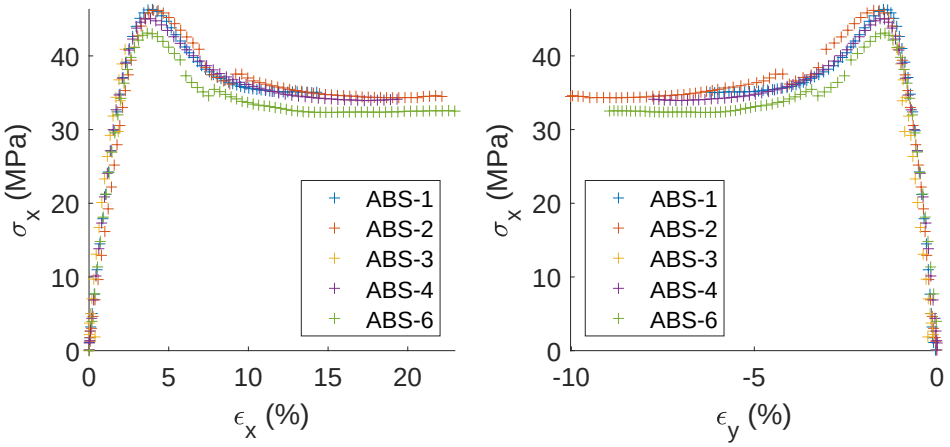

Figure 5.11: Stress-strain curves of the ABS-like 3D printed plastic under tensile load

Table 5.4: Summary of material properties of the composite FishBAC wind tunnel wing model. Note that ν_{23} is obtained from a common assumption for CFRP UD laminates, whereas $G_{23} = E_{22}/2(1+\nu_{23})$.

Material	E_{11}	E_{22}	G_{12}	G_{13}	G_{23}	ν_{12}	ν_{13}	ν_{23}
8552/IM7	169.50 GPa	8.58 GPa	5.03 GPa	5.03 GPa	2.96 GPa	0.28	0.28	0.45
ABS Plastic	2.01 GPa			0.73 GPa			0.38	
Silicone Sheet	1.219 MPa			0.44 MPa			0.39	

5.7 Actuation Characterisation

angleA total of four KST X10 High Voltage servo actuators are used to drive the tendon spooling pulleys in this FishBAC wind tunnel wing model. They are arranged in mirrored pairs to drive two tendons, each one mounted 415 mm in either direction from the centre of the wingspan. Each actuator measures 42 mm×42 mm×10 mm and is rated for a maximum torque of 1.059 N m at a maximum voltage of 8.4 V. Due to limited data provided by the manufacturer, a series of studies were performed to fully characterise these actuators. First, an angle test was performed to calibrate the input vs output rotation angles using a clinometer. Also, the torque available and torque-power relationship were studied, followed by a thermocouple study to assess the thermal properties of the actuators. Finally, since the Kevlar tendons were hand-stitched to the composite spine, the tendon-pulley system presents some slack due to difficulties controlling tendon length during the stitching process. This creates an initial angular range of spooling pulley rotation that does not create camber change, which is referred to in this thesis as the 'tendon deadband'. This tendon deadband was experimentally measured for each tendon using the Imetrum UVX Flexi Video Gauge camera system.

5.7.1 Angle Calibration

To calibrate the input rotation angles, the servo actuators were controlled using an Arduino-based servo control code that prescribes the rotation input angles. To determine the input-output angle relationship, a clinometer was attached to the actuator and an angle sweep was performed. Results show a linear trend between the input and measured angle output, with a maximum deviation of 6% from the expected value (Figure 5.12).

5.7.2 Torque-Power Relationship

Following the angle calibration test, a prescribed rotation torsional test was performed to study the relationship between torque available, voltage and power. A Tecquipment® SM1001 30 N m torsion testing machine was used to both prescribe the rotation angle and to measure the corresponding torque for a given actuator operating condition. Using two clamping plates, the servo actuator was clamped to a torque reaction cell in one end, whereas the other end was

connected to a rotating output head through the actuator's output arm, which is a plastic part that physically connects the spooling pulley to the actuator's output shaft. The rotating head consists of a hand wheel driving a rotating shaft through a worm gearbox, and has an angle sensor to track the rotation of the output shaft. Prescribed rotations were applied to the actuator by manually rotating the turning handle, and the corresponding torque generated by the actuator was measured as a reaction torque (Figure 5.13).

Once the actuator was fixed to the torque cell, the actuator control input was set to 0° rotation, and the rotating head was slowly turned while angle, torque, actuator voltage and actuator current drawn were recorded. Actuator power draw was then calculated from the voltage and current readings. Therefore, this test allows for the quantification of the relationship between power drawn and torque output for a range of different driving voltages, as shown in Figure 5.14. Note that the maximum torque available eventually saturates, after which increasing power does not increase torque generated. It can also be observed that, as driving voltage increases, the amount of torque at a given power value decreases. However, increasing voltage increases the maximum torque available.

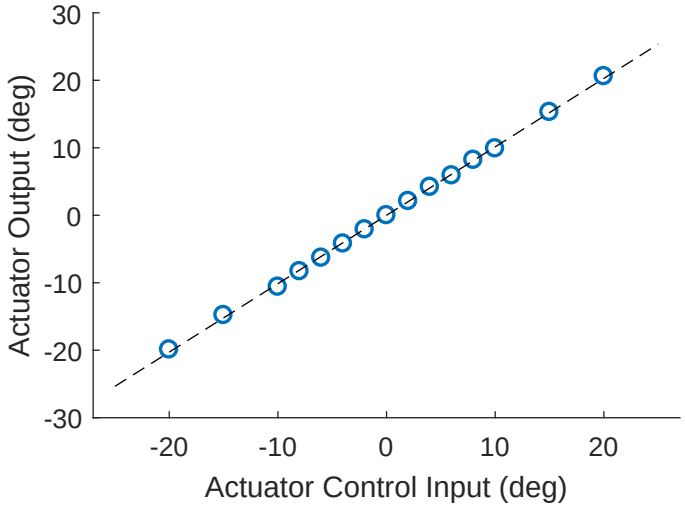

Figure 5.12: Actuator control input vs output angle. Output angles are measured using a clinometer. Dash line shows a linear trend, obtained via linear fit.

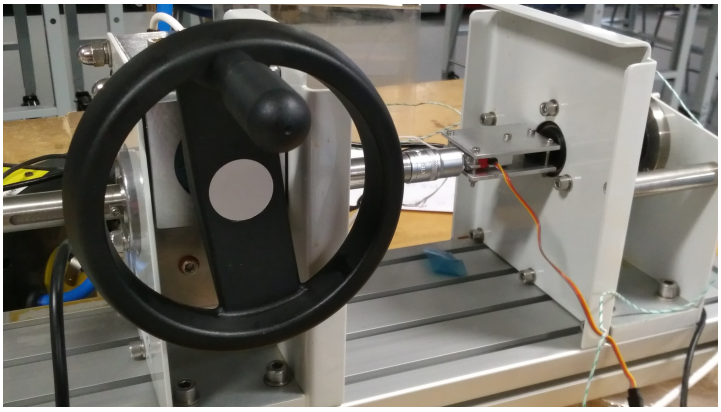

Figure 5.13: Torsion test rig used for actuator torque measurements

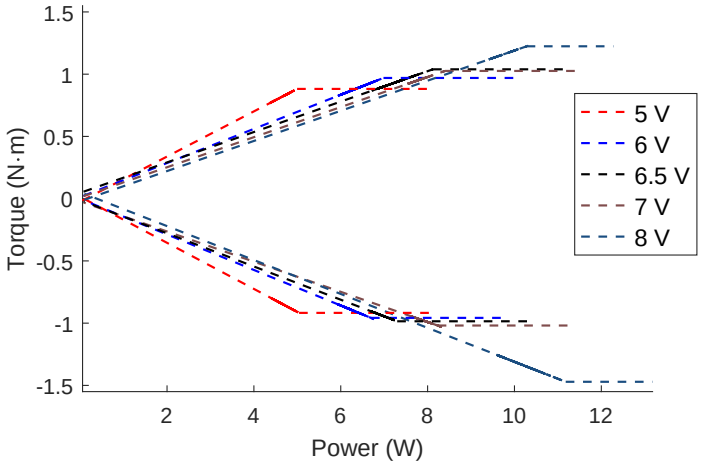

Figure 5.14: Power vs torque relationship as a function of voltage. Results obtained via linear fit.

5.7.3 Heating

One important aspect of electrical servo motors is self-heating under load, which can lead to damage if not properly monitored and controlled. Actuator temperature response over time and under load is therefore of interest in this study. According to the actuator's datasheet [118], the manufacturer's stated maximum operating temperature of the KST X10 actuators is 65 °C. Therefore, a set of thermocouples were used to monitor the increase in temperature, as a function of time and voltage. A Pico® TC-08 Thermocouple Data Logger was used to record the temperature of all four actuators when installed inside the wing. The thermocouples were attached to the metal frame of each actuator, and then the actuators were loaded to their maximum rotation angle and held at this position for several minutes. Also, two more temperature measurements were recorded: one on an actuator wire and one on the plastic surface of the wing. Results show a faster heating rate with increasing voltage, reaching temperatures as high as 80 °C at a voltage of 8 V (Figure 5.15). It can also be observed that the actuators driving the left-hand side tendon (i.e.

actuators 1 and 2) heat up faster than the ones in the right-hand side tendon. The cause of this is unknown, but it could be due to asymmetries and misalignment in the actuators' mounting. Finally, these results show that, for voltages between 6 V and 7 V, temperatures above 65 °C are achieved after the actuator runs for 8 to 10 minutes. Consequently, considering the results shown in Figure 5.14, the actuators will be run at a voltage between 6.5 V and 7 V. Even though the maximum temperature is exceeded at these voltages, it is important to consider that this test represents an extreme case: maximum actuator rotation angle with no wind speed. During the wind tunnel test, not all runs will be performed at this deflection, and the airflow will dissipate some heat. Nevertheless, the temperature will be monitored, at one of the actuators, during the wind tunnel test to ensure that no severe overheating occurs.

Additionally, one particular thermal/electrical property that needs to be investigated is whether torque degrades as temperature increases. To measure this, a thermocouple was added to the torque test setup described in Section 5.7.2. A prescribed rotation angle of 30° and a voltage of 6.5 V is set, and torque and temperature readings were recorded every 10 s. Results show that torque does decrease as temperature increases, showing a reduction of 15% after 10 min (Figure 5.16), with the shape of the output torque closely following the temperature curve, and approaching an asymptote. Consequently, actuation torque input measurements should be performed and monitored throughout the wind tunnel test as the applied torque magnitudes are expected to vary as a function of time.

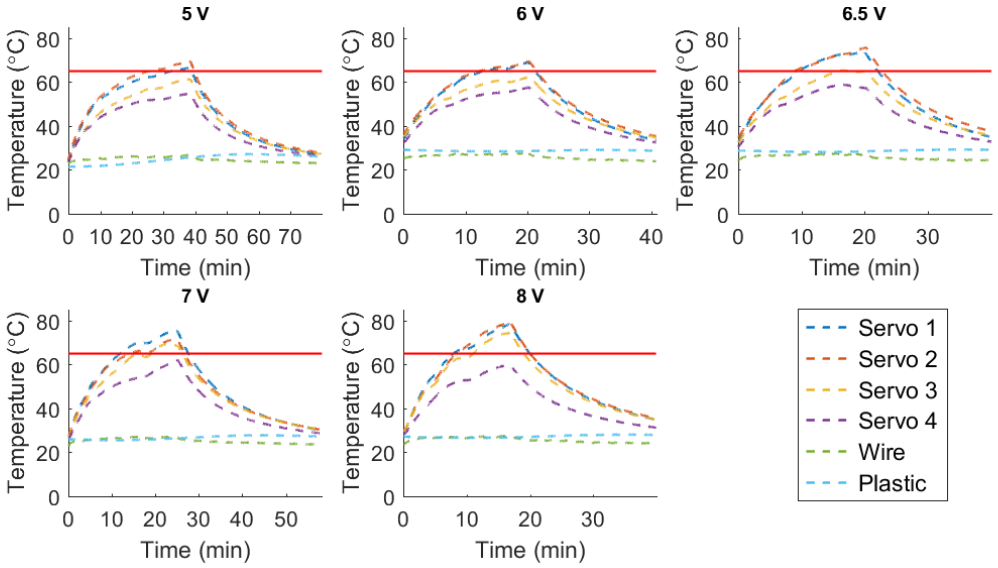

Figure 5.15: Thermocouple temperature recordings of actuators temperature at maximum actuation angle and as a function of voltage.

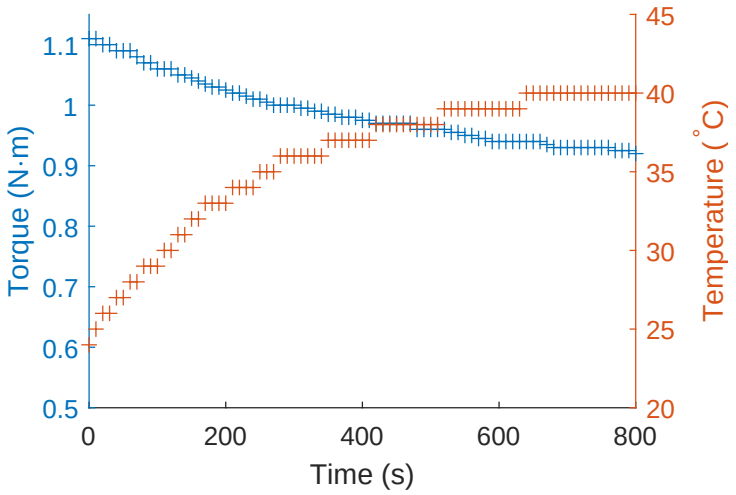

Figure 5.16: Torque and actuator temperature as a function of time. This measurement is performed at a fixed voltage of 6.5 V and actuation angle of 30°.

5.7.4 Tendon Rotation Deadband

Since the tendons are hand-stitched to the carbon spine, they may lose tension during the stitching process. As a consequence, the spooling pulley needs to rotate a certain number of degrees in each direction before it starts to apply tension on the tendon. These initial degrees of rotation are defined as the 'tendon deadband', and will vary between tendons and rotation direction. To determine these deadbands, a two-camera Imetrum video extensometer system was used to track the tip deflection at both spanwise edges of the FishBAC as a function of actuation angle. Results show a roughly bi-linear response behaviour in both tendons, where the tip deflection slope is very shallow at low angles, and then becomes steeper as the angle increases (Figure 5.17). This shows that the tendons are able to apply some small amount of driving torque even before they are fully tensioned, but there is also a clear kink in the response upon removal of the slack. The exception to this is the curve for negative rotation angles of the left tendon, which does not show any discernible deadband. These deadbands are compensated for adding angle offsets on the servo controller to the desired values, where the deadband angle for each case is found from the intersection of the two linear fits (dashed lines) in Figure 5.17.

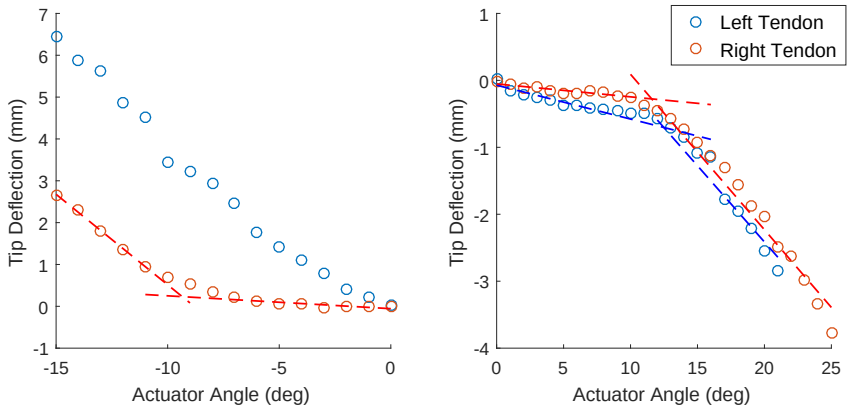

Figure 5.17: Tip displacement measurements at both spanwise FishBAC ends. Results are used to study the tendon rotation deadband in each tendon-pulley system. Dashed lines are obtained via bi-linear curve fitting.

5.8 Structural Characterisation: Displacements

A two-camera point tracking Imetrum video gauge system was used to measure the static transverse displacement of the FishBAC under actuation along the trailing edge and on one of the chordwise ends. Total voltage and current measurements were recorded from a benchtop power supply used to power the actuators. A total of 13 points chordwise and 41 points spanwise were tracked. Three different actuation scenarios were evaluated: uniform loading (i.e. similar tip displacements in both spanwise edges), single actuation input (only one actuator applying torque) and asymmetric actuation loading (different values for each actuator, average input not zero).

5.8.1 Uniform Loading

The objective of the uniform loading case is to obtain similar displacements in both spanwise edges. Since there are differences between each actuation-tendon setup—and potentially structural and material imperfections—the pulley angle inputs are adjusted until similar displacements are obtained. Figure 5.18 shows both chordwise and spanwise deflections under six different actuation inputs. The chordwise edge in Figure 5.18 corresponds to the spanwise location $y = 1000\,\text{mm}$ (right end of the wing). There are a few dropped data points in the spanwise plot due to point tracking issues caused by lighting and reflection, but the overall shapes are well captured. Results show uniform tip deflections at each spanwise end, with a significant variation along the span due to elastic washout. The difference between the deflection at each end (i.e. near the actuation points) and the midspan is between 30% and 43% for all actuation cases. This particular FishBAC was not designed with spanwise elastic washout in mind, and the use of plastic stringers significantly hampers spanwise stiffness.

Incorporation of higher stiffness materials (e.g. composite) into the stringers would be expected to significantly decrease such washout, and therefore should be considered in future designs.

5.8.2 Offset Differential Loading

The objective of this case is to determine the maximum achievable variation in transverse deflection along the span, when actuation inputs differ in magnitude and direction. The first case to analyse is when only the right end of the FishBAC is actuated, whereas the other end is kept at zero actuation angle. Figure 5.19 shows this case, and it can be observed that the transverse displacement can vary as much as 13 mm, which represents a normalised differential displacement of $\Delta(z/c) \approx \pm 4.5\%$ in a 1 m span.

A second aspect to investigate is whether different shapes can be obtained by applying a constant actuation input on the left-end of the wing—instead of remaining zero. Figure 5.20 shows three different scenarios where the left-side actuators are given different inputs, while the right-side actuators are kept at a fixed angle. It can be observed that similar tip deflections are achieved; however, the 'average displacement' moves with the different right-side actuation inputs, achieving different spanwise shapes. In each case, spanwise variations—per metre span—of $\Delta(z/c) \approx \pm 4.5\%$, $\Delta(z/c) \approx \pm 5\%$ and $\Delta(z/c) \approx \pm 4\%$ can be achieved, respectively. This ability to achieve spanwise variations in camber deflection can be later exploited for spanwise lift control and induced drag minimisation.

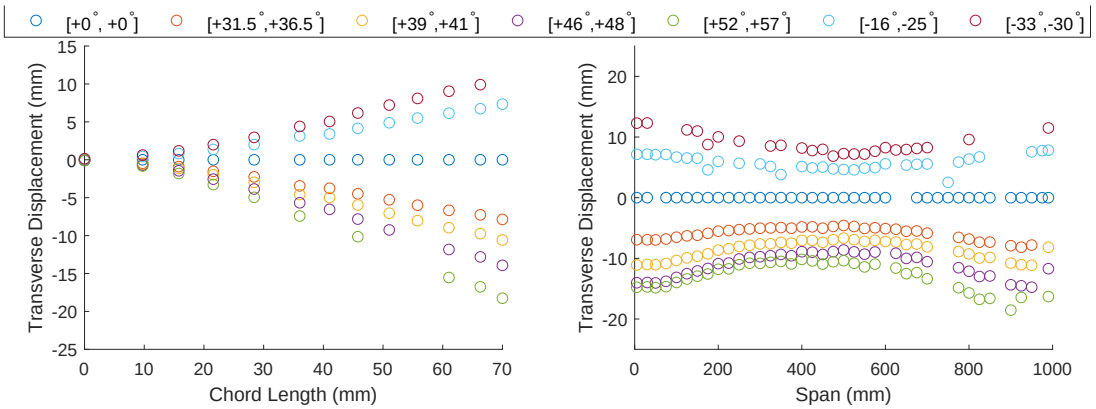

Figure 5.18: Chordwise (left) and spanwise(right) transverse displacement measurements under symmetric actuation loading. Pulley angles are displayed as [left,right].

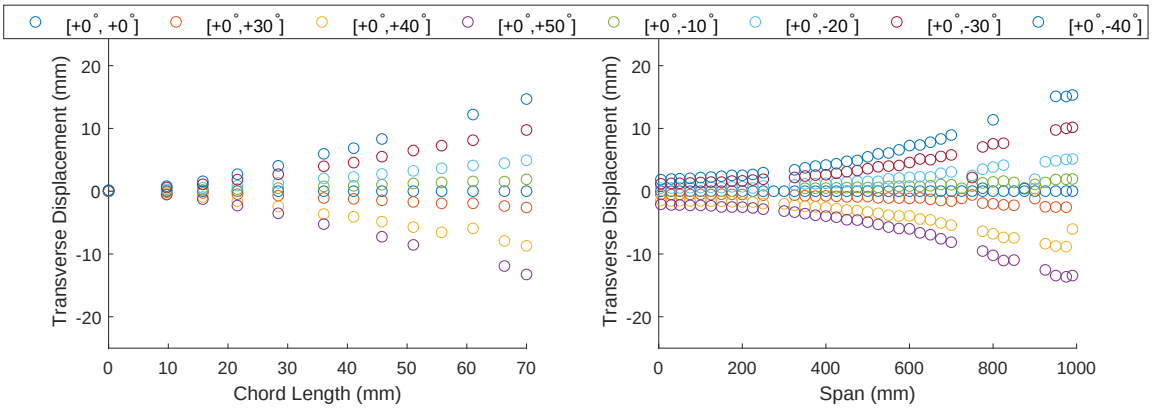

Figure 5.19: Chordwise (left) and spanwise(right) transverse displacement measurements under actuation of the right hand side of the wing only. Pulley angles are displayed as [left,right].

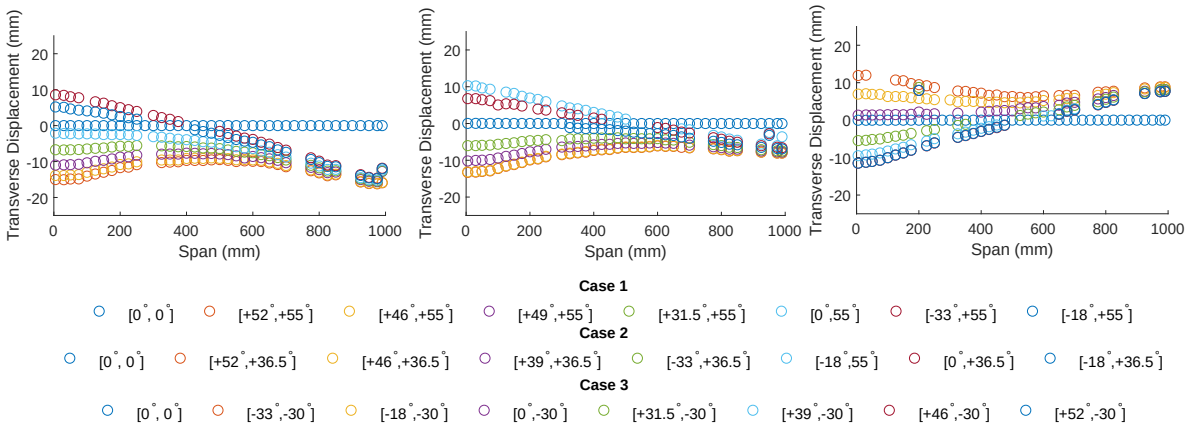

Figure 5.20: Spanwise transverse displacement measurements under three different offset asymmetric actuation loading cases (1 to 3 going from left to right). Pulley angles are displayed as [left,right].

5.9 Conclusions

This chapter introduces the design, manufacture and characterisation of a composite FishBAC morphing wing. A two-dimensional discontinuous Kirchhoff-Love plate model—presented in Chapter 3—has been used to design and analyse the static behaviour of a composite FishBAC structure. The composite FishBAC spine has been sized based on actuation energy requirements needed to obtain a target tip deflection of 10% chord, under representative aerodynamic loads obtained using an Euler-Bernoulli/XFOIL-based FSI analysis of the FishBAC. Based on these results, it was decided that a $[90/0/90]_T$ carbon spine, with a total thickness of 0.375 mm will be used as the main load-bearing member of the FishBAC. The design process was completed by developing a detailed CAD model of the composite FishBAC wind tunnel wing model.

The composite FishBAC prototype was then manufactured using a combination of materials—carbon fibre prepreg, 3D printed plastic, aluminium machined parts, silicone sheets and Kevlar fabric tape—and manufacturing techniques, ranging from prepreg hand layup to 3D printing and machining. A comprehensive structural, material and actuator characterisation was performed, and the chordwise and spanwise displacements under several actuation load cases were tracked using a video gauge point tracking system. Results show that a maximum spanwise variation in transverse displacement of 13.5 mm can be obtained when the FishBAC is loaded asymmetrically (i.e. actuation inputs of opposite directions). This corresponds to a variation of $\Delta(z/c) \approx \pm 5\%$ per metre span, which can later be exploited to control spanwise lift distribution and reduce induced drag. Finally, this composite FishBAC prototype is used in wind tunnel tests, where structural and aerodynamic measurements were performed. These wind tunnel tests results are presented in Chapter 6.

The composite FishBAC wind tunnel wing model developed in this chapter represents a significant step forward in the development of composite FishBAC wings for fixed-wing applications. This first of its kind demonstrator is useful not only for demonstrating the possibility of adapting conventional manufacturing techniques to produce composite morphing devices, but also for experimental validation of the structural models presented in Chapters 3 and 4. Also, this wing was used for wind tunnel testing, as presented in Chapter 6. These wind tunnel results are crucial to further understand the benefits that camber morphing, and more specifically the FishBAC, can bring to fixed-wing aircraft.

Chapter 6

Wind Tunnel Testing of a Composite FishBAC Morphing Wing

This chapter introduces the wind tunnel test of the composite FishBAC wing model that was introduced in Chapter 5. The FishBAC wing model was tested on a quasi-2D configuration, and results were directly compared to a non-morphing (rigid) NACA 23012 wing and one equipped with a traditional hinged trailing edge flap. Besides measuring aerodynamic forces, the wind tunnel test also included FSI optical measurements via Particle Image Velocimetry (fluid) and stereo videogauge point tracking (structure). These wind tunnel tests results show that the FishBAC is able to achieve a large degree of lift control authority while developing significantly higher lift-to-drag ratios when compared to both rigid and flapped wings.

6.1 Introduction

Throughout the literature, several recent camber morphing concepts have been introduced as aerodynamically efficient alternative to hinged flaps. These concepts exploit recent developments in smart materials and lightweight composite structures, as summarised in Chapter 2. However, it is also observed in the literature that most of the research efforts have focused on structural design and analysis. Aerodynamic comparisons between these devices and traditional hinged flaps——specifically wind tunnel data—are scarce. Early studies in the late 1980s and early 1990s introduced preliminary experimental results that show improvements of aerodynamic efficiency of up to 9% when variable camber morphing is used. However, these results are not related to specific morphing concepts [126–128]. Moreover, another preliminary study based on wind tunnel data even predicts a 3 to 6 per cent reduction in fuel consumption, for a long/medium range civilian aircraft [10].

Daynes and Weaver [129] carried out a wind tunnel test of a compliance-based trailing edge device, where an increase of lift coefficient of $\Delta C_L \approx 0.5$ can be observed when actuating the morphing device between $\pm 10^\circ$ deflection. No flap comparison was performed in this study. Bilgen et al. [130] conducted a 2D wind tunnel test comparison of a flapped aerofoil versus a Macro-Fibre-Composite (MFC) actuated variable camber wing and results showed higher lift-to-drag ratios of 10%-50% for the camber morphing wing.

However, it is important to highlight that this experiment was performed at low Reynolds numbers below $Re < 120,000$ and that the achieved lift-to-drag ratios are lower than $L/D < 12$. Moreover, large voltage inputs (up to 1800 V) are required to actuate the morphing mechanism and, therefore, it is perhaps infeasible to implement this morphing device on large-scale applications. Ai et al. [131] also presented a wind tunnel comparison of several camber morphing cases versus a hinged flap. Although they showed improvements in aerodynamic efficiency, these are limited to low angles of attack, having an L/D improvement of about 9% at zero-degree angle of attack. Additionally, Yokozeki et al. [132] presented wind tunnel test results for a corrugated camber morphing device. These results do not show significant improvement in aerodynamic efficiency when compared to a flap. However, it is important to note that this particular morphing device presents a smooth skin on the top surface only, leaving the core corrugations exposed on the bottom surface, which likely added drag to the camber morphing device.

As described in Chapter 2.5, the subject of this study—the FishBAC—has already shown promising aerodynamic benefits. A preliminary wind tunnel test of this device [25] showed a potential improvement in lift-to-drag ratio between 20 and 25 per cent, compared to a 25%-chord trailing edge hinged flap. The FishBAC also showed a lift control authority of $\Delta C_L \approx 0.72$. However, the authors discussed the presence of 3D effects due to the nature of their wind tunnel setup.

The FishBAC concept has evolved since that preliminary wind tunnel test: the morphing section is now localised, approximately between $0.75c$ and $0.9c$, instead of between $0.35c$ and $0.85c$ and actuation loads are applied at multiple points along the span as described in Chapter 5. Therefore, new wind tunnel tests are needed to more robustly and thoroughly assess the aerodynamic properties of the FishBAC wing developed in this thesis, in a quasi-2D wind tunnel test scenario.

The objective of this wind tunnel experiment is to reassess the benefits of the FishBAC, experimentally, using an improved design of this morphing device installed into a longer span wing and tested in closed return and closed test section wind tunnel for improved flow quality. Also, the instrumentation used to quantify the performance was significantly improved. Force balances and a pressure-based wake rake were used for more reliable aerodynamic forces measurements and optical measurements of structural and fluid response were performed using Particle Image Velocimetry (PIV) and a stereo videogauge point-tracking system (VG). These PIV measurements provide direct physical insight into the aerodynamic performance of the FishBAC and help to address the complete lack of flow visualisation studies of camber morphing devices in the literature. These two types of measurements not only enhance the understanding of the benefits of camber morphing by studying the changes in wake patterns and comparing them to the wake of a hinged flap, but also provide insight into the coupled aeroelastic response of the morphing system that is useful for design improvements and for future validation of FSI analysis.

This chapter is structured as follows: first, an introduction of the test methodology and test cases are presented, followed by a summary of the wind tunnel data corrections, and presentation of the aerodynamic coefficients and optical measurements (PIV and VG). Finally, the conclusions summarise the major findings of this experimental study.

6.2 Methodology

This section introduces the wind tunnel testing methodology, including details of the tunnel itself, the equipment and instrumentation used, and the configurations tested.

6.2.1 Wind Tunnel & Equipment

The Swansea University closed return low-speed wind tunnel with a 1.5 m wide×1 m tall closed test section was used for this experiment (Figure 6.1). This tunnel has a maximum freestream velocity of 50 $\mathrm{m\,s^{-1}}$, and flow characterisation studies have measured turbulence intensity, velocity uniformity and flow angularity values of 0.175%, 0.04% and ±0.1°, respectively. A turntable with a movable range of ±90° and accuracy of ±0.05° controls the angle of attack of the wing. Furthermore, the wing was mounted vertically in the test section and was attached to two strain-gauge based AMTI MC12-1000 six-axis force balances, one on each end. Equipped with a temperature control system, the tunnel target temperature of 20 °C is maintained within ±2°. A closed-loop feedback system controls wind speed using real-time velocity calculations based on a precision differential pressure sensor with a range of ±2500 Pa [133], measuring the pressure difference at the contraction section upstream of the test section.

6.2.1.1 Pressure Wake Rake

A pressure-based wake rake for wake survey (Figure 6.2) has recently been added to the Swansea Low-Speed Wind Tunnel. The rake consists of 60 total pressure and 3 static pressure tubes mounted 4.5 chords downstream of the wing trailing edge, to allow for pressure recovery in the wake. The total and static pressure tubes are aligned in the thicknesswise direction (which is horizontal with a vertical wing mounting) with a spanwise offset between the total and static pressure tubes to avoid interference. A *Scanivalve* MPS4264 miniature pressure scanner is connected to the rake tubes. The total pressure tubes have variable thicknesswise spacing of between 3.9 mm (at centre) and 15.9 mm (toward the ends), covering a total thicknesswise width of 500 mm. This variable spacing provides more pressure readings in the wake region, improving the accuracy of drag measurement.

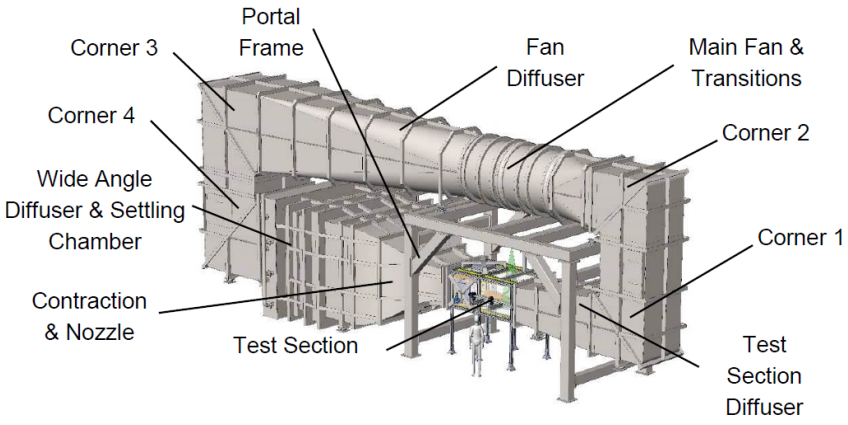

Figure 6.1: Swansea University's Low-Speed Wind Tunnel

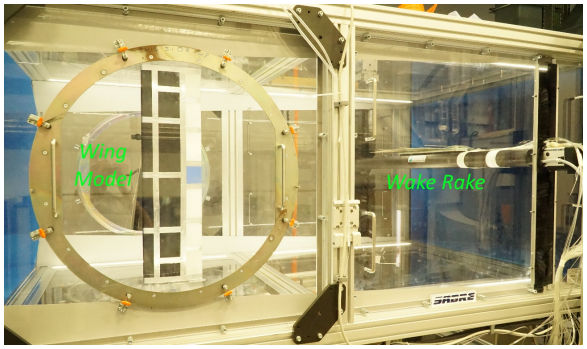

Figure 6.2: Wind tunnel test section with pressure-based wake survey system at Swansea University's Low Speed Wind Tunnel.

6.2.1.2 Image Measurements

This section introduces the equipment used for both PIV and displacement measurements via stereo point tracking.

1. **Particle Image Velocimetry**

   A *LaVision*® PIV system was used for flow field velocity measurements, controlled with the DaVis 10 software platform. An sCMOS 5.5 –megapixel double shutter camera was located at the trailing edge of the wing and was used to measure the wake of both FishBAC and flap in a quasi-static flow condition. This camera can take two images within 120 ns, making them suitable for PIV applications. Also, the camera has an exposure time range between 15 µs and 100 ms and a frame rate of 50 fps. A particle generator was used to generate seeding particles with an average diameter of 1 µm. Lastly, a dual cavity, double pulse 200 mJ Nd:YAG green laser with a wavelength of 532 nm was used to illuminate the measuring plane. Figure 6.3 shows a schematic of the PIV setup.

2. **Stereo Point Tracking System**

   In terms of structural displacement measurements, an *Imetrum*® 3D Precision Displacement Tracker was used to track out-of-plane displacements. The system consists of two 5-megapixel cameras in a stereo configuration, recording at a rate of 117 Hz. These two cameras are mounted to a 3D measurement head ICA-3D-0500-03, which is a pre-calibrated frame where both cameras are installed at a fixed angle and distance from each other. Since the cameras' focus cannot be altered from their default configuration and the 3D frame fixes the position and angles between the cameras, no further calibration is required. For the selected 3D measurement head, a measurement area of 600 mm x 600 mm, with a 14 µm accuracy can be achieved [122]. A series of 5 mm diameter bullseye stickers were used as target points. Figure 6.3 shows a schematic of the videogauge setup.

   Additionally, current was measured at each one of the four actuators to then calculate torque input on the FishBAC structure. These current measurements were performed by using four (one per actuator) LEM® 6 A CASR 6-NP Hall Effect current sensors. These sensors are the same as those used in Chapter 4.5.3. Finally, voltage and current measurements were recorded using a National Instruments® USB-6211 data acquisition card.

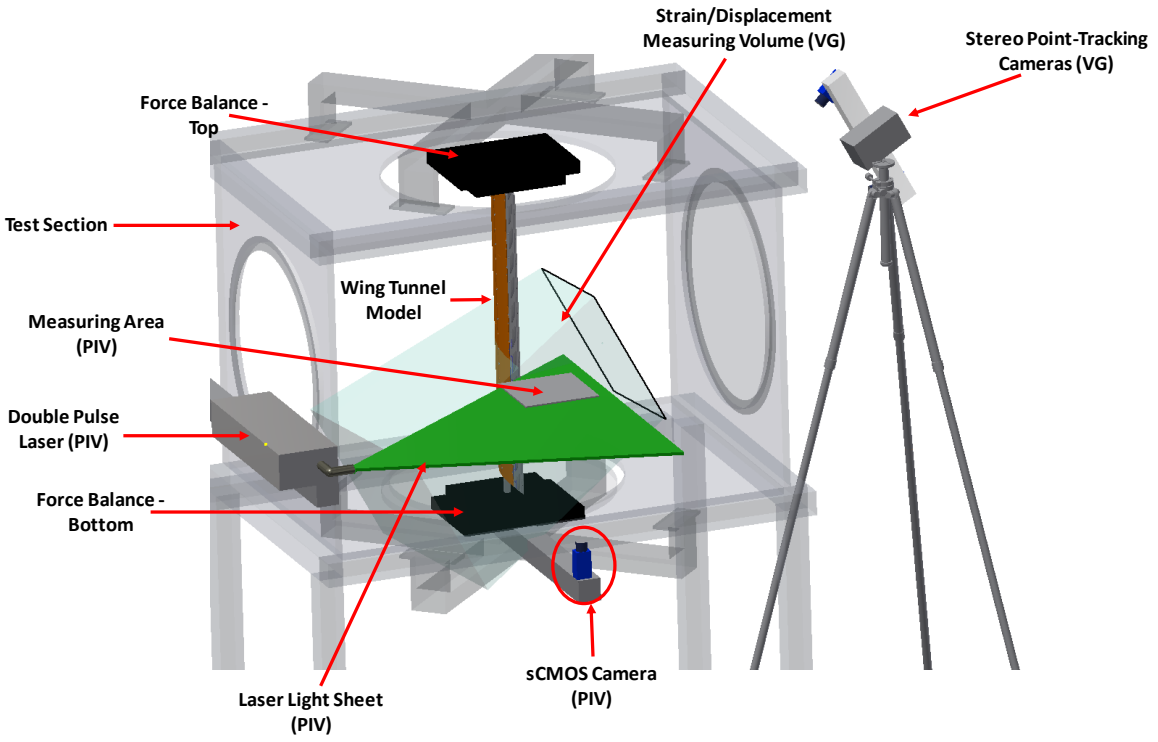

Figure 6.3: Schematic of the wind tunnel test setup, including wind tunnel wing model, force balances and PIV and VG equipment.

6.2.2 Wind Tunnel Wing Model

A two-dimensional wind tunnel wing model of a NACA 23012 aerofoil was designed and manufactured for this test. The wing spans the 1-metre height of the test section (Figure 6.2) and has a chord length of 270 mm. As described in more detail in Chapter 5, the wing has two main parts: a front rigid section that starts at the leading edge and ends at 75% of the chord, and a trailing edge section. The front rigid section is composed of 3D printed plastic leading edge and centre sections that are bolted to an aluminium (6082T alloy) box spar located at the quarter chord. Three interchangeable, cartridge-like, trailing edge sections were created to allow testing of the baseline NACA 23012, a 25% trailing edge flap version, and the 25% trailing edge composite FishBAC (see Chapter 5). The bottom of the wing spar is clamped to the bottom force balance and rotates with the turntable. Since the top force balance does not rotate, the top of the spar connects to the upper force balance via a spherical bearing to allow for angle of attack rotation and minimises the bending moments reacted into the upper balance. Details of the construction of the three configurations are as follows:

1. Rigid NACA 23012 aerofoil

   A 3D printed rigid NACA 23012 trailing edge section was tested to obtain a baseline data set, used to acquire lift and drag properties of this aerofoil section when no changes of camber occur. Results from the baseline aerofoil were used to validate the tunnel instrumentation, before being used as a reference against which the hinged flap and FishBAC were later compared.

2. Trailing Edge Flap

   A 3D printed hinged flap of the same chord dimension of the FishBAC was tested to directly compare the two approaches. The flap is mounted to a steel shaft and actuated by two KST X10 High Voltage servos that are connected to the flap by a system of two external control horns and linkage bars. Each control horn converts torque and rotation of the servo motor into force and translation of the flap linkage, which is then converted again into torque and rotation on the flap. The hinged flap is a 'plain flap', with no aerodynamic overhang (which is sometimes used to reduce hinge moments at the expense of added drag) and with the minimal realisable gap between the flap and the rigid wing section, on the order of 2 mm. The flap has an unloaded deflection range of $\pm 30°$.

3. Camber Morphing: FishBAC

   A composite-spine FishBAC device was designed and manufactured for this wind tunnel test. Details on the design, manufacture and structural characterisation of this composite morphing trailing edge device were presented in Chapter 5.

6.2.3 Numerical Comparison: XFOIL

To help ensure the wind tunnel measurements were reliable, results for the baseline NACA 23012 wing were compared against values from the literature and against two-dimensional numerical predictions of the aerodynamic performance from XFOIL—a widely used panel method software [134]. XFOIL is based on the principle of potential flow theory, where the flow field around an aerofoil is constructed by superimposing the freestream flow, a vortex sheet and source sheet around the aerofoil surface. The aerofoil surface is discretised into a series of N flat panels, each one with unknown and uniform vortex and source strengths γ_N and σ_N, respectively. These unknown vortex and source strengths can then be found by setting up a system of equations using potential flow theory, and by applying the Kutta Condition as a boundary condition. This condition states that the vortex strength at a sharp trailing edge must be zero, such that

$$\gamma(\mathrm{TE}) = 0\,. \tag{6.1}$$

XFOIL corrects for viscosity by implementing a viscous boundary layer solver that models skin friction drag and flow separation based on the wall transpiration concept [134, 135].

As a freely available code, XFOIL has been widely used for two-dimensional aerofoil analysis under low freestream speeds and Reynolds number condition [134]. In terms of inputs, XFOIL requires the non-dimensional aerofoil coordinates, the angle of attack, Mach number and Reynolds number to be provided. Reynolds and Mach number were set to match the test conditions. Also, to roughly match the turbulence intensity of the Swansea University Wind Tunnel, a value of N_{crit} (turbulence level factor) equal to 5 was used for all XFOIL estimates.

6.3 Test Cases

All experiments presented in this chapter were performed at a freestream velocity of 30 m/s and a temperature of 20 °C, which corresponds to a Reynolds number of $Re \approx 543{,}000$. The angle of attack was varied from $\alpha = -5^\circ$ to $\alpha = +14^\circ$, in increments of $\alpha = 1^\circ$. Force balance data was recorded for 30 s for each test condition at a sampling rate of 300 Hz, and then time-averaged to give quasi-steady results. The same data recording process was used for wake survey, which was synchronised with balance data, using a sampling time of 20 s at a rate of 10 Hz. Two types of wake rake measurements were performed: *(i)* actuation and angle of attack sweeps with the wake rake at a fixed spanwise location, and *(ii)* spanwise wake rake location sweeps at a fixed angle of attack and actuation input. These two types of measurements allow drag to be quantified as a function of both angle of attack and spanwise location. A summary of test cases can be found in Table 6.1.

Table 6.1: Wind tunnel test configurations and test cases

Configuration	Actuation Input Angle	PIV	Videogauge
Baseline	N/A	No	No
Flap	$\delta = [-20°, +30°]$, $\Delta\delta = +10°$	Yes	No
FishBAC	$\delta = [+0°, +40°]$, $\Delta\delta = +10°$	Yes	Yes

6.4 Data Processing

The following section outlines the data analysis process, including equations used to process balance and wake rake data, the wind tunnel corrections for three-dimensional effects and post-processing parameters of both the PIV and stereo VG point tracking systems.

6.4.1 Force Balance Data

Aerodynamic forces and moments were measured by the two force balances, and these two measurements are then combined to calculate the total forces and moments. Each balance measures in its own respective coordinate frame. Since the bottom balance rotates with the turntable while the top balance is fixed, the forces measured by the bottom balance need to be converted to the global coordinate frame. Hence, the total lift and drag forces are calculated by

$$L = F_{y_1} cos(\alpha_u) - F_{x_1} cos(\alpha_u) - F_{y_2} \quad \text{and} \quad D = F_{x_1} cos(\alpha_u) + F_{y_1} cos(\alpha_u) + F_{x_2} \ , \tag{6.2}$$

where F_{x_1} and F_{y_1} correspond to the bottom balance and F_{x_2} and F_{y_2} correspond to the top balance. Furthermore, zero wind speed tare measurements were recorded before and after each angle of attack sweep. These were later subtracted from the force balance data set to account for any offsets or time drift in the measured values. Once the total lift and drag forces were calculated, the non-dimensional lift and drag coefficients were estimated by normalising the total forces by the dynamic pressure and the wing planform area, as described by the expressions

$$C_{L_u} = \frac{2L}{\rho V_\infty^2 S} \quad \text{and} \quad C_{D_u} = \frac{2D}{\rho V_\infty^2 S} \ . \tag{6.3}$$

Since accurate two-dimensional drag measurements from balance setups such as the one used can be difficult, due in part to the large differences between lift and drag forces, the range of the load cells used, and the presence of end gaps and wall effects, wake survey measurements were used to give more accurate two-dimensional measurements of drag. These drag estimates are based on wake momentum deficit [136].

6.4.2 Wake Rake Data

Drag can be measured by comparing the momentum of the air in the freestream against that measured in the flow behind the model. This method assumes that the wind tunnel walls are parallel and with negligible shear stresses. This theory is based on the assumption that, as the flow passes over a wind tunnel model, it suffers a loss of momentum that is equal to the profile drag of the body [136], such that

$$D = \dot{m}\Delta V = \iint (\rho V)(V_B - V_0)da \ , \tag{6.4}$$

where V_0 is the freestream velocity, V_B is the final flow speed in the wake and da is the differential area perpendicular to the aerofoil at the wake. If normalised by the dynamic pressure, the profile drag coefficient can be obtained using the expression

$$C_{d0} = 2\iint \left(\frac{V}{V_0} - \frac{V^2}{V_0^2}\right)\frac{da}{S} \ . \tag{6.5}$$

Combined with Bernoulli's equation, Equation 6.5 can be derived in terms of total and static pressures, as expressed by

$$C_{d0} = 2\int \left(\sqrt{\frac{H_p - p}{H_{p_0} - p_0}} - \frac{H_p - p}{H_{p_0} - p_0}\right)\frac{dy}{c} = 2\int \left(\sqrt{\frac{q}{q_0}} - \frac{q}{q_0}\right)\frac{dy}{c} = \int F_{wd}dy \ , \tag{6.6}$$

where H_p, p and q are the total, static and dynamic pressures at the wake, respectively, and H_{p_0}, p_o and q_0 are the same pressure quantities in the freestream. F_{wd} is defined as the function wake drag in this chapter. Figure 6.4 shows a schematic of the wake deficit of a wing inside a wind tunnel. Note that drag calculations using wake pressure measurements are only strictly valid for attached flow, and therefore, measurements after stall angle are ignored.

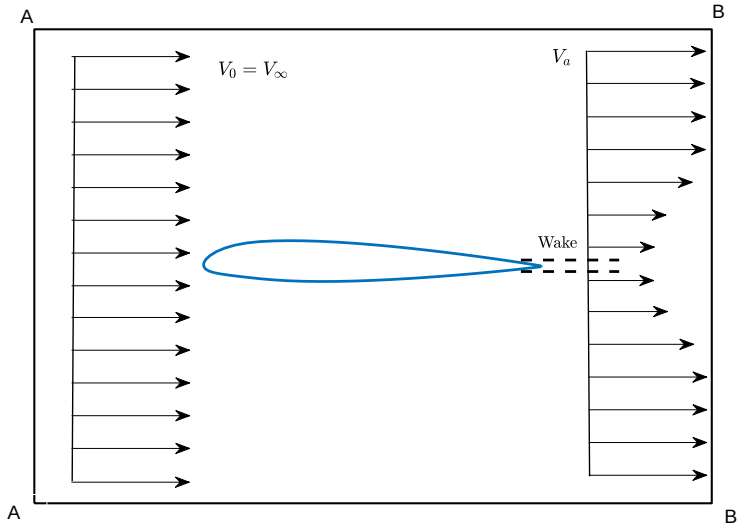

Figure 6.4: Wind tunnel model's downstream wake

6.4.3 Wind Tunnel Corrections

To correct for three-dimensional effects, wind tunnel corrections are applied to account for solid and wake blockage and streamline curvature. The correction factors implemented in this study are the standard ones given by Barlow et al. [136]. Solid blockage occurs due to the reduction of the area through which the airflow caused by the presence of the wind tunnel model and the constraint of the tunnel walls. Thus, the area reduction results in a flow velocity increase around the model. This correction factor is a constant value that does not change throughout the experiment and it is defined as

$$\epsilon_{\text{sb}} = \frac{K_1 V_{\text{model}}}{C^{1.5}} \ , \tag{6.7}$$

where V_{model} corresponds to 70% of the wing tunnel model volume, K_1 is approximately equal to 0.52 for wind tunnel models that span the tunnel's height and C is equal to the test section's cross-sectional area [136]. The second correction factor is for wake blockage, which occurs due to the airflow being restricted by the presence of the wake behind the model. This correction factor varies during the experiment as it depends on the size of the wake, which correlates to the drag coefficient. This correction factor is defined as

$$\epsilon_{\text{wb}} = \frac{c/h}{2} C_{d_u} \ , \tag{6.8}$$

where h corresponds to the wind tunnel height and c correspond to the wing's chord length. Moreover, the existence of restrictions on streamline curvature near the wind tunnel walls is corrected using a geometric non-dimensional factor that relates the size of the wind tunnel wing model and the test section. This correction factor is defined as

$$\sigma = \frac{\pi^2}{48} \left(\frac{c}{h} \right)^2 \ . \tag{6.9}$$

These three correction factors are then used to correct the lift and drag coefficients, as well as the angle of attack and Reynolds number. These corrected expressions are defined as:

$$C_l = C_{l_u} [1 - \sigma - 2(\epsilon_{\text{sb}} + \epsilon_{wb})] \tag{6.10a}$$

$$C_d = C_{d_u} (1 - 3\epsilon_{\text{sb}} - 2\epsilon_{\text{wb}}) \tag{6.10b}$$

$$\alpha = \alpha_u + \frac{57.3}{2\pi} (C_{l_u} + 4C_{m_u}) \tag{6.10c}$$

$$Re = Re_u [1 + (\epsilon_{\text{sb}} + \epsilon_{\text{wb}})] \ . \tag{6.10d}$$

6.4.4 Particle Image Velocimetry

Two-dimensional PIV measurements were performed to measure the flow velocity in a portion of the near field wake of both FishBAC and hinged flap configurations. A 200 mm × 200 mm calibration plate was used to define the measuring area, which was placed at a spanwise location of $0.467b$. This location is well outside the wind tunnel wall-effect regions, hence, the wake measurements closely represent two-dimensional flow. All PIV measurements were performed at a fixed angle of attack equal to $\alpha = 5°$ to ensure attached flow. To compare the impact of camber deflection on wake size and velocity for both the morphing and hinged flap devices, a total of four FishBAC and flap deflections were sampled.

For each configuration, a total of 1000 images were taken at a frequency of 10 Hz, with a differential time of dt =13.5 µs between the two laser pulses. To filter noise, a minimum image intensity was calculated for each data set, and then subtracted from all images in that set. Post-processing of images was performed using LaVision® DaVis 10 software. A seeding particle size of 1 µm was used throughout the experiment. An interrogation area of 48 pixels was chosen (equivalent to 3.6 mm in both directions), as suggested by DaVis 10 for a flow velocity of 30 m/s. Under this configuration, each pixel has dimensions of 92.6 µm × 78.1 µm—i.e. each seeding particle is approximately two orders of magnitude smaller than each pixel. Finally, the time-average of each velocity field data set was calculated, resulting in a single time-average image per configuration.

6.4.5 Videogauge Point Tracking System

To study the FishBAC's deformation under aerodynamic loads, displacements were measured at a number of points along the FishBAC's chord and span. As mentioned in Section 6.2.1.2, 5 mm bullseye stickers were used as tracking points. These tracking points were placed every 50 mm along the spanwise free edge, as well as every 10 mm along the chord at the following locations: three-quarter-span and at the centre of the tendon. The three-dimensional position and displacements of each point were directly obtained from the point tracking software, and time averages are calculated at each point. The presence of outliers was determined based on shape continuity, and were later removed from each data set.

Furthermore, to later validate FSI models (which is not part of this dissertation), it is necessary to correlate the measured displacements to the actuation input. One way of doing this is to use the actuator rotation angle as the input measurement; however, this quantity does not provide any physical information regarding torque input nor is a good measure of actuation energy requirement. Therefore, as described in Chapter 4.5.3, it is more appropriate to estimate the torque input of each actuator and one way of obtaining these torque values is to measure the current draw of each actuator. These current values can then be used to estimate torque by assuming a linear relationship between torque and current as described in Equation 4.14. A detailed explanation on how this current-torque relationship is implemented is described in

Chapter 4.5.3, whereas torque constant estimates—for a constant voltage of 6 V, held throughout the wind tunnel test—were obtained from the torque-power study presented in Figure 5.14 on Chapter 5.7.2.

6.5 Results

The following section introduces the wind tunnel test results. These include a comparison between the aerodynamic behaviour of FishBAC versus hinged flap using both balance data and pressure-based wake survey measurements. Additionally, PIV and stereo VG results are also introduced in this section.

6.5.1 Aerodynamic Forces

This subsection directly compares the 3D printed NACA 23012 rigid aerofoil configuration with previous experimental data from the literature and 2D XFOIL predictions. Figure 6.5 shows both experimental and predicted lift and drag curves. The experimental data were obtained from Ashenden et al. (1996) [137] and Pouryoussefi et al. (2016) [138], which both tested at similar Reynolds numbers—$Re = 550000$ and $Re = 600000$, respectively. However, unlike in the wind tunnel test presented in this chapter, these two experiments used pressure taps on the wing surface to measure both lift and drag.

Figure 6.5 shows that the lift curve measured in this work is similar to Pouryoussefi et al.'s results [138], whereas Ashenden et al. [137] has similar behaviour to XFOIL. This reduction in measured lift performance could be due to the different measuring techniques: Ashenden et al. measured local section lift coefficient using pressure taps, whereas the results presented in this chapter correspond to the average total lift as measured by the force balances. Furthermore, Leishman (1990) [139] and Jacobs and Sherman (1939) [140] showed NACA 23012 experimental maximum lift coefficients for similar Reynolds numbers. Both results show a maximum lift coefficient of $C_{L_{\max}} \approx 1.25$, which is closer to the $C_{L_{\max}} \approx 1.14$ obtained in this experiment and suggests that XFOIL may over-predict maximum lift coefficient. Lastly, it is important to point out that results suggest the existence of an angle of attack misalignment on this wind tunnel test setup, as the lift coefficient at $\alpha = 0^\circ$ is close to zero, which does not correspond to a cambered aerofoil (Figure 6.5). This misalignment was likely introduced during the wing mounting process, where the wing model was mechanically clamped to the bottom force balance using brackets and bolts. Any slight misalignment of the mounting brackets, when tightening the bolts, could result in a small wing angle rotation. Thus, the force balance wind axis ($x-$axis) would no longer be aligned with the wing chord.

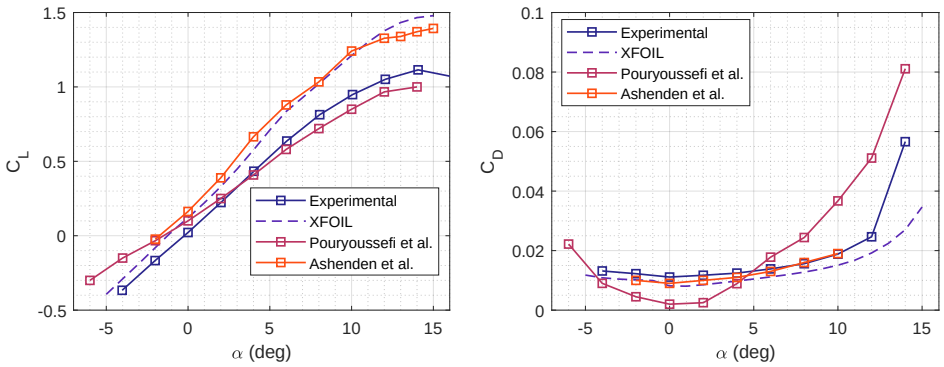

Figure 6.5: NACA 23012 rigid configuration experimental lift and drag curves vs 2D panel method results (XFOIL) and experimental data from the literature.

When analysing the drag coefficient results in Figure 6.5, it is observed that the obtained experimental results (wake rake) are similar to those obtained by Ashenden et al. [137]. Unlike lift coefficient, drag coefficient was calculated using local section wake rake data instead of average forces (force balance). This is a likely explanation of the better agreement between the currently measured drag results with Ashenden et al.'s results than that seen with the lift results.

In summary, the NACA 23012 baseline results agree reasonably well with previous experimental and XFOIL measurements. However, it is observed that the obtained results have lower lift coefficients than some previous tests in the literature and than XFOIL estimates. One potential reason for this is the 'modularity' of the wind tunnel wing model, which presents gaps that are covered with aluminium tape as explained in Chapter 5. Surface quality is very important at low Reynolds number and the presence of chordwise steps (such as the edge of the tape) can reduce performance. Also, it is worth noting that the primary aim of this study is to compare the FishBAC to the hinged flap, and so the relative (as opposed to absolute) aerodynamic performance is of key importance, and any issues caused by the construction of the model are present in both configurations.

6.5.1.1 FishBAC vs. Flap

A comparison between measured lift and drag coefficients for the FishBAC and hinged flap are shown in Figures 6.6 and 6.7, respectively. It is observed in these figures that deflecting both the FishBAC and flap has a similar impact on the lift curves. As expected, increasing camber moves the lift curve up and to the left, increasing lift at a given angle of attack and maximum lift coefficient, but also lowering the angle at which stall occurs.

In terms of lift control authority, the FishBAC and flap show an overall $\Delta C_L \approx 0.55$ and $\Delta C_L \approx 0.57$, respectively—considering trailing edge down deflections only. Furthermore, the amount of extra lift ΔC_L that it is generated for each deflection increment diminishes. This was

also observed in previous FishBAC studies and this diminishing return in increasing lift was attributed to pressure losses due to flow separation as camber deflections increase [113].

While the FishBAC and hinged flap both have a very large lift control authority, comparison of the associated drag coefficients in Figures 6.6 and 6.7 shows that the flap configuration incurs a much higher drag penalty. This drag increase ranges from 74% to 80% for the $\delta = +10$ and $\delta = +30$ configurations, respectively (Figure 6.7). To directly compare aerodynamic efficiency, lift-to-drag ratios as a function of both angle of attack and lift coefficient are presented in Figures 6.8 and 6.9 for the FishBAC and flap, respectively. It is observed that, for a given deflection, the FishBAC presents a higher efficiency that ranges between 22% and 83% increase, depending on the input angle.

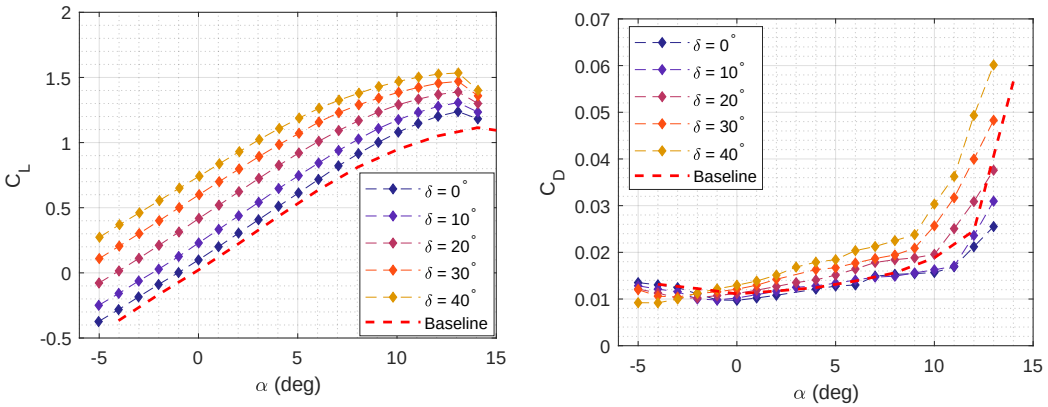

Figure 6.6: FishBAC lift and drag coefficients as a function of actuation input angle.

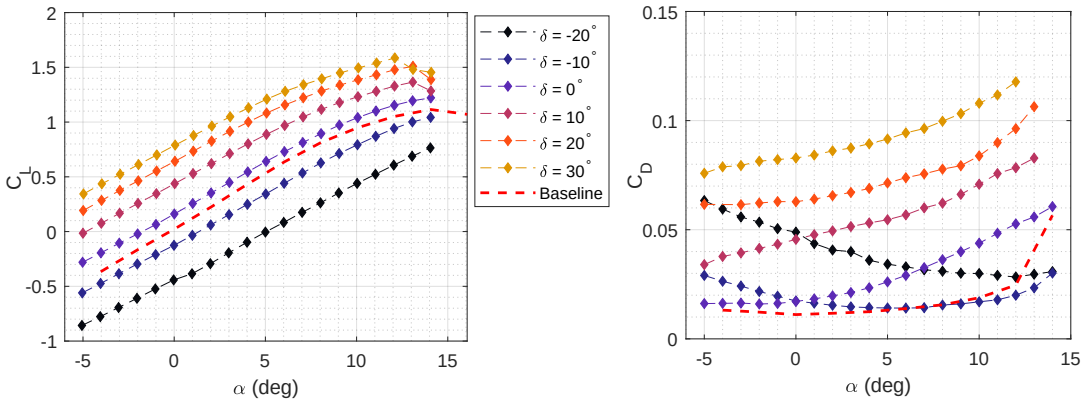

Figure 6.7: Flap lift and drag coefficients as a function of actuation input angle.

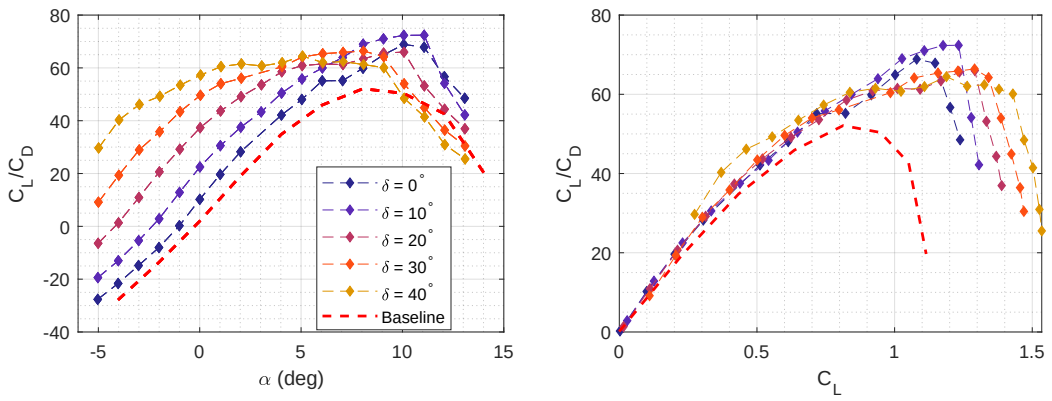

Figure 6.8: FishBAC aerodynamic efficiency as a function of both angle of attack and lift coefficient.

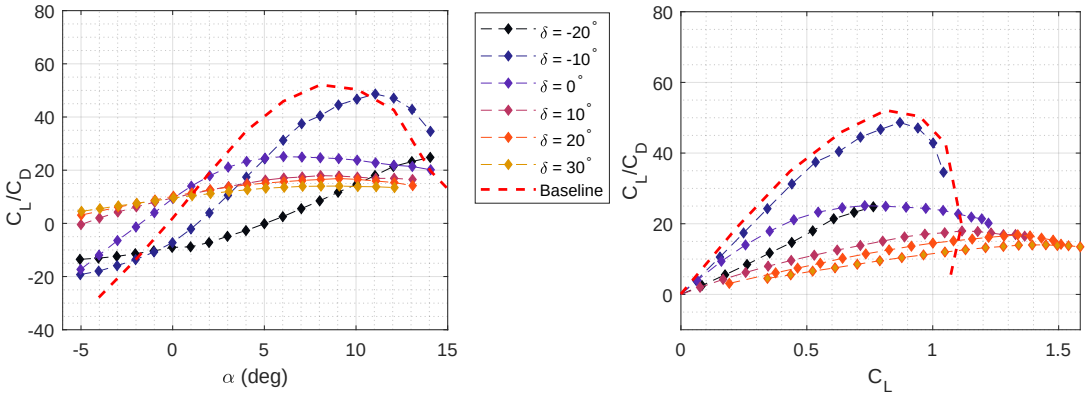

Figure 6.9: Flap aerodynamic efficiency as a function of both angle of attack and lift coefficient.

To further visualise these efficiency improvements and to compare the performance of the three tested configurations, an 'efficiency envelope' that displays each configuration's best obtainable lift-to-drag ratio, as a function of achieved lift coefficient, is introduced. By doing so, the two parameters that can vary lift coefficient—angle of attack and actuation input—are condensed in a single curve that describes the best attainable performance for each configuration (Figure 6.10) [141]. These efficiency envelopes show that the FishBAC achieves significantly higher lift-to-drag ratios than the flap configuration over the full range of angles of attack tested. This improved efficiency increase ranges from 160% to 27%, for low ($0° < \alpha < 5°$) and high ($\alpha > 10°$) angles of attack, respectively. When shown in terms of lift coefficient, the control of which is the explicit purpose of camber change, it can be seen that the FishBAC performs better over the full range of achieved lift coefficients. The FishBAC is also significantly better at moderate to high lift coefficients (i.e. $C_L > 1$), achieving an efficiency above 50% for $C_L = 1 - 1.3$—a range of lift coefficients particularly relevant to the use of camber change for vehicle control inputs (e.g. aileron lift coefficients during roll). For lower lift coefficients, the FishBAC has lift-to-drag ratios

that are at least 16% higher than the flap's (Figure 6.11), with an average improvement of 40% for typical operating lift coefficients (i.e. $0.5 > C_L > 1.0$).

In summary, the FishBAC is more aerodynamically efficient than the hinged flap at all angles of attack and lift coefficients; however, the benefit of camber morphing is particularly remarkable at higher lift coefficients. The minimum efficiency improvement is of 16%, whereas improvements above 250% are observed at higher lift coefficients. It is important to note that the FishBAC's drag measurements were performed at a 'high drag' region—near the actuation tendon, where the largest camber deflections and tunnel wall-model interaction occur–whereas the flap's drag measurements were performed at midspan, far away from the external control horns required to drive the flap and any wall effects. Lastly, it is important to note that differences between undeflected FishBAC and flap and rigid wing results exist. In the FishBAC's case, the $\delta = 0°$ shows a higher lift than baseline NACA 23012. This higher lift is most likely due to the FishBAC having a small downward deflection, induced by either a small positive actuation input or an uneven skin tension between the top and bottom surfaces. Moreover, in the flap's case, the increased lift is potentially due to a small positive deflection angle due to an input offset. This offset is likely due to a mismatch between the actuation angle input and the flap angle. This is consistent with the higher drag results for the undeflected configuration (Figure 6.6).

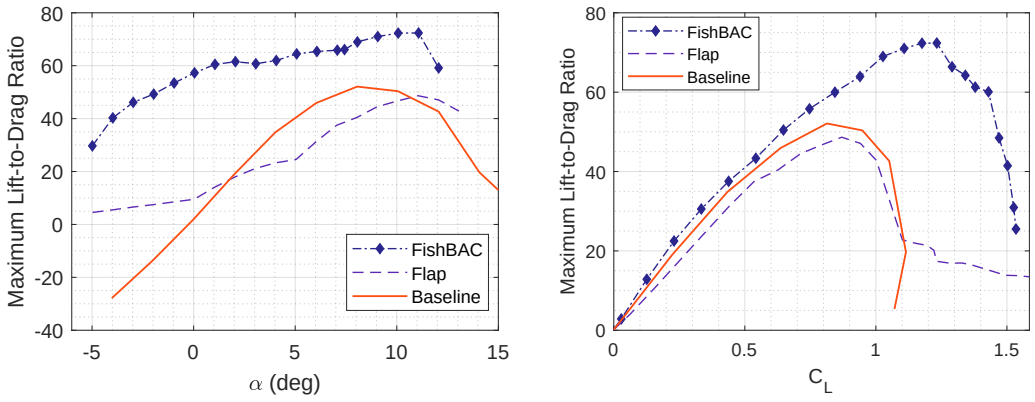

Figure 6.10: Efficiency envelope, where the best lift-to-drag ratios that both FishBAC and flap can achieved, are displayed.

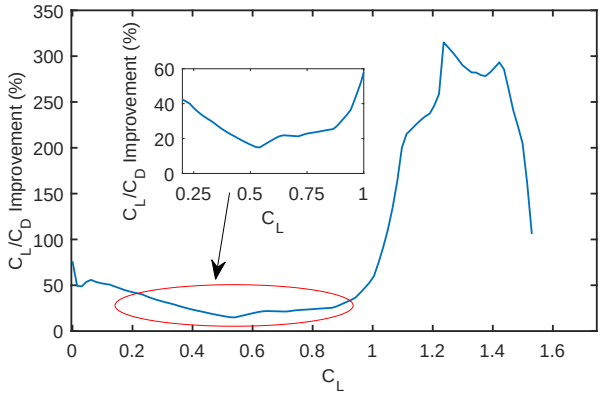

Figure 6.11: Percentage improvements in FishBAC aerodynamic efficiency when compared to the flap.

6.5.2 Spanwise Wake Rake Drag Measurements

Wake rake survey measurements were performed at different spanwise locations to further investigate how drag varies along the span. For these measurements, both angle of attack and actuation input angle remained constant. Figure 6.12 presents wake rake drag measurements for the FishBAC, at a fixed angle of attack ($\alpha = 5°$) and actuation input ($\delta = +40°$). Results show a drag coefficient variation of 22% between the lowest and highest values—at midspan and at quarter-span, respectively. Also, the wake distribution data shows that the wake shifts up and down in the thicknesswise direction as the rake traverses along the span, having a maximum location difference of 40 mm. This variation is likely due to variation in camber along the span due to elastic washout. Additionally, the peak values are fairly uniform, with a maximum variation of 6% between the lowest and highest value. These observed differences in wake drag functions explain the variation in drag coefficients. In summary, these spanwise differences in drag coefficient and wake drag function are potentially due to camber variations along the span and also due to imperfections or variations in the model geometry.

Similarly, Figure 6.13 shows wake rake drag measurements for the hinged flap at several spanwise locations. Once again, the angle of attack was fixed at $\alpha = 5°$, while the actuation deflection input was fixed at $\delta = +20°$, to give lift performance as close as possible to the $\delta = +40°$ FishBAC case shown above. Recall that the FishBAC angles are actuator inputs, not deflections achieved. Also, to highlight the drag increase due to the presence of external actuator control horns on the flap, extra measurements were performed around this location (Figure 6.13). Results show a higher variation in drag coefficient of 55% between the lowest (at midspan) and highest (at quarter-span) values—even when excluding drag coefficient measurements at the control horn. A 466% increase in drag coefficient is observed at the control horn. This increase shows that the control horn significantly disrupts the flow and, therefore, highlights that the decision to show midspan flap drag measurements in Section 6.5.1.1 gives a "best case" result for the flap.

Lastly, it is observed that, near the control horn, there are two separate but overlapping wake regions, perhaps due to the control horn shedding a separate wake.

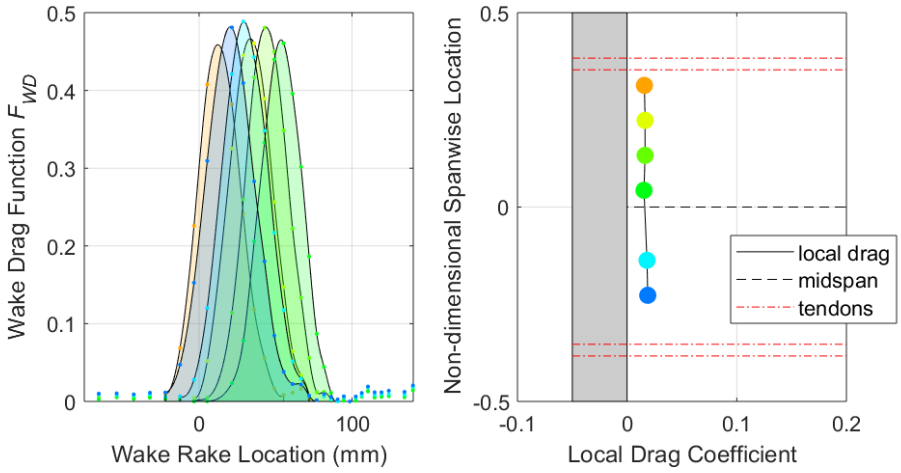

Figure 6.12: FishBAC's wake drag function distribution (left) and variation in drag coefficient (right), at several spanwise locations. Results correspond to an angle of attack of $\alpha = 5°$ and actuator deflection input of $\delta = +40°$.

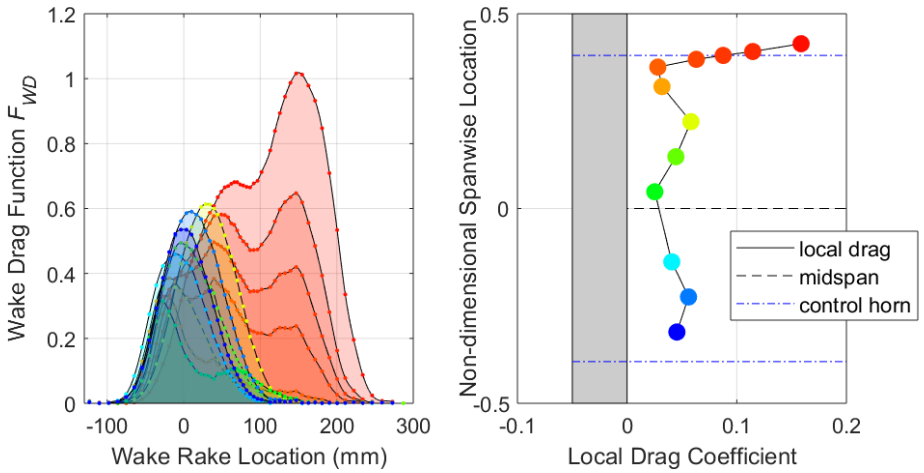

Figure 6.13: Flap's Wake drag function distribution (left) and variation in drag coefficient (right), at several spanwise locations. Results correspond to an angle of attack of $\alpha = 5°$ and actuator deflection input of $\delta = +20°$.

6.5.3 Particle Image Velocimetry

Particle Image Velocimetry wake measurements were performed to visualise the differences in the wakes behind the FishBAC and the flap. These results are useful to further establish the reasons for the significant improvement in performance seen with the FishBAC. These measurements were performed at four different actuation input angles: $\delta = -10°, 0°, +10°, +20°$. Figures 6.14 and 6.15 show images of both FishBAC and hinged flap wakes, respectively.

The wake thickness was calculated by measuring the distance, across the wake, at a location of $0.1c$ aft of the trailing edge. The wake limits were assumed to be the points just before the flow speed becomes equal to the freestream. Wake thickness results are summarised in Table 6.2. Results show that the wake thickness of the FishBAC does not significantly grow with increasing deflection (over the range of δ shown here), achieving a stable value of approximately 16 mm (i.e. 6% of chord length). These results are consistent with the marginal drag increases with increasing deflection that are observed in Figure 6.6. Unlike the FishBAC, the wake thickness of the flap increases significantly with deflection. For example, it ranges from 28.59 mm to 47.02 mm (i.e. 10.5% and 17.5% of chord length), for inputs of $\delta = 0°$ and $\delta = +20°$, respectively. When compared to the FishBAC, these flap results represent an increase of between two to three times in wake thickness, which correlates to the significant higher drag shown in Section 6.5.1.1.

Table 6.2: FishBAC's and flap's wake thickness for different actuation inputs. Results correspond to a fixed angle of attack of $\alpha = 5°$ and freestream velocity of $V = 30$ m/s.

Configuration	Input Angle (deg)	Wake Thickness (mm)	Normalised Wake Thickness (t/c)
FishBAC	−10	16.08	0.0595
	0	14.65	0.0543
	+10	16.18	0.0599
	+20	16.27	0.0603
Flap	−10	29.90	0.1117
	0	28.59	0.1059
	+10	31.93	0.1183
	+20	47.02	0.1741

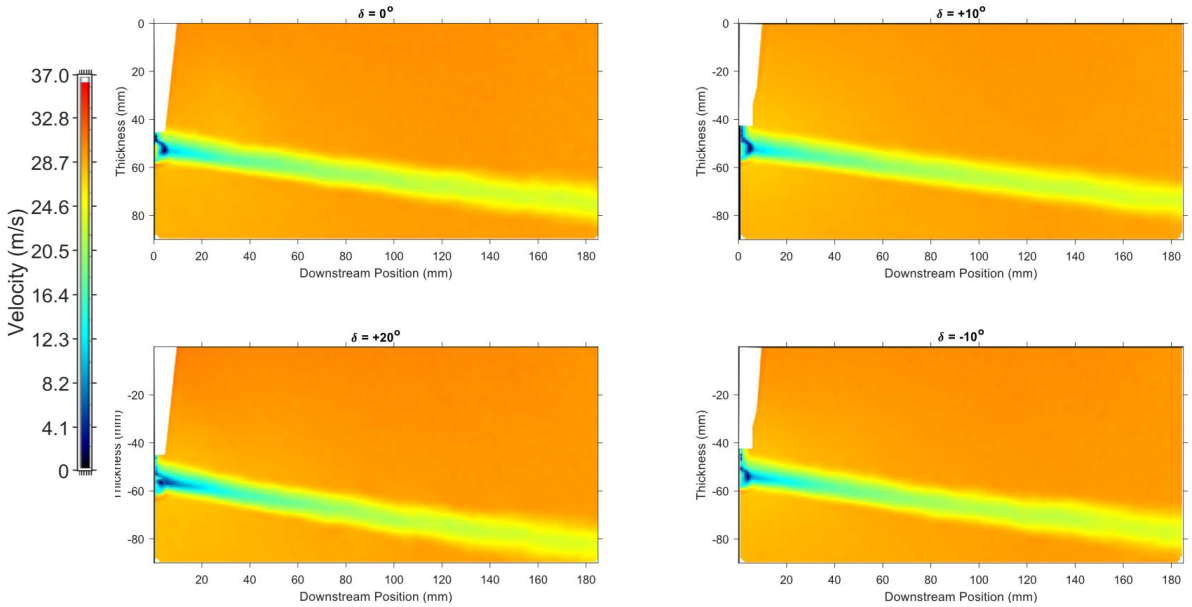

Figure 6.14: FishBAC's wake images obtained using 2D Particle Image Velocimetry. The measuring plane was located at a spanwise location of $0.467b$.

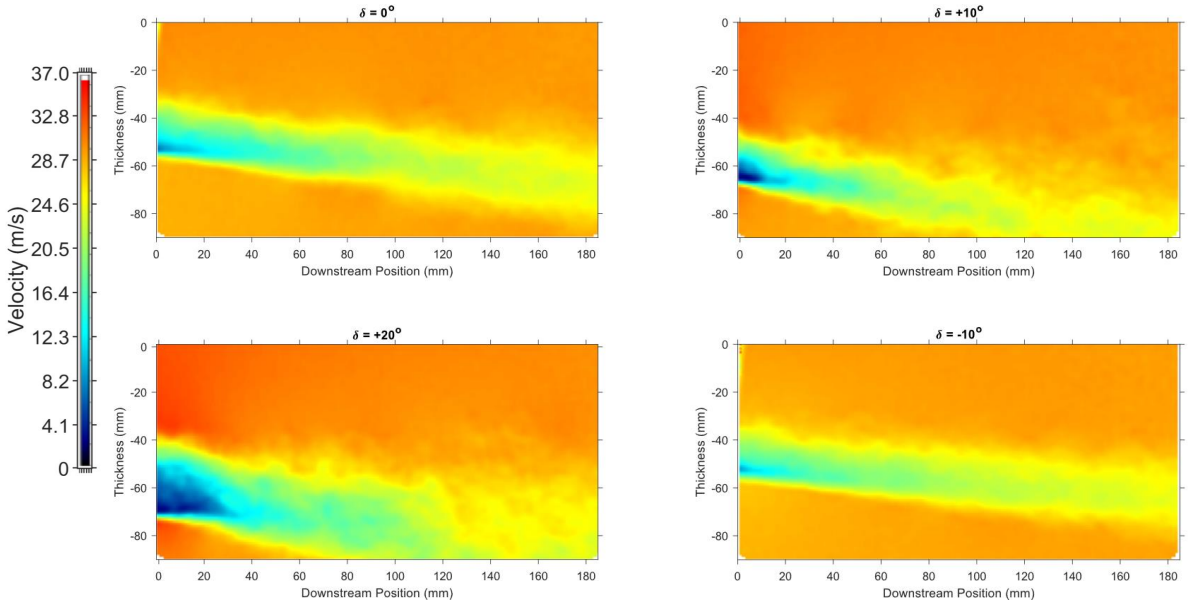

Figure 6.15: Flap wake images obtained using 2D Particle Image Velocimetry. The measuring plane was located at a spanwise location of $0.467b$.

6.5.4 Displacements: Point Tracking System

Following on from the PIV measurements, three-dimensional displacement fields of the morphed FishBAC under aerodynamic loads were measured using a point tracking stereo videogauge system. These measurements were performed at two angles of attack—$\alpha = 0°$ and $\alpha = 5°$—and at a freestream velocity of $V = 30$ m/s. Figures 6.16 and 6.17 show the FishBAC displacement with varying actuation input at $\alpha = 0°$ along the chordwise and spanwise directions, respectively. Likewise, Figures 6.18 and 6.19 show the displacement at $\alpha = 5°$, along the chordwise and spanwise directions, respectively. Note that, for all these configurations, the chordwise displacements were measured at the centre tendon and at the three-quarter span, whereas the spanwise displacements were measured at the trailing edge. Table 6.3 shows the actuation torque estimates for each given flow condition and actuation input, which were calculated using Equation 4.14 (see Chapter 4.5.3). Finally, to provide insight into the impact of aerodynamic loading on displacement, measurements were also taken at zero freestream velocity (Figures 6.20 and 6.21). Table 6.4 shows a summary of maximum transverse displacements at three different locations—midspan, three-quarter-chord and tendon—for each test configuration.

As expected, it is observed in Table 6.4 that aerodynamic loads reduce the FishBAC's maximum displacements (at tendon) by between 30% and 40% for the $\alpha = 0°$ case, and by between 42% and 60% for the $\alpha = 5°$ case. This reduction is consistent with the fact that aerodynamic pressure resists actuation loads, and increasing angle of attack increases aerodynamic loads.

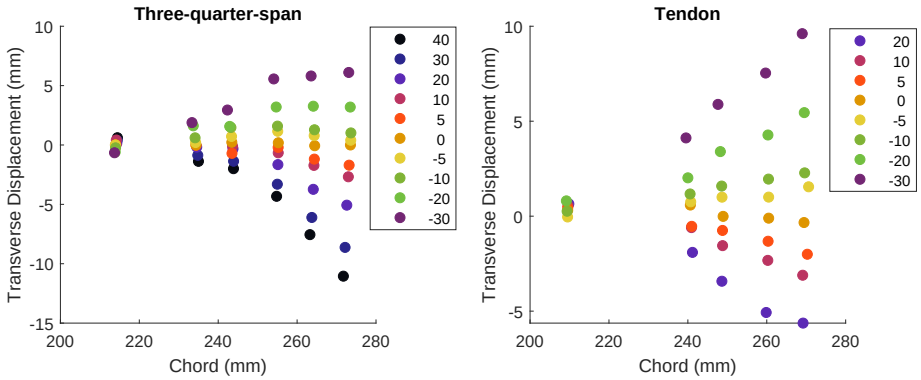

Figure 6.16: FishBAC's chordwise deflection about the three-quarter-span (left) and tendon (right) locations. Both freestream velocity and angle of attack were fixed at $V = 30$ m/s and $\alpha = 0°$.

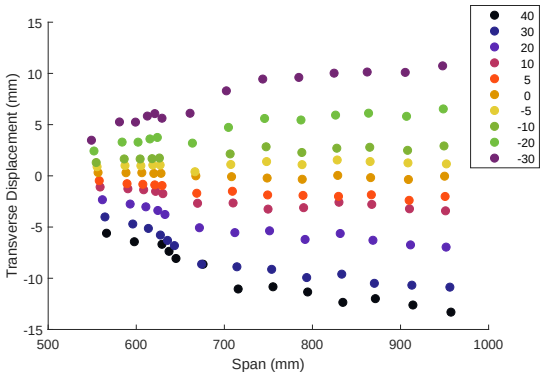

Figure 6.17: FishBAC's spanwise deflection along the spanwise free edge. Both freestream velocity and angle of attack were fixed at $V = 30\,\text{m/s}$ and $\alpha = 0°$.

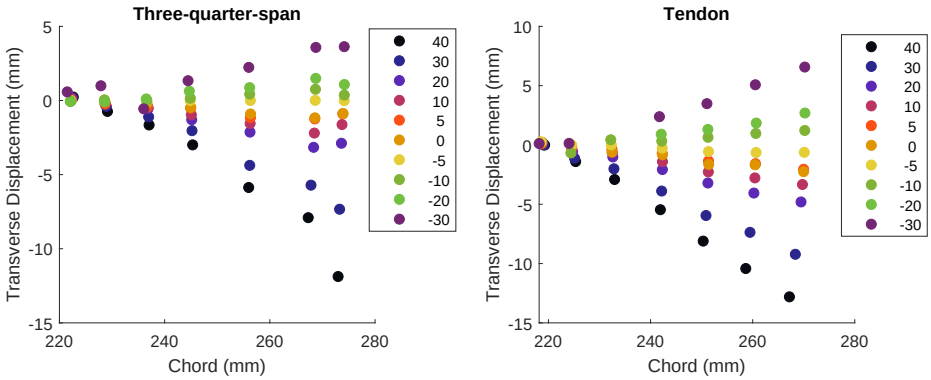

Figure 6.18: FishBAC's chordwise deflection about the three-quarter-span (left) and tendon (right) locations. Both freestream velocity and angle of attack were fixed at $V = 30\,\text{m/s}$ and $\alpha = 5°$.

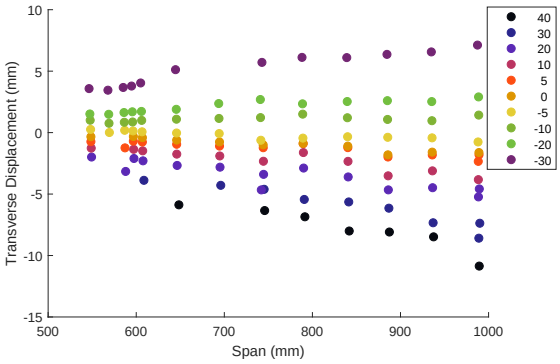

Figure 6.19: FishBAC's spanwise deflection along the spanwise free edge. Both freestream velocity and angle of attack were fixed at $V = 30\,\text{m/s}$ and $\alpha = 5°$.

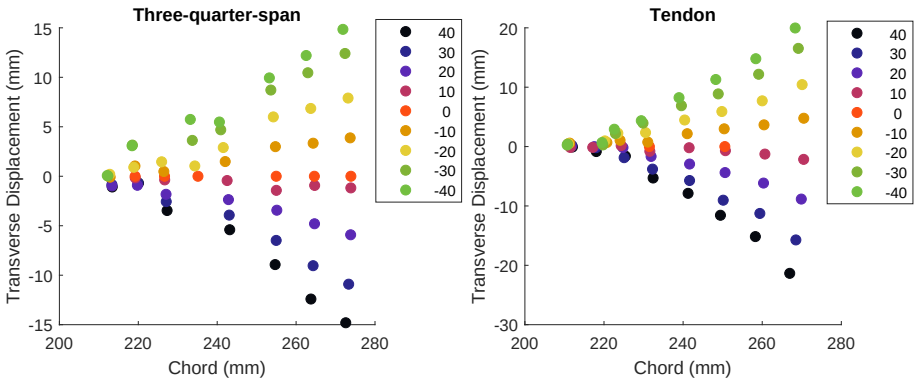

Figure 6.20: FishBAC's chordwise deflection about the three-quarter-span (left) and tendon (right) locations. Both freestream velocity and angle of attack were fixed at $V = 0$ m/s and $\alpha = 0°$.

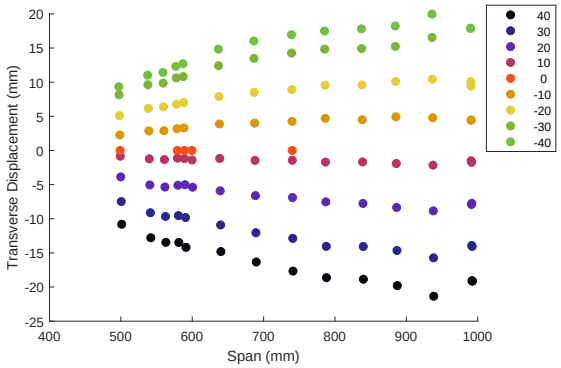

Figure 6.21: FishBAC's spanwise deflection along the spanwise free edge. Both freestream velocity and angle of attack were fixed at $V = 0$ m/s and $\alpha = 0°$.

Table 6.3: FishBAC's actuation torque estimates as a function of actuation input angle, angle of attack and freestream velocity. Torque estimates $[M_{x_2}, M_{x_4}]$ refer to to the actuators near the top and bottom force balances, respectively.

Velocity (m/s)	AOA (deg)	Torque $[M_{x_2}, M_{x_4}]$ (Nm)							
		$\delta = +40°$	$\delta = +30°$	$\delta = +20°$	$\delta = +10°$	$\delta = 0°$	$\delta = -10°$	$\delta = -20°$	$\delta = -30°$
30	0	[0.63, 0.77]	[0.54, 0.52]	[0.28, 0.28]	[0.18, 0.20]	[0.20, 0.12]	[−0.27, −0.22]	[−0.33, −0.38]	[−0.65, −0.57]
	5	[0.66, 0.75]	[0.53, 0.54]	[0.30, 0.33]	[0.17, 0.19]	[0.20, 0.12]	[−0.25, −0.23]	[−0.33, −0.37]	[−0.63, −0.59]
0	0	[0.60, 0.66]	[0.52, 0.39]	[0.21, 0.23]	[0.19, 0.15]	[0.21, 0.11]	[−0.24, −0.23]	[−0.33, −0.38]	[−0.60, −0.57]

Table 6.4: FishBAC's maximum deflections at three different spanwise locations, and as a function of angle of attack and freestream velocity.

	Velocity (m/s)	AOA (deg)	Midspan		Three-quarter-span		Tendon	
			$\delta = +40°$	$\delta = -30°$	$\delta = +40°$	$\delta = -30°$	$\delta = +40°$	$\delta = -30°$
Displacement (mm)	30	0	−5.60	3.47	−10.8	9.45	−13.3	10.7
		5	N/A	3.58	−6.34	5.71	−10.9	7.12
	0	0	−10.8	8.16	−17.7	14.3	−19.1	17.9

Lastly, to compare the actuation energy requirements of both FishBAC and flap, the total power draw by the entire actuation mechanism was measured using the Hall Effect current sensor described in Chapter 4.5.3. Table 6.5 shows the average power draw as a function of actuation input angle. Results show that, while the power draw for both wings is quite low in real terms ($\approx 20\,\text{W}$ max), the FishBAC does require significantly more power than the flap (on average $4x$ the power draw) to achieve the desired changes in camber. These results are consistent with the fact that camber morphing devices have both the elastic stiffness and aerodynamic loads resisting the change in camber, whereas the hinged flap only has the aerodynamic loads and a small hinge friction resisting the motion. Results shown in Table 6.5 are then plotted in Figure 6.22, where it is observed that the FishBAC power draw increases nonlinearly with increasing actuation input. Therefore, besides the observed diminishing returns in increasing ΔC_L as camber deflections increase, there are also diminishing returns in terms of actuation energy requirements. However, it is important to clarify that this composite FishBAC wing model was not designed to minimise actuation energy requirements. Therefore, additional work is needed to optimise the FishBAC structure for actuation energy minimisation, so that a fair comparison between these morphing devices and hinged trailing edge flaps can be established. Additionally, future work should research into other actuation mechanisms that could potentially provide a better power-to-weight ratio than servo motors.

Table 6.5: FishBAC and flap total power draw as a function of actuation angle input

Configuration	Power (W)							
	$\delta = +40°$	$\delta = +30°$	$\delta = +20°$	$\delta = +10°$	$\delta = 0°$	$\delta = -10°$	$\delta = -20°$	$\delta = -30°$
FishBAC	20.37	13.49	8.67	5.37	4.60	6.95	10.03	17.64
Flap	N/A	3.19	2.88	2.15	1.060	1.047	2.72	N/A

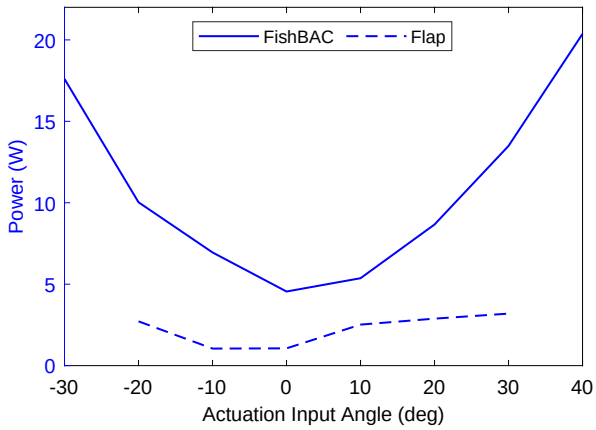

Figure 6.22: FishBAC and Flap total power draw as a function of actuation angle input

6.6 Conclusions

An experimental wind tunnel study was performed to investigate the aerodynamic performance of the FishBAC camber morphing device and to compare it against traditional trailing edge hinged flaps. A 1-meter long NACA 23012 wind tunnel wing model was designed and manufactured (see Chapter 5) to allow testing three different trailing edge configurations—baseline, FishBAC, and flapped. The wing was designed to span the height of the chosen wind tunnel to create a quasi-two-dimensional flow condition. Force balance and wake rake survey data were used to quantify the aerodynamic performance of the different configurations at a range of angles of attack and camber deflections at a freestream velocity of 30 m/s. Additionally, optical aerodynamic and structural measurements were performed using PIV and a stereo VG point tracking system, respectively. These optical measurements provide a more detailed understanding of the aeroelastic behaviour of the FishBAC. Consideration of the experimental data leads to the following conclusions:

1. Results for the rigid NACA 23012 wing were compared to previous experimental results presented in the literature, as well as XFOIL numerical simulations. Results show similar trends (lift curve linear regions) to those in the literature and XFOIL estimates, and the main differences with previous experimental results are attributed to different measuring techniques—force balance and wake rake versus aerofoil pressure taps.

2. The FishBAC shows a significantly higher lift-to-drag-ratio than the hinged flap. This improvement is even more remarkable at moderate to high lift coefficients (i.e. $C_L > 1$), where the improvement are of at least 50%. For typical operating lift coefficients in the range $0.5 > C_L > 1$, the improvement is on average 40% (and at least 16%). In general, the FishBAC presents a significantly higher aerodynamic efficiency than the flap, for all angles of attack and lift coefficients.

3. Wake rake results show that, for a fixed angle of attack and similar actuation input, the flap drag coefficient varies significantly along the span, whereas the FishBAC drag coefficient remains relatively constant.

4. PIV results show that the FishBAC's wake thickness is nearly constant with increasing deflection, having a stable value of 6% of chord length. Conversely, the wake thickness of the flap increases by 64% from its undeflected value, achieving a maximum wake thickness of 17.4% of chord length. Additionally, when comparing the two configurations, the flap has a wake that is two to three times the thickness of the FishBAC's wake. These results suggest that the flow is highly separated in the flap case, which is consistent with the drag increments observed in the wake rake survey results.

5. Aerodynamic loading was shown to decrease FishBAC's maximum deflections by between 42% and 60% at $\alpha = 0°$ and $\alpha = 5°$, respectively. It is expected that this reduction in deflection

will increase with increasing angle of attack and freestream velocity, and highlights the importance of appropriate sizing of the actuation system—by performing FSI analysis—to the expected load levels.

6. The FishBAC has significantly higher actuation power requirements than the hinged flap, requiring 300% more power on average. Also, it was observed these power requirements grow nonlinearly with increasing FishBAC deflection.

The wind tunnel test results presented in this chapter highlight the aerodynamic benefits of the FishBAC device when compared to a traditional hinged trailing edge flap. It also presents novel PIV wake measurements of the FishBAC and flap, where the benefits of camber morphing are visually highlighted. To complement these PIV measurements, displacement measurements were performed under aerodynamic loads.

Chapter 7

Numerically Efficient Three-Dimensional Fluid-Structure Interaction Analysis for Composite Camber Morphing Aerostructures

This chapter presents a newly developed three-dimensional Fluid Structure Interaction analysis of the Fish Bone Active Camber concept which couples three-dimensional viscous-corrected aerodynamic loads with the multi-component Mindlin-Reissner plate model introduced in Chapter 3. The methodology is explained, and predictions are validated against existing modelling tools. Additionally, this chapter presents results on the use of the FishBAC device for drag reduction in fixed-wing applications.

7.1 Introduction

As discussed in Chapters 1 and 2, camber morphing devices offer a more aerodynamically efficient control surface alternative to rigid hinged flaps. Also, because camber morphing deflections present 'low' drag penalties as seen in Chapter 6, they may also be used to continuously adapt wing geometry throughout flight, potentially leading to higher lift-to-drag ratios at all flight stages. However, these camber deflections lead to significant changes in the aerodynamic forces acting on the structure, and vice versa. Therefore, the structural and aerodynamic behaviour of morphing wings is strongly coupled, and accurate prediction of their performance requires analysis methods that couple the different physics. These modelling routines are known as Fluid-Structure Interaction analysis, and their implementation is crucial to successfully model and design compliance-based morphing structures. Failing to perform FSI analysis in morphing wings is likely to lead to inaccurate prediction of aerodynamic response, and may lead to structural failure or overdesign, incorrect actuation sizing, and incorrect performance predictions, among other potential issues.

Specifically for the case of a composite FishBAC device for fixed-wing applications, it is important to develop an FSI routine that captures the structural behaviour of the composite plate-based structure, as well as the 3D aerodynamic effects, present due to the finite span of the wing and due to spanwise variations in camber. Also, the coupled routine must be capable of capturing local changes in structural and aerodynamic behaviour due to local changes in aerofoil geometry along the wingspan, as well as accounting for viscous drag.

Finally, it is important that this routine is computationally efficient and with an appropriate level of fidelity—not too low as to be unsuitably inaccurate, but not so high as to be prohibitively complex and computationally expensive—so that it can be used for extensive design studies and structural optimisation.

The Mindlin-Reissner structural model presented in Chapter 4 represents an appropriate modelling technique to capture the structural behaviour of a three-dimensional composite FishBAC. However, an aerodynamic solver that captures aerofoil level changes in performance (lift and drag) due to FishBAC deflections, as well as 3D aerodynamic effects still needs to be implemented. Thus, this chapter focuses on four main aspects: *(i)* implementing a 3D aerodynamic solver for a FishBAC finite wing, *(ii)* coupling the aerodynamic solver to the Mindlin-Reissner structural model developed in Chapter 4, *(iii)* initial investigations into the control authority and drag reduction achievable on a representative fixed-wing geometry via actuation of a 3D FishBAC device and *(iv)* a direct comparison between FishBAC and a plain flap of equal percentage chord, which was analysed using the aerodynamic model presented in this chapter.

7.2 Fluid-Structure Interaction of Morphing Aerostructures: Background

Fluid-Structure Interaction analysis techniques solve the coupled, multi-physics response of deformable bodies interacting with fluid flow fields. They are classified as either one-way or two-way routines; the former one occurs when the structural deformation affects the fluid motion—but not vice versa—whereas the latter refers to routines where both structural deformations and fluid motion affect each other [142].

Additionally, FSI routines can be classified into loosely-coupled and strongly-coupled algorithms. On the one hand, the loosely-coupled ones consist of separate structural and aerodynamic models which are coupled and then iterated until a converged solution is achieved. On the other hand, strongly-coupled algorithms find the converged solution using a single model that simultaneously accounts for both the structure and the aerodynamics [142].

Although strongly-coupled algorithms are generally more stable, they may be difficult to program and implement as both structural and aerodynamics solvers may require significant modification to combine them into a single system of equations [143]. Conversely, loosely-coupled algorithms may not be as stable, but their main advantage is that they allow the combination of previously developed efficient and stable independent structural and aerodynamic solvers.

As explained in Section 7.1, it is of extreme importance to develop two-way FSI routines for morphing wings, especially compliance-based morphing, as large changes in shape trigger significant aerodynamic changes, and vice versa.

There are several examples in the literature of FSI analysis for variable camber applications. Most of these models are based on loosely-coupled routines that used FEM and CFD solvers for structural and aerodynamic analysis, respectively. There are also examples in the literature of successful implementation of lower fidelity techniques to these sorts of problems.

7.2.1 CFD/FEM-based models

Krawczyk et al. (2013) developed a model based on FEM and CFD for camber morphing wind turbine blades. This FSI routine was then used to obtain aerodynamic forces and moments. However, no specific metrics to assess computational efficiency and convergence were provided [144]. Similarly, Macphee and Beyene (2016) also developed a loosely-coupled model for morphing wind turbine blades, which is based on OpenFoam's CFD solver with a FEM-based finite strain analysis as a structural solver. One of the main findings in this study is the potential use of camber morphing as passive pitch control mechanisms. Once again, no specific morphing concept is used in the analysis, and no measure of computational efficiency is performed [145].

Some authors have developed two-dimensional FSI models for specific camber morphing concepts. For example, Oehler et al. (2012) [146] performed an ABAQUS-based CFD and FEM analysis for SMA-based morphing devices. Similarly, Heo et al. (2013) [147] followed a similar approach—using ANSYS instead—for a compliance-based camber morphing cellular structures. Moreover, Barlas and Akay (2018) [148] also developed a 2D FEM and CFD-based algorithm using ANSYS solvers for optimisation of a morphing flap.

There have also been developments in the FSI modelling of three-dimensional wings. For example, De Gaspari et al. (2014) [83] identified the need to study camber morphing at the 3D wing level, and therefore developed a model based on 3D CFD and 3D FEM. Miller et al. (2015) [149] also developed a FEM/CFD routine for variable camber wings, which also implemented a 3D interpolation algorithm to handle the dissimilar meshes used for structural versus aerodynamic analysis. After experimental validation, it was determined that the FSI model tends to underpredict lift coefficients and trailing edge displacements, and they suggest that a mesh refinement in both FEM and CFD models may improve results. Finally, Fasel et al. (2019) [150] also implements a 3D CFD and 3D FEM FSI routine for aeroservoelasticity studies of a morphing aeroplane for energy harvesting.

In summary, all these FSI models focused on using CFD and FEM as structural and aerodynamic solvers, respectively. Even though this is a workable approach that is capable of finding converged solutions, their computational expense is significant, and geometry definition and meshing remain significant challenges in the context of design space exploration. While CFD and FEM can provide very meaningful levels of insight into the detailed aeromechanics of morphing, these two modelling techniques are not an ideal starting point if wide-ranging explorations into the design space of 3D morphing wings are desired.

This is particularly relevant given the sensitivity of meshing (for both FEM and CFD) to geometry changes, which is at odds with the need for fast and robust generation of a large number of significantly different geometries while exploring a design space. Therefore, a natural solution is to start with a lower fidelity analysis to reduce computational expense, and to do so within a parametric design framework that allows very quick changes in geometry and operating conditions.

7.2.2 Lower Fidelity Models

There are two relevant examples of lower fidelity FSI models for camber morphing devices. First, Daynes and Weaver (2012) [129] developed an FSI model for a composite bistable camber morphing trailing edge device. Even though the authors did use FEM as structural solver, XFOIL was used to obtain the aerodynamic loads. Results showed that XFOIL provides sufficient aerodynamic information for validation of 2D wind tunnel test data, and a much lower computational expense than CFD.

Woods et al. (2014) [27] went one step further in reducing computational expense by also using XFOIL as the aerodynamic solver, but by replacing FEM by an analytical Euler-Bernoulli beam theory structural model. This FSI routine was developed for the FishBAC device specifically, and represents a fast and inexpensive routine for two-dimensional aerofoil analysis, design and optimisation of this morphing concept. For example, due to its efficiency, this FSI model was used for a multi-objective optimisation study of the FishBAC [89]. However, this model cannot be used for three-dimensional wing analysis as it is a two-dimensional model with no ability to capture the structural or aerodynamic impact of variations along the span.

From this brief review of relevant literature, it can be seen that a fully three-dimensional, computationally efficient FSI routine is needed to analyse, design and optimise composite FishBAC camber morphing wings. This new model will allow for a more thorough exploration into the aerodynamic performance of camber morphing wings than what has been achieved to date, and can be used to identify regions of the design space where higher fidelity analysis and wind tunnel testing should be targeted.

7.3 3D FSI for Composite FishBAC Wings

A 3D FSI analysis for modelling the aeroelastic behaviour of a composite FishBAC wing is proposed in this section. From the aerodynamics point-of-view, this model must be able to account for local changes in 2D aerofoil shapes due to varying camber, as well as for 3D aerodynamic effects. It should include profile drag, skin friction drag, and induced drag, and should be able to properly capture the impact on lift of 2D camber changes and of 3D finite wing lift effects—including wing tip vorticity/downwash and spanwise variations of camber.

From the structural point-of-view, it needs to capture the stiffness discontinuities of the FishBAC, the use of different types of material—including composite laminates—and the chordwise taper due to the aerofoil geometry. Since a stable and efficient structural solver has already been developed (Chapter 4), a loosely-coupled approach will be implemented. The following section describes the implemented modelling techniques that addresses all these requirements.

7.3.1 Aerodynamic Model

One feasible option to fully capture the 3D aerodynamics of a finite wing is to use 3D panel methods, which discretise the outer surface of the wing into a series of chordwise and spanwise panels, hence capturing local changes in aerofoil shape and thickness effects [151]. Although panel methods are significantly more efficient than CFD, it is difficult to incorporate viscosity effects into them, and viscous effects are an important contributor to the overall drag. Another option is to use inviscid, vorticity-based numerical methods that are derived from thin aerofoil assumptions, such as Vortex Lattice Method (VLM) [152] and its precursor, Weissinger Lifting-Line Theory [153]. These two techniques implement finite vortex filaments to calculate lift and induced drag. Although these methods are very computationally efficient, they still neglect viscosity and do not model aerofoil thickness. Hence, LLT and VLM are unable to predict viscous effects (including stall) or obtain accurate pressure distributions due to local changes in aerofoil geometry.

An alternative approach to LLT, that allows for the inclusion of viscosity and thickness effects, is to couple the 3D lift distribution from LLT to 2D aerofoil data that can be obtained from either experiments [154, 155] or a 2D aerofoil analysis tool [156], followed by iterating the 2D and 3D solutions until certain convergence criterion is met. Anderson et al. (1980) successfully implemented this technique for modelling the stall behaviour of a finite wing with a drooped leading edge [155]. Their model coupled Prandlt's LLT with 2D aerofoil experimental data. They concluded that their coupled model had a maximum percentage difference of 20%, when compared to experimental data. However, the authors noted that it is important to be aware that LLT can be inaccurate at high angles of attack due to the flow becoming highly three-dimensional. An appropriate three-dimensional solver should be used for such cases.

Sugar-Gabor et al. implemented both LLT [157] and VLM [156] routines using XFOIL as a two-dimensional flow solver. Their LLT was validated against CFD for Mach numbers between $M = 0.05$ and $M = 0.2$ and angles of attack between $\alpha = -2$ and $\alpha = +8°$. They observed good agreement between CFD and LLT lift and pitch moment coefficients; however, drag coefficients start to diverge at angles of attack greater than $\alpha = 4°$. They also suggested in their VLM study that drag accuracy could be improved by introducing experimental results to the VLM + XFOIL algorithm [156]. Additionally, they used their model to study the aerodynamics of a morphing wing, and were successfully able to quantify the aerodynamic performance gains of

their morphing concept. Therefore, due to similarities in application, an LLT-based model coupled with XFOIL will be used as an aerodynamic solver.

In summary, an LLT model with viscous corrections is a suitable approach for modelling the FishBAC's 3D aerodynamics at an appropriate level of fidelity for use in design space exploration and initial optimisation work. However, it is important to treat results at high angles of attack with care, as these may be inaccurate due to LLT's limitations on modelling fully 3D flows.

7.3.1.1 3D Aerodynamics: Downwash & Induced Drag

Due to pressure differences between top and bottom wing surfaces, the flow at the wing tips of finite wings tends to curl around the tips, generating a spanwise flow component that does not exist in 2D aerofoil sections. These wingtip vortices induce a downward velocity component on the wing which, combined with the freestream flow, produce a local relative velocity vector known as downwash. Hence, the geometric angle of attack is no longer the angle of attack that the wing perceives due to the existence of this new relative velocity vector (Figure 7.1). Note that, by definition, the angle of attack is the angle between the aerofoil's chord line and the freestream flow. Therefore, a new 'effective' angle of attack is defined as the angle between the local chord line and the local relative velocity vector, defined as

$$\alpha_{\text{eff}} = \alpha - \alpha_i \,, \tag{7.1}$$

where α is the geometric angle of attack and α_i corresponds to the induced angle of attack—defined by how much the new relative velocity vector is inclined below the freestream velocity vector.

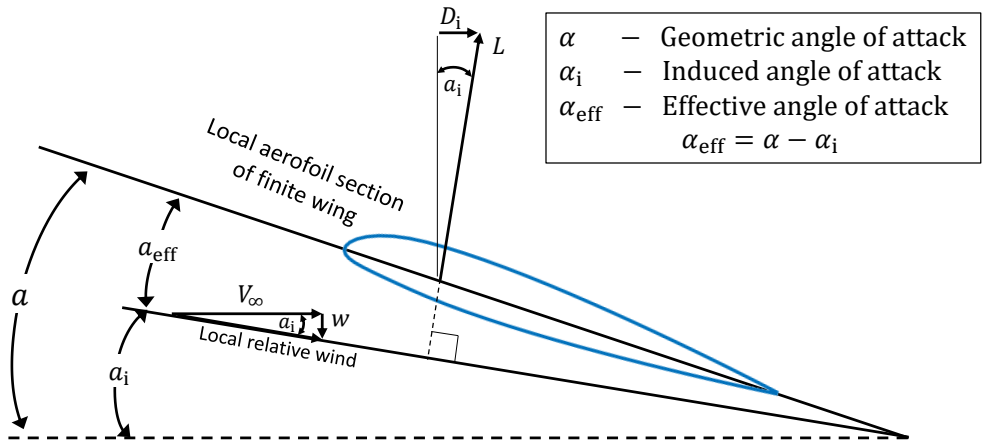

Figure 7.1: Effective angle of attack caused by downwash. Reproduced from Anderson (2010) [90].

7.3.1.2 Weissinger's Lifting-Line Method

The Weissingner's Lifting-Line Method is a numerical modelling tool used to calculate the local downwash and effective angle of attack of a finite wing. It is considered to be a nonlinear extension of Prandlt's Lifting-Line Theory as it combines LLT with nonlinear aerofoil section data. Thus, unlike Prandlt's LLT, the Weissingner's nonlinear LLT can be used to predict aerodynamic nonlinearities at stall. LLT assumes that a finite wing can be replaced by a spanwise vortex filament (bound vortex) of variable strength along the span and a series of trailing vortices (Figure 7.2). Once the bound vortex strength distribution $\Gamma(y)$ is calculated, the local lift per unit span can be calculated using Kutta-Joukowski theorem, such that

$$L' = \rho_\infty V_\infty \Gamma(y). \tag{7.2}$$

The main effect of the trailing vortices is to induce downwash velocities, which are then used to calculate the effective angles of attack [155]. Each set of one finite bound vortex—located at each panel's quarter-chord—and two trailing vortices is known as a horseshoe vortex element (Figure 7.3).

To implement Weissingner's Lifting-Line Method, the wing is partitioned into a number of spanwise elements, with each one containing a horseshoe vortex. In terms of chordwise elements, LLT uses only one element along the chord. This is the main difference between Weissingner's Lifting-Line Method and Vortex Lattice Method, where horseshoe vortices are also used, but with multiple chordwise elements. In both techniques, the bound vortices are placed at the quarter-chord (in the chordwise direction) on each panel, and a control point is set at the element three-quarter-chord position. Each horseshoe vortex induces a velocity at each control point, which can be calculated using Biot-Savart Law

$$dV = \frac{\Gamma}{4\pi} \frac{dl \times r}{|r|^3}. \tag{7.3}$$

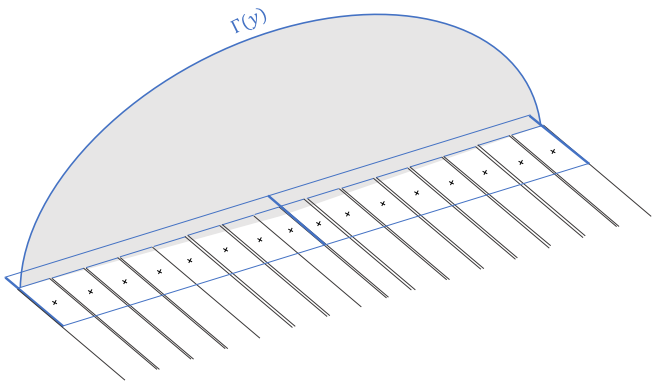

Figure 7.2: Vortex strength distribution of a finite wing

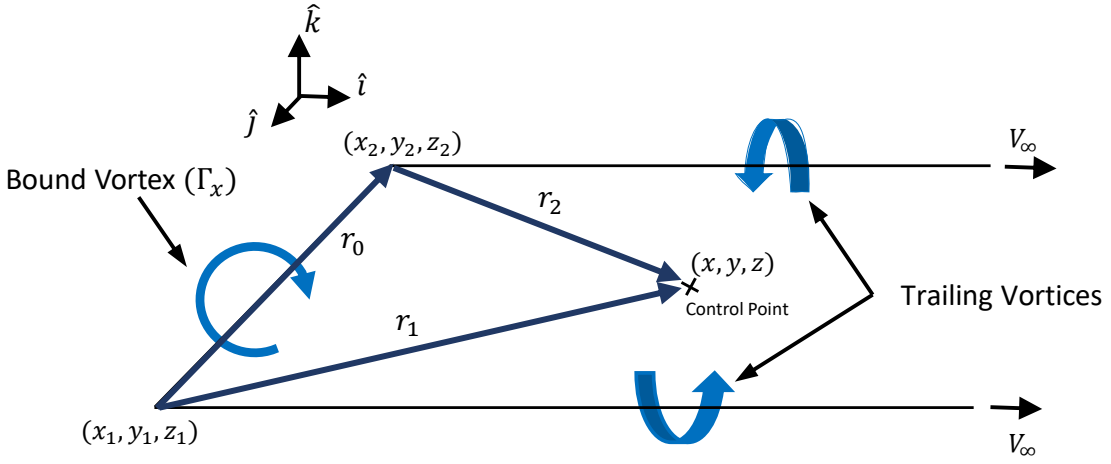

Figure 7.3: Horseshoe vortex diagram. Reproduced from Chadwick (2005) [158] and Şugar-Gabor et al. (2013) [157] with authors' permission.

For each horseshoe element, the induced velocity at a given point is given by the sum of the induced velocity from the bound vortex

$$V_{AB} = \frac{\Gamma}{4\pi} \frac{r_1 \times r_2}{|r_1 \times r_2|^2} \left[r_0 \left(\frac{r_1}{|r_1|} - \frac{r_2}{|r_2|} \right) \right] \tag{7.4a}$$

and the two semi-infinite trailing edge vortices

$$V_{A\infty} = \frac{\Gamma}{4\pi} \left\{ \frac{r_{1_k} j - r_{1_j} k}{(r_{1_k})^2 + (-r_{1_j})^2} \right\} \left[1 + \frac{r_{1_i}}{|r_1|} \right] \tag{7.4b}$$

$$V_{B\infty} = \frac{\Gamma}{4\pi} \left\{ \frac{r_{2_k} j - r_{2_j} k}{(r_{2_k})^2 + (-r_{2_j})^2} \right\} \left[1 + \frac{r_{2_i}}{|r_2|} \right], \tag{7.4c}$$

where r_0, r_1 and r_2 define the geometric position of each horseshoe vortex with respect to each control point. Figure 7.3 shows a horseshoe element with its respective control point and the position vectors r_0, r_1 and r_2.

Once all the induced velocities have been calculated using Equation 7.4, a system of linear equations can be set to solve for the horseshoe vortex strengths. These vortex strengths are assumed to be uniform across the horseshoe element. One boundary condition needs to be satisfied: the zero normal flow at each control point, defined as

$$\Delta(\Phi + \Phi_\infty) \cdot n = 0, \tag{7.5}$$

where Φ_∞ refers to the potential of the freestream flow, Φ represents the potential from the induced velocities by the horseshoe elements, and n is the normal vector to each control point at the three-quarter-chord of each element. This normal vector can be expressed in terms of the local twist angle (θ), wing dihedral (ϕ) and the local camber line slope (dz/dx), such that

$$n = \sin\left(\theta - \frac{dz}{dx}\right)\cos(\phi)\hat{i} + \sin(\phi)\hat{j} + \cos\left(\theta - \frac{dz}{dx}\right)\cos(\phi)\hat{k}\,. \tag{7.6}$$

This zero normal flow at control points is applied by setting the sum of the freestream velocity and the induced velocities equal to zero, along the normal direction

$$[(V_{AB} + V_{A\infty} + V_{B\infty}) + V_{\infty}] \cdot n = 0\,. \tag{7.7}$$

Equation 7.4 can be substituted into Equation 7.7 to obtain a system of $1 \times N$ equations—N corresponds to the number of spanwise horseshoe elements—of the form

$$[f_{mn}][\Gamma_n] = [-V_{\infty} \cdot n], \tag{7.8}$$

where f_{mn} are known as the influence coefficients [156, 159]. The calculated vortex strengths can then be used to calculate the lift-per-unit span at each horseshoe element by using Kutta-Joukowski theorem. However, these still need to be corrected for viscosity, which will be introduced in the following section. Finally, the effective angle of attack can be calculated at each spanwise element using the expression

$$\alpha_{\text{eff}_n} = \tan^{-1}\left(\frac{V_{\text{eff}} \cdot \hat{n}}{V_{\text{eff}} \cdot \hat{c}}\right), \quad \text{where} \qquad V_{\text{eff}} = V_{\infty} + V_{A\infty} + V_{B\infty}\,. \tag{7.9}$$

This effective angle of attack is calculated at the local wing plane [160] and, therefore, the freestream vector and the chordwise and normal-to-chord unit vectors are defined as

$$V_{\infty} = V_{\infty}(\cos\alpha\,\hat{\imath} + \sin\alpha\,\hat{k}), \quad \hat{n} = \hat{k} \quad \text{and} \quad \hat{c} = \hat{\imath}\,. \tag{7.10}$$

7.3.1.3 2D Aerofoil Aerodynamic Solver

XFOIL is used to obtain local aerofoil section data—i.e. local 2D aerodynamic coefficients and pressure distributions. As mentioned in Chapter 6.2.3, XFOIL requires the non-dimensional aerofoil coordinates, the angle of attack, Mach number and Reynolds number as inputs. To obtain the aerofoil coordinates, the wing is divided into two sections: the main rigid section (i.e. $0 < x/c < 0.744$)—maintained rigid throughout the analysis—and the morphing portion (i.e. $0.744 < x/c < 1$).

The main rigid section's aerofoil profile is obtained from the NACA 5-digit equations [161], using the NACA 23012 input parameters. As the FishBAC's structural solver models the spine's displacement, the aerofoil geometry needs to be constructed from the spine's transverse displacement field. To achieve this, a sixth-order polynomial fit is performed to capture the local spine deformation at a given spanwise location. A high-order polynomial fit ensures that complex spine deflections can be captured [113]. The aerofoil shape is rebuilt on top of the current deflected spine shape by applying the aerofoil's thickness distribution at each point along the length of the spine normal to the local tangent of the spine.

This process is identical to the NACA method of defining aerofoils, and also reflects the role of the stringers in maintaining the thickness distribution with camber change. This aerofoil reconstruction process is performed at the centre of each spanwise LLT horseshoe element (see Section 7.3.1.2).

7.3.1.4 Nonlinear Lifting-Line Solution

The use of nonlinear section lift data to enhance Lifting-Line Theory was first introduced by Sivells and Neely (1947) [154], describing this method as an alternative to estimate maximum lift coefficients of high aspect ratio and unswept wings. Anderson et al. (1980) [155] later applied this technique to model drooped leading-edge wings. They described the procedure as follows: first, LLT is used to calculate the effective angle of attack at each panel (i.e. using Equation 7.9), and with that initial effective angle of attack distribution, local lift coefficients can be interpolated from 2D aerofoil data, be it experimental data, or in this work XFOIL results. With those interpolated lift coefficients, the lift per unit-span can be calculated at each horseshoe element using the lift equation

$$L^{'} = \frac{1}{2}\rho_{\infty}V_{\infty}^{2}c_{n}(y)c_{l}\,, \tag{7.11}$$

where c_n corresponds to the local aerofoil chord length and c_l is the 2D lift coefficient. If the lift equation and Kutta-Joukowski theorem are combined, a local circulation from the 2D aerofoil data can be calculated as shown by the following expressions

$$L' = \frac{1}{2}\rho_{\infty}V_{\infty}^{2}c_{n}(y)c_{l} = \rho_{\infty}V_{\infty}\Gamma_{\text{new}} \quad \text{and} \quad \Gamma_{\text{new}} = \frac{V_{\infty}c(y)c_{l}(y)}{2}. \tag{7.12}$$

The second step is to calculate the lift per unit-span at each horseshoe element from LLT. Using the bound vortex strength distribution previously obtained (Equation 7.8), the lift per unit-span at each horseshoe element can be calculated using Kutta-Joukowski theorem. These two different estimates of the vortex strength distribution (one obtained from XFOIL and one from LLT) are used to generate the next iteration's vortex strengths, such that

$$\Gamma_{n+1} = \Gamma_{\text{old}} + DF(\Gamma_{\text{new}} - \Gamma_{\text{old}})\,. \tag{7.13}$$

With this new vortex strength distribution, a new effective angle of attack distribution can be calculated, followed by another set of interpolations from 2D aerofoil data. The process is repeated until a specified convergence criterion is met (Figure 7.4). In this application, the convergence criterion is a 0.5% difference between iterations. The use of a fixed relaxation factor (DF) is introduced to assist convergence.

7.3.1.5 Relaxation Factors

Relaxation factors are used in numerical methods to stabilise solutions that are obtained via iterative methods, hence, assisting convergence. They act by slowing down the 'rate of advance' between two iterations. In other words, they reduce the step size between two expected solutions, reducing the likelihood of undesired fluctuations that may lead to divergence. Consequently, it can be said that relaxation factors add 'damping' to the numerical solution [113, 162, 163]. There are two main types of relaxation parameters: fixed and variable. Fixed relaxation factors remain constant throughout the iterative process, whereas variable ones are changed to speed up the analysis as convergence is approached.

As mentioned in the previous subsection (Section 7.3.1.4), the use of a fixed relaxation factor DF is used to assist convergence between the 2D and 3D aerodynamic solutions. Previous studies have determined a value of $DF = 0.05$ is sufficient to assist convergence [153, 155], however, these studies noted that this relaxation factor is highly dependant on the specific geometry and operating condition. Due to large changes in camber in this application, it was observed that additional damping was needed to assist convergence. Therefore, a value of $DF = 0.001$ is used in this FSI model. Lastly, once a converged vortex strength distribution is obtained, a converged set of pressure distributions is interpolated from the 2D aerofoil data. This pressure distribution is then applied to the structural model, which will be presented in the following section.

7.3.1.6 Aerodynamic Coefficients

Once a converged set of vortex strength distributions is obtained, the total lift coefficient and induced drag due to lift are calculated using the following expressions:

$$C_L = \frac{2}{V_\infty S}\int_{-b/2}^{b/2}\Gamma(y)dy \quad \text{and} \quad C_{D_i} = \frac{2}{V_\infty S}\int_{-b/2}^{b/2}\Gamma(y)\sin(\alpha_i)dy\,. \tag{7.14}$$

The profile drag and pitching moment coefficients can be integrated from the interpolated XFOIL results, such that

$$C_{D_0} = \int_{-b/2}^{b/2} c_{d_0}(y)dy \quad \text{and} \quad C_m = \int_{-b/2}^{b/2} c_m(y)dy\,. \tag{7.15}$$

Finally, the total drag coefficient is defined as the sum of profile and induced drag coefficients, defined as

$$C_D = C_{D_0} + C_{D_i}\,. \tag{7.16}$$

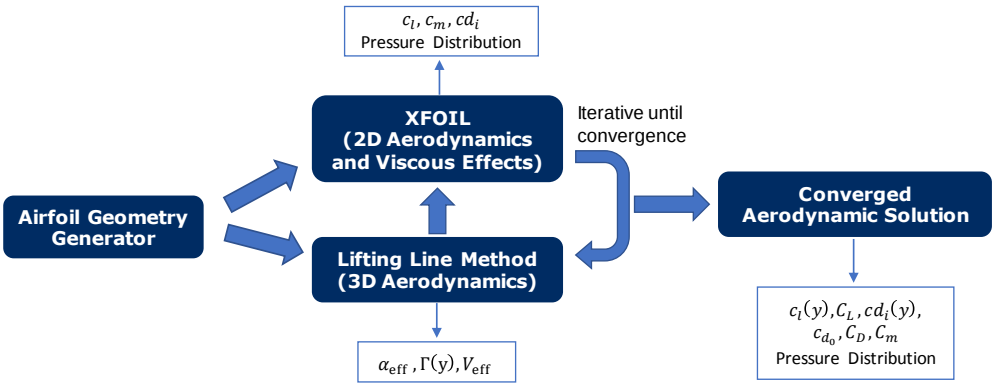

Figure 7.4: Aerodynamic model convergence diagram

7.3.2 Structural Model

The structural model used in this FSI routine is the discontinuous composite plate model based on Mindlin-Reissner Plate Theory that was presented in Chapter 4. This structural model is suitable for FSI analysis as the aerodynamic pressure distribution—obtained using the nonlinear LLT solver—and the actuation loads can be directly applied to the structure, and the FishBAC spine displacement is directly obtained as an output. Also, this structural model represents a fast, parametrically driven, robust approach to modelling the behaviour of the FishBAC morphing device that requires only 1% of the DOFs required for a converged FEM model. Consequently, this structural model is a more computationally efficient alternative to FEM and hence a more suitable approach for design and optimisation FSI studies. A detailed derivation of this structural model formulation, shape functions, material properties, structural configuration and dimensions, actuation loads and solution method are presented in Chapter 4. Additionally, Chapter 3.6 describes how the aerodynamic pressure loads obtained in Section 7.3.1 are applied to the FishBAC structure.

7.3.3 FSI Analysis Numerical Implementation

The 3D composite FishBAC FSI routine 'loosely' couples the structural and aerodynamic solvers. In this case, the aerodynamic solver runs ahead of the structural solver; hence, the aerodynamic solution in the first iteration corresponds to a rigid NACA 23012 wing with no deformations. These initial aerodynamic results are used as input by the structural solver along with the actuation input settings, leading to an initial FishBAC displacement field that is then used to generate a deformed set of aerofoil geometries in the second iteration.

7.3.3.1 Coupling Algorithm

Once the aerofoil geometries have been generated, the aerodynamic solver obtains converged pressure distributions and aerodynamic coefficients along each spanwise LLT control point. To ensure matching coordinates between the structural and the aerodynamic models, the structural model's spanwise partitions are assigned so that each partition boundaries are aligned with the local horseshoe element. The pressure distribution at each control point is then applied to the structural model along with the external actuation moment inputs. The analysis is then iterated in this fashion with the updated deformations informing the aerodynamic analysis and vice versa. The structural model outputs a converged FishBAC displacement field, followed by a convergence check on the total lift coefficient. The FSI routine is said to be converged when the change in lift coefficient between two subsequent iterations is less than 0.5%, such that

$$C_{L_{\text{err}}} = \frac{[C_L(k) - C_L(k-1)]}{C_L(k-1)} \leq 0.005\,, \tag{7.17}$$

where k refers to the FSI iteration counter. Additionally, once the convergence criterion in lift coefficient (Equation 7.17) is met, a final 'check' on the 3D drag coefficient is performed. This drag coefficient check consists of calculating the average difference in C_D between the final two FSI iterations and comparing them with respect to each other. Since the final value C_D depends on interpolations from 2D aerofoil XFOIL results, this convergence check ensures that there are no 'jumps' in drag coefficient—that may be introduced by XFOIL failing to converge for certain angles of attack—between the final two iterations. Once these two criteria are met, the FSI is said to be converged. Figure 7.5 shows a schematic of the implemented coupling algorithm.

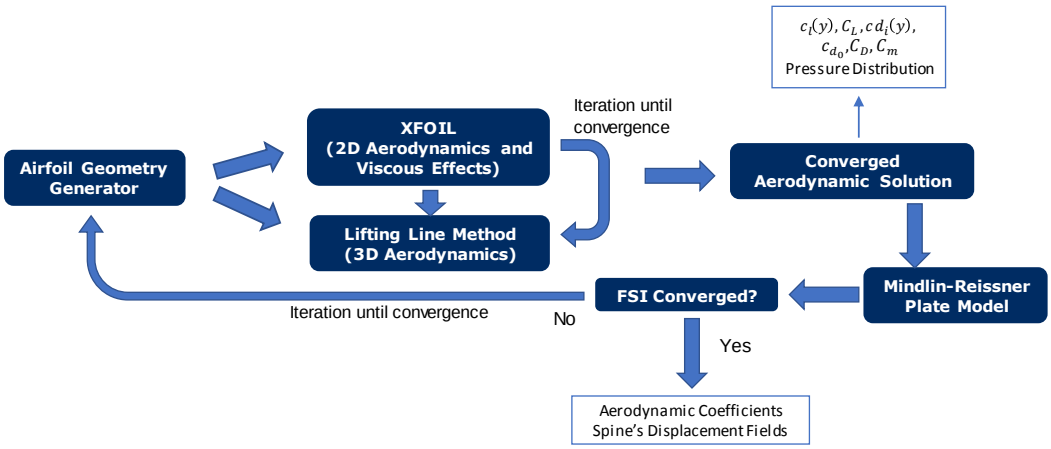

Figure 7.5: Schematic of the loosely-coupled fluid-structure interaction (FSI) routine.

Similarly, as in Section 7.3.1.5, relaxation can be applied to assist convergence. In FSI algorithms, relaxation factors are normally applied between the structural and aerodynamic interfaces. For this 3D FishBAC FSI analysis, fixed relaxation parameters are applied to both structural and aerodynamic solutions. For the structural solution, relaxation is applied to the spine displacement field, as described by

$$w^r_{\text{new}}(x,y) = \frac{w_{\text{new}}(x,y)\lambda_{\text{w}} + w_{\text{old}}(x,y)}{\lambda_{\text{w}} + 1}, \tag{7.18}$$

where λ_{w} refers to the relaxation factor on the spine displacement. Also, relaxation is applied to the net aerodynamic pressure obtained from the aerodynamic solver, such that

$$q^r_i(x,y) = \frac{q_i(x,y)\lambda_{\text{p}} + q_{\text{i-1}}(x,y)}{\lambda_{\text{p}} + 1}, \tag{7.19}$$

where λ_{p} is the relaxation factor for pressure distribution. Increasing the value of the relaxation parameters λ_{w} and λ_{p} would lead to a slow but stable solution, whereas a value of zero corresponds to no relaxation. Although widely used in numerical methods, it is important to note that the selection of these relaxation values is highly empirical, and hence, they must be 'tuned' for each application [164]. For this FSI model, a value of λ_{w} and λ_{p} between 0.1 and 0.5 was found to be sufficient for convergence.

7.3.3.2 Model Implementation

The FSI analysis is implemented in MATLAB using an open-source wrapper that executes XFOIL [165]. The remaining structural and aerodynamic calculations are all written directly in MATLAB. For the study undertaken in this chapter, a generic UAV scale fixed-wing geometry was used, with the objective of studying the response of this simple wing to changes in active camber morphing. The wing model has a chord of 270 mm and a span of 2000 mm, resulting in an aspect ratio of $AR = 7.4$. A NACA 23012 aerofoil was selected as the baseline profile, and the morphing FishBAC portion of that aerofoil starts at $x/c = 0.744$. The remaining non-morphing section of the wing is assumed to be rigid; hence, it does not deform during the FSI analysis. Lastly, a taper ratio of 1 (untapered) and a dihedral angle $\phi = 0$ were used for this analysis.

Regarding the structural model, three different material properties are used to model the morphing section: 8552/IM7 carbon fibre-reinforced prepreg (spine), 3D printed ABS plastic (stringers and trailing edge) and silicone rubber sheet (skin). These materials properties were obtained by performing a series of material characterisation experiments, which are thoroughly discussed in Chapter 5. Additionally, a comprehensive convergence study of the discontinuous plate-based Mindlin-Reissner model was performed and introduced in Chapter 4. In that study, it was determined that using a total of five Chebyshev Polynomial terms in both chordwise and spanwise shape functions is sufficient for convergence. Also, it was estimated that a stiffness of $k = 1 \cdot 10^7$N/m on all artificial penalty springs guarantees a converged solution. More spe-

cific details on how the structural model is implemented—including internal dimensions and assumptions—can be found in Chapters 3 and 4.

Finally, four aerodynamic input parameters are needed to execute the FSI model: freestream velocity, air density, angle of attack and Reynolds number. In this study, the freestream velocity was set to $V = 30\,\text{m/s}$, which corresponds to a Mach number of $M = 0.089$ at standard sea level (SLS) conditions, and is again representative of a generic UAV. Additionally, the air density at SLS conditions is equal to $\rho_\infty = 1.225\,\text{kg/m}^3$, resulting in a Reynolds number of $Re \approx 543{,}000$. An angle of attack sweep from $\alpha = -4^\circ$ to $\alpha = +14^\circ$, in increments of $+2^\circ$, was performed for each test case. A total of 107 actuation input combinations were run in this analysis, including uniform actuation inputs at both actuators, single actuation (i.e. only one actuator being used) and different permutations of differential torque input (i.e. both actuators active, but with different torque values).

7.4 Model Validation

The aerodynamic model was validated against a related nonlinear LLT model developed by Tornero (2017) [166] as well as the XFLR5 open-source code. XFLR5 is a 3D wing analysis software capable of analysing the aerodynamics of finite wings using either Lifting-Line Theory, Vortex Lattice Method or 3D Panel Method. Additionally, it corrects for viscous effects by interpolating XFOIL results at local aerofoil sections. For the LLT case, the viscous analysis is fully coupled, and it iterates both 2D viscous and 3D solutions until convergence is met. For the VLM and 3D panel case, a viscous correction is implemented to the final drag value. Therefore, the viscous LLT option is used for validation as it more fully includes viscous effects, as long as the code is used within LLT's limitations [167].

It is important to note that XFLR5's drag calculations differ from traditional LLT ones as it calculates it using far-field methods, i.e. at the Trefftz Plane. Far-field methods are based on conservation of momentum downstream of the body, whereas LLT calculates drag in the near-field, i.e. at the wing's surface [167]. Even though drag calculations at the near-field tend to be higher than at the far-field, near-field estimates tend to be very robust as they only depend on the local flow properties at the wing surface. In contrast, Trefftz-plane drag calculations tend to be more accurate, but may lead to incorrect results if calculations are performed inside the wake [168]. In summary, XFLR5 drag estimates are expected to be lower than those obtained by the implemented aerodynamic model, which calculates drag in the near-field.

Additionally, to ensure consistent and accurate results, a convergence study on the required number of spanwise horseshoe elements was performed. To evaluate this, the angle of attack was set to $\alpha = 5^\circ$ (to ensure fully attached flow), and an actuation input of $M_x = -2\,\text{N m}$ was applied at each actuation point. Under these conditions, a maximum FishBAC deflection of $x/c \approx 9\%$ is achieved. Lastly, the spanwise panel number was varied from 20 to 120, in increments of 10.

The model is said to be converged when the change in 3D lift coefficient with increasing number of spanwise elements is less than 0.1%. Based on this convergence study, a total of 60 spanwise elements are used.

Lastly, to validate the FSI coupling algorithm, a 2D comparison was performed against Woods and Friswell's XFOIL/Euler-Bernoulli FSI model [27]. To establish this comparison, the composite spine stiffness was 'homogenised' to obtain an equivalent Young's modulus that can be input to the beam model (see Equation 5.1 in Chapter 5.3.1). Furthermore, to simulate a 2D flow condition, downwash was suppressed on the 3D FSI model, and the span was set to 25 mm, which corresponds to the width of one of the actuation tendons.

7.5 Comparison: FishBAC vs. Flap

As mentioned in Section 7.1, to directly compare the FishBAC to a traditional control surface, a plain flap of equal percentage chord was evaluated using the built-in flap functionality of XFOIL and the same 3D aerodynamic nonlinear LLT solver developed in this chapter. These flapped aerofoils are likely to have unrealistically low drag values due to the lack of a gap between the flap the rest of the wing and the lack of control horns, but it does provide a useful initial comparison. Flap deflections of between $\delta = -30°$ and $\delta = +20°$, in increments of $+10°$, were evaluated at the same operating condition as the rigid and FishBAC wings.

7.6 Results

This section presents the FSI model results. The section is divided into two main subsections: model validation and camber morphing wing performance studies.

7.6.1 Model Validation

The validation of the FSI routine involves three different aspects: aerodynamic model, structural model and FSI routine validations. Since the structural model was validated in a previous chapter (see Chapters 4.6.2 and 4.6.1), this section mainly focuses on the aerodynamic model and FSI routine validations.

7.6.1.1 Aerodynamic Model

To validate the nonlinear LLT model, a rigid NACA 23012 wing was analysed using a nonlinear LLT routine developed by Tornero (2017) [166], as well as XLFR5's nonlinear LLT solver [167]. Percentage differences in lift and drag coefficients between the FSI's LLT model and Tornero's and XFLR5 models were calculated (Figure 7.6). Results show good agreement between Tornero's model and the FSI's aerodynamic model, with an average percentage difference of 0.658% and 1.001% in lift and drag, respectively.

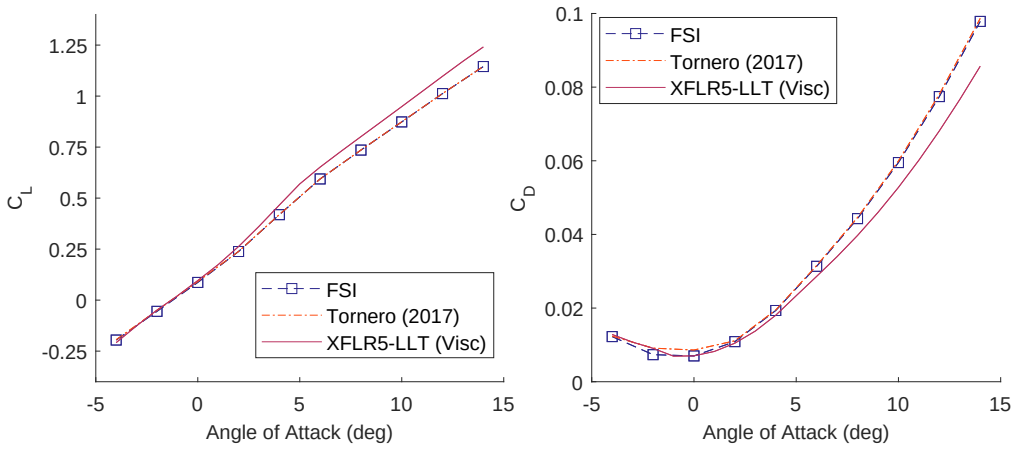

Figure 7.6: Aerodynamic model validation: lift and drag coefficient comparison

Moreover, the percentage difference with respect to XFLR5's LLT's model becomes 8.42% and 8.62% in lift and drag, respectively. It is important to note that, when looking at single values of drag coefficients, there is a direct correlation between the increasing angle of attack and increasing percentage difference, with the LLT's FSI model presenting higher drag values. This discrepancy is potentially due to XFLR5's drag calculations being performed at the Trefftz plane, whereas both Tornero's (2017) and the FishBAC FSI's nonlinear LLT model calculate drag at the near-plane. As described by XFLR5's user guide, drag calculations at the near-field tend to be higher, especially at high angles of attack [167].

In summary, the FSI nonlinear LLT model accurately predicts lift coefficient when compared to two other LLT-based solvers. However, discrepancies in drag exist, especially at high angles of attack. These discrepancies are likely due to slight differences in modelling techniques between traditional nonlinear LLT and XFLR5's nonlinear LLT. Therefore, it is important to treat drag estimates at high angles of attack with care, especially when it is well known that LLT may become inaccurate in modelling separated flows.

7.6.1.2 FSI Validation

The FSI algorithm validation was performed in two steps: *(i)* a 2D comparison to Woods and Friswell's 2D FSI [27] and *(ii)* a 3D aerodynamic comparison of the converged deformed shapes using XFLR5's.

1. 2D Validation

The 3D FishBAC FSI was directly compared to a previously developed 2D FishBAC FSI [27]. Figure 7.7 shows a comparison of lift and drag coefficients obtained by using each modelling technique. The lift and drag coefficient results show a good agreement between 2D FSI (beam model + XFOIL) and 3D FSI (plate model + LLT) routines.

Percentage differences in lift coefficients of less than 3% are observed for all five actuation cases. Additionally, the deformed shapes were also compared. Figure 7.8 shows the converged spine deflections as a function of torque input. An average discrepancy of less than 5% is observed between the two modelling techniques. In summary, the two models agree with each other, which confirms that the coupling routine of the 3D composite FishBAC FSI works accordingly.

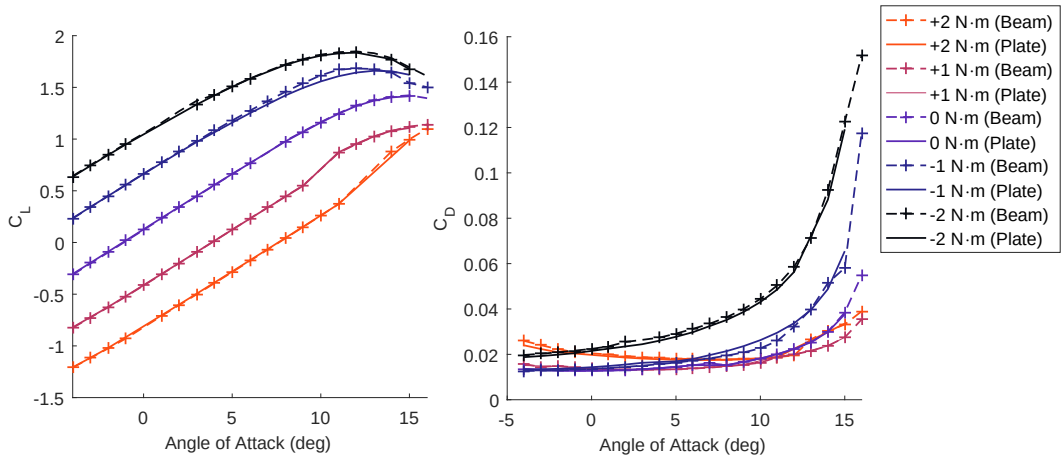

Figure 7.7: 2D FSI validation—lift and drag coefficients as a function of angle of attack.

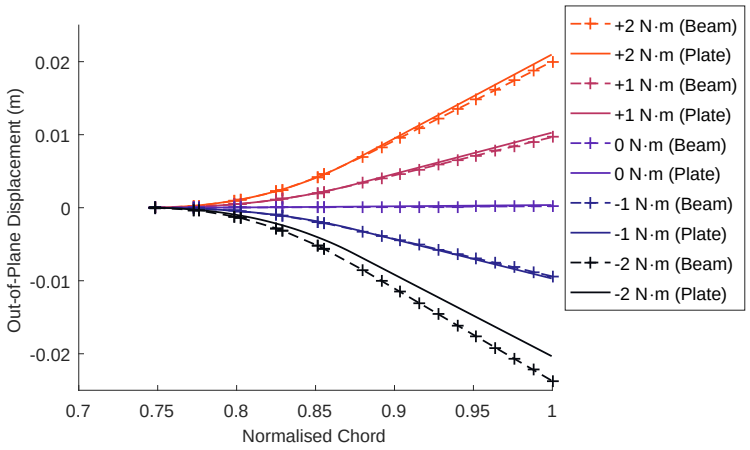

Figure 7.8: 2D FSI validation—FishBAC spine deflection.

2. 3D Comparison

The final step of the validation process is to compare the aerodynamic behaviour of several FSI converged, deformed shapes. To perform this comparison, three different load cases were considered at several angles of attack: (i) $M = -1\,\mathrm{N\,m}$ uniform actuation input at both actuators, inducing a large downward FishBAC deflection (ii) $M = +0.25\,\mathrm{N\,m}$ uniform actuator input, resulting on a small upward FishBAC deflection and (iii) a single actuation input of $M = -0.75\,\mathrm{N\,m}$ at the outboard actuator only, inducing significant spanwise variations in transverse displacements.

These deformed aerofoil shapes were extracted from the FSI solver and then input into XFLR5 and were analysed using the nonlinear viscous LLT analysis. Five different angles of attack were considered: two negative ($\alpha = -4°, -2°$), zero ($\alpha = 0°$), low positive ($\alpha = +5°$) and a high positive angle of attack ($\alpha = +12°$). Figure 7.9 shows the uniform negative actuation case as an example. Percentage differences in lift and drag coefficients were calculated and results are summarised in Table 7.1.

It is observed in Table 7.1 that an average percentage difference in lift and drag coefficients of 7.82% and 8.81%, respectively, exist. It is also observed that these values are highly dependent on the load case and angle of attack. For example, the lift coefficient percentage difference ranges between 2.90% to 13.27%, whereas the drag coefficient varies between 1.01% and 14.55%. These discrepancies could be due to either slight differences in calculating aerodynamic forces—as explained in the previous subsection—or due to discrepancies in the 2D aerofoil data used for viscous corrections. As previously mentioned, the 2D aerofoil data is obtained by running XFOIL using the local aerofoil geometry at each horseshoe element, for a wide range of angles of attack. XFOIL sporadically fails to converge at certain aerofoil geometries and angles of attack, and therefore, the effective angle of attack interpolations may be affected due to the lack of certain data points. One important observation from these results is that the highest percentage difference in drag values occur at the highest camber deflection—when both actuation inputs were $M_x = -1\,\mathrm{N\,m}$. Consequently, it was decided to reduce the maximum torque input per actuator to $M_x = -0.75\,\mathrm{N\,m}$. In summary, for the majority of cases, the FSI aerodynamic results agree with XFLR5's estimates with a percentage difference of less than 9%. However, these differences may increase up to 13% for certain cases, especially when larger camber deflections occur. In general, overall spanwise trends are well captured by the FSI's LLT and, therefore, this FSI analysis is suitable for design space explorations.

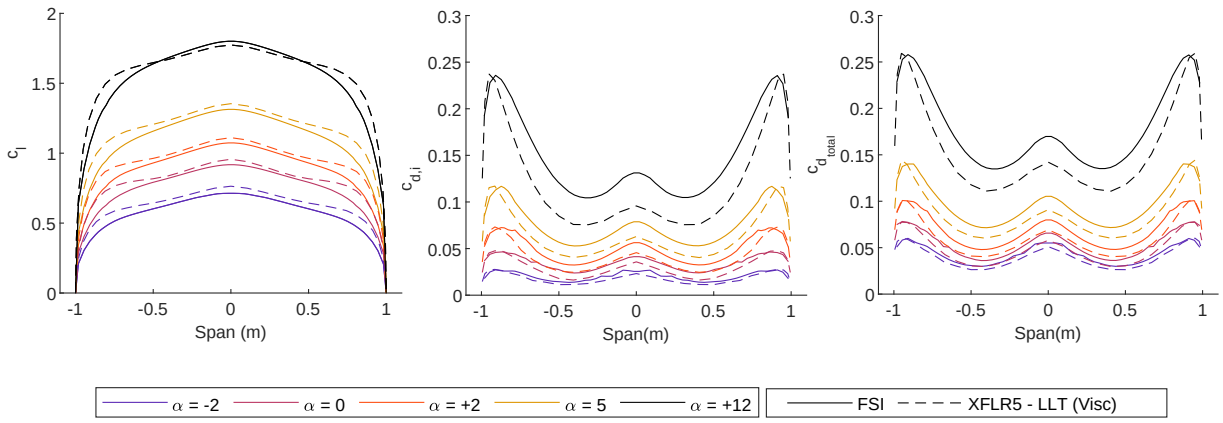

Figure 7.9: Aerodynamic Comparison between FSI converged aerodynamics and XFLR5's LLT, for an actuation input of $[M_{x_1}, M_{x_2}] = [-1, -1]$ N m.

Table 7.1: FSI validation test cases in terms of percentage difference in lift and drag coefficients (NC = not converged).

Load Case $[M_{x_1}, M_{x_2}]$	α (deg)	ΔC_L (%)	ΔC_D(%)
$[-1, -1]$ N m	-2	8.55	9.49
	0	6.34	12.62
	2	5.89	14.55
	5	6.14	13.31
	12	2.90	8.78
$[+0.25, +0.25]$ N m	-2	NC	NC
	0	NC	NC
	2	NC	NC
	5	9.58	4.77
	12	6.19	8.90
$[0, -0.75]$ N m	-2	13.27	1.010
	0	10.135	3.90
	2	8.679	4.915
	5	8.294	8.128
	12	NC	NC
Average		7.82	8.81

7.6.2 Aerodynamic Coefficients

This subsection introduces how the three main aerodynamic coefficients—C_L, C_D and C_m— vary with increasing FishBAC deflection. The first case to be considered is symmetric load input, where both actuators in each half-wing apply the same amount of torque.

7.6.2.1 Case 1: Symmetric Actuation

Figure 7.10 shows the lift, drag and moment coefficients as a function of angle of attack and symmetric actuation inputs. Results show that the FishBAC presents a lift control authority of $\Delta C_L \approx 0.5$ when only downward FishBAC deflections are considered. As expected, increasing deflection also increases drag, resulting in a change of drag coefficient that ranges from $\Delta C_D \approx 0.02$ to $\Delta C_D \approx 0.08$, for angles of attack between $\alpha = 0°$ and $\alpha = +14°$. Furthermore, a change in pitching moment coefficient between $\Delta C_m \approx 0.1$ and $\Delta C_m \approx 0.14$ is achieved when downward FishBAC deflections are considered. Although these results highlight the FishBAC's control authority, they do not provide sufficient information to assess aerodynamic efficiency. Therefore, lift-to-drag ratios as a function of angle of attack and lift coefficient are presented in Figure 7.11. It is observed in Figure 7.11 that a higher aerodynamic efficiency than the rigid NACA 23012 aerofoils can be achieved at low angles of attack and low lift coefficients. However, these efficiency gains decrease as the lift coefficient increases. Since the majority of the drag at high lift coefficients comes from the induced drag due to lift, having higher camber deflections at the wing root and gradually reducing them towards the wingtip may be beneficial for reducing induced drag. Therefore, if the actuation inputs are applied such that the wingtips are 'offloaded', higher aerodynamic efficiencies may be achieved. To assess the potential of these asymmetric deflections, a load case where only one actuator applies torque is considered in Section 7.6.2.2.

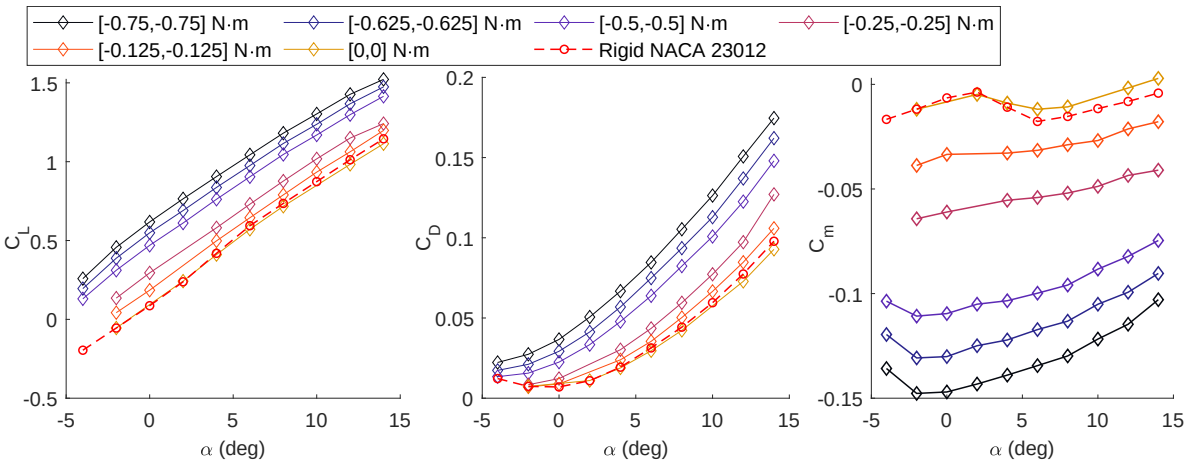

Figure 7.10: Lift, drag and moment coefficient as a function of angle of attack and FishBAC deflection. Actuation inputs are symmetric.

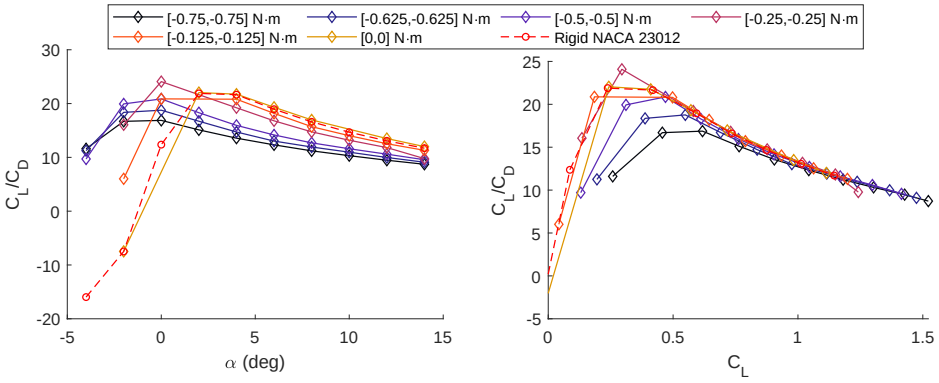

Figure 7.11: Aerodynamic efficiency as a function of angle of attack and lift coefficient. Actuation inputs are symmetric.

7.6.2.2 Case 2: Single Actuation Input

One way to estimate whether higher aerodynamic efficiency can be achieved by asymmetric actuation is to compare how aerodynamic coefficients vary if only one actuator is used in each half-wing. To determine the effect of using the inboard versus the outboard actuators, torque magnitude is kept constant and the actuation location is changed from inboard to outboard actuators. Figure 7.12 shows the lift, drag and moment coefficients for two pairs of actuation inputs: $-0.75\,\mathrm{N\,m}$ and $-0.625\,\mathrm{N\,m}$ at both inboard and outboard actuators, respectively. Results show that there is no significant change in lift coefficient with varying actuation location, however, a drag coefficient reduction between 2% and 5% is observed when the inboard actuator is used. In general, using the inboard actuator yields lower drag coefficients for all angles of attack. When compared in terms of aerodynamic efficiency as a function of both angle of attack and lift coefficient (Figure 7.13), it is observed that an increase in efficiency between 10% and 50% is achieved at low lift coefficients (i.e. $C_L < 0.5$), whereas an increase between 3.5% and 6.75% is observed for higher lift coefficients. These results are consistent with the fact that generating less lift near the wingtips would lead to a reduction in downwash at the wingtips—where it normally has its highest value in finite wings. Therefore, offloading the tips leads to lower induced drag and, thus, higher efficiency. However, using one actuator only comes at the expense of achieving lower lift coefficients due to lower camber deflections. Therefore, an alternative to obtain higher lift and lower drag coefficients, respectively, is to apply different non-zero actuation inputs at both inboard and outboard actuators.

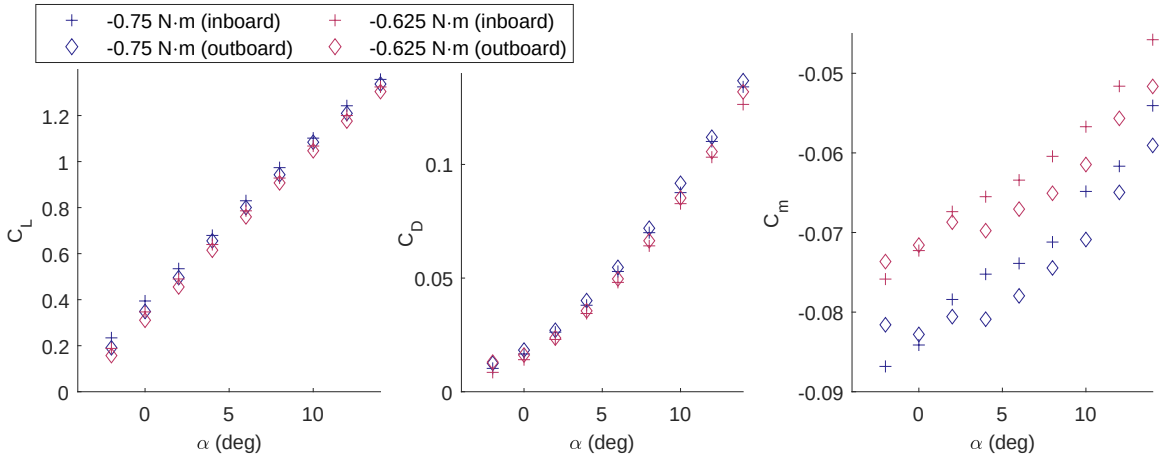

Figure 7.12: Lift, drag and moment coefficient as a function of angle of attack when only one actuator is used

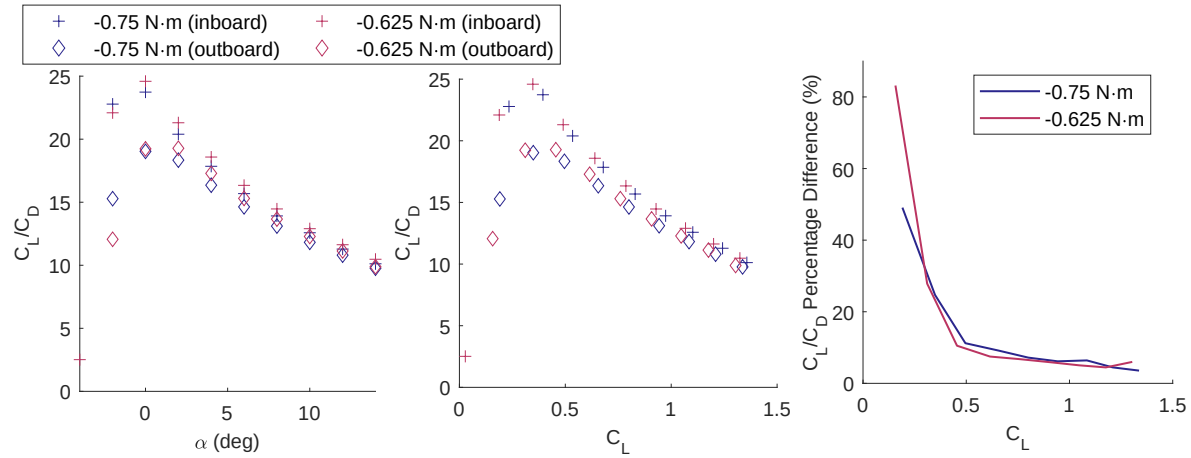

Figure 7.13: Aerodynamic efficiency as a function of angle of attack and lift coefficient when only one actuator is used

7.6.2.3 Case 3: Asymmetric Actuation Inputs

The third actuation case to be considered is when asymmetric actuation inputs are used—i.e. when the torque inputs at each inboard and outboard actuators are not equal. To fully explore the 'control space', a total of 117 configurations were studied, with torque values ranging from $-0.75\,\mathrm{N\,m}$ to $0.25\,\mathrm{N\,m}$ and for angles of attack between $\alpha = -4°$ and $\alpha = +14°$, in increments of $\alpha = 2°$. One way of analysing the resulting aerodynamic properties is to estimate the lift (Figure 7.14) and drag (Figure 7.15) coefficients, respectively, as a function of torque inputs and angle of attack. Each of the coloured surfaces in Figure 7.14 represents the FishBAC's lift control authority at a given angle of attack when all combinations of positive and negative actuation inputs are considered. An average lift control authority of $\Delta C_L = 0.58$ is achieved across all angles of attack, having a maximum value of $\Delta C_L = 0.63$ at $\alpha = 6°$ and a minimum value at $\Delta C_L = 0.50$ at $\alpha = 14°$. Also, an average change in drag coefficient of $\Delta C_D = 0.066$ is observed in Figure 7.15.

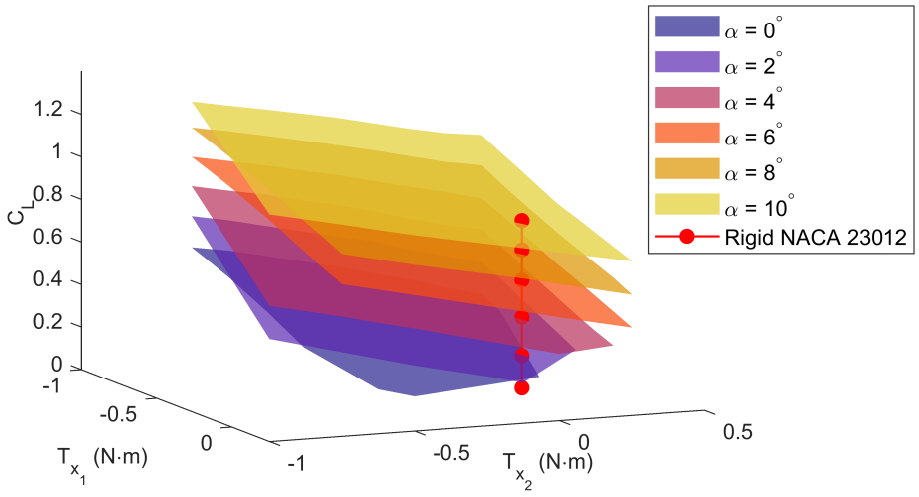

Figure 7.14: Lift coefficient as a function of angle of attack and actuation torque inputs.

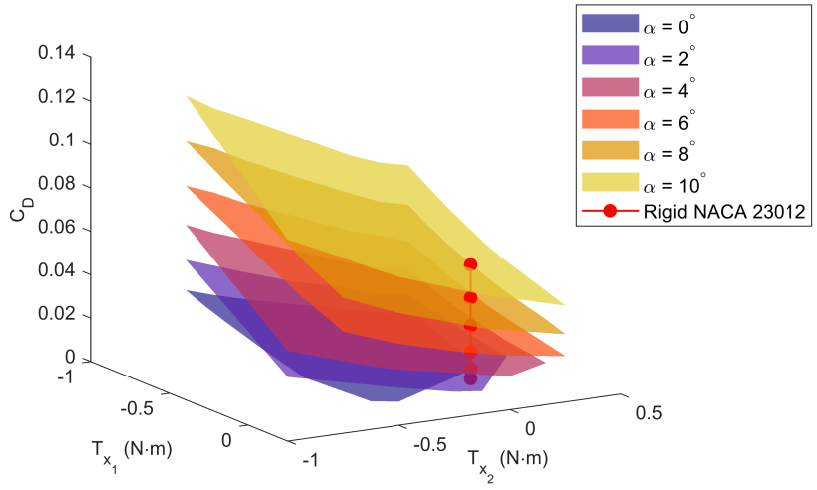

Figure 7.15: Drag coefficient as a function of angle of attack and actuation torque inputs.

These results show that a wide range of lift coefficients can be achieved without varying angle of attack. Also, results suggest that the additional drag due to these camber deflections is at least one order of magnitude lower than the increase in lift.

When observed in terms of lift-to-drag ratio (Figure 7.16), it is seen that C_L/C_D can widely vary with torque input. Hence, it may be difficult to estimate for a given desired lift coefficient what combination of actuation input and angle of attack yields the best aerodynamic efficiency. Since angle of attack and torque inputs can be controlled and set to a desired value—within torque available limits—one approach is to calculate the maximum achievable lift-to-drag ratio given freely varying angle of attack and camber morphing across the range of achievable lift coefficients. By doing so, the aerodynamic performance can be analysed in terms of a condensed metric that inherently considers all possible combinations of actuation inputs, angles of attack and camber deflections.

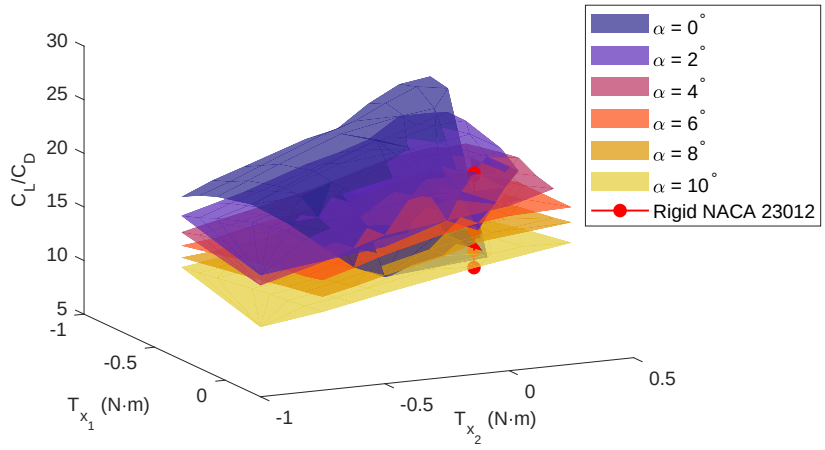

Figure 7.16: Lift-to-drag ratio as a function of angle of attack and actuation torque inputs

This condensed metric is particularly useful when comparing the aerodynamic performance of different trailing edge devices (e.g. FishBAC vs flap), as it can establish a direct comparison between different configurations that is independent of variables that may be different depending on the device—e.g. actuation inputs, camber deflections, angles of attack and flap angles.

Consequently, the aerodynamic efficiency (lift-to-drag ratio) of the FishBAC wing is now analysed as a function of achievable lift coefficients. Figure 7.17 shows all the lift-to-drag ratios corresponding to the different angles of attack and actuation combinations that were considered. In this figure, the left-hand side plot (Figure 7.17a) represents all the achieved lift-to-drag ratios for each angle of attack, whereas the right-hand side plot (Figure 7.17b) represents the best aerodynamic efficiency that can be achieved at each angle of attack, as a function of lift coefficient.

Moreover, angle of attack can be removed from this comparison by selecting the best aerodynamic efficiency that can be achieved at a given lift coefficient. By doing so, a direct comparison between FishBAC's and other configurations' best performances can be established.

As mentioned in Section 7.5, a rigid plain flap of equal chordwise dimension was analysed using the 3D aerodynamic model, and the resulting aerodynamic coefficients were used to directly compare the FishBAC with a plain flapped wing. Results show that the FishBAC has an aerodynamic efficiency improvement over the flap of at least 16% for lift coefficients between $C_L = 0.2$ and $C_L = 0.42$ (Figure 7.18). However, these efficiency improvements reduce to 5% for lift coefficients greater than $C_L = 0.42$. Although the FishBAC is more efficient than the flap at all lift coefficients, there is a clear reduction in efficiency gains as lift coefficient increases. These results suggest that this is potentially due to a rapid increase in induced drag as lift increases.

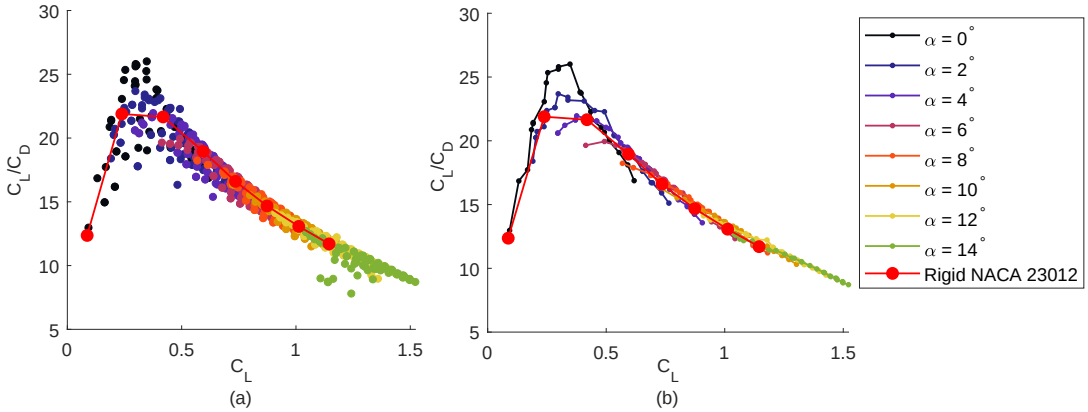

Figure 7.17: Achievable lift-to-drag ratios as a function of lift coefficient: (a) achieved lift-to-drag ratios for each angle of attack (b) best aerodynamic efficiency that can be achieved at each angle of attack.

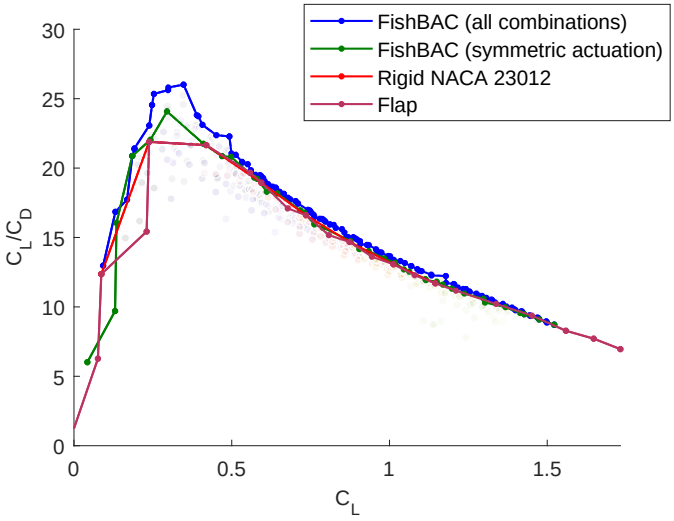

Figure 7.18: FishBAC and flap 3D aerodynamic efficiency comparison

To further investigate the increase in induced drag with increasing lift, the corresponding total, induced and profile drag coefficients for the best performing examples (as a function of lift coefficient) of each configuration are compared. Figure 7.19 shows these results, plotted on a double y-scale with the induced drag contribution to the total drag coefficient shown as a percentage. These results consistently show that profile drag dominates for lift coefficients lower than $C_L \approx 0.38$. At lift coefficients above $C_L \approx 0.4$, induced drag rapidly grows, and it represents approximately 85% of the total drag for lift coefficients above $C_L > 1.3$ in both FishBAC and flap configurations. These results explain why the aerodynamic efficiency improvements of the FishBAC diminish at higher lift coefficients. Therefore, it can be concluded that for the wing design investigated here, the benefit of using the FishBAC is more significant when profile drag is higher than induced drag.

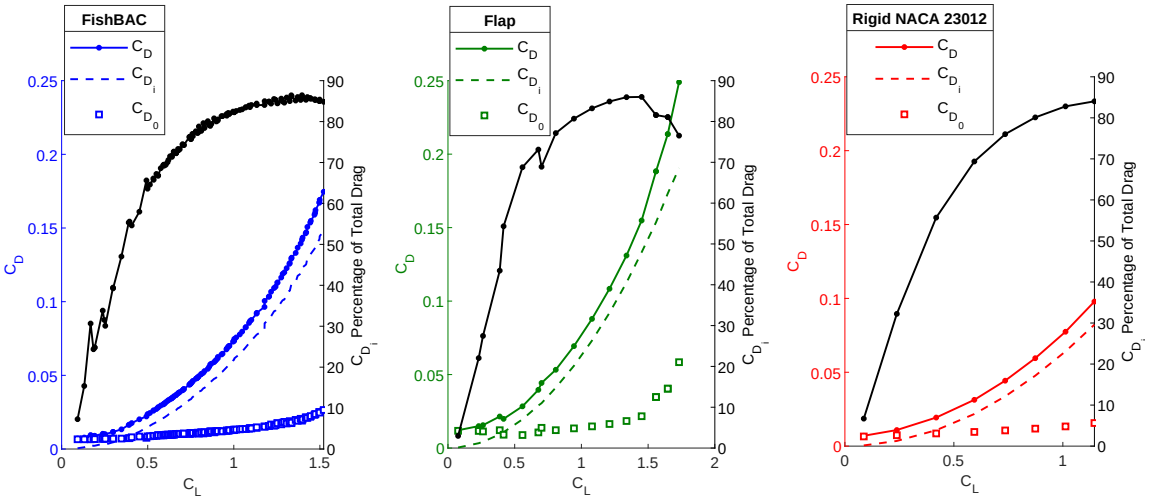

Figure 7.19: Comparison between total, induced and profile drag coefficients.

It is worth noting that the chosen rectangular planform, untwisted wing geometry of modest aspect ratio does not have particularly good performance with respect to induced drag. Therefore, it will be interesting in future work to consider a wider range of wing geometries, which will build off on and reinforce this initial investigation into the aerodynamics of camber morphing wings.

7.6.2.4 Case Study: Constant Lift Coefficient

Aeroplanes spend the majority of a flight at cruise condition. These cruise operations normally occur in a wings-level equilibrium flight condition—i.e. when lift equals weight and no vertical acceleration occurs. However, as the weight of the aircraft decreases due to fuel burn, the required lift to maintain equilibrium also decreases. One way of reducing the lift force to compensate for this weight reduction is to change the angle of attack. However, aerofoils typically have their maximum lift to drag ratio over a fairly narrow band of angles of attack, implying a drag penalty for changing AOA. Also, there may also be a drag penalty due to an increase in fuselage drag if angle of attack is changed. An alternative is to 'trim' the aircraft by actively using control surfaces, also resulting in a drag penalty (trim drag) that is usually lower than the increase in drag due to change in angle of attack [169]. A third option is to decrease lift by increasing altitude, which reduces the aerodynamic forces due to a reduction in air density. Although effective, these changes in altitude are limited by flight control operations and the need to gain permission for flight level changes, hence the stepped cruise profile common for commercial air traffic. The adaptability of a morphing wing could allow for efficient variations in lift without varying angle of attack and/or altitude, and without the associated drag penalty of hinged control surfaces.

To further study this hypothesis, the best achievable drag coefficients at constant lift coefficients and angles of attack have been interpolated from the FishBAC data set using a triangulation linear interpolation function. Figure 7.20 shows the resulting minimum achievable drag coefficients as a function of angle attack for lines of constant lift coefficient (achievable through morphing). There are two main points that can be inferred from these results: *(i)* a change in lift coefficient of at least $\Delta C_L = 0.4$ (and often up to $\Delta C_L = 0.8$) can be achieved at each angle of attack and *(ii)* the minimum achievable drag associated with each lift coefficient is relatively constant and independent of angle of attack. In other words, a significant change in lift coefficient can be achieved without changing angle of attack. This ability to change lift coefficient at a constant angle of attack may be desirable in certain manoeuvres, as lower fuselage and empennage drag could be achieved by aligning the fuselage with the incoming flow. Also, Figure 7.20 shows that certain lift coefficients can be achieved at a wide range of angles of attack without significant drag increases. These results highlight how adaptive a FishBAC morphing wing is and how this can be exploited for improving aerodynamic efficiency at a broad range of angles of attacks and lift coefficients.

Finally, these resulting constant lift coefficients can be observed as a function of their corresponding drag coefficients as seen in Figure 7.21. Given this range of obtainable results, the non-dominated points across the entire data set can be determined to create the Pareto frontier of each set [170]. This Pareto frontier represents the lift coefficients that can be achieved at the lowest drag penalty, thus maximising lift-to-drag ratio for a desired C_L. Also, Figure 7.21 shows the converged flap results and its corresponding Pareto frontier. As observed, the FishBAC presents lower drag coefficients for all lift coefficients and the area between the two Pareto frontiers represents the aerodynamic efficiency gains.

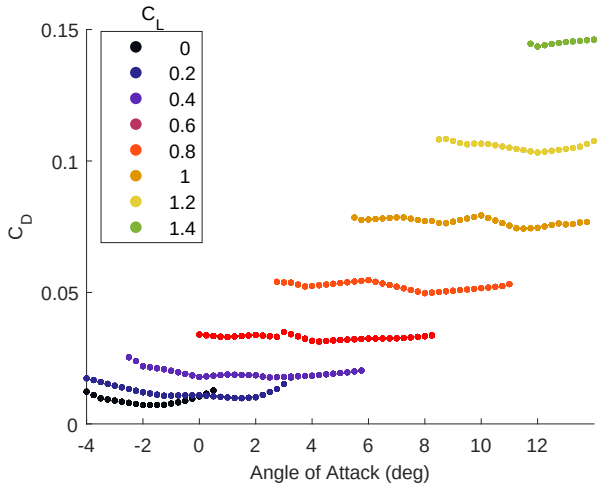

Figure 7.20: Drag coefficients as a function of fixed lift coefficients and angle of attack.

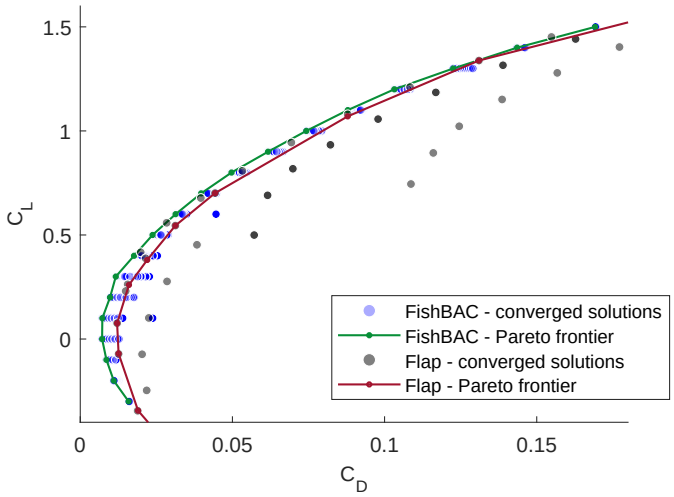

Figure 7.21: Pareto frontier of achievable lift coefficients as a function of drag coefficients.

7.7 Conclusions

This chapter introduced a 3D FSI analysis of a composite FishBAC camber morphing wing. The loosely-coupled routine is based on a discontinuous Mindlin-Reissner plate model (introduced in Chapter 4) and a viscous corrected nonlinear Lifting-Line Model for the structural and aerodynamic solvers, respectively. This model is capable of obtaining converged three-dimensional lift, drag and moment coefficients and aerodynamic pressure distributions for different combinations of Mach number, angle of attack, actuation torque inputs and Reynolds number. After performing an analysis at a Mach number of $M = 0.089$ and a Reynolds number of $Re \approx 543{,}000$ on a simple rectangular planform wing test case, the following conclusions were drawn:

1. The 3D composite FishBAC device has a lift control authority of between $\Delta C_L = 0.5$ and $\Delta C_L = 0.63$, for the actuation inputs considered.

2. Actuation inputs that induce lower camber deflections in the outboard section of the wing lead to a higher overall aerodynamic efficiency. Offloading the tip has a direct impact in reducing induced drag. An increase in lift-to-drag ratio between 5% and 7% can be achieved by this induced drag reduction.

3. The FishBAC wing is capable of achieving a wide range of constant lift coefficients across a wide range of angles of attack by varying actuation input. At these constant lift coefficient cases, the drag coefficient remains relatively stable when varying angle of attack. This feature highlights how adaptive the FishBAC morphing wing can be for a wide range of angles of attack and lift coefficients.

4. The FishBAC presents a 16% higher aerodynamic efficiency than a plain flap wing, for low lift coefficients between $C_L = 0.2$ and $C_L = 0.42$. However, this percentage improvement decreases to 5% when lift coefficients above $C_L = 0.42$ are considered. This decrease in benefit is due to induced drag becoming significantly larger than profile drag at higher lift coefficients—an effect exacerbated by the rectangular, untwisted planform considered here as an initial test case. Lastly, it is important to remind that the flapped configuration is a "best case" scenario, with neither structural gap nor control horns.

5. In terms of components of total drag, profile drag dominates for lift coefficients below $C_L = 0.38$. For lift coefficients above this value, induced drag rapidly grows, and becomes > 85% of the total drag for lift coefficients greater than $C_L > 1.3$. Therefore, introducing design features to reduce induced drag (e.g. twist, taper, and higher aspect ratio) could potentially lead to further enhanced FishBAC behaviour for more sophisticated wing designs operating at higher lift coefficients.

This chapter introduced a Fluid-Structure Interaction routine that models the coupled structural and aerodynamic behaviour of a 3D composite FishBAC in a fixed-wing configuration. Additionally, this model was used to explore the potential aerodynamic benefits of the FishBAC in 3D finite wings. Results in this chapter suggest that the FishBAC can bring significant benefits to 3D wings, including induced drag minimisation and large lift control authority. Future work should include wing planform features for induced drag reductions (e.g. taper, twist, sweep and higher aspect-ratio), and should also consider higher Mach and Reynolds numbers.

Chapter 8

Conclusions and Future Work

Traditional fixed-wing aircraft vary their wing geometries during flight by deflecting a series of hinged flaps that are attached to the trailing edge of their wings. Although effective in producing changes in aerodynamic loads that allow for aircraft control and trim, the use of hinged flaps comes with a cost: a drag penalty caused by the sharp and discontinuous change in shape and the structural gap that must exist on the wing surface to allow flap rotation about its hinge.

A potential solution to avoid the drag penalties associated with hinged flaps is the use of camber morphing trailing edge devices, which are aerostructures that have been carefully engineered to vary aerofoil geometry without surface discontinuities or gaps. These devices can achieve similar lift control authority as flaps, but with a much lower drag penalty. In addition to the benefits in all flight conditions created by the lower drag penalty, morphing also opens up the option of continuously varying wing camber to optimise aerodynamic performance throughout the course of a mission. By doing so, higher aerodynamic efficiencies may be achieved at all stages of flight, leading directly to reductions in fuel consumption. A particularly promising camber morphing concepts is the FishBAC, which was initially designed using 1-dimensional modelling tools and manufactured using 3D printed plastic. Preliminary wind tunnel tests of this initial FishBAC prototype showed favourable aerodynamic efficiency gains, motivating further study.

The research undertaken to support this thesis was driven both by the promising initial performance gains that the FishBAC has shown and by the desire to develop more sophisticated analysis methods and design solutions. The goal of these two is to provide a more thorough understanding of the FishBAC's behaviour and to push the concept towards real-world implementation. To scale up this technology, it is first necessary to develop modelling tools that can capture the structural, aerodynamic and aeroelastic behaviour of 3D FishBAC wings. Additionally, the use of high-performance aerospace grade materials is a crucial step towards implementing this concept in real aerostructures.

Based on the results presented in this thesis, from a general point-of-view, it can be concluded that using a composite FishBAC device in a 3D wing can lead to a reduction in drag between 5% and 20%, and with a lift control authority similar to that of hinged flaps (i.e. $\Delta C_L = 0.5 - 0.7$). Results also show that the FishBAC has significantly higher actuation energy requirements than hinged flaps and, therefore, actuation energy must be coupled with structural and aerodynamic loads in future FSI analysis and design iterations. If actuation energy is included in these future design iterations, it will ensure that *(i)* the FishBAC structure is designed to minimise actuation energy requirements and *(ii)* the power-to-weight ratio of the actuation mechanism is taken into account, which is especially important if different types of actuators are to be considered. In

summary, the FishBAC is still showing promising results in terms of improving aerodynamic efficiency, however, more work is needed at the systems level to ensure that the aerodynamic efficiency gains are not offset by actuation and structural weight penalties.

8.1 Review of Aims and Objectives

As presented in Chapter 1, the aims of this thesis are: *(i)* to develop modelling tools that can capture both chordwise and spanwise structural behaviour of composite FishBAC devices, as well as the 3D aerodynamics of FishBAC morphing wings; and *(ii)* to design and manufacture a carbon-fibre FishBAC device that can be used to experimentally validate both structural and aerodynamic simulations, and to obtain additional wind tunnel data to further understand the potential benefits of using the FishBAC instead of hinged flaps. Based on these aims, the objectives of this thesis were defined as:

1. To develop a two-dimensional parametrically driven structural model capable of capturing both chordwise and spanwise behaviour of a composite FishBAC under both structural and aerodynamic loads. This structural model must be more computationally efficient than modelling the FishBAC using FEM.

2. To develop a 3D FSI analysis to consider both the structural and aerodynamic response of the FishBAC in a coupled routine. This structural model must be more computationally efficient than FEM/CFD-based FSI solvers so that it can be used for design space exploration and optimisation.

3. To design, manufacture and test a composite FishBAC wind tunnel wing model. The following tests are to be performed:

    a) Static structural test for structural model validation.

    b) Wind tunnel test for both understanding the aerodynamic benefits of the FishBAC and for future validation of FSI analysis.

8.2 Major Contributions & Main Findings

The major research contributions introduced by this thesis are presented in this section. These major contributions are classified based on the two aims.

8.2.1 Methods for Modelling Three-Dimensional Composite FishBACs

To successfully model three-dimensional composite FishBAC wings, three different aspects must be modelled: the structures, the aerodynamics and the interaction between the two. Consequently,

structural and aerodynamic models have been developed and then coupled in an FSI routine. This subsection summarises the major findings from developing these new modelling techniques.

8.2.1.1 Structural Modelling of Discontinuous Composite Morphing Structures

Two parametrically-driven structural plate-based models were developed in this thesis: the first one is based on Kirchhoff-Love Plate Theory, whereas the second one is based on Mindlin-Reissner Plate Theory. The two discontinuous plate-based models can capture the static behaviour of fully anisotropic FishBAC devices (i.e. chordwise and spanwise displacements and rotations) using a single system of linear equations. The Kirchhoff-Love and Mindlin-Reissner formulations use 84% and 99% fewer degrees of freedom, respectively, than converged FEM models.

The novelty of these models lies in their ability to capture the complex structural nature of the FishBAC by discretising its geometry into a series of individual composite plates, each one with an equivalent stiffness at the mid-plane, that are joined together using a series of artificial penalty springs. This modelling approach allows for rapid modification of the structural and material parameters (e.g. spine stacking sequence, dimensions, stringer spacing) and, due to its mesh-independence and semi-analytical nature, it can compute converged displacement fields by solving a fixed number of linear equations. These two-dimensional composite models are a significant extension on a previously developed 1D isotropic beam model of the FishBAC, which is unable to model spanwise displacements nor composite laminates.

Additionally, one of the major findings in developing these models was the existence of transverse shear stresses under certain load cases (i.e. asymmetric load inputs that induce twist on the FishBAC).

Transverse Shear Effects on Discontinuous Plate Structures

Although the FishBAC's spine meets the thin plate criterion (i.e. $t/c < 1/30$), the presence of several spanwise stringers—where local $t/c > 1/5$ are achieved—results in significant transverse shear stresses for actuation inputs that induce structural twist about the yz-plane. These load cases cannot be modelled using Kirchhoff-Love Plate Theory as this formulation neglects transverse shear effects. This limitation was addressed by developing the Mindlin-Reissner model, which accounts for transverse shear effects by implementing the First-Order Shear Deformation Theory. The Mindlin-Reissner model was validated against both FEM and experimental results, showing its ability to predict the static behaviour of composite FishBAC devices under all actuation load cases. In summary, this model fulfils the above-stated objective of developing a structural model that can capture the chordwise and spanwise displacements of a composite FishBAC subjected to both actuation and aerodynamic loads. Due to its computational efficiency, the model is suitable for FSI analysis and for design and optimisation studies.

8.2.1.2 Fluid-Structure Interaction of Three-Dimensional Composite FishBACs

A Fluid-Structure Interaction routine has been developed by combining the Mindlin-Reissner plate model with an XFOIL augmented nonlinear Lifting-Line aerodynamic model. This FSI routine is capable of analysing the aerodynamic behaviour of 3D FishBAC wings for a wide range of incompressible freestream velocities, Reynolds numbers, angles of attack and actuation inputs. This aerodynamic model can capture aerodynamic pressure changes due to localised changes in aerofoil shape, three-dimensional aerodynamic effects (i.e. downwash), as well as viscous drag. This new 3D FSI for FishBAC wings is a more capable analysis than the 2D FSI reported in the literature, which is unable to model 3D wings. To make use of this new capability to analyse the coupled aeroelastic behaviour of 3D FishBAC wings, the 3D FSI routine introduced in this thesis was used for preliminary design space explorations of FishBAC wings for aeroplanes.

These preliminary design explorations were based on aerodynamic performance estimations of a composite 3D FishBAC wing at different actuation input combinations and angles of attack. Results show that the FishBAC has a lift control authority between $\Delta C_L = 0.5$ and $\Delta C_L = 0.63$, for a wide range of angles of attack. Additionally, these lift coefficient gains come with low drag penalties, which makes the FishBAC suitable for continuously optimising wing geometry during flight.

The 3D FishBAC wing was directly compared to a plain flapped wing analysed using the same aerodynamic modelling tool and input conditions. The FishBAC shows an increase in aerodynamic efficiency of 16% for lift coefficients between $0.2 > C_L > 0.43$. For higher lift coefficients, this efficiency increase reduces to 5%, which is caused by a rapid increase in induced drag. These results were then used to further investigate the potential benefits that the FishBAC may bring to a 3D wing, for example, in reducing induced drag by controlling spanwise changes in camber.

Induced Drag Reduction and Aerodynamic Efficiency

The FishBAC can be used to reduce induced drag by decreasing the amount of camber in the outboard sections of the wings. This can be achieved by applying higher torque inputs in the actuators located near the wing root and lower torque inputs in the actuators located near the wingtips. This actuation combination offloads the wingtips, and leads to aerodynamic efficiency gains between 3% and 5%. A rigid hinged flap configuration is unable to achieve these gradual changes in camber along the wing span and, therefore, cannot achieve these reductions in induced drag. However, one main observation from these 3D wing results is that the FishBAC's aerodynamic efficiency gains diminish with increasing lift coefficient; thus, the efficiency gains at high lift coefficients are significantly lower than the ones observed at the 2D level (Chapter 6). It was concluded that this efficiency reduction is due to induced drag becoming the highest drag contribution at lift coefficients greater than $C_L > 0.4$. Additionally, it was estimated that induced drag can contribute up to 85% of the total drag for lift coefficients greater than $C_L > 1.3$.

Therefore, a planform design that reduces induced drag may improve the aerodynamic benefits of camber morphing across a broader range of lift coefficients.

8.2.2 Design, Manufacture & Wind Tunnel Test of Composite FishBAC

A first of its kind composite spine FishBAC wind tunnel wing model was designed and manufactured using a combination of materials and manufacturing techniques. This process demonstrated the possibility of producing a composite spine FishBAC. Additionally, the resulting wing model underwent a series of structural and aerodynamic wind tunnel experiments to investigate the static structural and aerodynamic behaviour of this composite FishBAC wing model. The structural results were used to experimentally validate the Mindlin-Reissner plate model, whereas the wind tunnel results were used to further investigate the aerodynamic benefits of camber morphing.

8.2.2.1 Static 2D Wind Tunnel Test

The most extensive wind tunnel test campaign on the FishBAC concept to date is presented in this thesis, as well as the most complete and detailed comparison between flaps and camber morphing present in the literature. Force balance and wake rake survey data were used to quantify the aerodynamic performance of both FishBAC and flap configurations, at a wide range of angles of attack and camber deformations and at freestream velocity of 30 m/s. Additionally, optical aerodynamic and structural measurements were performed using PIV and a stereo VG point tracking system, respectively. These optical measurements provide a more detailed understanding of the aeroelastic behaviour of the FishBAC.

Aerodynamic Efficiency

Results show that the FishBAC has significantly higher aerodynamic efficiency than the hinged plain flap. These efficiency gains are remarkable at moderate to high lift coefficients (i.e. $C_L > 1$), where the improvement is at least 50%. For typical operating lift coefficients (i.e. $0.5 > C_L > 1$), these efficiency gains are of 40% on average (and at least 16%). In general, the FishBAC presents a higher aerodynamic efficiency than the flap, across all tested angles of attack and achievable lift coefficients, which is an exceptional performance when compared against other camber morphing aerodynamic studies presented in the literature.

Optical Measurements

PIV and VG tests were performed to visually measure wake velocities and structural displacements, respectively. These PIV and VG are the first optical displacement and aerodynamic measurements, respectively, that are performed on the FishBAC device. PIV results show that the FishBAC's wake remains stable and thin over a wide range of camber deflections. Conversely,

the flap's wake thickness increases by around 60% (compared to its undeflected value) with increasing flap deflections. These results show the extent to which flap deflections induce flow separation, and how much better the FishBAC is—results which are corroborated by the wake survey.

Lastly, Videogauge displacement measurements on the FishBAC showed that aerodynamic loads significantly reduce the maximum camber deflections that the FishBAC can achieve. Specifically, they showed that even at low angles of attack, this deflection reduction could be as large as 60%. These results highlight the importance of designing and sizing the FishBAC and its actuation mechanism using a fully coupled FSI analysis, as the aerodynamic stiffness is as relevant as the structural stiffness in compliance-based morphing structures.

8.3 Future Work

Based on the work presented in this thesis, this section suggests potential routes for future work. These routes can be divided into computational and experimental work.

8.3.1 Computational

1. **Dynamic analysis of the FishBAC:** the Mindlin-Reissner structural model can be expanded to perform dynamic analysis of the FishBAC. Using the same Rayleigh-Ritz formulation, the dynamics of the FishBAC can be incorporated in terms of kinetic energy. A dynamic analysis would allow for the investigation of the natural frequency and mode shapes of the system, its damping properties and its overall dynamic stability. Also, the aerodynamic model could potentially be modified to perform time-dependent analysis, where dynamic perturbations, such as gust, could be introduced. If successfully implemented, a dynamic FSI analysis could study the use of the FishBAC as a load alleviation device.

2. **Higher-fidelity aerodynamic model for FSI:** the nonlinear Lifting-Line theory that was introduced in this thesis is capable of capturing the aerodynamics of 3D camber morphing wings. However, it is well known that the use of Lifting-Line Theory should be limited to the analysis of unswept wings under fully attached flow regimes and at incompressible Mach numbers. These conditions are highly relevant for a wide range of applications, but improved methods would allow for consideration of performance at higher Mach numbers and more severe angles of attack.

3. **Structural Optimisation of FishBAC device:** the developed FSI model can be used for optimising the FishBAC structure. Parameters such as stringer thickness and spacing and the stacking sequence of the composite spine can be optimised to achieve selected design objectives, e.g. minimum mass, maximum lit-to-drag-ratio and minimum actuation energy requirements.

4. **Investigate FishBAC's aerodynamic control properties:** another study that can be performed using the FSI routine is to investigate the FishBAC's ability to work as a control surface by quantifying stability derivatives (e.g. roll and pitch rates).

8.3.2 Experimental

5. **Design, manufacture and test of composite FishBAC 3D wing:** a 3D cantilever wind tunnel test should be performed to experimentally investigate aerodynamic behaviour of a 3D FishBAC wing. This requires the design, manufacture and test of another wind tunnel wing model with a higher aspect ratio. Additionally, this test can also be used to experimentally measure stability derivatives.

6. **Fatigue:** the fatigue properties of the FishBAC are yet to be investigated. This is another important task that must be performed for technology maturity purposes. If the FishBAC is used as a control surface, for aerodynamic optimisation and for load alleviation, the structure and actuation mechanism would perform many deflection cycles per flight. Therefore, the structural life cycle and material degradation due to cyclic use must be investigated.

7. **Manufacture of fully composite FishBAC devices:** future FishBAC structures can incorporate a higher number of composite parts. For example, the stringers and the trailing edge strip—currently 3D printed—should be made using fibre-reinforced polymers. However, due to the slenderness of the stringers, this may be a difficult task to perform by hand layup. Therefore, an alternative would be to automate the manufacturing process, for example, by introducing Automated Tape Laying (ATL) or Automatic Fibre Placement (AFP).

8. **Wing skin materials:** the elastomeric skin materials used in this work are not certified for commercial flight operations, and would need to undergo a very rigorous testing process to be certified. Other elastomeric materials are available which have been certified for various aerospace applications (e.g. elastomeric leading edge erosion coatings) but they are not as highly strained as the skins used in this thesis. Therefore, further work is needed on either identifying alternative materials or developing and certifying novel elastomeric matrix composites for morphing applications.

9. **Actuator selection:** one important characteristic of the FishBAC is that it is actuation agnostic. Therefore, the actuation mechanism is not restricted to being servo-based. Other types of lightweight and fatigue-resistant actuators, such as Pneumatic Artificial Muscles (PAMs), may represent an efficient alternative to servo motors.

Bibliography

[1] "Facts and Figures: World Aviation and the World Economy," *International Civil Aviation Organization*, 2019.

[2] "IATA Forecast Predicts 8.2 billion Air Travelers in 2037," *IATA Press Release No.: 62*, pp. 3–7, 2018.

[3] D. Koenig, "A New Report Says U.S. Airline Carbon Emissions Are Growing Fast," *Time*, 2019.

[4] J. J. Lee, "Can we accelerate the improvement of energy efficiency in aircraft systems?," *Energy Conversion and Management*, vol. 51, no. 1, pp. 189–196, 2010.

[5] "Aviation Emissions, Impacts and Mitigation: A Primer," *Office of Environment and Energy, Federal Aviation Administration (FAA)*, no. January, pp. 1–38, 2015.

[6] L. L. Gamble and D. J. Inman, "A tale of two tails: Developing an avian inspired morphing actuator for yaw control and stability," *Bioinspiration and Biomimetics*, vol. 13, no. 2, 2018.

[7] S. Barbarino, O. Bilgen, R. M. Ajaj, M. I. Friswell, and D. J. Inman, "A Review of Morphing Aircraft," *Journal of Intelligent Material Systems and Structures*, vol. 22, no. 9, pp. 823–877, 2011.

[8] C. Thill, J. Etches, I. Bond, K. Potter, and P. Weaver, "Morphing skins," *Aeronautical Journal*, vol. 112, no. 1129, pp. 117–139, 2008.

[9] M. Recksiek, "Advanced High Lift System Architecture With Distributed Electrical Flap Actuation," in *2nd International Workshop on Aircraft System Technologies*, (Hamburg, Germany), pp. 1–11, 2009.

[10] E. Greff, "The development and design integration of a variable camber wing for long/medium range aircraft," *The Aeronautical Journal*, vol. 94, no. 939, pp. 301–312, 1990.

[11] H. Parker, "The Parker Variable Camber," Tech. Rep. 77, National Advisory Committee for Aeronautics, Washington, DC, 1920.

[12] H. J. Hogan, "Variable Camber Airfoil," *U.S. Patent 1 ,868,748*, 1932.

[13] R. Chilton, "Variable Area-and-Camber Wing," *U.S. Patent 2,222,935*, 1940.

[14] O. Bilgen, M. I. Friswell, K. B. Kochersberger, and D. J. Inman, "Surface Actuated Variable-Camber and Variable-Twist Morphing Wings Using Piezocomposites," *Structures, Structural Dynamics and Materials Conference*, vol. 19, no. April, pp. 1–13, 2011.

[15] S. Kota, J. A. Hetrick, R. Osborn, D. Paul, E. Pendleton, P. Flick, and C. Tilmann, "Design and application of compliant mechanisms for morphing aircraft structures," *Proc. SPIE*, vol. 5054, no. November, pp. 24–33, 2003.

[16] A. Sofla, S. Meguid, K. Tan, and W. Yeo, "Shape morphing of aircraft wing: Status and challenges," *Materials & Design*, vol. 31, no. 3, pp. 1284–1292, 2010.

[17] S. Barbarino, R. Pecora, L. Lecce, A. Concilio, S. Ameduri, and E. Calvi, "A novel SMA-based concept for airfoil structural morphing," *Journal of Materials Engineering and Performance*, vol. 18, no. 5-6, pp. 696–705, 2009.

[18] C. G. Diaconu, P. M. Weaver, and F. Mattioni, "Concepts for morphing airfoil sections using bi-stable laminated composite structures," *Thin-Walled Structures*, vol. 46, no. 6, pp. 689–701, 2008.

[19] S. Daynes, S. Nall, P. Weaver, K. Potter, P. Margaris, and P. Mellor, "Bistable Composite Flap for an Airfoil," *Journal of Aircraft*, vol. 47, no. 1, pp. 334–338, 2010.

[20] J. Rivas-Padilla, A. F. Arrieta, and D. M. Boston, "Design of selectively compliant morphing structures with shape-induced bi-stable elements," in *AIAA Scitech 2019 Forum*, 2019.

[21] R. R. Larson, "Flight Control System Development and Flight Test Experience With the F-111 Mission Adaptive Wing Aircraft," tech. rep., NASA Ames Research Center, Edwards, California, 1986.

[22] J. N. Kudva, "Overview of the DARPA Smart Wing Project," *Journal of Intelligent Materials Systems and Structures*, vol. 15, no. 4, pp. 261–267, 2004.

[23] G. Molinari, M. Quack, V. Dmitriev, M. Morari, P. Jenny, and P. Ermanni, "Aero-Structural Optimization of Morphing Airfoils for Adaptive Wings," *Journal of Intelligent Material Systems and Structures*, vol. 22, no. 10, pp. 1075–1089, 2011.

[24] B. K. S. Woods and M. I. Friswell, "Preliminary Investigation of a Fishbone Active Camber Concept," in *ASME Conference on Smart Materials, Adaptive Structures and Intelligent Systems*, 2012.

[25] B. K. S. Woods, O. Bilgen, and M. I. Friswell, "Wind tunnel testing of the fish bone active camber morphing concept," *Journal of Intelligent Material Systems and Structures*, vol. 25, no. 7, pp. 772–785, 2014.

[26] B. K. S. Woods and M. I. Friswell, "Structural Characterization of the Fish Bone Active Camber Morphing Airfoil," in *22nd AIAA/ASME/AHS Adaptive Structures Conference, AIAA SciTech*, pp. 1–11, 2014.

[27] B. K. S. Woods, I. Dayyani, and M. I. Friswell, "Fluid/Structure-Interaction Analysis of the Fish-Bone-Active-Camber Morphing Concept," *Journal of Aircraft*, vol. 52, no. 1, pp. 307–319, 2014.

[28] G. D. Padfield and B. Lawrence, "The birth of flight control: An engineering analysis of the wright brothers' 1902 glider," *Aeronautical Journal*, vol. 107, no. 1078, pp. 697–718, 2003.

[29] C. H. Grant, "Variable Camber Wing," *US Patent 2,146,014*, 1939.

[30] I. Chopra, "Review of state of art of smart structures and integrated systems," *AIAA Journal*, vol. 40, no. 11, pp. 2145–2187, 2002.

[31] T. A. Weisshaar, "Morphing aircraft systems: Historical perspectives and future challenges," *Journal of Aircraft*, vol. 50, no. 2, pp. 337–353, 2013.

[32] J. Sun, Q. Guan, Y. Liu, and J. Leng, "Morphing aircraft based on smart materials and structures: A state-of-the-art review," *Journal of Intelligent Material Systems and Structures*, vol. 27, no. 17, pp. 2289–2312, 2016.

[33] J. Makhonine, "Variable Surface Wings and Tail Fins in Flying Machines," *US Patent 2,550,278*, 1951.

[34] T. C. Harper, "Extensible Structure for Varying Configuration of an Aircraft Surface," *US Patent 2,504,684*, 1950.

[35] J. Blondeau and D. J. Pines, "Design and Testing of a Pneumatic Telescopic Wing for Unmanned Aerial Vehicles," *Journal of Aircraft*, vol. 44, no. 4, pp. 1088–1099, 2007.

[36] A. Leite, J. Vale, F. Lau, and A. Suleman, "Development of Morphing Strategies for a Flight Demonstrator Remotely Piloted Vehicle," in *50th AIAA/ASME/ASCE/AHS/ASC Structures, Structural Dynamics, and Materials Conference*, pp. 1–15, 2009.

[37] D. R. Bye and P. D. McClure, "Design of a Morphing Vehicle," in *48th AIAA/ASME/ASCE/AHS/ASC Structures, Structural Dynamics, and Materials Conference*, vol. 44, pp. 1–16, 2007.

[38] J. J. Henry and D. J. Pines, "A mathematical model for roll dynamics by use of a morphing-span wing," in *Collection of Technical Papers - AIAA/ASME/ASCE/AHS/ASC Structures, Structural Dynamics and Materials Conference*, vol. 1, pp. 76–91, 2007.

[39] T. M. Seigler, J.-S. Bae, and D. J. Inman, "Flight Control of a Variable Span Cruise Missile," in *ASME International Mechanical Engineering Congress and Exposition*, no. 47063, (Anaheim, California), pp. 565–574, ASME, 2004.

[40] P. Bourdin, A. Gatto, and M. I. Friswell, "Potential of Articulated Split Wingtips for Morphing-Based Control of a Flying Wing," in *25th AIAA Applied Aerodynamics Conference*, pp. 1–16, 2007.

[41] M. D. Skillen and W. A. Crossley, "Modeling and Optimization for Morphing Wing Concept Generation II Part I : Morphing Wing Modeling and Structural Sizing Techniques," *NASA Report*, no. February, pp. 1–45, 2008.

[42] X. Lachenal, P. M. Weaver, and A. Pirrera, "Concept for a Deployable Wing," in *Proceedings of the ASME 2014 Conference on Smart Materials, Adaptive Structures and Intelligent Systems*, pp. 1–8, 2014.

[43] J.-S. Bae, T. M. Seigler, and D. J. Inman, "Aerodynamic and Static Aeroelastic Characteristics of a Variable-Span Morphing Wing," *Journal of Aircraft*, vol. 42, no. 2, pp. 528–534, 2005.

[44] J. L. Reed, C. D. Hemmelgarn, B. M. Pelley, and E. Havens, "Adaptive wing structures," in *Proceedings Smart Structures and Materials*, vol. 5762, pp. 5711–5762, 2005.

[45] D. A. Perkins, J. L. Reed, and E. Havens, "Morphing wing structures for loitering air vehicles," in *Collection of Technical Papers - AIAA/ASME/ASCE/AHS/ASC Structures, Structural Dynamics and Materials Conference*, pp. 1–10, 2004.

[46] J. D. Anderson, *Introduction to Flight*.
New York, New York: McGraw-Hill, 8th ed., 2016.

[47] P. de Marmier and N. Wereley, "Control of Sweep Using Pneumatic Actuators to Morph Wings of Small Scale UAVs," in *AIAA/ASME/ASCE/AHS/ASC Structures, Structural Dynamics, and Materials Conference*, (Norfolk, Virginia), American Institute of Aeronautics and Astronautics, 2003.

[48] Y. Yu, X. Li, W. Zhang, and J. Leng, "Investigation on adaptive wing structure based on shape memory polymer composite hinge," *Proceedings of SPIE - The International Society for Optical Engineering*, vol. 6423, no. 2, pp. 64231D–64231D–7, 2007.

[49] F. Mattioni, A. Gatto, P. M. Weaver, M. Friswell, and K. Potter, "The application of residual stress tailoring of snap-through composites for variable sweep wings," in *47th AIAA/ASME/ASCE/AHS/ASC Structures, Structural Dynamics, and Materials Conference*, no. May, (Newport, Rhode Island), pp. 1–12, American Institute of Aeronautics and Astronautics, 2006.

[50] G. D. Miller, "Active Flexible Wing (AFW) Technology," tech. rep., Rockwell International, 1988.

[51] E. Pendleton, "Back To the Future Active Aeroelastic Wing Technology & the X-53 an Approach To Morphing," *RTO AVT Symposium on Active Control Technology for Enhanced Performance Operational Capabilities of Military Aircraft, Land Vehicles and Sea Vehicles*, pp. 1–6, 2000.

[52] N. K. Yoon, C. H. Chung, Y. H. Na, and S. J. Shin, "Control reversal and torsional divergence analysis for a high-aspect-ratio wing," *Journal of Mechanical Science and Technology*, vol. 26, no. 12, pp. 3921–3931, 2012.

[53] O. Stodieck, J. E. Cooper, P. M. Weaver, and P. Kealy, "Aeroelastic Tailoring of a Representative Wing Box Using Tow-Steered Composites," *AIAA Journal*, vol. 55, pp. 1–15, 2016.

[54] K. E. Griffin and M. A. Hopkins, "Smart Stiffness for Improved Roll Control," *Journal of Aircraft*, vol. 34, no. 3, pp. 445–447, 1997.

[55] P. C. Chen, D. Sarhaddi, R. Jha, D. D. Liu, K. Griffin, and R. Yurkovich, "Variable Stiffness Spar Approach for Aircraft Maneuver Enhancement Using ASTROS," *Journal of Aircraft*, vol. 37, no. 5, pp. 865–871, 2000.

[56] J. E. Cooper, "Adaptive Stiffness Structures for Air Vehicle Drag Reduction," in *Multifunctional Structures / Integration of Sensors and Antennas Meeting Proceedings RTO-MP-AVT-141*, pp. 1–13, 2006.

[57] H. Garcia, M. Abdulrahim, and R. Lind, "Roll Control for a Micro Air Vehicle Using Active Wing Morphing," in *AIAA Guidance, Navigation, and Control Conference and Exhibit*, 2003.

[58] B. Stanford, M. Abdulrahim, R. Lind, and P. Ifju, "Investigation of Membrane Actuation for Roll Control of a Micro Air Vehicle," *Journal of Aircraft*, vol. 44, no. 3, pp. 741–749, 2007.

[59] R. M. Ajaj, M. I. Friswell, D. D. Smith, G. Allegri, and A. T. Isikveren, "Roll Control of a UAV Using an Adaptive Torsion Structure," in *52nd AIAA/ASME/ASCE/AHS/ASC Structures, Structural Dynamics and Materials Conference*, pp. 1–15, 2011.

[60] E. F. Crawley and J. de Luis, "Use of piezoelectric actuators as elements of intelligent structures," *AIAA Journal*, vol. 25, no. 10, pp. 1373–1385, 1987.

[61] S. M. Ehlers and T. A. Weisshaar, "Static aeroelastic behavior of an adaptive laminated piezoelectric composite wing ," *31st AIAA/ASME/ASCE/AHS/ASC Structures, Structural Dynamics and Materials Conference*, pp. 1611–1623, 1990.

[62] D. Sahoo and C. Cesnik, "Roll Maneuver Control of UCAV Wing Using Anisotropic Piezoelectric Actuators," in *43rd AIAA/ASME/ASCE/AHS/ASC Structures, Structural Dynamics, and Materials Conference*, pp. 1–11, 2002.

[63] M. L. Wilbur and W. K. Wilkie, "Active-Twist Rotor Control Applications for UAVs," *U.S. Army Research Laboratory Vehicle Technology Directorate*, pp. 185–192, 2004.

[64] C. A. Martin, J. D. Bartley-Cho, J. S. Flanagan, and B. F. Carpenter, "Design and fabrication of Smart Wing wind tunnel model and SMA control surfaces," in *Proc. SPIE 3674, Smart Structures and Materials: Smart Structures and Materials 1999: Industrial and Commercial Applications of Smart Structures Technologies*, (Newport Beach, CA), 1999.

[65] Y. K. Changho Nam, Aditi Chattopadhyay, "Application of shape memory alloy (SMA) spars for aircraft maneuver enhancement," in *Proc. SPIE 4701, Smart Structures and Materials 2002: Smart Structures and Integrated Systems*, (San Diego, CA), 2002.

[66] D. M. Elzey, A. Y. N. Sofla, and H. N. G. Wadley, "A bio-inspired high-authority actuator for shape morphing structures," *Proceedings of SPIE*, vol. 5053, pp. 92–100, 2003.

[67] A. Pagano, S. Ameduri, V. Cokonaj, A. Prachar, Z. Zachariadis, and D. Drikakis, "Helicopter Blade Twist Control Through Sma Technology : Optimal Shape Prediction , Twist Actuator Realisation and Main Rotor Enhanced Performance Computation," *35th European Rotorcraft Forum*, pp. 1–11, 2009.

[68] S. Hadjiloucas, G. C. Walker, J. W. Bowen, and L. S. Karatzas, "Performance limitations of piezoelectric and force feedback electrostatic transducers in different applications," *Journal of Physics: Conference Series*, vol. 178, p. 012036, 7 2009.

[69] S. K. Nah and Z. W. Zhong, "A microgripper using piezoelectric actuation for micro-object manipulation," *Sensors and Actuators, A: Physical*, vol. 113, no. 1, pp. 218–224, 2007.

[70] J. Mohd Jani, M. Leary, A. Subic, and M. A. Gibson, "A review of shape memory alloy research, applications and opportunities," *Materials & Design (1980-2015)*, vol. 56, pp. 1078–1113, 4 2014.

[71] J. D. Bartley-Cho, D. P. Wang, C. A. Martin, J. N. Kudva, and M. N. West, "Development of High-rate, Adaptive Trailing Edge Control Surface for the Smart Wing Phase 2 Wind Tunnel Model," *Journal of Intelligent Materials Systems and Structures*, vol. 15, no. 4, pp. 279–291, 2004.

[72] W. Raither, M. Heymanns, A. Bergamini, and P. Ermanni, "Morphing wing structure with controllable twist based on adaptive bending-twist coupling," *Smart Materials and Structures*, vol. 22, no. 6, 2013.

[73] O. Stodieck, J. E. Cooper, P. M. Weaver, and P. Kealy, "Improved aeroelastic tailoring using tow-steered composites," *Composite Structures*, vol. 106, pp. 703–715, 2013.

[74] G. Francois, J. E. Cooper, and P. Weaver, "Impact of the Wing Sweep Angle and Rib Orientation on Wing Structural Response for Un-Tapered Wings," in *57th AIAA/ASCE/AHS/ASC Structures, Structural Dynamics, and Materials Conference*, 2016.

[75] A. Shelton, A. Tomar, J. Prasad, M. Smith, and N. Komerath, "Active Multiple Winglets for Improved Unmanned-Aerial-Vehicle Performance," *Journal of Aircraft*, vol. 43, no. 1, pp. 110–116, 2006.

[76] P. Bourdin, A. Gatto, and M. I. Friswell, "Aircraft Control via Variable Cant-Angle Winglets," *Journal of Aircraft*, vol. 45, no. 2, pp. 414–423, 2008.

[77] A. Gatto, P. Bourdin, and M. I. Friswell, "Experimental Investigation into Articulated Winglet Effects on Flying Wing Surface Pressure Aerodynamics," *Journal of Aircraft*, vol. 47, no. 5, pp. 1811–1815, 2010.

[78] J. Manzo and E. Garcia, "Demonstration of an insitu morphing hyperelliptical cambered span wing mechanism," *Smart Materials and Structures*, vol. 19, no. 2, 2010.

[79] B. A. Grohmann, C. Maucher, T. Prunhuber, P. Janker, O. Dieterich, B. Enenkl, M. Bauer, E. Ahci, A. Altmikus, and H. Baier, "Multidisciplinary design and optimization of active trailing edge for smart helicopter rotor blade," *Mechanics of Advanced Materials and Structures*, vol. 15, no. 3-4, pp. 307–324, 2008.

[80] F. Previtali, G. Molinari, A. F. Arrieta, M. Guillaume, and P. Ermanni, "Design and experimental characterisation of a morphing wing with enhanced corrugated skin," *Journal of Intelligent Material Systems and Structures*, vol. 27, no. 2, pp. 1–15, 2015.

[81] A. P. Milojević and N. D. Pavlović, "Development of a new adaptive shape morphing compliant structure with embedded actuators," *Journal of Intelligent Material Systems and Structures*, vol. 27, no. 10, pp. 1306–1328, 2016.

[82] S. Vasista, J. Riemenschneider, B. van de Kamp, H. P. Monner, R. C. M. Cheung, C. Wales, and J. E. Cooper, "Evaluation of a Compliant Droop-Nose Morphing Wing Tip via Experimental Tests," *Journal of Aircraft*, vol. 54, no. 2, pp. 519–534, 2017.

[83] A. De Gaspari, S. Ricci, and L. Riccobene, "Design, Manufacturing and Wind Tunnel Validation of an Active Camber Morphing Wing Based on Compliant Structures," in *25th International Conference on Adaptive Structures and Technologies (ICAST 2014)*, pp. 1–12, 2014.

[84] N. P. Werter, J. Sodja, G. Spirlet, and R. De Breuker, "Design and experiments of a warp induced camber and twist morphing leading and trailing edge device," in *24th AIAA/AHS Adaptive Structures Conference*, no. January, pp. 1–20, 2016.

[85] N. Nguyen, K. Trinh, K. Reynolds, J. Kless, M. Aftosmis, J. Urnes, Sr., and C. Ippolito, "Elastically Shaped Wing Optimization and Aircraft Concept for Improved Cruise Efficiency," pp. 1–44, 2013.

[86] Flexsys, "flexfoil Variable Gemoetry Control Surfaces," 2014.

[87] S. Ramsey, "NASA Successfully Tests Shape-Changing Wing for Next Gen Aviation," 2015.

[88] D. P. Raymer, *Aircraft Design: A Conceptual Approach, Volume 1*.
No. v. 1 in AIAA Educational Series, American Institute of Aeronautics and Astronautics, 4 ed., 2006.

[89] B. K. S. Woods and M. I. Friswell, "Multi-objective geometry optimization of the Fish Bone Active Camber morphing airfoil," *Journal of Intelligent Material Systems and Structures*, vol. 27, no. 6, pp. 808–819, 2016.

[90] J. D. Anderson, *Fundamentals of Aerodynamics*.
New York, New York: McGraw-Hill, 2010.

[91] J. M. Whitney, *Structural Analysis of Laminated Anisotropic Plates*.
Lancaster, Pennsylvania: Technomic Publishing, 1987.

[92] S. Ilanko, L. Monterrubio, and Y. Mochida, *The Rayleigh-Ritz Method for Structural Analysis*.
Iste Series, London and New York: Wiley, 2015.

[93] M. H. Hyer, *Stress Analysis of Fiber-Reinforced Composite Materials*.
New Delhi: McGraw-Hill, 2014.

[94] A. E. Green, "Double fourier series and boundary value problems," *Mathematical Proceedings of the Cambridge Philosophical Society*, vol. 40, no. 3, pp. 222–228, 1944.

[95] C. Fo-van, "Bending of Uniformly Cantilever Rectangular Plates," *Applied Mathematics and Mechanics*, vol. I, no. 3, pp. 371–383, 1980.

[96] K. Bhaskar and B. Kaushik, "Simple and exact series solutions for flexure of orthotropic rectangular plates with any combination of clamped and simply supported edges," *Composite Structures*, vol. 63, no. 1, pp. 63–68, 2004.

[97] M. Khalili, K. Malekzadeh, and R. Mittal, "A new approach to static and dynamic analysis of composite plates with different boundary conditions," *Composite Structures*, vol. 69, no. 2, pp. 149–155, 2005.

[98] R. B. Bhat, "Plate Deflections Using Orthogonal Polynomials," *Journal of Engineering Mechanics*, vol. I, no. 11, pp. 1301–1309, 1986.

[99] R. F. Rango, F. J. Bellomo, and L. G. Nallim, "A general ritz algorithm for static analysis of arbitrary laminated composite plates using first order shear deformation theory," *Journal of Engineering Research*, vol. 10, no. 2, pp. 1–12, 2013.

[100] M. Abramowitz and I. A. Segun, eds., *Handbook of Mathematical Functions with Formulas, Graphs and Mathematical Tables*.
New York: Dover Publications, Inc., 5th ed. ed., 1968.

[101] J. P. Boyd and R. Petschek, "The relationships between Chebyshev, Legendre and Jacobi polynomials: The generic superiority of chebyshev polynomials and three important exceptions," *Journal of Scientific Computing*, vol. 59, no. 1, pp. 1–27, 2014.

[102] Z. Wu, G. Raju, and P. M. Weaver, "Comparison of Variational, Differential Quadrature, and Approximate Closed-Form Solution Methods for Buckling of Highly Flexurally Anisotropic Laminates," *Journal of engineering mechanics*, vol. 139, no. 8, pp. 1073–1083, 2012.

[103] B. H. Coburn, Z. Wu, and P. M. Weaver, "Buckling analysis of stiffened variable angle tow panels," *Composite Structures*, vol. 111, no. 1, pp. 259–270, 2014.

[104] M. P. O'Donnell and P. M. Weaver, "RAPID analysis of variable stiffness beams and plates: Legendre polynomial triple-product formulation," *International Journal for Numerical Methods in Engineering*, 2017.

[105] R. Vescovini and C. Bisagni, "Buckling analysis and optimization of stiffened composite flat and curved panels," *AIAA Journal*, vol. 50, no. 4, pp. 904–915, 2012.

[106] N. Jaunky, N. Knight, and D. Ambur, "Buckling of arbitrary quadrilateral anisotropic plates," *AIAA Journal*, vol. 33, no. 5, pp. 938–944, 1995.

[107] B. H. Coburn, *Buckling of stiffened variable stiffness panels*.
PhD thesis, University of Bristol, 2015.

[108] A. K. Cline, C. B. Moler, G. W. Stewart, and J. H. Wilkinson, "An Estimate for the Condition Number of a Matrix," *SIAM Journal on Applied Mathematics*, vol. 16, no. 2, pp. 368–375, 1979.

[109] R. M. Groh, *Non-classical effects in straight-fibre and tow-steered composite beams and plates*.
PhD thesis, University of Bristol, 2015.

[110] S. Adeeb, *Introduction to Solid Mechanics & Finite Element Analysis. Retrieved from https://sameradeeb-new.srv.ualberta.ca*.
2020.

[111] M. H. Datoo, *Mechanics of Fibrous Composites*.
London: Elsevier Science Publishers LTD, 1991.

[112] Cambridge University Engineering Department, *Materials Data Book*.
2003.

[113] B. K. S. Woods and M. I. Friswell, "Fluid-Structure Interaction Analysis of the Fish Bone Active Camber Mechanism," in *54th AIAA/ASME/ASCE/AHS/ASC Structures, Structural Dynamics, and Materials Conference*, (Boston, Massachusetts), pp. 1–15, 2013.

[114] S. P. Timoshenko, "LXVI. On the correction for shear of the differential equation for transverse vibrations of prismatic bars," *Philosophical Magazine Series 6*, vol. 41, no. 245, pp. 744–746, 1921.

[115] E. Oñate, *Thick/Thin Plates. Reissner-Mindlin Theory*.
Dordrecht: Springer Netherlands, 2013.

[116] R. M. Groh and P. M. Weaver, "Static inconsistencies in certain axiomatic higher-order shear deformation theories for beams, plates and shells," *Composite Structures*, vol. 120, pp. 231–245, 2015.

[117] Z. Wu, G. Raju, and P. M. Weaver, "Framework for the Buckling Optimization of Variable-Angle Tow Composite Plates," *AIAA Journal*, vol. 53, no. 12, pp. 3788–3804, 2015.

[118] KST, "X10 Wing Servo," 2017.

[119] D3039, "Standard Test Method for Tensile Properties of Polymer Matrix Composite Materials," *ASTM International*, vol. 08, pp. 1–13, 2014.

[120] D3518, "Standard Test Method for In-Plane Shear Response of Polymer Matrix Composite Materials by Tensile Test," *ASTM International*, vol. 94, no. Reapproved, pp. 1–7, 2007.

[121] D638, "Standard test method for tensile properties of plastics," *ASTM International*, pp. 1–16, 2013.

[122] Imetrum, "3D Measurement Head Range," 2018.

[123] Maxon, "maxon DC motor and maxon EC motor," 2014.

[124] "Shape Adaptive Blades for Rotorcraft Efficiency," 2019.

[125] Hexcel, "HexPly 8552," *Product Data Sheet*, 2016.

[126] J. Szodruch, "The influence of camber variation on the aerodynamics of civil transport aircraft," *23rd Aerospace Sciences Meeting*, 1985.

[127] J. Szodruch and R. Hilbig, "Variable wing camber for transport aircraft," *Progress in Aerospace Sciences*, vol. 25, no. 3, pp. 297–328, 1988.

[128] L. F. Campanile and D. Sachau, "Belt-rib concept: a structronic approach to variable camber," *Journal of Intelligent Material Systems and Structures*, vol. 11, no. 3, pp. 215–224, 2000.

[129] S. Daynes and P. M. Weaver, "Morphing Blade Fluid-Structure Interaction," in *53rd AIAA/ASME/ASCE/AHS/ASC Structures, Structural Dynamics and Materials Conference*, no. April, (Honolulu, Hawaii), 2012.

[130] O. Bilgen, K. Kochersberger, E. Diggs, A. Kurdila, and D. Inman, "Morphing Wing Micro-Air-Vehicles via Macro-Fiber-Composite Actuators," in *48th AIAA/ASME/ASCE/AHS/ASC Structures, Structural Dynamics, and Materials Conference*, pp. 1–16, 2007.

[131] Q. Ai, H. Kamliya Jawahar, and M. Azarpeyvand, "Experimental investigation of aerodynamic performance of airfoils fitted with morphing trailing edges," *54th AIAA Aerospace Sciences Meeting*, 2016.

[132] T. Yokozeki, A. Sugiura, and Y. Hirano, "Development and Wind Tunnel Test of Variable Camber Morphing Wing," in *22nd AIAA/ASME/AHS Adaptive Structures Conference*, pp. 6–13, 2014.

[133] A. AEROTECH, "Operational Manual for Swansea University Low Speed Wind Tunnel," 2017.

[134] M. Drela, "XFOIL: An Analysis and Design System for Low Reynolds Number Airfoils," in *Lecture Notes in Engineering* (T. Mueller, ed.), pp. 1–12, Berlin, Heidelberg: Springer, 54 ed., 1989.

[135] S. Fournier and B. K. Woods, "Surrogate Model of Fish Bone Active Camber concept," in *AIAA Scitech 2019 Forum*, (San Diego, CA), pp. 1–12, American Institute of Aeronautics and Astronautics, 2019.

[136] J. Barlow, W. Rae, and A. Pope, *Low-Speed Wind Tunnel Testing*. Wiley, 3rd ed., 1999.

[137] R. Ashenden, W. Lindberg, and J. D. Marwitz, "Two-dimensional NACA 23012 airfoil performance degradation by super cooled cloud, drizzle, and rain drop icing," in *34th Aerospace Sciences Meeting and Exhibition*, 1996.

[138] S. G. Pouryoussefi, M. Mirzaei, M. M. Nazemi, M. Fouladi, and A. Doostmahmoudi, "Experimental study of ice accretion effects on aerodynamic performance of an NACA 23012 airfoil," *Chinese Journal of Aeronautics*, vol. 29, no. 3, pp. 585–595, 2016.

[139] J. G. Leishman, "Dynamic stall experiments on the NACA 23012 aerofoil," *Experiments in Fluids*, vol. 9, pp. 49–58, 1990.

[140] E. N. Jacobs and A. Sherman, "Airfoil Section Characteristics as Affected by Variations of Reynolds Number," tech. rep., National Advisory Committee for Aeronautics, Langley Field, Virginia, 1939.

[141] S. J. Huntley, C. B. Allen, and B. K. Woods, "Computational Analysis of the Aerodynamics of Camber Morphing," in *AIAA Aviation Forum*, (Dallas, Texas), pp. 1–20, 2019.

[142] A. Y. Tang and N. Amin, "Some Numerical Approaches to Solve Fluid Structure Interaction Problems in Blood Flow," *Abstract and Applied Analysis*, vol. 2014, pp. 1–8, 2014.

[143] G. Sieber, *Numerical Simulation of Fluid-Structure Interaction Using Loose Coupling Methods*.
PhD thesis, 2002.

[144] P. Krawczyk, A. Beyene, and D. MacPhee, "Fluid structure interaction of a morphed wind turbine blade," *International Journal of Energy Research*, vol. 37, pp. 1784–1793, 2013.

[145] D. W. MacPhee and A. Beyene, "Fluid-structure interaction analysis of a morphing vertical axis wind turbine," *Journal of Fluids and Structures*, vol. 60, pp. 143–159, 2016.

[146] S. D. Oehler;, D. J. Hartl;, T. L. Turner;, and D. C. Lagoudas, "Modeling fluid structure interaction with shape memory alloy actuated morphing aerostructures," in *Proc. SPIE 8343, Industrial and Commercial Applications of Smart Structures Technologies*, (San Diego, CA), p. 834305, 2012.

[147] H. Heo, J. Ju, and D. M. Kim, "Compliant cellular structures: Application to a passive morphing airfoil," *Composite Structures*, vol. 106, pp. 560–569, 2013.

[148] A. K. Barlas and B. Akay, "Optimization of morphing flaps based on fluid structure interaction modeling," in *AIAA SciTech Forum*, (Kissimmee, Florida), pp. 1–15, 2018.

[149] S. C. Miller, M. P. Rumpfkeil, and J. J. Joo, "Fluid-Structure Interaction of a Variable Camber Compliant Wing," in *AIAA SciTech Forum*, pp. 1–12, 2015.

[150] U. Fasel, D. Keidel, G. Molinari, and P. Ermanni, "Aeroservoelastic Optimization of Morphing Airborne Wind Energy Wings," in *AIAA Scitech 2019 Forum*, (San Diego, CA), 2019.

[151] K. Dixon, C. J. Simão Ferreira, C. Hofemann, G. Van Bussel, and G. Van Kuik, "A 3D unsteady panel method for vertical axis wind turbines," in *European Wind Energy Conference and Exhibition 2008*, vol. 6, (Brussels, Belgium), pp. 2981–2990, 2008.

[152] S. Pinzón, "Introducción a la teoría VLM (Vortex Lattice Theory)," *Ciencia y Poder Aéreo*, vol. 10, no. 1, p. 39, 2017.

[153] D. Owens, "Weissinger's model of the nonlinear lifting-line method for aircraft design," in *36th AIAA Aerospace Sciences Meeting and Exhibit*, pp. 1–10, American Institute of Aeronautics and Astronautics, 1998.

[154] J. C. Sivells and R. H. Neely, "Method for Calculating Wing Characteristics by Lifting-Line Theory using Nonlinear Section Lift Data," *NASA Technical Note No. 1269*, 1947.

[155] J. Anderson, S. Corda, and D. Van Wie, "Numerical lifting line theory applied to drooped leading-edge wings below and above stall," *Journal of Aircraft*, vol. 17, no. 12, pp. 898–904, 1980.

[156] O. Şugar Gabor, A. Koreanschi, and R. M. Botez, "A new non-linear vortex lattice method: Applications to wing aerodynamic optimizations," *Chinese Journal of Aeronautics*, vol. 29, no. 5, pp. 1178–1195, 2016.

[157] O. Şugar-Gabor, A. Koreanschi, and M. R. Ruxandra, "An efficient numerical lifting line method for practical wing optimization through morphing on the Hydra Technologies UAS-S4," in *CASI AERO 2013 Conference*, (Toronto, Canada), pp. 1–11, 2013.

[158] E. Chadwick, "A slender-wing theory in potential flow," *Proceedings of the Royal Society A: Mathematical, Physical and Engineering Sciences*, vol. 461, no. 2054, pp. 415–432, 2005.

[159] J. Katz and A. Plotkin, *Low-Speed Aerodynamics: From Wing Theory to Panel Methods*. Singapore: McGraw-Hill, 1991.

[160] W. F. Phillips and D. O. Snyder, "Modern Adaptation of Prandtl's Classic Lifting-Line Theory," *Journal of Aircraft*, vol. 37, no. 4, pp. 662–670, 2000.

[161] W. Mason, *Appendix A: Geometry for Aerodynamicists*.
Virginia Polytechnic Institute and State University, 1997.

[162] T. Craft, *Numerical Solution of Equations*.
Manchester, UK: The University of Manchester, 2008.

[163] J. H. Ferziger and M. Peric, *Computational Methods for Fluid Dynamics*.
Springer-Verlag Berlin Heidelberg, 3rd ed., 2002.

[164] R. M. Barron and A. A. S. Neyshabouri, "Effects of under-relaxation factors on turbulent flow simulations," *International Journal for Numerical Methods in Fluids*, vol. 42, pp. 923–928, 2003.

[165] R. Oliveira, "rafael-aero/XFOILinterface (https://www.github.com/rafael-aero/XFOILinterface)," *GitHub*, 2019.

[166] G. Tornero, "Non-Linear Weissinger Lifting-Line Model for Preliminary 3D Aerodynamic Analysis of Morphing Wings," *Masters of Engineering Project. University of Bristol*, pp. 1–22, 2017.

[167] A. Deperrois, "Guidelines for XFLR5: Analysis of foils and wings operating at low Reynolds numbers," no. February, pp. 1–72, 2013.

[168] S. C. Smith, "A Computational and Experimental Study of Nonlinear Aspects of Induced Drag," *NASA Report No 3598*, 1996.

[169] M. V. Cook, *Static Equilibrium and Trim*.
Butterworth-Heinemann, 2nd ed., 2013.

[170] M. K. Lotov A.V., *Visualizing the Pareto Frontier. In: Branke J., Deb K., Miettinen K., Słowiński R. (eds) Multiobjective Optimization. Lecture Notes in Computer Science*.
Berlin, Heidelberg: Springer, 2008.